



**Universidad Carlos III de Madrid**  
*Dpto. Ciencia e Ingeniería de Materiales e  
Ingeniería Química*

# ***An Approach to Design New Coatings for Biomedical Applications***

Tesis Doctoral presentada por  
**Amir Abdelsamie El-hadad**

**Directores:**

Dr. Juan Carlos Galván

Dra. Violeta Barranco

**TESIS DOCTORAL**

Leganés, Octubre 2012



TESIS DOCTORAL

***An Approach to Design New Coatings for  
Biomedical Applications***

Autor: **Amir Abdelsamie El-hadad**

Directores: Dr. Juan Carlos Galvan  
Dra. Violeta Barranco

Firma del Tribunal Calificador:

Firma

Presidente: (Nombre y apellidos)

Vocal: (Nombre y apellidos)

Vocal: (Nombre y apellidos)

Vocal: (Nombre y apellidos)

Secretario: (Nombre y apellidos)

Calificación:

Leganés, de de



*To My Family*



## *Acknowledgment*



## ACKNOWLEDGMENT

---

### ACKNOWLEDGMENT

My warmest thanks go to my advisor, Dr. Juan Carlos Galvan, who has been the best possible guide I could ever hope to have, not only scientifically. Similarly, I would like to thank my co-advisor Dr. Violeta Barranco, whose friendship has been precious to me.

I am deeply grateful to my tutor in Universidad Carlos III de Madrid, Dr Antonia Jiménez Morales for her support, and for her continuous encouragement.

Massive thanks for Dr. Javier González Benito Universidad Carlos III de Madrid, for his help during my administration procedures in the UC3M.

I would especially like to thank Mr. Diogenes Carbonell Boix for all the heart-warming encouragements and support he gave me.

I am greatly and deeply indebted to Prof. Carole Perry for giving me the opportunity to carry out a part of this research at her laboratory in the Nottingham Trent University. Also for taking the time to provide me with support and training in various techniques and uses of equipments.

Most cordial thanks also to Dr. David Belton, Dr. Marco Demurtas, Dr.Valeria Puddu and Graham Hickman who helped me so much during my staying in Nottingham Trent University , UK with their hospitality. Working with them has been a very important and pleasurable experience.

A special thanks to my colleagues at National Centre for Metallurgical Research CENIM and at Carlos III University - Madrid for their stimulating suggestions and help during the PhD.

The financial support of the CSIC is gratefully acknowledged.

Finally, I am grateful to my engaged and family members for their continued support, encouragement and understanding throughout my time in Spain.

I couldn't have done it without you **Sara** ...Love you.



## *Contents*



# Contents

	Page
Acknowledgement-----	I
Contents -----	II
Resumen -----	III
Abstract -----	IV
<b>Chapter (1)</b>	
<b>Theoretical Aspects</b>	
<b>1.1 - Biomaterials</b>	
1.1.1- Definition-----	1
1.1.2- Classification -----	2
I- According to its nature-----	2
II- According to its functionality-----	10
a) First generation-----	11
b) Second generation-----	11
c) Third generation-----	11
1.1.3- Structure of bone -----	12
<b>1.2- Tissue-Metallic Implant Interface -----</b>	<b>16</b>
1.2.1- Description-----	16
1.2.2-Tissue-metallic implant interaction-----	16
a ) Corrosion of Ti and Ti6Al4V alloy-----	17
b ) Protection of Ti and Ti6Al4V alloy -----	19
- Ti-Al oxides thermally generated-----	19
- Sol-gel coatings-----	20
a) Dip-coating-----	20
b) Spin-coating-----	21
c) Types of sol-gel coatings-----	22
c.1) Inorganic sol-gel coatings-----	22
c.2) Organic-inorganic hybrid sol-gel coatings-----	22
<b>1.3- Sol-gel technology -----</b>	<b>24</b>
1.3.1 Powders-----	26
1.3.2 Coatings-----	26
1.3.2.1 Bioactive coatings-----	26
1.3.2.2 Anticorrosive coatings-----	27

## CONETENTS

---

1.3.2.3 Multifunctional two layers system-----	28
1.4-Characterization techniques-----	29
1.4.1- Physico-chemical structural characterization-----	29
1.4.1.1 Differential thermal analysis (DTA)- -----	29
1.4.1.2 Thermo-gravimetric analysis (TGA) -----	30
1.4.1.3 X-ray diffraction (XRD) -----	31
1.4.1.4 Infrared (IR) spectroscopy-----	32
1.4.1.5 Nuclear magnetic resonance (NMR) -----	33
1.4.1.6 Contact angle ( $\theta$ )-----	33
1.4.1.7 Stylus profilometer-----	34
1.4.1.8 Scanning electron microscope (SEM) -----	34
1.4.2 Functionality-----	35
I. Biological characterization techniques -----	35
1.4.2.1 Simulated body fluid (SBF) -----	36
1.4.1.2 Bradford protein assays-----	36
1.4.2.3 Cellular cytotoxicity / proliferation-----	37
II. Electrochemical characterization technique-----	37
- Electrochemical characterization spectroscopy-----	37

## Chapter (2)

### Aim of the work

Aim of the work-----	49
----------------------	----

## Chapter (3)

### Materials & Methods

3.1- Inorganic Coating-----	52
3.1.1 Preparation-----	52
-HAp sol-----	52
-HAp Inorganic coating-----	53
3.1.2 Characterization-----	55
3.1.2.1 Thermal analysis: (DTA/TGA) -----	55
3.1.2.2 X-ray diffraction (XRD) -----	55
3.1.2.3 Fourier transform infrared spectroscopy (FTIR) -----	55
3.1.2.4 Immersion in SBF-----	56
3.1.2.5 Inductively coupled plasma (ICP) -----	56
3.1.2.6 Scanning electron microscope (SEM/EDX) -----	57

## CONETENTS

---

3.1.2.7 Corrosion behaviour-----	57
<b>3.2- Organic-Inorganic coatings</b>	<b>58</b>
3.2.1 Silanes/phosphorus mixture: properties & preparation-----	58
3.2.2 Optimization the preparation conditions ,(hydrolysis study) -----	61
3.2.2.1 MAPTMS/TMOS sol preparation -----	61
3.2.2.2 Preparation of MAPTMS/TMOS/ HAp hybrid-----	62
3.2.2.3 Preparation of MAPTMS/TMOS/TEP hybrid-----	62
3.2.2.4 Preparation of MAPTMS/TMOS/DMTSP hybrid-----	62
3.2.3- Organic-Inorganic coating application onto Ti6Al4V substrate ----	63
3.2.3.1 Substrate Preparation-----	63
3.2.3.2 Dip-coating of O-I hybrid on Ti6Al4V-----	63
3.2.4 Characterization	68
3.2.4.1 Fourier transforms infrared spectroscopy (FTIR) -----	68
3.2.4.2 Liquid-state nuclear magnetic resonance (NMR) -----	68
3.2.4.3 Thermogravimetric analysis (DTA/TGA) -----	68
3.2.4.4 Attenuated total reflectance-infrared spectroscopy -----	68
3.2.4.5 Solid state nuclear magnetic resonance (NMR) -----	69
3.2.4.6 X-ray diffraction (XRD) -----	69
3.2.4.7 Scanning electron microscope (SEM/EDX) -----	69
3.2.4.8 Viscosity -----	70
3.2.4.9 Coating thickness-----	70
3.2.4.10 Wettability -----	70
3.2.4.11 Confocal microscope-----	70
3.2.5- In-vitro bioactivity	71
3.2.5.1 Protein adsorption -----	71
3.2.5.2 Neutral Red cell viability/cytotoxicity assay-----	72
3.2.5.3 Immunofluorescence-----	72
3.2.5.4 Statistical analysis-----	73
3.2.5.5 Corrosion behaviour-----	73

## Chapter (4)

### Inorganic sol-gel derived thin films and hydroxyapatite powders

- Introduction -----	74
- Aim -----	75
4.1- Characterization of the sol-gel derived HAp powders-----	75

## CONETENTS

---

4.1.1. Thermal analysis (DTA/TGA) -----	76
4.1.2. Fourier transform infrared spectroscopy analysis (FTIR)-----	78
4.1.3. X-ray Diffraction Analysis (XRD) -----	81
4.2. In-vitro evaluation of functional properties of the resulting sol-gel derived HAp materials-----	89
- Stage One: Immersion tests of HAp powders in Kokubo's simulated body fluid (SBF) -----	90
- Stage Two: Immersion tests of the HAp coating/Ti6Al4V alloy system in Kokubo's simulated body fluid (SBF) -----	90
4.2.1. Bioactivity evaluation of the sol-gel HAp powders -----	90
4.2.2. Evaluation of the surface bioactivity and the corrosion protection behaviour of the sol-gel derived HAp coatings -----	97
- Immersion tests of HAp-coatings/Ti6Al4V alloy system in SBF-----	98
- Interactions of SBF with the HAp-coating/Ti6Al4V alloy system. Corrosion protection behaviour-----	99
- Selection of the electrical equivalent circuit which describes the studied systems-----	103
- Interpretation of the results obtained -----	106
Conclusions-----	109

### Chapter (5)

#### Organic-inorganic hybrid sol-gel – Optimization of the synthesis processes of the hybrid matrix

- Introduction -----	111
- Aim-----	113
5.1- Fourier transform infrared spectroscopy (FTIR) -----	114
5.2- Nuclear magnetic resonance (NMR) -----	118
5.2.1- <sup>29</sup> Si-NMR-----	118
5.2.2- <sup>13</sup> C-NMR-----	123
- Conclusions-----	127

### Chapter (6)

#### Organic-inorganic hybrid sol-gel thin films modified with Hydroxyapatite particles

Introduction-----	128
Aim -----	130

## CONETENTS

---

6.1 Characterization-----	130
6.1.1 Thermal Analysis (TGA) -----	131
6.1.2 Attenuated Total Reflectance Infrared Spectroscopy (ATR-IR) -----	133
6.1.3 Solid state Nuclear Magnetic Resonance (NMR) -----	135
6.1.3.1 <sup>29</sup> Si -NMR spectroscopy-----	135
6.1.3.2 <sup>13</sup> C -NMR spectroscopy-----	138
6.1.3.3 <sup>31</sup> P -NMR spectroscopy-----	139
6.1.4 X-ray Diffraction (XRD)-----	140
6.1.5 Rheology -----	141
6.1.6 Film Thickness -----	143
6.1.7 Wettability (Contact Angle) -----	144
6.1.8 Scanning Electron Microscope (SEM/EDX) -----	145
6.1.9 Topography-----	148
6.2 In-vitro bioactivity-----	150
6.2.1 Protein adsorption-----	150
6.2.1.1 Amounts of adsorbed fibrinogen-----	151
6.2.2 Osteoblast – film interaction-----	154
6.2.2.1 Osteoblast viability/cytotoxicity-----	154
6.2.2.2 Osteoblasts adhesion-----	156
6.2.3 Immersion in SBF-----	158
6.3 In vitro corrosion protection behaviour -----	160
- Conclusions-----	172

## Chapter (7)

### Organic-inorganic hybrid sol-gel thin films modified with Triethylphosphite as phosphorous precursor

Introduction-----	173
Aim-----	173
7.1 Characterization-----	174
7.1.1 Thermal Analysis (TGA) -----	174
7.1.2 Attenuated Total Reflectance Infrared Spectroscopy-----	175
7.1.3 Solid state Nuclear Magnetic Resonance (NMR) -----	178
7.1.3.1- <sup>29</sup> Si -NMR spectroscopy-----	178
7.1.3.2- <sup>13</sup> C -NMR spectroscopy-----	181
7.1.4 Scanning Electron Microscope (SEM/EDX) -----	182
7.1.5 Phase separation problem with more TEP content-----	184
7.1.6 Rheology-----	185

## CONETENTS

---

7.1.7	Film Thickness -----	185
7.1.8	Wettability (Contact Angle) -----	186
7.1.9	Confocal microscope-----	188
7.2	In-vitro bioactivity-----	190
7.2.1	Protein adsorption-----	190
7.2.1.1	Amounts of adsorbed fibrinogen-----	191
7.2.2	Osteoblast – film interaction-----	192
7.2.2.1	Osteoblast proliferation/cytotoxicity-----	192
7.2.2.2	Osteoblasts adhesion-----	194
7.2.3.3	Immersion in SBF-----	196
7.3	In vitro corrosion protection behaviour -----	197
-	Conclusions-----	209

### Chapter (8)

#### Organic-inorganic hybrid sol-gel thin films modified with Dimethylsilylphosphite as phosphorous precursor

-	Introduction & Aim-----	210
8.1	Characterization -----	210
8.1 .1	Thermogravimetric analysis (TGA)-----	211
8.1.2	Attenuated total reflectance infrared (ATR-IR)-----	213
8.1.2.1	<sup>29</sup> Si-NMR-----	214
8.1.3	Scanning Electron Microscope (SEM/EDX) -----	215
8.1.4	Contact angle-----	217
8.2	In-vitro bioactivity-----	217
8.2.1	Cytotoxicity, proliferation-----	217
8.2.2	Cell adhesion-----	219
8.3	In vitro corrosion protection behaviour -----	221
-	Conclusion-----	233

### Chapter (9)

#### Comparison of functionalities of the O-I hybrid coatings /Ti6Al4V

9.1	Biological Protein adsorption-----	234
9.2	Cytotoxicity /viability-----	235
9.3	Osteoblasts adhesion-----	237

# CONETENTS

---

<b>9.4 corrosion protection behavior-----</b>	<b>239</b>
<b>General Conclusions-----</b>	<b>242</b>
<b>List of figures -----</b>	<b>245</b>
<b>List of Tables -----</b>	<b>252</b>
<b>Bibliographic Research -----</b>	<b>255</b>
<b>List of Publications-----</b>	<b>269</b>
<b>Participations in Conferences-----</b>	



## *Resumen*



## Resumen

Las aleaciones de Ti6Al4V son ampliamente utilizadas como biomaterial metálico para prótesis e implantes dentales debido a sus buenas propiedades mecánicas, excelente resistencia a la corrosión y buena biocompatibilidad. Sin embargo, son necesarios varios meses para una buena osteointegración debido a la naturaleza inerte de la aleación.

Un método innovador para solucionar esta desventaja consiste en el desarrollo de nuevos recubrimientos que confieran bioactividad a la superficie de la aleación Ti6Al4V a la vez que mejoran su resistencia a la corrosión. Por esta razón, distintos tipos de estrategias se han desarrollado estos últimos años para modificar la superficie de los implantes fabricados a partir de la aleación Ti6Al4V. Todas ellas tienen como objetivo principal mejorar la interfase implante-hueso activando la formación de tejido óseo y mejorando su estabilidad en la fase inicial de osteointegración. Uno de los mejores métodos para conseguir estas interfases se basa en la aplicación de recubrimientos bioactivos sobre la superficie de la aleación. Concretamente, mediante el método sol-gel se pueden obtener recubrimientos bioactivos híbridos órgano-inorgánicos sobre la superficie de la aleación.

El método sol-gel es de gran interés para la obtención de este tipo de recubrimientos porque ofrece la posibilidad de diseñar a medida las propiedades del material y/o recubrimiento deseado mediante la variación de la composición relativa de los precursores utilizados.

El objetivo principal de esta tesis se centra en el desarrollo de nuevos recubrimientos multifuncionales con buenas propiedades bioactivas y anticorrosivas. El procedimiento seguido para la consecución del objetivo principal ha consistido en varias etapas. La primera ha sido partir de la síntesis de un material de bioactividad conocida, Hidroxiapatita (HAp), y optimizar los parámetros del proceso sol-gel para conseguir las mejores propiedades bioactivas tanto en forma de nanopartículas como aplicado como recubrimiento inorgánico sobre la superficie de la aleación Ti6Al4V. Para ello, se ha

estudiado el efecto de la temperatura de tratamiento tanto en la respuesta bioactiva de las nanopartículas de HAp, como en la bioactividad y la resistencia a la corrosión del recubrimiento inorgánico de HAp sobre la aleación. La respuesta bioactiva *in-vitro* y la resistencia a la corrosión se han estudiado en presencia de fluido fisiológico simulado (SBF). Se han obtenido nanopartículas de HAp con una excelente bioactividad. En el caso de los recubrimientos inorgánicos de HAp, debido a las altas temperaturas para conseguir la forma cristalina de la HAp, se generaron algunas grietas en los recubrimientos. A pesar de ello, en la evaluación de bioactividad mostraron precipitación de apatita con estructura similar a la ósea. Dicha precipitación también contribuyó a mejorar el efecto barrera del recubrimiento, mediante el bloqueo de poros y grietas, evitando así la incorporación de iones tóxicos provenientes de la superficie de la aleación al fluido fisiológico.

La protección frente a la corrosión de un recubrimiento depende, en parte, de su habilidad para actuar como barrera evitando el acceso de especies corrosivas a la superficie metálica. Este hecho pone de manifiesto la necesidad de desarrollar otro tipo de recubrimientos, actuando como estímulo para la consecución de los siguientes objetivos de esta tesis. De esta forma, partiendo de los resultados obtenidos en la primera etapa con los recubrimientos inorgánicos de HAp, posteriormente, se ha ido aumentando la complejidad de los nuevos recubrimientos desarrollados hasta alcanzar los objetivos propuestos, bioactividad y resistencia a la corrosión.

Con el fin de obtener nuevos recubrimientos viables, así como sus óptimas condiciones de preparación, primeramente se desarrolló un nuevo estudio cuyo objetivo concreto ha sido la optimización del método de preparación de un nuevo recubrimiento híbrido órgano-inorgánico mediante el estudio de los cambios estructurales que tienen lugar durante los procesos de hidrólisis y condensación de una mezcla de  $\gamma$ -metacriloxipropiltrimetoxisilano (MAPTMS) y tetrametilortosilicato (TMOS) en solución después de la adición de agua y etanol. Este estudio se realizó mediante Espectroscopia Infraroja (IR) y Resonancia Magnético-Nuclear (RMN) del  $^{29}\text{Si}$  y  $^{13}\text{C}$  en estado líquido. Los resultados indicaron que la hidrólisis de estos dos precursores es un proceso dependiente del tiempo y cuatro horas de reacción es el tiempo óptimo para obtener recubrimientos

viables de ser aplicados y posteriormente poder actuar como matriz híbrida de recubrimientos más complejos.

Tras los resultados obtenidos en estas dos primeras etapas descritas, se han diseñado y obtenido tres nuevos recubrimientos híbridos órgano-inorgánico con las propiedades requeridas.

Dichos recubrimientos se basan en una matriz de MAPTMS/TMOS que ha sido modificada con distintos precursores de fósforo para dotarles de la deseada bioactividad. Los precursores de fósforo utilizados han sido nanopartículas de HAp, como precursor sólido de fósforo y trietilfosfito (TEP) y dimetilsililfosfito (DMTSP) como precursores líquidos de fósforo. Estos precursores se han añadido en distintas cantidades con el objetivo de obtener nuevos recubrimientos de interés físico, químico y biológico.

En esta etapa, durante la investigación, se han tenido en cuenta los siguientes aspectos:

1. Evaluación del efecto de la adición de los diferentes precursores de fósforo en la densificación de la matriz siloxánica.
2. Caracterización físico-química de los recubrimientos obtenidos.
3. Evaluación *in-vitro* de la osteointegración a partir de ensayos de citotoxicidad y adhesión de osteoblastos humanos.
4. Evaluación del comportamiento frente a la corrosión de los recubrimientos.

Los principales resultados obtenidos a lo largo de este estudio han demostrado que todos los recubrimientos preparados tienen un comportamiento ligeramente más hidrofóbico que la superficie de la aleación Ti6Al4V. Todos los recubrimientos modificados con los distintos precursores de fósforo tienen mayor densidad que la matriz MAPTMS/TMOS de partida. Este hecho les confiere a estos recubrimientos unas buenas propiedades para actuar como una barrera física efectiva entre la superficie de la aleación y el medio fisiológico, mejorando así su comportamiento frente a la corrosión. La presencia de los precursores de fosforo en estado liquido, ha resultado en un aumento del grado de

## RESUMEN

---

entrecruzamiento creando al mismo tiempo el fósforo sitios activos preferentes para la adsorción de proteínas. La importancia del fósforo en la división y proliferación celular confiere a su vez a estos recubrimientos bioactividad.

De todos los recubrimientos obtenidos y estudiados, el recubrimiento basado en MAPTMS/TMOS/DMTSP mostró la mejor respuesta biológica en términos de proliferación y adhesión de osteoblastos. En relación con las propiedades barrera ofrecidas por los recubrimientos diseñados, el recubrimiento obtenido mediante modificación química con TEP de la matriz MAPTMS/TMOS de partida ha sido el que mejores propiedades barrera ha mostrado durante 30 días de inmersión en SBF.

*Abstract*



## Abstract

Ti6Al4V alloy is widely used as implants for orthopedic and dental applications because of its superior mechanical properties, excellent corrosion resistance and good biocompatibility. However, it takes long period of several months for Ti6Al4V implants to integrate with the bone tissue due to their bio-inert feature in nature.

An innovating and incipient method to solve the above mentioned drawbacks consist of the development of new coatings which could improve both the biological and corrosion protection performance of the Ti6Al4V alloy. Thus, a variety of strategies have been implemented to modify the surface of Ti6Al4V-based implants and enhance bone growth and their initial stability. A common approach is the deposition of bioactive hybrid coatings including inorganic and organic units on the surface of the Ti6Al4V alloy via sol-gel method.

The sol-gel route is of great interest as it offers the possibility of tailoring the material properties by variation of the relative composition of the precursors used.

The aim of this thesis is focused on the development of new coatings, starting with inorganic hydroxyapatite (HAp) deposited onto Ti6Al4V substrate prepared through sol-gel route. The effect of thermal treatment temperature on both *in-vitro* bioactivity and corrosion performance has been studied in simulated body fluid solution (SBF). A complete physical-chemical characterization was done in all the thermally treated coatings obtained. *In-vitro* tests in SBF were carried out in order to investigate the biological performance of the films.

Due to the high temperature required for synthesizing HAp in crystalline form, porous and cracked coatings have been obtained, as a result of the thermal treatments applied to the prepared coatings. Although of these cracks, on the film was produced the precipitation of bone-like apatite after immersion in SBF. These precipitation products lead also to an improvement of the corrosion performance through blocking effect.

## ABSTRACT

---

The corrosion protection of the coating depends on its ability to act as a physical barrier preventing the penetration of corrosive species to reach the metal surface. This fact stimulated us to reach other goals through the preparation of sets of various new organic-inorganic hybrids. These new coatings have been also prepared through sol-gel route.

To obtain workable films and their optimum preparation conditions, a new study has been carried out. The aim of this new study has been to optimize the organic–inorganic hybrid preparation method through studying the structural changes which take place during the hydrolysis and condensation processes of a mixture of  $\gamma$ -methacryloxypropyltrimethoxysilane (MAPTMS) and tetramethylorthosilicate (TMOS) in solution after the addition of water and ethanol. FTIR, liquid-state  $^{29}\text{Si}$  and  $^{13}\text{C}$  nuclear magnetic resonance (NMR) have been applied for this purpose. The results indicated that, the hydrolysis process of the two silane precursors is a time-dependent process and four hours of reaction are required for obtaining workable films.

Then, after the results obtained in the first two stages of this PhD thesis, three different organic-inorganic hybrid coatings have been prepared. These coatings have been based on the MAPTMS/TMOS matrix modified with different phosphorous precursors; HAp as solid phosphorus precursor and triethylphosphite (TEP) and dimethylsilylphosphite (DMTSP) as liquid phosphorus precursors. These precursors have been added in different amounts with the aim to obtain new materials of physical-chemical and biological interest.

At this level, during investigation, the following four aspects have been taken into account:

1. Evaluation of the effect of the addition of the different phosphorous precursors on the densification of the siloxane network.
2. Physical-chemical characterization of the resulting coatings.
3. Evaluation of the *in-vitro* osteointegration of the coatings through assays of normal human osteoblast cytotoxicity and adhesion.

#### 4. Evaluation of the corrosion performance of the coatings.

The results obtained along this study have shown that, all the prepared coatings are relatively hydrophobic with respect to the un-coated alloy. All the modified films are denser than the control one based on the MAPTMS/TMOS matrix. This fact allows these coatings to act as effective physical barriers against corrosion. The presence of phosphorus precursors results in further cross-linking and at the same time act as binding sites for protein adsorption. The importance of phosphorus in cell division and proliferation make also these coatings bioactive. The coating based on MAPTMS/TMOS/DMTSP showed the best biological performance in terms of cell proliferation and adhesion. Concerning the barrier properties provided by the designed hybrid films, the sol-gel films obtained by the chemical modification of the MAPTMS/TMOS matrix with TEP, showed the best barrier properties when immersed in SBF for 30 days.



*Chapter (1)*  
*Theoretical Aspects*



## 1.1- Biomaterials

### 1.1.1- Definition

Biomaterials have been defined as “substance or combination of substances, synthetic or natural in origin, which can be used for a period of time, as a whole or as a part of a system which treats, augments, or replaces any tissue, organ, or function of the body”<sup>[1]</sup>. The materials used as implants should be non toxic and should not cause any inflammatory or allergic reactions in the human body. The success of the biomaterials is mainly dependent on the reaction of the human body to the implant, and this measures the biocompatibility of a material. The material to be accepted when implanted with in the body should exhibit:

- Biocompatibility: the implant should be accepted by the surrounding tissues without any adverse response from the body and vice versa.
- Bio-adaptability: should have capacity to collaborate with surrounding tissue and replace the removed body part in best way.
- Bio-functionality: should perform successfully the specific function of the replaced body part.

The degree of biocompatibility between living (tissue) and nonliving (implant) is used to determine the ability of a material to perform with an appropriate host response reaction of living system <sup>[2,3]</sup>. The success of the implant in the body (Biocompatibility) also depends on many parameters (Figure 1.1) <sup>[4]</sup>. The general criteria for materials selection for bone implant materials are:

- ✓ It is highly bioactive and form bond with the surrounding tissue and does not cause an inflammatory or toxic response beyond an acceptable tolerable level.
- ✓ It has appropriate mechanical properties, closest to natural bone.
- ✓ Nontoxic, with little or no foreign body reaction and be chemically stable or corrosion resistant.

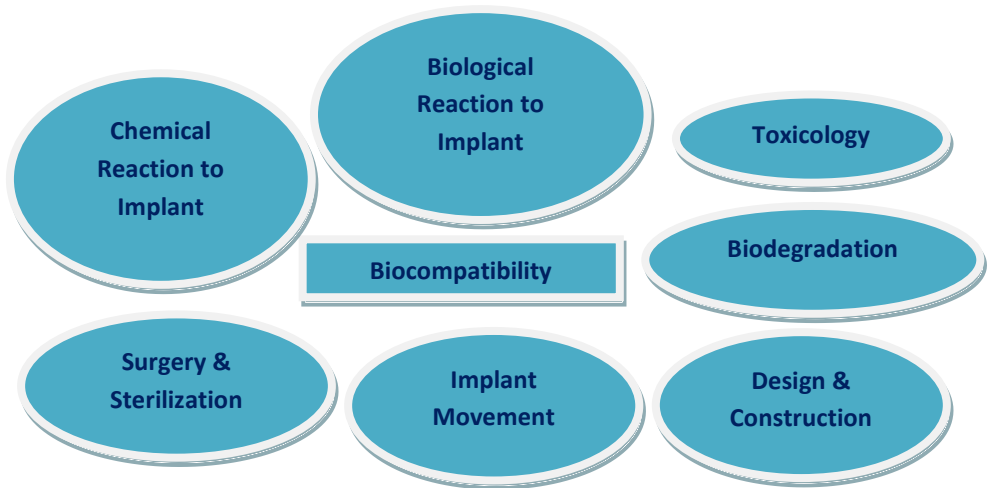


Fig. 1.1. Biocompatibility depending on a variety of system parameters.

### 1.1.2.-Classification

#### I. According to its nature:

According to its nature, bone-grafting materials can be divided into two main groups,

##### *1.1.2.1- Natural grafts*

Natural graft or autograft (organs, tissues or even proteins), which are transferred from healthy parts of the same patient. The bone autograft still the 'gold standard' for bone repair, especially because of the absence of immune rejection after surgery. The drawback of autograft is the requirement of an additional surgical operation that may lead to donor site morbidity and limited availability <sup>[5]</sup>.

Unlike bone autograft, allograft, the transplantation of organs or tissues from fresh cadavers to a living one, and xenografts, the graft taken from an animal, are widely available and do not require additional surgery on the patient. However, allograft bone has to undergo irradiation or freeze-drying to remove all immunogenic proteins, in order to avoid any risk of immunogenic reaction <sup>[6]</sup>. This in turn, has a negative effect on the osteoinductive and osteoconductive potential of the allograft, decreases their

biological performance as compared to autograft. Figure 1.2 shows an allograft heart valves (A) and, a skin graft (B).



**Fig. 1.2.** Types of natural grafts, allograft heart valves (A) skin graft (B).

### *1.1.2.2- Synthetic grafts*

There are four major types of materials: metals, ceramics and polymer and their composites used as biomaterials.

#### *a) Metals*

Metallic materials are most commonly used for load bearing application and internal fixation devices. They considered being more resistant to deformation compared with ceramics or polymeric materials due to combination of high mechanical strength and fracture toughness. The most commonly used metals as implants are titanium, stainless steel and cobalt chromium alloys <sup>[3]</sup>. Figure 1.3 shows a typical hip implant with titanium femoral (A) and, a dental implant (B).



**Fig.1.3** A typical hip implant with titanium femoral (A) dental Implant (B).

The drawback of metals is that, it may corrode due to the aggressive action of the physiological fluids. Corrosion is defined as the destruction or deterioration of a material because of reaction with its environment. Corrosion in body fluid is more complicated than in natural environments, because the degradation rate is affected by a variety of factors such as protein, pH <sup>[7]</sup>.

The corrosion of most conventional surgical alloys results in ions release from the implants which cause different biologically adverse reactions which finally lead to the failure of the implant <sup>[8,9]</sup>. Due to the composition difference between the metals and the body tissues, the metal implant does not form bond with bone. As a result, the immune system will isolate it from the surrounding bone by surrounding it by fibrous capsule <sup>[10]</sup>. Within the fibrous capsule the implant is free to perform a type of movement called micromotion. This motion of implant may results in local inflammation and leads to deterioration of implant function or the tissue at the interface of both <sup>[10,11]</sup>.

### ***b) Polymers***

Polymers are long chain molecules consisting of large number of small repeating units known as monomers. They have physical properties similar to those of the soft tissue, for that they are commonly used to replace tissues of the body e.g. skin, tendon, cartilage, vessel walls etc <sup>[3]</sup>. Synthetic polymeric biomaterials range from hydrophobic, non-water-absorbing materials, such as silicon rubber to hydrophilic ones such as poly (hydroxyethyl methacrylate) and beyond, to water-soluble materials such as (poly ethylene glycol). Two examples of polymeric materials are showed in Figure 1.4.

Successful examples of polymers used as implants are resorbable polymers such as (poly lactic acid - polyglycolic acid) (PLA-PGA) used for sutures. By the time, the suture will metabolize into carbon dioxide and water which can be absorbed by the host tissue. This type of degraded polymers is acting for a period of time and then disappears. This can be considered as good benefit but in real it is difficult to adjust the degradation rate with the rate of new tissue formation <sup>[11]</sup>.

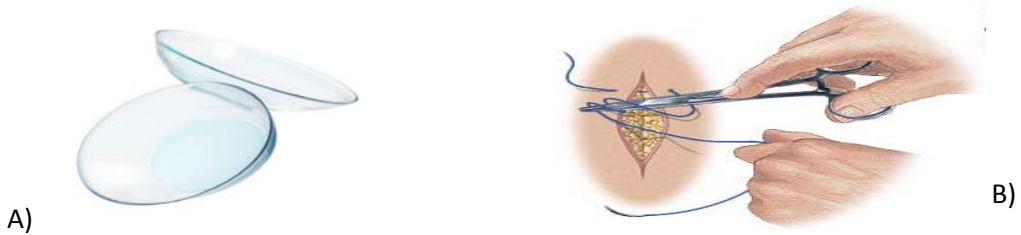


**Fig.1.4.** Polymeric biomaterials, contact lens (A), sutures (B).

### *c) Ceramics*

The term ceramic refers to inorganic compounds of metallic or nonmetallic materials, with interatomic bonding as ionic or covalent bonds which are generally formed at elevated temperatures. Bio-ceramics are a class of ceramics which used for skeletal or hard tissue repair<sup>[11]</sup>.

#### *c.1) Bioglasses*

“A bioactive material is one that elicits a specific biological response at the interface of the material, results in formation of a bond between the tissues and the material”<sup>[12]</sup>. Hench 1971s discovered that certain compositions of glasses in the system  $\text{SiO}_2$ ,  $\text{CaO}$ ,  $\text{Na}_2\text{O}$  and  $\text{P}_2\text{O}_5$  were able to form chemical and biological bond with the bone upon implantation<sup>[13]</sup>. These glasses when it become in contact with physiological fluids, a bone-like apatite layer equivalent to the inorganic minerals of natural bone will deposit on their surface. As this layer is formed, it will incorporate the collagen molecules and provide a media for the proliferation of the osteoblast cells. The rate of bonding of bioactive glasses depends on their compositions: the most rapid rates of bonding for bioactive glasses composed of  $\text{SiO}_2$ ,  $\text{CaO}$ ,  $\text{Na}_2\text{O}$  and  $\text{P}_2\text{O}_5$  are obtained with  $\text{SiO}_2$  contents of 45-52 wt %. Glass of this composition capable of bonding to both soft and hard connective tissue within 5-10 days<sup>[14]</sup>.

Table 1.1 shows the material composition of 45S5 bioglass. Glasses or glass ceramics containing 55-60%  $\text{SiO}_2$  require a longer time to form a bond with bones, and do not bond to soft tissues.

## Theoretical Aspects

**Table 1.1** .Effect of the composition variation of 45S5 bioglass <sup>[11]</sup>.

	Class"A" Bioactivity (wt %)	Class"B" Bioactivity (wt %)
SiO <sub>2</sub>	42-50	52- 58
Na <sub>2</sub> O	14- 28	3- 20
CaO	12- 26	8- 20
P <sub>2</sub> O <sub>5</sub>	3- 9	3- 12
Al <sub>2</sub> O <sub>3</sub>	0 - 1	0- 3
MgO	0 - 3	0- 12
K <sub>2</sub> O	0 - 6	0- 12
CaF <sub>2</sub>	0 - 12	0- 18

Glass compositions with more than 60% SiO<sub>2</sub> do not bond either to bone or to soft tissues, and elicit formation of a non adherent fibrous interfacial capsule. Based upon chemical composition which affect the rate of tissue response to the implant material, there are two categories of bioactivity have been denoted as Class A and Class B <sup>[15]</sup>.

### *c.2) Bioceramics*

Bioceramics are class of ceramics used for repair, construction and replacement of damaged and diseased parts of the body <sup>[16-18]</sup>. This type of ceramic exhibit many advantages over metal, they produce no wear debris, and can be designed to more closely match the material properties of natural bone <sup>[18]</sup>. These materials cannot be scratched, and can be used on both the ball and socket components of femoral head and the acetabular cup of a hip implant, (Figure 1.5).



**Fig.1.5** HIP alumina and zirconia ceramics as orthopaedic implants.

## 1) Calcium phosphate bioceramic

Calcium phosphate bioceramics include hydroxyapatite (HAp), tricalcium phosphate (TCP)  $\text{Ca}_3(\text{PO}_4)_2$ , and tetracalcium phosphate  $\text{Ca}_4\text{O}(\text{PO}_4)_2$  (T-TCP) are used in various orthopedic and dental applications because of their composition and morphologic similarities to natural bone [13]. These materials have shown no local or system toxicity, no inflammation, and apparent ability to attach to bone tissues [15]. The biodegradation of calcium phosphate ceramics is due to (1) physiochemical dissolution; (2) physical disintegration into small particles due to preferential chemical attack of grain boundaries; and (3) biological factors, such as phagocytes [8].

## 2) Hydroxyapatite (HAp)

Hydroxyapatite (HAp) ceramics belong to a class of calcium phosphate-based materials, which have long been widely used as bone substitutes. Apatites form the inorganic component of bone and teeth and as such have much significance in biomedical applications. Figure 1.6 shows a schematic representation of the crystal structure of HAp [19].

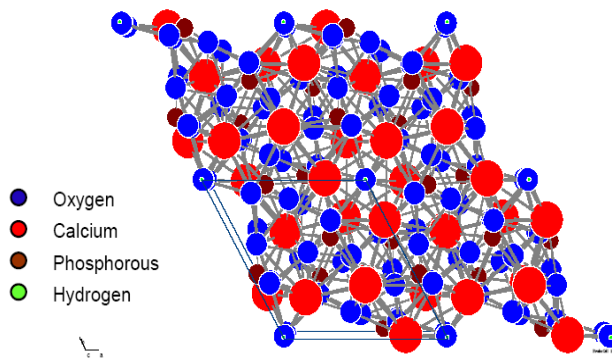


**Fig. 1.6** Schematic representation of the crystal structure of HAp [19].

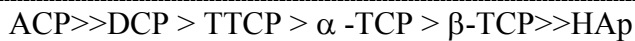
HAp has the general chemical formula  $\text{Ca}_{10}(\text{PO}_4)_6(\text{OH})_2$  with the Ca/P ratio of 1.67. The pure HAp powder is white and forms about 70% of bones and hard tissues in mammals. Therefore, it can be used as a filler to replace amputated bone or as a

## Theoretical Aspects

---

coating to promote bone in-growth into metallic implants. The  $\text{OH}^-$  ion can be replaced by fluoride, chloride or carbonate.

These substitutions induce properties change, fluoride substituting for hydroxide, producing fluorapatite, results in a more chemically stable compound. Property changes upon substitution have inspired the researchers to substitute ions trying to modify the properties and behavior of apatites. The HAp is the most stable phase of various calcium phosphate bioceramics as it is stable in body fluid and does not thermally decompose until  $1200^\circ\text{C}$  and, exhibit bioactivity when implanted in the body [18]. Generally, the order of relative solubility of CaP compounds is as follows:



Where ACP is the amorphous calcium phosphate, DCP the monetite ( $\text{CaHPO}_4$ ), TTCP the tetracalcium phosphate ( $\text{Ca}_4\text{P}_2\text{O}_9$ ), TCP is the tricalcium phosphate ( $\text{Ca}_3(\text{PO}_4)_2$ ), and HAp is the hydroxyapatite. The variation between the members of calcium phosphate bioceramics is depending on the Ca/P molar ratio [18].

Upon implantation of HAp, it will exhibit high bioactivity with no allergic effects, no toxicity, no immune response to strange bodies or inflammation, and apparent ability to attach to host tissues with living tissues and high osteoconductive behavior [20]. HAp offers a favorable environment for osteoconduction, protein adhesion and bone growth.

Such material when it become in contact with the biological tissues it will promotes the bone tissue formation at the interface and form chemical bond due to the exchange of Ca and P ions. This result in bone like apatite layer, upon which the bone forming cells will proliferate and differentiate results in biological bond formation between the implant and the body bone. This apatite layer can also be formed as the implant becomes in contact with physiological fluids outside the body "*in-vitro*" [21]. For that HAp will rapidly integrate into the human body, the body will not see it as foreign material and finally being accepted by the body.

### *3) Types of hydroxyapatite (HAp)*

#### *– Dense – compact HAp*

Dense HAp material is produced by compression of HAp powder into a given shape, then thermal treatment at high temperatures resulting in a dense ceramic material with less than 5% microporosity <sup>[22]</sup>. Dense HAp is not appropriate for being used in biomedical applications because the bone bonding will be restricted to the outer surface of the material because the lack of porosity, and will be encapsulated by fibrous connective tissue <sup>[23]</sup>.

#### *– Porous HAp*

Porous HAp should be used if bony in-growth is desirable. The porosity provides scaffolding and an interconnecting network of pores for cellular and vascular in-growth and subsequent bone development <sup>[24]</sup>. The porosity of the implant is required for the biomaterials as porous implant provides great percentage for the contact between the implant and the surrounding tissue. The porous structure favors ion exchange, as well as the penetration of blood-bearing vessels and cells, which provide bone precursors in the implant <sup>[25, 26]</sup>. Although of the high bioactivity of HAp, it is brittle, and not strong enough to be used for load-bearing applications <sup>[27]</sup>.

### *d) Composites*

Composites defined as combination of different materials to produce a single material with better properties. Human tissue has different properties than those of metals, polymers or ceramics. For that attention paid for the development of composites, to combine the benefits of materials while avoiding their drawbacks. For example, the coating of a bioinert material such as Ti6Al4V alloy with a bioactive material such as HAp. Upon implantation of such composite, the HAp will promote direct bone attachment, while the substrate provides good mechanical strength (Figure 1.7).



**Fig 1.7** (A) Natural and (B) artificial hip joints.

The fabrication of a material which possesses the combination of advantages, load bearing and biocompatibility allows inert material to be used as biomaterial, e.g. hip replacements <sup>[28]</sup>. The classification of biomaterials according to the body response is given in Table 1.2.

**Table 1.2** Types of tissue–implant attachment <sup>[29]</sup>.

Type of implant	Type of Attachment	Example
<b>Nearly inert</b>	Fibrous capsule formation (Micromotion)	Metals, alumina, zirconia,
<b>Porous</b>	In-growth of tissues into pores (Biological fixation)	Hydroxyapatite (HAp), HAp coated porous metals
<b>Bioactive</b>	Interfacial bonding with tissues (Bioactive fixation)	Bioactive glasses, HAp, bioactive glass-ceramics
<b>Resorbable</b>	Replacement with tissues (Degradation )	Tricalcium phosphate, polylactic acid (PLA)

### II- According to its functionalities

During engineering the design of the implant type, the material selection for specific application is governed by matching material properties with the requirements of this application. That, for an implant, biological, mechanical chemical and physical

should be considered during the selection process. According to the functionality of an implant, the biomaterials can be classified as following.

### *a) First generation*

The first successful substitutive joint prosthesis was the total hip prosthesis developed by Charnley in the very late 1950s<sup>[30]</sup>. In the first-generation biomaterials, the only factor that governs the selection was to achieve a suitable combination of physical properties to match those of the replaced tissue with a minimal toxic response of the host<sup>[31]</sup>. These include hip joint implant, breast implant, and heart valve. As a result of its inert nature, inability to form bonds with the biological tissue, the immune response was minimum. That, the material of this generation do not trigger any reaction in the host: neither rejected nor recognition. Upon implantation the body tries to isolate the implant through surrounding it by fibrous capsule grows on the material surface.

### *b) Second generation*

The development of bioactive interfaces eliciting a specific biological response and avoiding any fibrous layer has been one of the main driving forces in second generation biomaterials<sup>[32]</sup>. This generation has been appeared 1980, for ensuring a more stable performance in a long time through developing bioactive materials able to interact and form bond with the biological tissue. Also through developing of biodegradable materials with the ability to be degraded as the new tissue regenerate. This includes bioactive polymers (polyglycolide (PGA), polylactide (PLA), polydioxanone), bioglass, bioglass ceramic and ceramic<sup>[32]</sup>. Although metallic implants are inert but a way to make it bioactive could be through the deposition of the bioactive ceramic (HA and BGs) on the surface.

### *c) Third generation*

The third-generation biomaterials are new, bioactive, biodegradable materials which own the ability to stimulate specific cellular responses at the molecular level<sup>[33]</sup>.

This generation of implants appeared approximately at the same time as scaffolds for tissue engineering applications started to be developed.

Tissue engineering is recent research areas exploring how to repair and regenerate organs and tissues using stem cells, in combination with synthetic scaffolds together with nutrients delivery which must take place right after implantation.

### **1.1.3 -Structure of bone**

Bone is a complex, highly organized and mineralized connective tissue that contains collagen and calcium phosphate <sup>[34]</sup>. A way to get realize how is the bone healing process occurs, could be through understanding the complex structure of the bone tissue. This understanding could help well during selection of the bone implant type suit to reconstruct defects of normal bone.

#### ***1.1.3.1 Functions of bone***

Bone is a rather unique tissue with many functions. The main functions of the skeleton are mechanical support, maintenance of calcium homeostasis and haematopoiesis in the bone marrow <sup>[34]</sup>.

All bones have a mechanical function providing attachment to various muscle groups. In addition, in some parts of the body, bones provide a protective function to vital structures — skull (brain), ribs (lungs, heart) and pelvis (bladder, pelvic viscera). Some bones retain their haematopoietic function in adults — vertebrae, iliac crests, proximal parts of femur and humerus. All bones serve as a reservoir of calcium and actively participate in calcium homeostasis of the body

#### ***1.1.3.2 Structural types of bone***

Macroscopically, there are two types <sup>[35]</sup>:

- Cortical (compact) bone, with a dense outer layer — the cortex. This structure resists bending (Figure 1.8).

- Cancellous (spongy or trabecular) bone, Present in the interior of mature bones. This structure resists compression (Figure 1.8).

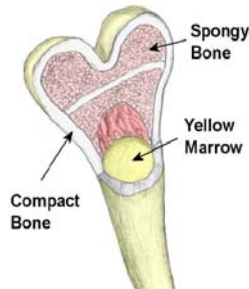


**Fig. 1.8** Schematic representation of the bone structure.

## II. Bone matrix

The bone matrix is composed of: Two constituents organic and inorganic solid, the inorganic solid is carbonate hydroxyapatite (CHAp) while the organic one is collagen [19].

### – Organic matter

Consisting of type I collagen molecules which bonded together to form fibers (Figure 1.9). In between these fibers there are small interstitial empty spaces, where inorganic matter is deposited.

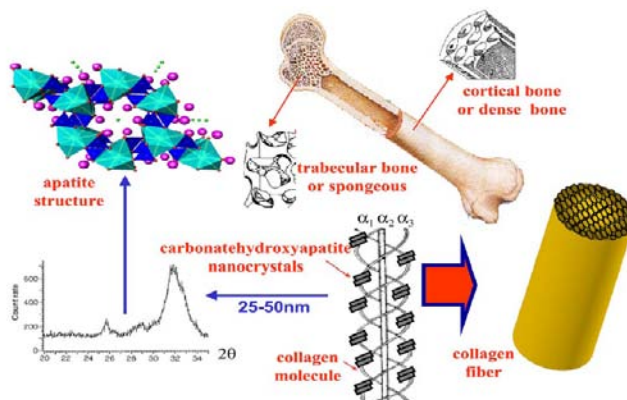


**Fig.1.9** Arrangement of HAp and collagen in the formation of hard tissues, Cortical or compact bone [19].

### – *Inorganic matter*

Made up of stiffening substances to resist bending and compression. The bone mineral is an analogue of crystals of calcium phosphate HAp which amounts to 70% of the total bone mass.

### *III. Cellular components*

There are three cell types that are found only in the bone. Their names start with the word Greek word "OSTEO" which means bone<sup>[36]</sup>.

- Osteoblasts: are the cells that form new bone "osteoid" which is made of bone collagen and other protein, they have only one nucleus. When active, they show high alkaline phosphatase activity. They are found on the surface of the new bone.
- Osteocytes: the cells occupying inside the bone. They come from osteoblasts. Some of the osteoblasts turn into osteocytes during the new bone being formed and the osteocytes then get surrounded by new bone. The function of these cells is to sense pressures or cracks in the bone and help to direct where osteoclasts will break down the old bone.
- Osteoclasts: the large, multi-nucleated cells formed by fusion of monocytes so the osteoclasts usually have more than one nucleus. They come from the bone marrow and are related to white blood cells. They are found on the surface of the bone mineral next to the dissolving bone<sup>[36]</sup>

### *IV. Osteoblast adhesion and proliferation.*

The surface as an interface between bulk material and biological tissue is crucial for a good acceptance of bone implants. Specific surface properties, such as composition, roughness, porosity, and surface charges, affect the interaction between cells and implants. That, the osteoblast attachment to materials, proliferation, and differentiation is sensitive to the topography of the surface<sup>[37]</sup>. Figure 1.10 shows a representative diagram of osteoblast cells.

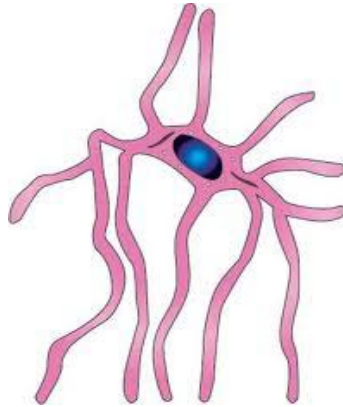


**Fig. 1.10** Representative diagram of osteoblast cells.

On rougher surfaces, osteoblasts assume a more differentiated morphology. Attachment is reduced and those cells that attach exhibit reduced proliferation <sup>[38]</sup>. Surface characteristics of materials, whether their topography, chemistry or surface energy, play an essential part in osteoblast adhesion on biomaterials.

Cell adhesion is involved in various natural phenomena such as, wound healing, metastasis as well as tissue integration of implant. The biocompatibility of an implant is very closely related to cell behaviour on contact with them and particularly to cell adhesion to their surface. Thus cell adhesion and spreading belong to the first phase of cell/implant interactions and the quality of this first phase will influence the cell's capacity to proliferate on contact with the implant <sup>[39]</sup>.

In the attachment stage, osteoblast filopodia (smaller hair-like protrusions) explored, sense and extend over significant distances to find areas appropriate for attachment on the substrate surface <sup>[40]</sup>.

The main proteins involved in cell adhesion are the cytoskeleton proteins. The sites of adhesion between the cells and implant surfaces are called focal contacts. The molecules responsible for cell adhesion involve adhesion receptors such as integrins, the actin cytoskeleton and cytoskeletally associated proteins like vinculin.

### 1.2- Tissue-metallic implant interface

#### 1.2.1 *Description*

The material surface plays an extremely important role in the response of the biological environment to artificial medical devices. Thus, the surface properties of a biomaterial dominate its interaction with the surrounding fluids, proteins and cells, etc. The tissue-implant interface plays the main role in implant integration and bone formation. Upon implantation of a metallic implant into the body, water adsorption onto the surface results in the formation of an initial hydrated layer known as the 'Helmholtz layer'. The proteins in the physiological environment adhere within this hydrated layer, forming the 'biofilm' with which cells interact <sup>[41]</sup>. The protein adsorption event occurs well before cells arrive at the surface. Thus the cells arriving at the implant surface interact with the biomaterial surface through the adsorbed protein layer <sup>[42]</sup>.

As a result of these events that occur at the titanium surface, ion release from the titanium into the surrounding tissues takes place. The released ions may have a harmful effect on the cells. In order to solve this problem, the metal implant could be coated with bioactive materials with good adhesion to metal and which could be also bonded interfacially to the bone.

#### 1.2.2 *Tissue-metallic implant interaction.*

The physiological environment is complex contain proteins such as fibrinogen and other blood proteins. The first interaction, in as short a time as can be measured after implantation into a living body (< 1 second), is the adsorption of proteins onto the surfaces. In seconds to minutes, a monolayer of protein adsorbs to most surfaces <sup>[43]</sup>. The protein adsorption event occurs well before cells arrive at the surface. Thus the cells arriving at the implant surface interact with the biomaterial surface through the adsorbed protein layer <sup>[44]</sup>. Therefore, cells see primarily a protein layer, rather than the actual surface of the biomaterial. In other words, the adsorbed protein converts the implant into a biologically recognizable material and helps it to be integrated in the biological system.

As soon as the cells arrive to the implant surface, they scan the protein layer covering the surface looking for activation factors to attach to, grow, differentiate, proliferate or die. Thus, the initial protein adsorption onto a biomaterial surface is critical in determining the biocompatibility, the rate of cell proliferation and thereby the bone bonding ability of the material [43,44]. This called Vroman effect, the protein layer helps the biomaterial to be integrated in the biological system [45]. The more the protein adsorbed on an implant, the more cells can attach and proliferate [46-48]. Such cell response can be controlled by understanding how the surface chemistry, topography affect the formation of the adsorbed protein layer. For that, the protein adsorption is responsible for the biocompatibility of biomaterials.

### 1.2.2.1 Corrosion of Ti and Ti6Al4V alloy

Corrosion is an electrochemical reaction involves two half-cell reactions; an oxidation reaction at the anode and a reduction reaction at the cathode. Figure 1.11 shows a scheme of the reaction steps (anodic and cathodic) occurring at the biomaterial surface during the corrosion process in liquid environments

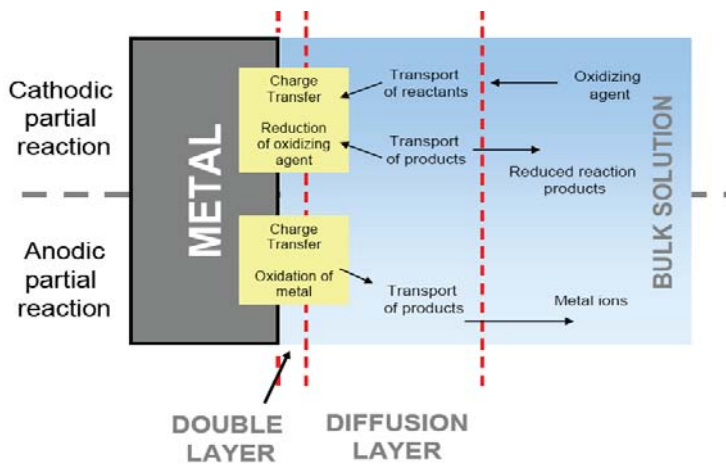


Fig. 1.11 Reaction steps during the corrosion of a metal in liquid environment [49].

. In a bio-system involving metallic biomaterials several electrochemical and corrosion phenomena can take place: active dissolution, passivation, passive dissolution, transpassive dissolution and localized corrosion [49].

## Theoretical Aspects

Ti6Al4V alloy is among the most used materials for in vivo applications, due to its good physical and mechanical properties such as low density, corrosion resistance and biocompatibility in the body environment <sup>[50]</sup>. It is an  $\alpha/\beta$  titanium alloy, once exposed to the atmosphere, a passive layer, mainly  $\text{TiO}_2$ , is formed on its surface, whose thickness can reach up to 6 nm after 1 year of exposure to normal ambient temperature <sup>[51]</sup>. This layer reduces the corrosion rate of the Ti6Al4V by blocking the transport of metallic ions.

The passive layer of Ti6Al4V is composed of  $\text{TiO}_2$  and alloying elements present in a proportion that is dependent on the previous treatment of the alloy. Different authors have found about a two- to threefold increase of the Al concentration in the oxide film in comparison to the corresponding value in the bulk metal, with a tendency to be more strongly enriched at the outermost surface <sup>[52]</sup>. The presence of Al has been found as  $\text{Al}^{3+}$ , suggesting that it exists in the form  $\text{Al}_2\text{O}_3$  in the naturally passivated layer. In the natural oxide film V is in a concentration below that in the bulk material (approximately 0.3 to 1 wt %). On the other hand, thermal treatments, particularly at temperatures above  $450^\circ\text{C}$ , change the proportion of alloying elements, as well as the microstructural properties of the oxide film that is formed mainly of microcrystalline rutile <sup>[52]</sup>.



**Fig. 1.12** Components of Ti based hip implant.

Unfortunately, the formed passive layer is rather poor, and it may be disrupted at very low shear stresses, even rubbing against soft tissues <sup>[53]</sup>. It has been reported that, the in vivo conditions can alter the stability of the passive layer. Localized corrosion, which usually results in pitting or crevice formation, is a multi-step process.

It is generally accepted that the following four steps are involved in localized corrosion (i) adsorption of reactive anions on the oxide covered titanium surface, (ii) reaction of the adsorbed anions with the titanium cations in the titanium oxide lattice or with the precipitated titanium hydroxide, (iii) thinning of the oxide by dissolution; and (iv) direct attack of the exposed metal by the anions, perhaps assisted by an anodic potential. This is sometimes called pitting propagation <sup>[54,55]</sup>.

As a result, titanium and other alloying metal ions as aluminum and vanadium, release from the implants being accumulated in the nearby tissues, due to the aggressive action of the biological fluids <sup>[56]</sup>.

A way to solve this is to coat the Ti6Al4V alloy with a bioactive material which could bond with the bone <sup>[57]</sup>. Several coating techniques have been adopted to improve the corrosion resistance of metal alloys. These include plasma spray, <sup>[58]</sup>, chemical conversion <sup>[59]</sup>, sol-gel method <sup>[60-62]</sup>, etc.

### *1.2.2.2 Protection of Ti and Ti6Al4V alloy*

#### **a) Ti-Al oxides thermally generated**

The metal surface under atmospheric conditions or in solutions always forms a layer of reactive film. The film that is formed in solution displays low solubility, and provided it has been formed without pores and is highly adhesive; it becomes resistant to corrosion (an inert/passive film). The passive film that is formed is transparent and is as thin as 1-5 nm <sup>[51]</sup>.

A way to increase the thickness of this oxide layer and to enhance its efficiency of protecting the metal surface from corrosion is to thermally treat the metal at adequate temperature to avoid the deterioration of its mechanical proprieties.

### b) Sol-gel coatings

This technique has attracted a considerable interest, as it is considered as a non-toxic substitute for chromium (VI) conversion. The sol-gel method provides a low temperature route for the preparation of thin coatings<sup>[63]</sup>. Dip coating or spin coating techniques can be used to deposit a film of these sols to a substrate.

#### *b.1) Dip-coating*

The sol-gel dip-coating process is used mainly for the production of coatings on plane substrate such as flat glass plates, or complex objects, such as tubes, rods, pipes and fibers. Simply, a clean surface is dipped into a solution and then withdrawn at constant speed which determines the thickness of the film. Thus for a given solution, the film thickness of a single layer is governed by withdrawal speed<sup>[64]</sup>. Figure 1.13 shows representative schematic of the dip-coating process.

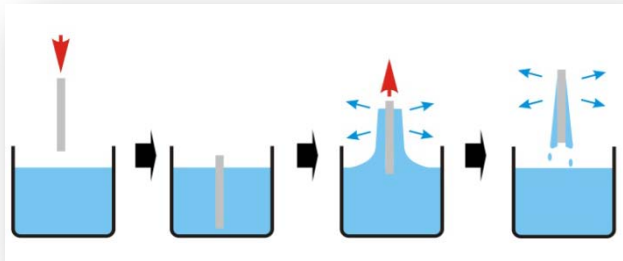


**Fig. 1.13** Schematic diagram of a sol-gel dip-coating process.

During dipping, the formation of weak hydrogen bonds takes place and the molecules self-organize themselves onto the surface of the metal. Figure 1.14 explains the formation of bonds between the substrate and the deposited film.

After dipping, a heat treatment in oven followed the layers deposition. The heat treatment provides to the sol-gel coating the thermal energy for the condensation reactions. The condensation reactions occur both between the different hydrolyzed molecules and between the metal hydroxide and the silane hydrolyzed molecules. This step finally leads to the formation of covalent bond between the metal surface and the deposited layer, Figure 1.14. Curing the film at certain temperatures depends on the

composition of the film and the desired properties to be achieved. This method has the advantage of being capable of producing multiple coatings with a high degree of uniformity. The film thickness can be modified by changing the physical properties of the solution, like viscosity and density, as well as the number of layers.

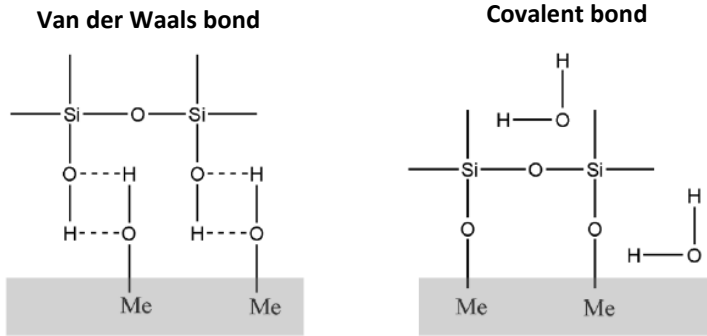


**Fig. 1.14** Schematic representation of the formation of bonds between the substrate and the sol-gel film during dipping and after curing process.

### *b.2) Spin-coating*

Spin-coating is a process suited to flat shapes, such as disks, and plates. The process can be separated into three stages. As with dip-coating, evaporation can take place throughout the entire coating process. The first stage involves delivering excess liquid to the substrate while it is stationary or spinning. During the second stage, rotation causes the liquid to cover the entire surface, owing to centrifugal forces. Figure 1.15 shows representative schematic of the spin-coating process for film deposition onto substrate surface.

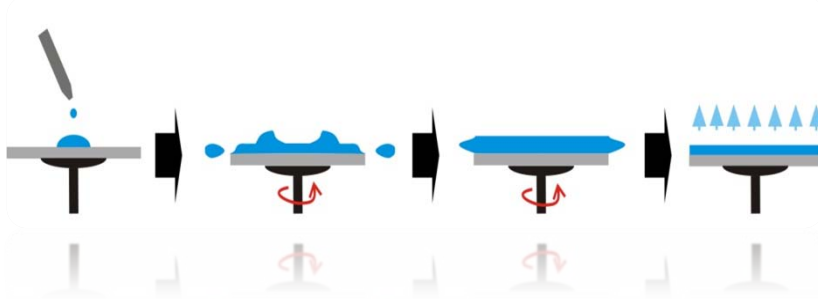


**Fig 1.15** Schematic diagram of a sol-gel spin-coating process.

In stage three, excess liquid flows to the perimeter and detaches in the form of droplets. As the film thins, flow decreases as drag forces increase, and thinner films are affected more by evaporation, which raises the solution viscosity by concentrating non-volatiles. Evaporation becomes the dominant process once spin-off has ceased <sup>[65]</sup>.

### c) Types of sol-gel coatings

#### *c.1) Inorganic sol-gel coatings*

The inorganic coatings prepared by sol-gel method can provide good protection on metal substrates <sup>[66-69]</sup>. There are still some major drawbacks of these coatings, from the standpoint of corrosion resistant:

- Oxide films are brittle and thicker coatings (>1  $\mu\text{m}$ ) are difficult to be achieved without cracking. The cracks may affect several properties and may be deleterious in wet corrosive media <sup>[70,71]</sup>.
- Relatively high curing and sintering temperatures (400–800°C) are often required for densification of the film <sup>[72]</sup>.

The cracks are formed during drying of the deposited layer because the inorganic network cannot withstand the high shrinkage stress generated by the extensive release of volatiles. Cracks also may form as a result of stresses in the sol-gel film due to shrinkage and thermal expansion mismatches between the substrate and the deposited layer <sup>[73]</sup>. These disadvantages make inorganic sol-gel films poor physical barriers that cannot provide adequate corrosion protection.

A way to overcome these disadvantages, brittleness and crack formation can be achieved by introduction of organic component into the inorganic sol to form the organic-inorganic hybrid sol-gel coatings <sup>[73]</sup>.

#### *c.2) Organic-inorganic hybrid sol-gel coatings*

The combination of organic groups with the inorganic film cause the resulted film to be flexible, adhere well to the substrate surface. There are some major advantages of these coatings, from the standpoint of corrosion resistant:



### 1.3- Sol-gel technology

The traditional methods of melt processing used for the synthesis of inorganic materials limits the inclusion of organic or biologic components within the system due to processing at high temperatures. Furthermore, these high temperatures result in lower purities by providing the activation energy for a number of side reactions.

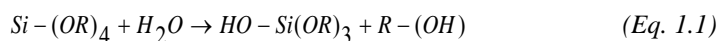
The sol-gel process is a cheap, *low-temperature* and so is attractive technique of preparing different oxide materials like HAp, SiO<sub>2</sub>, ZrO<sub>2</sub> or Al<sub>2</sub>O<sub>3</sub>.<sup>[80]</sup>

The sol-gel process is based on the hydrolysis and condensation of metal alkoxides (MA) in water-alcohol medium before being brought out of multi-component *materials* in the form of solution, either as a colloidal gel or a polymerized macromolecular network<sup>[81]</sup>.

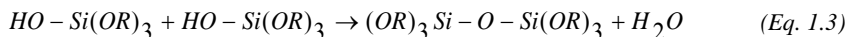
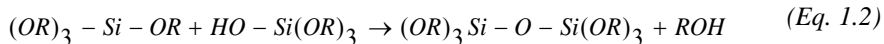
In general, the sol-gel process pass through stages: (a) Hydrolysis, (b) Condensation and polymerization of monomers to form chains and particles, (c) Growth of the particles, (d) Agglomeration of the polymer structures followed by the formation of networks that extend throughout the liquid medium resulting in thickening, which forms a gel<sup>[82]</sup>.

The preparation of sol solutions involves the use of solvents. These solvents are usually organic alcohols. The objective of the solvent is to dilute liquid precursors.

The hydrolysis time of the sol solution is an important step; throughout this period the hydrolysis process takes place and generates more –OH groups which have significant impacts on the effectiveness of the solution and consequently the film being deposited<sup>[83]</sup>. A metal alkoxide has the structure formula M-(OR)<sub>x</sub>, describing a central metallic ion (M) bound to functional organic groups (R) through an oxygen linkage (O)<sup>[84]</sup>. The hydrolysis of such metal alkoxide results in replacement of alkoxy groups with hydroxyl ones, to yield an alcohol (equation 1.1)<sup>[85]</sup>.



Where  $-(OR)$  represents an alkoxy functional group. After hydrolysis, a series of condensation reactions which results in the liberation of alcohol and water and contribute to the growth of the reacted metal alkoxide chain, (equations 1.2 and 1.3). These reactions can be illustrated as follow:



Hydrolysis and condensation steps generate low-molecular weight by-products such as alcohol and water. Upon drying, these small molecules are driven off and the network shrinks as further condensation may occur. The advantages of the sol-gel technique include:

- Synthesis at room temperature which benefits the metal substrates where the mechanical degradation or phase transition of the underlying Ti or Ti alloys (i.e.  $\alpha \rightarrow \beta$  phase transition, occurring at 883 and 960°C, respectively) can be prevented<sup>[84]</sup>.
- The use of low temperature also avoids the thermal volatilization and degradation of entrapped species in the sol matrix, such as organic inhibitors.
- Owing to mixing of the precursors at molecular scale, stoichiometric, homogenous and pure products are easily obtained<sup>[85]</sup>.
- Allows the coating of complex geometry substrates.
- As the sol-gel has a solution-based nature which allows functional coatings to be developed by inserting anticorrosive, organic, biomolecules or medicine in the sol, etc.
- Inserted materials retain their form, physical characteristics, chemical and biological prosperities and are able to react with the external reagents through the pore network.
- Provide porous products which can act as nucleation sites for apatite layers. So ceramic prepared by sol-gel exhibit greater bioactivity<sup>[85, 86]</sup>.
- The chemical bonding of coating to substrate resulting in high adherence.

## 1.3.1 Powders

### 1.3.1.1 Hydroxyapatite (HAp)

Various processes have been employed to prepare HAp, including chemical co-precipitation [87], sol-gel [88-91] etc. Among all processes, sol-gel is the most promising method because of its simplicity of experimental operations, low operating temperature and high yields of pure products.

## 1.3.2 Coatings

### 1.3.2.1 Bioactive coatings

Silica has many applications in the corrosion protection of metals as it is a good barrier to oxygen diffusion.  $\text{SiO}_2$  can improve the oxidation and acidic corrosion resistance of metals under different temperatures due to its high heat resistance and chemical resistance [92]. The silica system is an attractive material to apply to metallic substrates, because sol-gel derived silica are known to have excellent bioactivity and exhibit chemical bonding to the surrounding tissues, particularly bone [93].

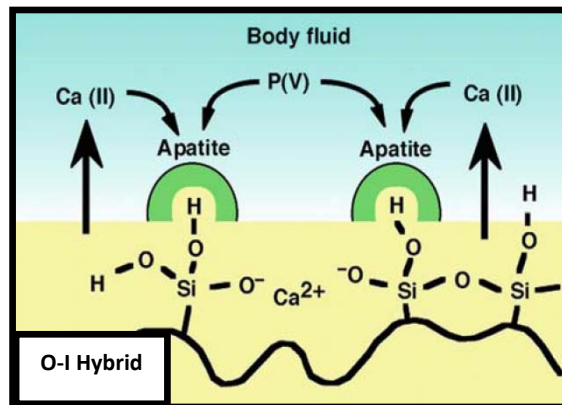


Fig. 1.17 Representative diagram of bioactivity mechanism of silane–metal coatings

The role of silica in the formation of bone-like apatite on the substrate has been investigated by many researchers [94,95].

Figure 1.17 show a representative diagram of bioactivity mechanism of O-I hybrid coating. Upon implantation of an organic-inorganic silane hybrid coated metal

substrate in the body, the degradation of the silica network leads to the formation of Si–OH groups at the metal–solution interface. These silanol groups provide favorable sites for nucleation of the apatite; attract the calcium and phosphate ions from the body fluid through electrostatic interactions and forms bone-like apatite layer on the surface<sup>[96,97]</sup>.

Once the apatite nuclei are formed<sup>[98]</sup>, they grow spontaneously by consuming the calcium and phosphate ions from the surrounding body fluid. During this process, the amorphous calcium phosphate incorporates OH<sup>-</sup> and CO<sub>3</sub><sup>2-</sup>, Na, K and Mg<sup>2+</sup> ions from the solution and finally crystallizes into apatite.

### 1.3.2.2 *Anticorrosive coatings*

The corrosion resistance of the hybrid sol-gel coatings is based on their physical barrier properties. Therefore, a homogenous crack-free material is required. During curing of the sol-gel film, water and ethanol evaporate results in pores that permit the diffusion of electrolyte and aggressive species towards the metal surface and localized corrosion attack can occur in this region. Therefore, such sol-gel coatings do not provide an active corrosion protection. A way to overcome this problem is through using sol-gel thin film which could act as reservoir for storage and release of organic and inorganic corrosion inhibitors<sup>[99]</sup>. In neutral media, benzoate, nitrite, chromate, and phosphate act as good inhibitors. Inhibitors decrease or prevent the reaction of the metal with the media. They reduce the corrosion rate by

- Adsorption of ions/molecules onto metal surface,
- Increasing or decreasing the anodic and/or cathodic reaction,
- Decreasing the diffusion rate for reactants to the surface of the metal,
- Decreasing the electrical resistance of the metal surface.

The development of sol-gel coatings containing corrosion inhibitors enables to obtain an active protection when defects or damage affect the homogeneity of the coating.

### *1.3.2.3 Multifunctional two layers system*

Other way to overcome the problem of the pores and defects that form during the curing step of the deposited film. The two layer system could achieve multifunction system with bioactivity and corrosion protection. The prolonged corrosion resistance requires the inner layer to be hydrophilic while the outer layer should be hydrophobic for water and corrosive ions resistance purpose <sup>[100]</sup>.

## 1.4 -Characterization of studied materials

A quite large number of characterization techniques that have been used in the study of the chemical composition, structure, physical properties as well as the biological behavior of the prepared films.

### 1.4.1- Physico-chemical structural and morphological characterization

#### – Thermal analysis

Thermal analysis is a group of analytical techniques developed to study the properties of materials as they change with temperature in a controlled atmosphere. The atmosphere may be purged with an inert gas to prevent oxidation or other undesired reactions<sup>[101]</sup>. Several techniques belong to this branch; depending on the property being measured these techniques can be distinguished from one another:

#### 1.4.1.1 Differential thermal analysis (DTA)

Differential Thermal Analysis technique measures the temperature difference between a reference materials and the sample being analyzed<sup>[101]</sup>. Figure 1.18 shows a schematic diagram of the DTA equipment.

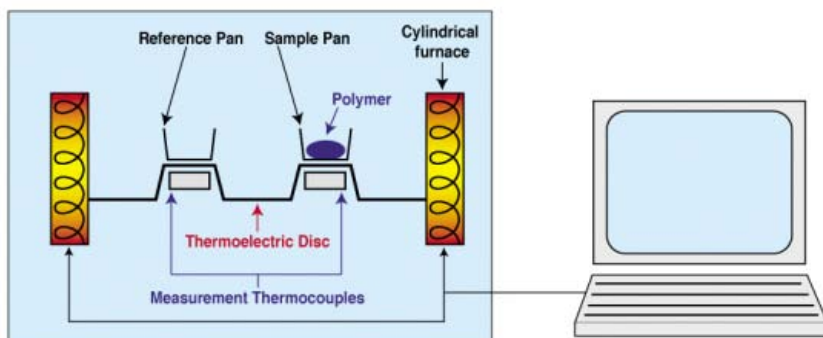


**Fig.1.18** Schematic of a differential thermal analysis.

The reference material is inert which exhibits no phase change over the temperature range chose for characterization<sup>[102]</sup>. The sample and the reference material ( $\text{Al}_2\text{O}_3$ ) have the same mass and are held in two separate crucibles (typically platinum), which

## Theoretical Aspects

are subject to the same heating schedules <sup>[102]</sup>. The temperature difference between the reference and the sample under investigation is measured via “differential” thermocouple in which one junction is in contact with the sample crucible, and the other is in contact with the reference crucible, (Figure 1.18).

As the sample undergoes a transformation, the change in temperature with respect to the reference can be either exothermic or endothermic. The DTA equipment then will indicate the transformation as an “endothermic” or “exothermic” on a plot of temperature difference ( $\Delta T$ ) versus time or temperature.

### 1.4.1.2 Thermo-gravimetric analysis (TGA)

Thermo-Gravimetric Analysis (TGA) is a technique in which the mass of a substance is measured as a function of temperature and/or time while the sample is subjected to controlled temperature schedule <sup>[103]</sup>. The components of TGA instrument is shown in figure 1.19.

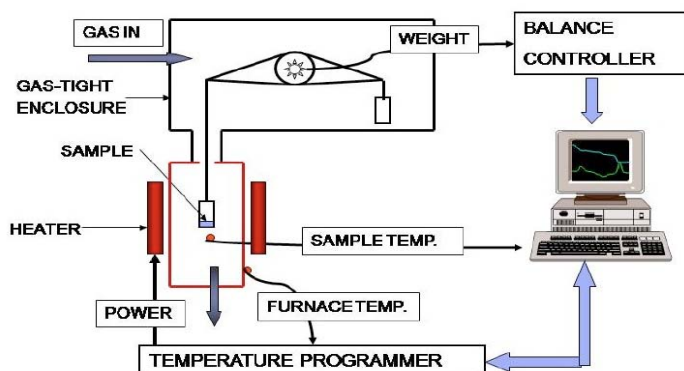


**Fig.1.19** Diagram of a thermo-gravimetric analysis Instrument.

The TGA analysis provides information about the temperature at which the degradation of a material occurs, the content of organic and inorganic components in the sample. It consists of a high-precision balance with a platinum crucible loaded with the sample. The crucible is placed in a small electrically heated furnace with a thermocouple that accurately measures the temperature and a computer that used to

control the instrument. Analysis is carried out by raising the temperature gradually and plotting weight against temperature, (Figure1.19).

### 1.4.1.3 X-ray diffraction (XRD)

The x-ray diffraction pattern is the fingerprint of periodic atomic arrangements in a given material based on the fact that, the atoms or molecules in a crystal lie on regularly spaced sets of planes <sup>[104]</sup>.

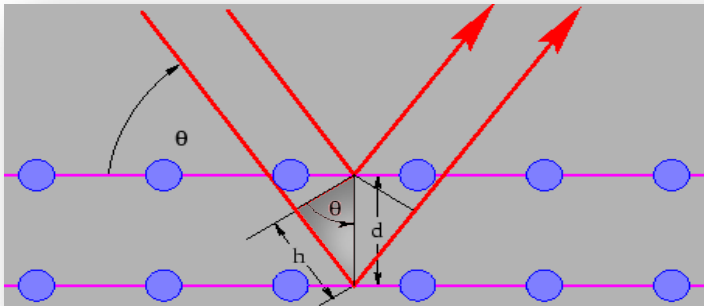


**Fig.1.20.** Schematic diagram for determining Bragg's law.

In Figure 1.20, when the crystal is held in an X-ray beam, each of these planes acts as a partial reflector. Although a strong beam is reflected from the whole crystal only if the individual reflections from successive planes reinforce one another, that is if the path difference between the rays reflected by successive planes is equal to a whole number of wavelengths. This condition which leads to the well known Bragg's law <sup>[104]</sup>.

$$d = \frac{n\lambda}{2 \sin \theta} \quad (\text{Eq.1.4})$$

Where: d is the distance between the nearest lattice planes,  $\lambda$  is the wavelength and, n is the order of the corresponding reflection.

From the experiment condition we can define  $\lambda$  ,  $\theta$ . the order of diffraction is usually equals unity, consequently other information about the crystal as particle size can be calculated.

### 1.4.1.4 Infrared (IR) spectroscopy

Spectroscopy is the study of matter and its interaction with electromagnetic radiation. The IR region spans a section of electromagnetic spectrum having wavenumbers from 13000 to 10  $\text{cm}^{-1}$  or  $\lambda$  from 0.78 to 1000  $\mu\text{m}$ . The IR spectroscopy can give valuable information about the energy of molecular vibrations and is a helpful tool for distinguishing the different functional groups of compounds<sup>[105]</sup>.

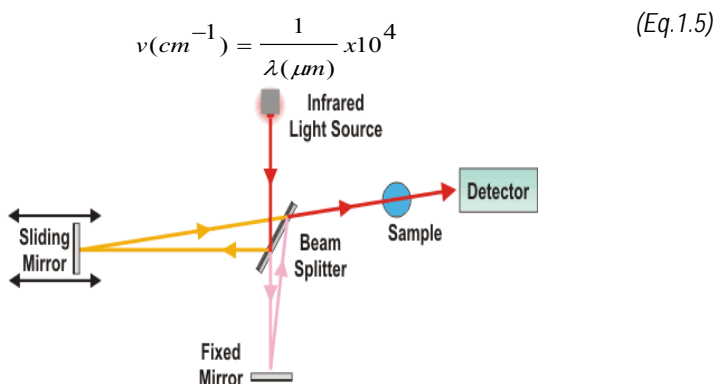


**Fig.1.21.** Schematic diagram of an IR Instrument.

The obtained information is presented in the form of a spectrum with  $\lambda$  or wavenumber as the x-axis and absorption intensity or percent transmittance as the y-axis. Transmittance,  $T$ , is the ratio of radiant power transmitted by the sample ( $I$ ) to the radiant power incident on the sample ( $I_0$ ). Absorbance ( $A$ ) is the logarithm to the base  $I_0$  of the reciprocal of the transmittance ( $T$ ).

$$A = \log_{10}(1/T) = -\log_{10} T = -\log_{10} I/I_0 \quad (\text{Eq.1.6})$$

The IR spectroscopy exploits the fact that molecules absorb specific frequencies that are characteristic of their structure. These absorptions are resonant frequencies, i.e. the frequency of the absorbed radiation matches the frequency of the bond or group that vibrates. By this way, the functional groups and composition of a material can be determined. In attenuated total reflectance (ATR-IR), the incident IR beam first passes through a ZnSe, Ge, or diamond crystal, improving the surface sensitivity of the technique:

### 1.4.1.5 Nuclear magnetic resonance (NMR)

Liquid state NMR techniques are a well-known powerful is nondestructive research technique that used for characterization of solutions and solids [76]. It is a way to determine the physical and chemical properties of atoms or molecules in a material by studying the magnetic properties of certain atomic nuclei in a magnetic field that will absorb and re-emit electromagnetic radiation. The NMR technique can provide detailed information about the structure, dynamics, reaction state, and chemical environment of molecules [76, 106]. The most investigated nuclei in the field of hybrid materials are  $^1\text{H}$ ,  $^{29}\text{Si}$ , and  $^{13}\text{C}$ .

### 1.4.1.6 Contact angle ( $\theta$ )

The wettability is an important factor that influences the biocompatibility of the biomaterial [107]. Upon implantation, the implant surface will subject to being wetted by the body physiological fluids. The hydrophobicity/hydrophilicity of the implant surface controls the adsorption of proteins and the consequent cell attachment to the surface. Generally, the wettability of a surface is dependent of its chemical composition, topography, and surface charge. This criterion can be measured by application of the contact angle technique. Contact angle ( $\theta$ ) measurement is a simple method to assess the surface wettability by measuring how much a droplet of water spreads on a surface. It is a quantitative measure of the wetting of a solid by a liquid [108]. Contact angle can be defined as the angle formed between the liquid surface and solid surface when liquid and solid have made contact, (Fig 1.22).

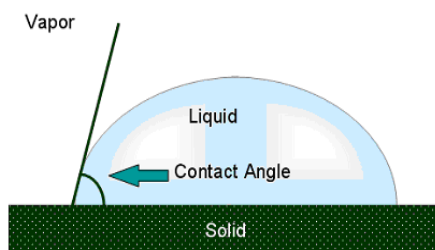


**Fig.1.22.** Schematic drawing to show the contact angle.

If  $\theta$  is less than  $90^\circ$ , this indicates that the solid is relatively hydrophilic. For solids

where complete or perfect wetting occurs,  $\theta$  will be zero degrees. If  $\theta$  is greater than  $90^\circ$ , it is said to be non-wetting, indicative that the material surface is relatively more hydrophobic.

### 1.4.1.7 Stylus profilometer

A profilometer is a basic tool that allows to quickly measuring the thickness of films, providing a non coated part of the substrate is available. Simply it contains a diamond tip dragged on a surface with very light pressure to get information about surface topography. <sup>[109]</sup>.

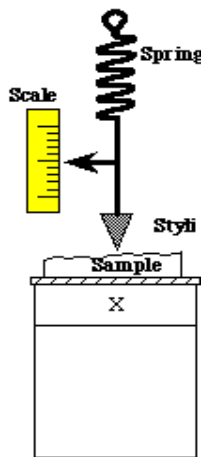


**Fig.1.23.** Schematic diagram of the profilometer stylus.

### 1.4.1.8 Scanning electron microscope (SEM)

The scanning electron microscope (SEM) is a scientific instrument that images the sample surface by scanning it with a high-energy beam of electrons in a raster scan pattern <sup>[110]</sup>.

A beam of electrons is produced at the top of the microscope by an electron gun. The electron beam follows a vertical path through the microscope, which is held within a vacuum, see figure 1.24.

The beam travels through electromagnetic fields and lenses, which focus the beam

down toward the sample. Once the beam hits the sample, electrons and X-rays are ejected from the sample. When a beam of electrons strikes the surface of a material, it emits secondary electrons and X-rays. The intensity of the secondary electrons is detected to generate a high resolution surface image. X-rays can be detected to conduct elemental analysis. Detectors collect these X-rays, backscattered electrons, and secondary electrons and convert them into a signal that is sent to a screen similar to a television screen. The magnification in a SEM can be controlled over a range of up to 6 orders of magnitude from about 10 to 500,000 times.

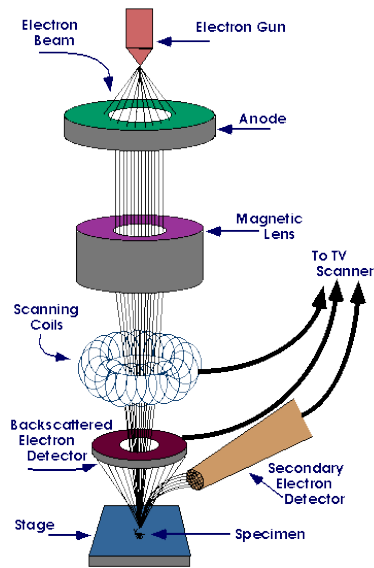


**Fig.1.24.** Diagram illustrating how the scanning electron microscope works.

## 1.4.2 Functionality

### 1. *Biological characterization techniques*

The bioactivity of materials is one of the important factors that determine the success of implant materials <sup>[3]</sup>. Bioactive material is the one that is able to react with physiological fluids or simulated body fluid (SBF) and forms bonelike apatite at the interface between implants and tissues <sup>[111]</sup>.

## Theoretical Aspects

### 1.4.2.1 Simulated body fluid (SBF)

Bioactive materials are characterized by their ability to react chemically with physiological fluids and to form bone-like apatite layer on their surface [111]. The simulated body fluid SBF proposed by **Kokubo** is a solution that has inorganic ion concentrations similar to those of human blood plasma [112], see table 1.3.

**Table 1.3.** Nominal ions concentration of SBF in comparison with those in human blood plasma [112].

	Ion concentrations( mM) of SBF and human blood plasma							
	Na <sup>+</sup>	K <sup>+</sup>	Mg <sup>2+</sup>	Ca <sup>2+</sup>	Cl <sup>-</sup>	HCO <sub>3</sub> <sup>2-</sup>	HPO <sub>4</sub> <sup>2-</sup>	SO <sub>4</sub> <sup>2-</sup>
Human blood plasma	142.0	5.0	1.5	2.5	103.0	27.0	1.0	0.5
Original SBF	142.0	5.0	1.5	2.5	147.8	4.2	1.0	0.5

The inorganic part of blood plasma contains different ionic concentrations like sodium, calcium, magnesium, and chloride ions. The pH of SBF is typically adjusted to 7.4 at 37 °C.

### 1.4.2.2 Bradford protein assays

Protein adsorption on the surface of implanted material also relates to the bioactivity. The first event that occurs on the surfaces of materials is the adsorption of proteins onto the surfaces, followed by responses of cells to the surfaces.

The main plasma proteins are albumin (3300-4000 mg/dL), globulin (880-3530 mg/dL) and fibrinogen (340-430 mg/dL) [113]. When an artificial implant is implanted in-vivo, its surface is immediately inducing a series of reactions in the physiological environment. Within few seconds, the surface of the implant will be covered with a biofilm of proteins. As proteins come in contact with a biomaterial surfaces, cellular adhesion and differentiation may be affected. These adsorbed proteins can provide attachment

sites for osteoblast cells bonding to the implant, which then leads to faster in-growth of bone.

Several methods exist for the determination of protein concentration in solution, including amido black and Bradford assay, which generate or change color upon complexing with protein <sup>[114]</sup>. In all, color development depends on quantity of protein present in the solution where the sample under study was immersed.

Bradford protein assay is a spectroscopic analytical procedure used to measure the concentration of protein in a solution. Use of the coomassie G-250 dye in a colorimetric reagent for the detection and quantitation of total protein was first described by Dr. Marion Bradford <sup>[114]</sup>. Protein binds to the coomassie dye in the acidic environment of the reagent which results in a spectral shift from the reddish/brown form of the dye (absorbance maximum at 465 nm) to the blue form of the dye (absorbance maximum at 610 nm). The difference between the two forms of the dye is greatest at 595 nm

### ***1.4.2.3 Cellular cytotoxicity / proliferation***

One of the most fundamental measurements that can be made with cells in culture is cell proliferation/viability. To study cell proliferation several methods are available. The neutral red uptake assay is one of the most used cytotoxicity tests with many biomedical applications <sup>[115]</sup>. It is a cell survival/viability assay based on the ability of viable cells to incorporate and bind dye. Following exposure to the test item, cells are incubated in the presence of neutral red dye. The dye readily penetrates cell membranes and accumulates intracellularly in lysosomes. If cell dies, the dye cannot be retained. Consequently, the amount of retained dye is proportional to the number of viable cells <sup>[116]</sup>.

## ***II. Electrochemical characterization techniques***

### ***– Electrochemical impedance spectroscopy***

Electrochemical impedance spectroscopy (EIS) has been widely used, with success, for the electrochemical characterization of corrosion protecting organic coating on metals <sup>[117–123]</sup>.

The final purpose of the EIS characterization of protecting coatings is to obtain information about the system properties such as the presence of defects, reactivity of the interface, adhesion, barrier properties to water, etc. In the present work, the barrier properties of the sol-gel polymer films strongly depend on the substrates, film structure and process parameters. The morphologies, chemistry and cross-linking of the sol-gel films play an important role in the water uptake process and thus in their barrier properties. The process of electrolyte penetration might take place through the development of conductive pathways. Consequently, it is of crucial importance to study the effect of the chemistry and morphology of the sol-gel films on the diffusion process of water through the films.

In the study of the barrier properties afforded by protective thin films, like sol-gel films and/or ultra thin films, specific parameters have to be found, which allow the correct interpretation of data. In some cases, the low thickness can complicate the interpretation of the impedance diagram <sup>[124-126]</sup>.

For example, if a pinhole is present in the coating, aqueous electrolyte, like SBF used in this work, can reach the metal/sol-gel interface in short time and it will be very difficult to evaluate the resistance and capacitance of the whole area because the EIS measurements are linked to the electrochemical activity of the hole. This thus requires a degree of sophisticated analysis to distinguish the different time constants, related to the coating properties and to the corrosion process. In order to clarify all this concepts and parameters which will be used along this study, a brief overview of EIS fundamentals, most important concepts used and the evaluation methodology is described further on.

– *EIS fundamentals:*

EIS is a nondestructive measurement, so it can be used to evaluate metallic surfaces, metal/coating systems and its changes along time without damage the system being measured. In Figure 1.25 is showed the instrumentation used to perform EIS measurements.

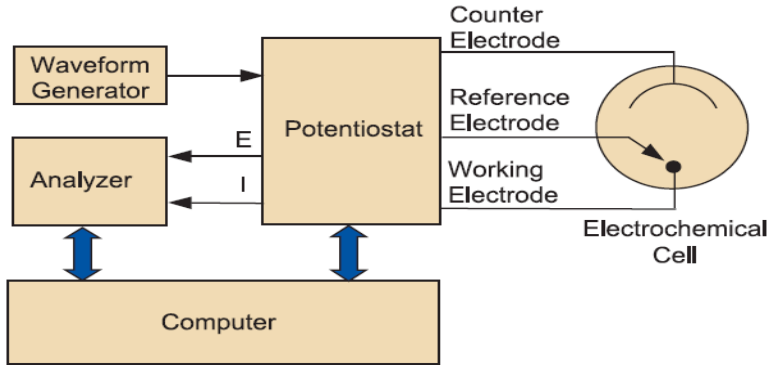


**Fig. 1.25** A block diagram of the instrumentation used to make the EIS measurements.

Electrochemical impedance is usually measured by applying small amplitude (5–10 mV) an AC potential to the sample by the potentiostat and measuring the current response [127].

The excitation signal, expressed as a function of time, has the form

$$E_t = E_0 \cdot \sin(\omega t) \quad (\text{Eq.1.7})$$

Where

$E_t$  is the potential at time  $t$ ,

$E_0$  is the amplitude of the signal,

$\omega$  is the radial frequency (expressed in radians/second).

The relationship between the radial frequency and frequency  $f$  (expressed in hertz) is

$$\omega = 2\pi f$$

In a linear system, the response signal,  $I_t$ , is shifted in phase ( $\phi$ ) and has a different amplitude  $I_0$ .

$$(\text{Eq.1.8})$$

$$I_t = I_0 \sin(\omega t + \Phi)$$

The impedance of the system then could be extracted by an expression analogous to Ohm's:

$$Z = \frac{E_0 \sin(\omega t)}{I_0 \sin(\omega t + \Phi)} = Z_0 \frac{\sin(\omega t)}{\sin(\omega t + \Phi)} \quad (\text{Eq.1.9})$$

## Theoretical Aspects

The impedance is therefore expressed in terms of a magnitude,  $Z_o$ , and a phase shift,  $\phi$ .

$$Z(\omega) = \frac{E}{I} = Z_o \exp(j\phi) = Z_o (\cos\phi + j\sin\phi) \quad (\text{Eq.1.10})$$

The impedance is then represented as a complex number,

### Data presentation

#### i. Nyquist plot.

The expression for  $Z(\omega)$  is composed of a real and an imaginary part. If the real part is plotted on the X-axis and the imaginary part is plotted on the Y-axis of a chart, we obtain a "Nyquist Plot". In the Nyquist plot, the Y-axis is negative and each point on the Plot is the impedance at one frequency. On the Nyquist Plot the impedance can be represented as a vector (arrow) of length  $|Z|$ . The angle between this vector and the X-axis, commonly called the "phase angle", is  $\phi$  ( $=\arg Z$ ).

The Nyquist Plot in Figure 1.27 results from the electrical circuit of Figure 1.26. The semicircle is characteristic of a single "time constant".

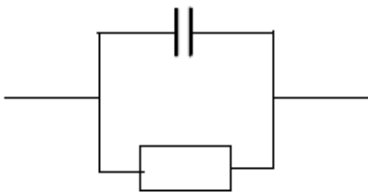


**Fig.1.26** Simple equivalent circuit with one time constant.

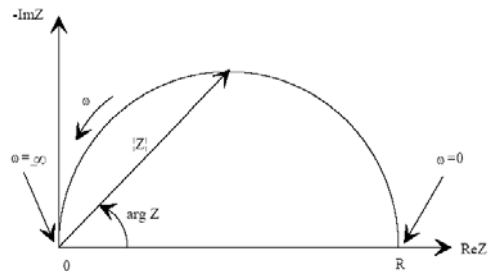


**Fig. 1.27** Nyquist plot with impedance vector.

#### ii. Bode plot.

Another way of presentation method is the Bode Plot. The impedance is plotted with log frequency on the X-axis and both the absolute values of the impedance ( $|Z|=Z_o$ ) and the phase-shift on the Y-axis.

The Bode Plot for the electric circuit of Figure 1.26 is shown in Figure 1.28. Unlike the Nyquist Plot, the Bode Plot does show frequency information.

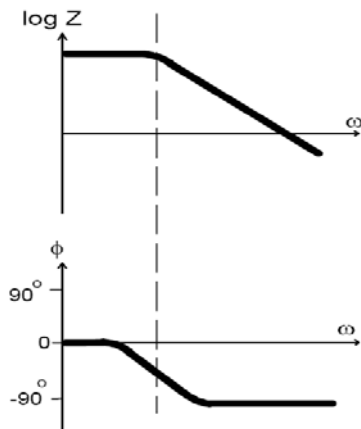


Fig. 1.28. Bode plot with one time constant.

– **Equivalent circuits**

The interpretation and quantification of the impedance plots requires the selection of an appropriate equivalent circuit. Is a way of thinking that the sample as a collection of electrical elements. So in the circuit each element should model a specific function of the sample.

– **Equivalent circuit elements**

i. **Electrolyte resistance**

Electrolyte resistance is the resistance of the electrolyte between the reference electrode and the working one. For studies of organic coatings, the solution is very conductive and so the electrolyte resistance is very low (1-50 ohms).

The resistance of an ionic solution depends on the ionic concentration, type of ions, temperature, and the geometry of the area in which current is carried. In a bounded area with area  $A$  and length  $l$  carrying a uniform current, the resistance is defined as,

$$R = \rho \frac{l}{A} \quad (\text{Eq.1.11})$$

Where

$\rho$  is the solution resistivity.

Because most of the electrochemical cells do not have uniform current distribution through a definite electrolyte area. It is difficult to calculate the electrolyte resistance but it could be calculated by fitting the data to a model.

### ii. Coating capacitance

For coatings that are relatively thick, the coating capacitance tends to be low in range of  $1\text{nf}/\text{cm}^2$ . In the case of thin coatings, like the sol-gel coatings, the coating capacitance tends to be in range of  $1\text{nf}/\text{cm}^2$  or high. The physical and chemical properties that affect the coating capacitance are,

$$C_{\text{coating}} = \frac{(\varepsilon)(\varepsilon_0)A}{d} \quad (\text{Eq.1.12})$$

Where

$\varepsilon$  is the dielectric constant of the coating,

$\varepsilon_0$  is electric constant =  $8.85 \times 10^{-14}$  Farad/ cm,

A is the area in  $\text{cm}^2$  and d is the thickness in cm.

The capacitance is related to the magnitude of the impedance by [Z] by

$$[Z] = \frac{1}{2\pi f C_{\text{coating}}} \quad (\text{Eq.1.13})$$

The absorption of water modifies the dielectric constant of the coating, and thus the coating capacitance. Since the relative dielectric constant of organic coatings is typically in the range 3-10, and for pure water it is 78.4 at 25°C, the uptake of water leads to a rise in the dielectric constant, resulting in a higher capacitance. For coatings exposed to an aqueous electrolyte, like Simulated Body Fluid (SBF) used in this work, the coating capacitance not only informs about the thickness, continuity, porosity and degree of coverage afforded by the coating. Also monitoring the evolution of the coating capacitance along the immersion time, usually it is possible to obtain valuable information about the electrolyte uptake and its diffusion through the coating.

### iii. Pore resistance

Due to the penetration of electrolyte into the micropores and/or nanopores of the coating, the resistance of the coating changes. Upon immersion, the pore resistance can be very high and usually decrease with time of exposure to the electrolyte. Sometimes as a result of formation of corrosion products which block the pores, the measured resistance can be increased due to the blocking effect.

### iv. Polarization resistance

The corrosion rate of the un-coated metal substrate or the metal substrate beneath the coating can be obtained from the polarization resistance values. The polarization resistance is inversely proportional to the corrosion rate. But this is a first approximation, since the polarization resistance includes the metal's charge-transfer resistance and the mass-transfer resistance, and the charge-transfer resistance of the metallic substrate is the one inversely related to the corrosion rate. Thus, to study the corrosion rate accurately it is necessary to measure the metal's charge-transfer resistance. EIS is the only electrochemical technique which allows separating the contribution of both resistances from the polarization resistance.

### v. Double layer capacitance

An electrical double layer exists on the interface between an electrode and its surrounding electrolyte. This double layer is formed as ions from the solution "stick on" the electrode surface. The charged electrode is separated from the charged ions. The separation is very small, often on the order of angstroms.

Charges separated by an insulator form a capacitor. The value of  $C_{dl}$  is usually in the range of 10-40  $\mu\text{F}/\text{cm}^2$ . The value of the double layer capacitance depends on many variables. Electrode potential, temperature, ionic concentrations, types of ions, oxide layers, electrode roughness, impurity adsorption, etc. are all factors.

vi. Constant phase element

Capacitors in EIS experiments often do not behave ideally. Several theories (surface roughness, "leaky" capacitor, non-uniform current distribution, etc.) have been proposed to account for the non-ideal behavior of the double layer. Instead, they act like a constant phase element (CPE). The impedance of a CPE can be expressed as:

$$Z = \left(\frac{1}{Y_0}\right)(j\omega)^{-\alpha} \quad (\text{Eq.1.13})$$

Where  $Y_0 = C$  = the capacitance and  $\alpha$  = an exponent that equals 1 for a capacitor. For a constant phase element, the exponent  $\alpha$  is less than one. The "double layer capacitor" on real cells often behaves like a CPE, not a capacitor.

– Common equivalent circuit models

To obtain all the above exposed parameters from the impedance response of a studied system, it is need to fit the system response to an appropriate equivalent circuit.

– Purely capacitive coating

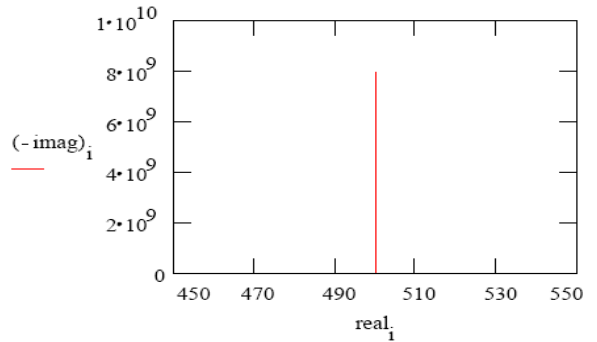
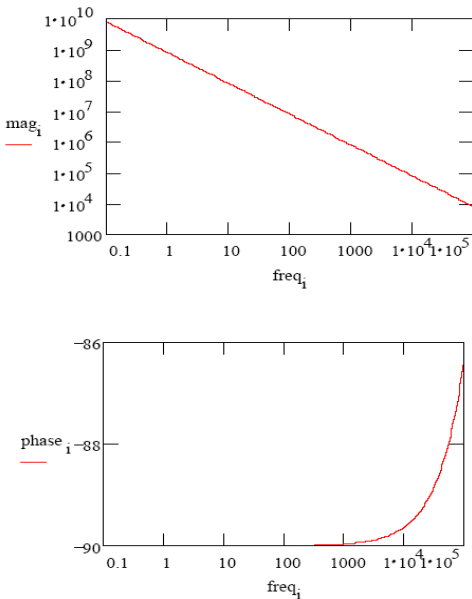


Fig. 1.29. Purely Capacitive Coating.

Fig.1.30. Typical Bode and Nyquist Plot for a perfect coating.

The appropriate equivalent circuits that can be used for an uncoated metal/electrolyte system and for a metal/coating/electrolyte system, accordingly to different degradation states are described further on.

A metal covered with an undamaged coating generally has very high impedance. The equivalent circuit for such a situation is in Figure 1.29. The model includes a resistor (due primarily to the electrolyte) and the coating capacitance in series.

– **Randles cell**

The Randles cell is combination of a capacitor and two resistors (Figure 1.31). This electrical circuit can be used to represent, in general terms, a corroding metal.  $R_s$  is associated with the electrolyte resistance.  $C_{dl}$  is associated with the double layer capacitance of the metal/electrolyte interface.  $R_{ct}$  is associated to the charge-transfer resistance of the metallic surface or with the polarization resistance when the mass-transfer resistance cannot be separated.

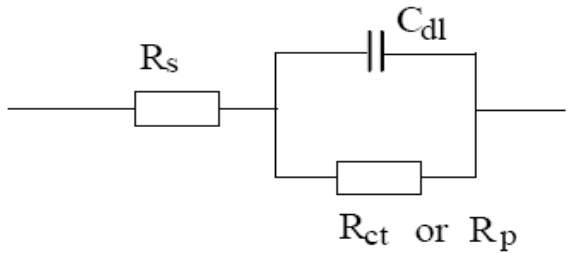


**Fig.1.31.** The Randles cell equivalent circuit.

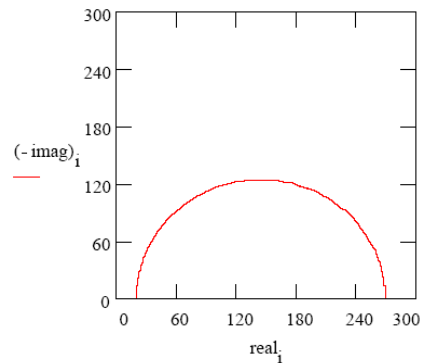
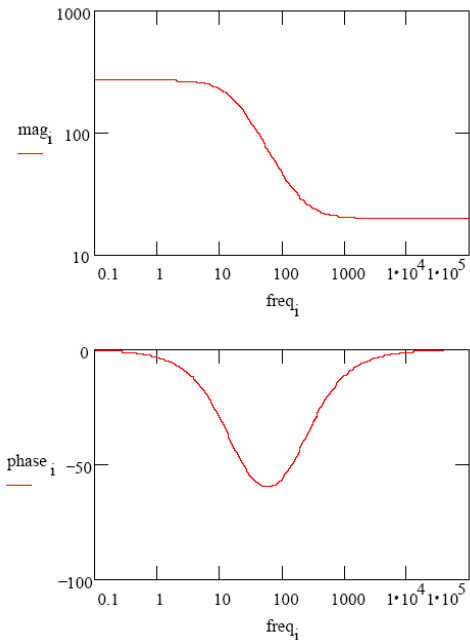


**Fig.1.32** Typical Bode and Nyquist Plot for a corroding bare metal.

In the Nyquist plot, the solution resistance ( $R_s$ ) can be found by reading the real axis value at the high frequency intercept. The real axis value at the other (low frequency) intercept is the sum of the polarization resistance and the solution resistance ( $R_s+R_p$ ).

### – EIS of coated metals.

Most coatings degrade with time when are exposed to an aggressive aqueous electrolyte. Usually, for thick or highly protective coatings, in the first stages of exposure to the electrolyte, the response of the coating/metal system is entirely dominated by the coating response, that is the coating capacitance and the ionic resistance of the coating impregnated with electrolyte. Then, after a certain amount of time; water and aggressive ions penetrate into the coating and form a new liquid/metal interface under the coating. Corrosion phenomena can occur at this new interface. Figure 1.33, show the typical Bode and Nyquist diagrams obtained. Obviously, this is just the general trend, since depending of the studied system the shape of the diagrams obtained can differ from this figure in lower or higher degree.

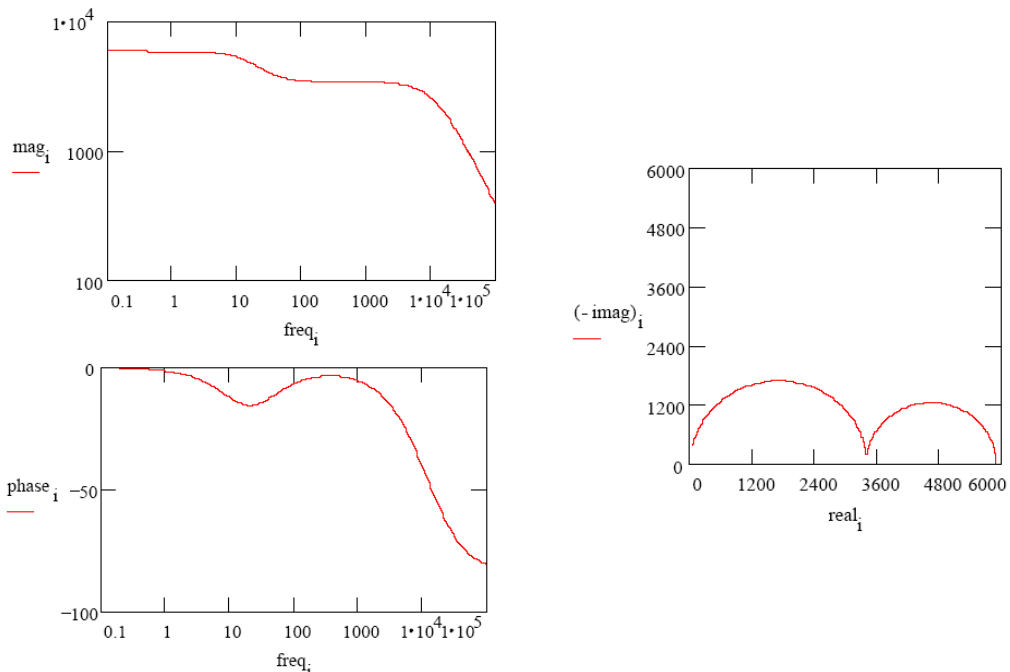


**Fig.1.33** Typical Bode and Nyquist Plot for a porous coated metal.

Then, after a certain time of exposure, the process of electrolyte penetration is taking place through the development of conductive pathways. Assuming the existence of electrolytic pathways in the coating leads to electrochemical reactions at the metal surface, the bode and Nyquist plots should show two time constants (Fig. 1.33); one time constant at high frequencies related to the coating capacitance and coating resistance, and a second time constant related to the charge-transfer resistance and the electrical double layer capacitance at the metal/solution interface. In order to explain the equivalent circuit proposed to characterize the sol-gel coatings obtained in this Thesis, a schematic picture of a cross-section of metal/sol-gel coating system in contact with an aqueous electrolyte is illustrated in figure 1.34. The equivalent circuit is superposed exactly over the corresponding parts of the studied system.

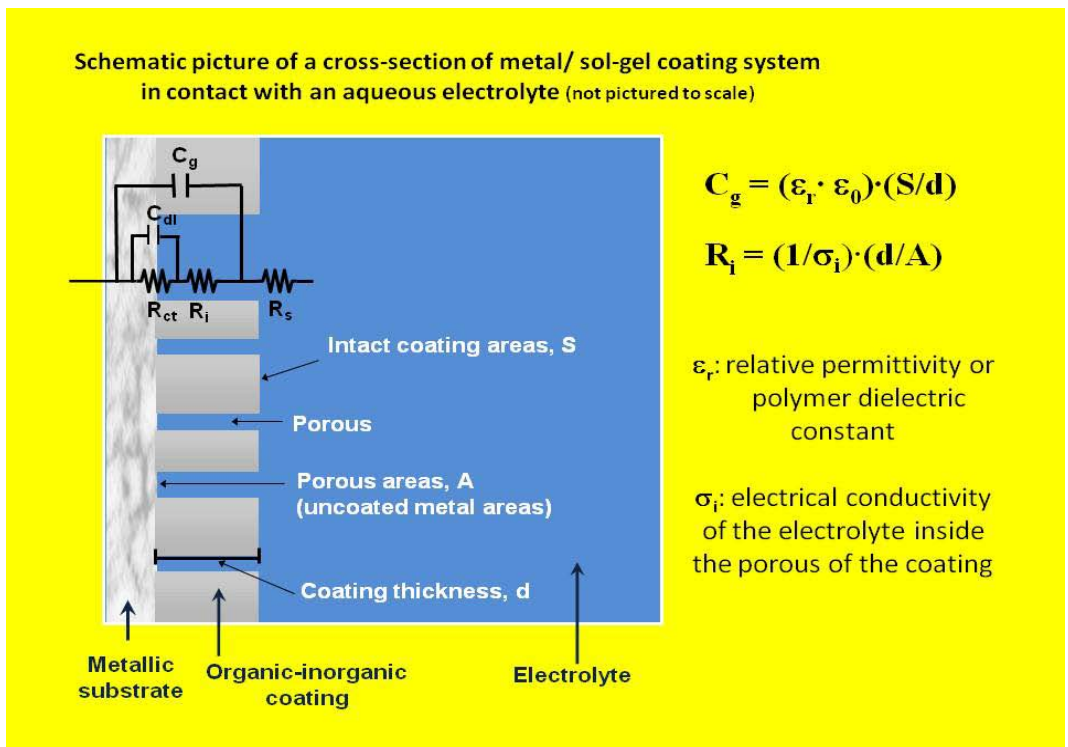


Fig.1.34. Equivalent Circuit for a porous Coating.

## Theoretical Aspects

---

Where  $R_s$  is the solution resistance (electrolyte resistance),  $C_g$  is the capacitance of the sol-gel coating,  $R_i$  the ionic resistance of the sol-gel coating impregnated with the electrolyte, which is related as showed in fig.1.34 with the electrical conductivity of the electrolyte inside the porous of the sol-gel coating,  $\sigma_i$ , with the coating thickness,  $d$ , and with the uncoated porous areas at the porous/metal interface.  $C_{dl}$  is the electrical double layer capacitance and  $R_{ct}$  is the charge-transfer resistance at the metal surface. According to this equivalent circuit, the low frequency arc in the impedance diagram (Nyquist plot) is related to the Faradaic process at the base of the pores or imperfections of the sol-gel coating, whilst the arc appearing at the high frequencies is related to the sol-gel coating itself.

## *Chapter (2)*

*Aim of the work*



### Objectives

The main aim of this PhD thesis has been to obtain multifunctional tailor-made thin films with pre-designed properties (corrosion protection and bioactivity properties). These thin films were prepared by using hydroxyapatite inorganic and organic-inorganic hybrid precursors by sol-gel route. The corrosion protection and bioactivity properties of the thin films were enhanced by applying laborious interactive methodologies of approaching. These methodologies were based on applying iterative methods of preparation, changing for example the synthesis conditions and/or the thermal treatments, in conjunction with the concourse of characterization techniques and the evaluation of the bioactivity and corrosion behaviour of such materials, until obtaining new derived sol-gel coatings with the desired properties.

The efficiency of the coating, generally, in terms of corrosion protection is based on its physical barrier properties, so homogenous crack-free films are required. Unfortunately during curing step and as result of evaporation of ethanol and water, small pores and pinholes are developed which provide paths for electrolyte and corrosive agents to diffuse through the coating and corrode the metallic implant. The corrosion of the metallic alloy could finally lead to undesirable cytotoxicity and failure of the implant.

The thesis aims to overcome this problem through usage of various inorganic and organic-inorganic hybrid coatings. We hypothesized that the combination of the silane precursors with solid particles of hydroxyapatite (HAp) or phosphorus precursors as triethylphosphite (TEP) and dimethylsilylphosphite (DMTSP) could lead to enhancement in the performance of the coatings by increasing their barrier properties and bioactivity.

In this contest the research work of this PhD thesis has been divided in the following three steps:

- 1) Preparation and characterization of hydroxyapatite (HAp) powders and coatings produced by the sol-gel route using calcium nitrate tetrahydrate

and triethylphosphite as calcium and phosphorus precursors and to do the following :

- (a) To determine the optimum thermal treatment temperature by using differential thermal analysis (DTA),
  - (b) To quantitatively measure the mass change as function of temperature by thermal gravimetric analysis (TGA),
  - (c) To evaluate the crystallinity, crystal size, unit cell volume, lattice parameters and phases developed by using X-ray diffraction (XRD),
  - (d) To study the *in-vitro* bioactivity of prepared samples in simulated body fluid (SBF),
  - (e) To study the degradation, ion release and precipitation of Ca and P ions in simulated body fluid (SBF) by using Inductively coupled plasma mass spectrometry (ICP),
  - (f) To study the changes of the functional groups by using Fourier transformer infrared spectroscopy (FTIR) before and after immersion in SBF,
  - (g) To apply the prepared and well characterized HAp sols upon Ti6Al4V alloys,
  - (h) To study the bioactivity and corrosion protection of the resulting HAp coatings on Ti6Al4V in SBF,
  - (i) To make surface characterization of the HAp coatings on Ti6Al4V surfaces by scanning electron microscopy and energy-dispersive X-ray spectroscopy (SEM/EDX analyses) before and after immersion in SBF,
  - (j) To study the corrosion resistance of HAp coatings on Ti6Al4V surfaces by using electrochemical impedance spectroscopy (EIS).
- 2) To study the reaction kinetics of  $\gamma$ -methacryloxypropyltrimethoxysilane (MAPTMS) and tetramethyl orthosilicate (TMOS) in water–ethanol medium. The

aim of this part of the study has been optimizing synthesis processes for obtaining adequate organic-inorganic matrices able to act as hosting of guest agents with barrier properties and bioactivity which will be added to those organic-inorganic matrices in a next step.

FTIR,  $^{29}\text{Si}$  and  $^{13}\text{C}$  NMR were used to study the interaction of MAPTMS and TMOS in  $\text{H}_2\text{O}$ -EtOH medium and to detect the structure of the intermediate species of sol formed as a result of condensation of metal alkoxide and then form three-dimensional networks. This step enables the selection of the optimum conditions to prepare workable hybrid films.

- 3) Synthesis and characterization of organic-inorganic hybrid coatings deposited on Ti6Al4V alloys by sol-gel route. These hybrid coatings are based in mixtures of MAPTMS and TMOS loaded with different phosphorous precursors (HAp, TEP, and DMTSP).
  - (a) To study the effect of the doping on the thermal stability and weight loss of the hybrid samples by using TGA,
  - (b) To confirm the formation of organic-inorganic hybrids in these deposited films on Ti6Al4V surfaces using ATR-IR,
  - (c) To study amorphous or crystalline nature of the films by using XRD,
  - (d) To study the morphology, topography, thickness and surface coating characteristics (wettability) of the prepared films,
  - (e) To study the biocompatibility of the coatings by Bradford protein assay,
  - (f) To study the in-vitro bioactivity of the MAPTMS/TMOS/HAp-Ti6Al4V ,MAPTMS/TMOS/TEP-Ti6Al4V and MAPTMS/TMOS/DMTSP-Ti6Al4V systems on cell viability/cytotoxicity and cell adhesion,
  - (g) To evaluate the electrochemical behavior by EIS of Ti6Al4V alloy coated with these hybrids sol-gel films exposed to a SBF solution.



*Chapter (3)*  
*Materials & Methods*



### 3.1 Inorganic Coating

#### 3.1.1 Preparation

##### 3.1.1.1 HAp sol

HAp sol was obtained by hydrolysis and condensation of triethyl phosphite (TEP),  $P(OCH_2CH_3)_3$  (Fluka, 98 %) and calcium nitrate tetrahydrate,  $Ca(NO_3)_2 \cdot 4H_2O$  (Panreac) as precursors of phosphorus and calcium respectively. In brief, 0.03 mol of TEP was first diluted in ethanol and hydrolyzed for 24 h with a fixed amount of distilled water in a parafilm-sealed glass container under stirring.

During TEP hydrolysis, due to the immiscibility between the phosphite and water, the mixture initially appears opaque, light being scattered by the emulsion phase. However, after approximately 24 hours of mixing the emulsion transformed into a clear solution suggesting that the phosphite was hydrolyzed. This was confirmed by the loss of phosphite odor of the mixture.

A stoichiometric amount (i.e. to maintain  $Ca/P=1.67$ ), 0.05 moles of  $Ca(NO_3)_2 \cdot 4H_2O$  is dissolved first in 25 ml ethanol then added drop wise into the hydrolyzed phosphite solution. The mixed sol solution was then continuously agitated for additional 30 min. The pH value was adjusted to be 7.5; the sol was aged static at  $60^\circ C$  for 16 h because of the slow reaction between the Ca and P precursors in the sol phase. The solvents were then driven off resulting in a viscous liquid. Further drying at  $80^\circ C/12$  h was done to obtain the prepared material in a powder form.

The as-prepared powder obtained is “amorphous calcium phosphate” (ACP). In order to be transformed to crystalline form, it was subjected to thermal treatment through one step of thermal treatment. The selection of the treatment schedule was depending upon the results obtained from DTA data in Figure 4.1. Table 3.1 shows the thermal treatment temperatures to which the prepared samples have been subjected. The obtained powder was placed in a steel die, and pressed to produce 13 mm diameter pellets which were thermally treated at various temperatures (600, 800, and  $1200^\circ C/2h$ ).

**3.1.1.2 HAp Inorganic coating**

Ti6Al4V disks of 2 cm of diameter and 0.4 cm of thickness were polished using different silicon carbide grit papers starting from #320 up to #1200 grades. The substrates were ultrasonically degreased with acetone for 10 min and washed with distilled water. Finally, the substrates were dried at 200°C for 1 hour in an air oven to form a titanium oxide surface.

After formation of TiO<sub>2</sub>, the substrates were dip coated with the prepared sol solution, with a dipping and withdraw speed of 12 cm/min. The sol-coated substrates were then immediately transferred into an oven and held at 80°C for 30 min to stabilize this first layer. To increase the thickness of the coating, the above process was repeated for three times and finally it was sintered at various temperatures (600, 800°C) for 2 hours.

**Table 3.1.** Thermal treatment temperatures of the as received powder samples.

Sample	Thermal treatment temperature (°C)	Time (hours)
S6	600	2
S8	800	2
S12	1200	2

– Inorganic HAp coating on Ti6Al4V surfaces, flowchart

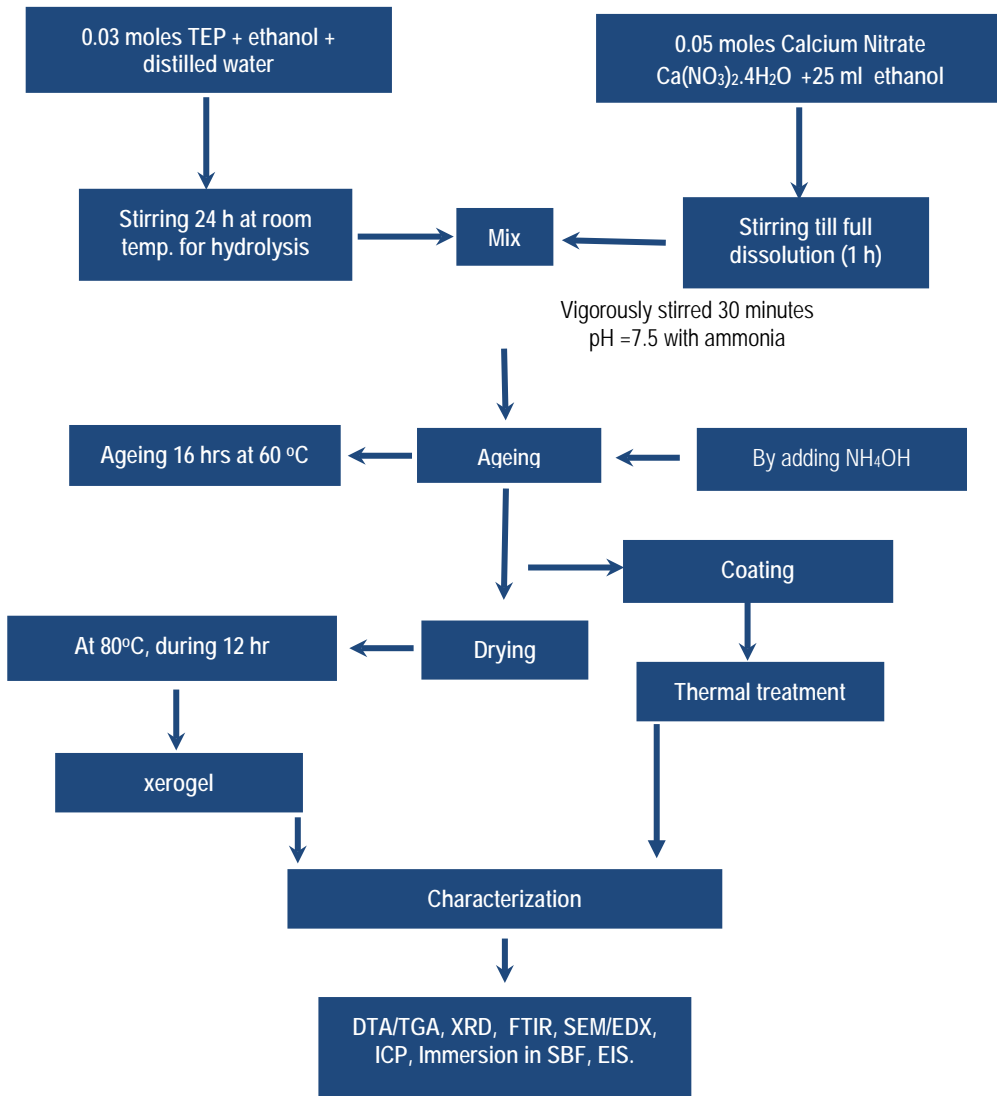


Fig. 3.1 Flow chart of the Preparation of HAp coatings on Ti6Al4V via sol-gel process.

### 3.1.2 Characterization

#### 3.1.2.1 Thermal analysis: (DTA/TGA)

The thermal behavior and mass loss of the ACP powder was carried out using a SETARAM DTA-TG Setsys Evolution-1750 equipment, with  $\alpha\text{-Al}_2\text{O}_3$  powders as a reference material. A powder sample with a weight of about 5 mg was analyzed. The sample and the reference material were heated from ambient temperature to 1300°C at a heating rate of 20°C/min in air.

#### 3.1.2.2 X-ray diffraction (XRD)

Following preparation of the HAp sol-gels and subsequent powdering, X-ray diffraction was undertaken. X-ray diffraction patterns of the thermally treated ACP powder have been recorded using a Siemens D5000 diffractometer equipped with scanning rate 0.1° in the 2 $\theta$  ranging from 10° to 100° step time 1 sec. The as prepared powder sample S1 and thermally treated samples, S6 "treated at 600°C", S8 "treated at 800°C" and S12 "treated at 1200°C" were examined with a high-resolution X-ray powder diffractometer using monochromatic Cu K $\alpha$  radiation ( $\lambda = 0.15406$  nm). Once the X-ray pattern had been recorded, the data obtained were compared to standard patterns available in the powder diffraction software.

#### 3.1.2.3 Fourier transform infrared spectroscopy (FTIR)

The as-prepared "S1" and thermally treated samples "S6, S8, S12" were tested by FTIR spectral analysis. Each sample was prepared according to standard procedure by mixing about 2.00 mg of powder sample with 200 mg of KBr, which was subsequently pressed into pellet in an evacuated die. All the spectra were measured by using a Nicolet Magna 550 infrared spectrometer at room temperature, which covers the wave number range of 4000 – 400 cm<sup>-1</sup> with a resolution of 4 cm<sup>-1</sup> at room temperature. A background reading was taken before collecting spectra from the samples and was subtracted from the sample spectra.

### 3.1.2.4 Immersion in SBF

The in-vitro bioactivity of the prepared HAp in powder and coating forms was tested by soaking in 50 ml of Kokubo's simulated body fluid (SBF)<sup>[112]</sup>. The pH of the SBF solution was buffered at 7.4. The specimens were immersed in separate plastic containers then incubated for 15 days at 37°C (Figure 3.2).

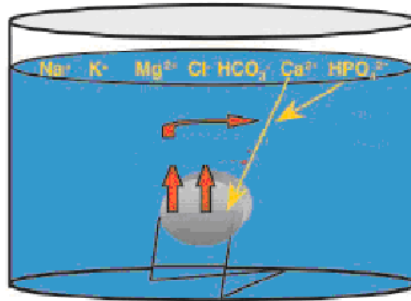


**Fig 3.2** Static SBF test in plastic container at constant temperature 37°C

A 20 ml sample of SBF was taken from each test tube after 1, 5 and 15 days and was stored frozen until being analyzed by inductively coupled plasma (ICP) technique. After withdrawn of a 20 ml solution, an equal volume of SBF was added in order to maintain a constant volume. After 15 days of immersion, the specimens were removed from the solution, rinsed with distilled water and left to dry at room temperature.

### 3.1.2.5 Inductively coupled plasma (ICP)

Inductively coupled Plasma technique (ICP) was applied by using a PERKIN ELMER mod. OPTIMA 2100 DV equipment to determine the Ca and P ion concentration in SBF during 15 days of immersion of the HAp pellets. The concentration of both ions is an indicative of the dissolution and precipitation of apatite from SBF upon the surface of the sample. Ca and P ion concentrations were measured as a function of immersion time.

### 3.1.2.6 Scanning electron microscopy and energy dispersive X-ray (SEM/EDX)

The surface morphology of the HAp-coatings/Ti6Al4V samples, before and after immersion in SBF, was analyzed by scanning electron microscopy (SEM) with a field emission gun (FEG) coupled with an energy dispersive X-ray (EDX) system (Oxford Inca microanalysis system and a windowless detector). For chemical analysis, the samples were examined in a JEOL-6500F microscope at 15 kV acceleration voltages. The samples were coated with ultra thin carbon conductive layer to avoid the charging due to the non-conductive nature of the studied samples.

### 3.1.2.7 Corrosion behaviour

The corrosion behaviour of the HAp-coatings/Ti6Al4V system in an electrochemical cell filled with Kokubo's solution was evaluated by applying electrochemical impedance spectroscopy (EIS) measurements<sup>[112]</sup>. For this purpose a potentiostat/galvanostat AutoLab EcoChemie PGSTAT30 (Eco Chemie, Utrecht, the Netherlands) equipped with a FRA2 frequency response analyzer module was used. A three electrode setup was applied. The working electrode was the investigated sample with an area of 2.14 cm<sup>2</sup>. The reference and the counter-electrode were a saturated calomel electrode (SCE) and a large size graphite sheet, respectively. The EIS measurements were made at the open circuit potential (OCP). Logarithmic frequency scans were carried out by applying sinusoidal wave perturbations of  $\pm 10$  mV in amplitude, in the range of 10<sup>5</sup>-10<sup>-3</sup> Hz. Five impedance sampling points were registered per frequency decade. The impedance data were analyzed by using the 'EQUIVCRT' program developed by Boukamp (AC-Immittance Data Analysis System, Version 4.5 (University of Twente, The Netherlands, 1993) and the the ZView software version 3.1c (Copyright 1990-2011, Scribner Associates Inc., NC, USA written by D. Johnson).

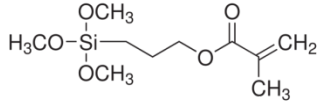
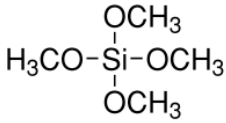
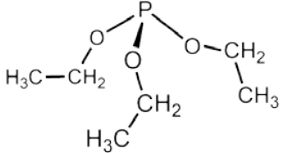
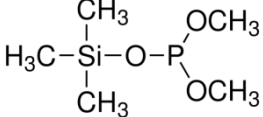
## 3.2 Organic-Inorganic coatings

### 3.2.1 Silanes/phosphorus mixture: properties & preparation

The main silane hybrid prepared in this thesis consists of a mix of two different silane molecules:  $\gamma$ -methacryloxypropyltrimethoxysilane (MAPTMS) and tetramethoxysilane (TMOS).

- i.  $\gamma$ -methacryloxypropyltrimethoxysilane (MAPTMS) (depicted in Figure 3.3, which is an organo-functional silane composed of a long backbone of carbon atoms with a silicon atom substituted with three  $-O-CH_3$  groups as head. The main organic fraction of the main MAPTMS/TMOS hybrid coating is carried into the film by this molecule. MAPTMS molecules contain one non-hydrolysable substituent linked to the silicon atom. The silicon/carbon bond is not hydrolysable, and, therefore, it is stable in water at room temperature <sup>[119]</sup>.

**Table 3.2.** Silane and phosphorus precursors used for preparation of different coatings.

Reagent	Molecular Weight	Structure
$\gamma$ -methacryloxypropyltrimethoxysilane (MAPTMS)	248.35	
Tetramethoxysilane (TMOS)	152.22	
Hydroxyapatite (HAp)		$Ca_5(PO_4)_3(OH)$
Triethylphosphite (TEP)	166.16	
Dimethylsilylphosphite (DMTSP)	182.23	

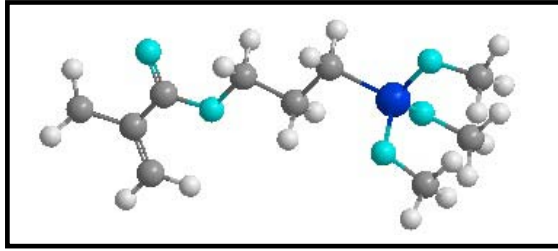


**Fig. 3.3** Schematic representations of  $\gamma$ -methacryloxypropyltrimethoxysilane (MAPTMS).

The silicon–oxygen bonds can hydrolyze in presence of water, leading to the formation of Si–OH bonds. The hydroxyl groups are responsible for the chemical bonding to metal substrate, by means of condensation reaction with the hydroxides present on metal substrates. Thus the MAPTMS molecules contains both alkoxide groups, which hydrolyze reacting with water, generate the sol-gel network and bond to the metal substrate, and organic functionalities which are embedded in the silane film can polymerize and chemically interact with an organic coating.

- ii. TMOS (depicted in Figure 3.4) is a simple molecule composed of a silicon atom bonded to four  $-\text{O}-\text{CH}_3$  groups. As a function of the hydrolysis condition, all the Si–( $\text{O}-\text{CH}_3$ ) bonds can, potentially, hydrolyze and form Si–OH bonds. For this reason, TMOS is a sort network former, owing to it promotes the formation of an inorganic network of silica. The inorganic phase is likely to be responsible of the improved barrier properties of the silane sol-gel films. Hydroxyl groups can interact with the metal substrate, leading to the formation of covalent bonds after curing.

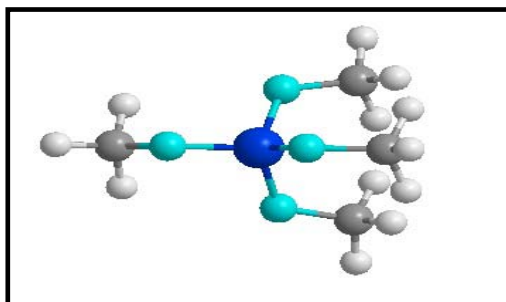


**Fig. 3.4** Schematic representations of tetramethoxysilane (TMOS).

## MATERIALS & METHODS

iii. Triethyl phosphite TEP, composed of phosphorus atom bonded to three ( $-\text{OCH}_2\text{-CH}_3$ ) which are susceptible to hydrolysis reactions and thus can lead to the formation of P-O-Si bonds.

From Figure 3.6 can be observed that during hydrolysis of TEP, as the time proceeds, the  $\text{CH}_2\text{-CH}_3$  could be substituted. When total substitution has taken place the hydrolysed TEP could react with the silanol groups resulted from the silane hydrolysis and forming Si-O-P bonds. The ethanol produced as a side product from this reaction can be easily driven off during curing of the deposited films.

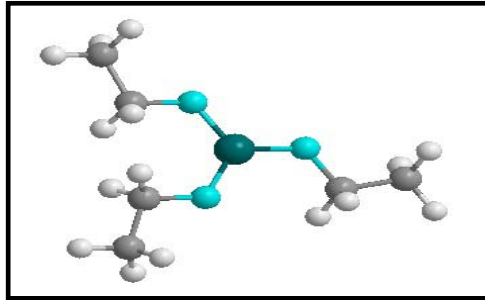


Fig. 3.5 Schematic representation of Triethyl phosphite (TEP).

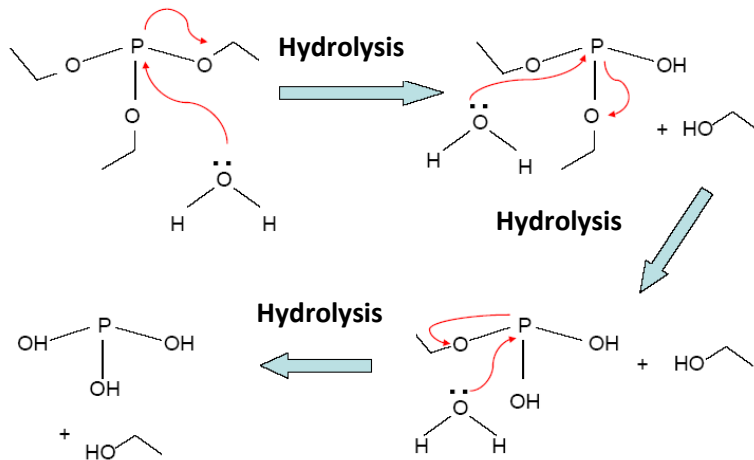
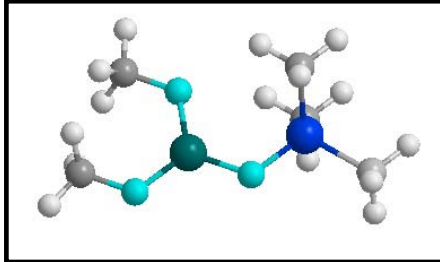


Fig. 3.6 Schematic diagrams showing the chemical process that is taking place as TEP is hydrolyzed.

- iv. Dimethylsilylphosphite (DMTSP), composed of one silicon – three methyl bonds which stable in water and one Si-O-P bond, where the P atom is bonded to two hydrozables –O-CH<sub>3</sub> which could finally leads to formation of more Si-O-P or PO<sub>4</sub><sup>3-</sup> bonds in the film.



**Fig. 3.7** Schematic representation of Dimethylsilylphosphite (DMTSP).

### 3.2.2 Optimization the preparation conditions of the organic-inorganic hybrid (hydrolysis study)

Hydrolysis and condensation of silane solution is a time-dependent process. A “workable” silane solution should contain a sufficient number of Si-OH groups for the subsequent condensations during silane surface treatment. Without sufficient hydrolysis, an oily silane film is obtained. Such film cannot provide corrosion protection due to the lack of a cross-linked structure and a good adhesion to substrates. The hydrolysis and condensation of the silane coating in this thesis was studied via application of FTIR and liquid state NMR techniques to determine the best condensations for obtaining workable coatings when applied on the surface of Ti6Al4V alloy.

#### 3.2.2.1 MAPTMS/TMOS sol preparation

Mixtures of  $\gamma$ -methacryloxypropyltrimethoxysilane (MAPTMS) and tetramethoxysilane (TMOS) were used as precursors of the organopolysiloxane matrices. A molar ratio MAPTMS/TMOS of 4:1 was used. Ethanol (C<sub>2</sub>H<sub>5</sub>OH, 99.8%) and dd H<sub>2</sub>O were used as solvents. MAPTMS was hydrolyzed with H<sub>2</sub>O through stirring, and then the solution was reacted with TMOS vigorously stirred at a rate of

700 rpm during 24 h at ambient temperature. The molar ratio of silane/water/ethanol was 1:3:3.

### 3.2.2.2 Preparation of MAPTMS/TMOS/HAp hybrid

A homogeneous dispersion of HAp particles in the prepared matrix is required for obtaining well-defined mechanical properties and consistent performance of the final composite material. Aggregation of the dispersed phase has a detrimental impact resulting in undesirable effects on the final composite as aggregates act as stress concentrators. During the sol-gel process the hybrid coatings were modified with dispersions of HAp particles previously prepared. A good dispersion of these HAp particles was achieved by using triton X-100 as an appropriate dispersant and exerting mechanical stirring and ultrasonic agitation, to break down any agglomerates. HAp powder with an average particle  $< 20 \mu\text{m}$  was dispersed with a powder concentration of 0, 0.5, 1 and 1.5 wt% respectively, relative to the amount of the silane sol. 2% of triton with respect to the HAp weight was added as dispersant and the suspensions were stirred by ultrasonic agitation during 5 min.

### 3.2.2.3 Preparation of MAPTMS/TMOS/TEP hybrid

The use of a phosphorous precursor such as triethyl phosphite (TEP) allowed the introduction at a molecular level of P into an organic-inorganic hybrid network. For the triethyl phosphite (TEP) containing hybrids, TEP (Fluka, 98 %) was added to the previously prepared MAPTMS/TMOS mixture with a volumetric ratio of 0.3, 0.6 and 0.9 ml TEP against 20ml MAPTMS/TMOS. These ratios have been chosen to be equivalent to the phosphorus content in the previously prepared MAPTMS/TMOS/HAp sol. Because of difficulty in hydrolyzing the TEP precursor, the mixture was stirred at 700 rpm for 12 hours at RT. A stirring time of 12 hours is required because the trialkylphosphates are more stable than silane precursors and are less susceptible to hydrolysis.

### 3.2.2.4 Preparation of MAPTMS/TMOS/ DMTSP hybrid

Dimethylsilylphosphite (DMTSP) has been used as another source for the introduction of P into the organic-inorganic hybrid network at molecular level. For the DMTSP (Aldrich) containing hybrids, the DMTSP was added to the previously prepared MAPTMS/TMOS mixture with a volumetric ratio of 0.3, 0.6 and 0.9 ml of DMTSP in 20ml MAPTMS/TMOS sol. This amount has been chosen to be equivalent to the phosphorus content in the MAPTMS/TMOS/HAp sol. The mixture then was stirred at 700 rpm for 12 hours at RT.

### 3.2.3 Organic-Inorganic coating application onto Ti6Al4V substrate

#### 3.2.3.1 Substrate Preparation

Ti6Al4V disks of 2 cm diameter and 0.4 cm thickness were used. The specimen surface was ground using a grit sand papers starting from 320 to 2000 grit size to achieve uniform surface condition. The specimens were rinsed with dd-H<sub>2</sub>O and ultrasonically cleaned in ethanol for 10 min for degreasing and removing any contamination on the surfaces and then dried in air.

#### 3.2.3.2 Dip-coating of O-I hybrid on Ti6Al4V

Deposition of a single layer system from the prepared organic-inorganic sols were made by immersion of Ti6Al4V alloy in freshly prepared sol followed by withdrawal at a constant velocity of 9 cm/min, with a holding time of 1 min, using a dip-coater at room temperature (Figure 3.8).



**Fig 3.8.** Dip coater used for deposition of sol-gel layer upon Ti6Al4V surface.

## MATERIALS & METHODS

---

The MAPTMS/TMOS/HAp-Ti6Al4V, MAPTMS/TMOS/TEP-Ti6Al4V and MAPTMS/TMOS/ DMTSP -Ti6Al4V coated specimens were placed in furnace for 2 hours at 120°C. The selection of curing at not too high temperature to avoid the decomposition of the organic component is the end step to obtain the Si–O–Si network or Me–O–Si bond between the deposited layers on the Ti6Al4V surface. The rest of the sols were dried at 120°C and crushed to obtain powders. Figures 3.9-3.11 show the scheme flowcharts of the different sol-gel coatings preparation on the Ti6Al4V surfaces.

**Table 3.3.** Sample name and compositions of the hybrid coatings.

Matrix	Sample			
		HAp	TEP	DMTSP
20 ml MAPTMS/TMOS	Control	-	-	-
	0.5 HAp	0.5wt %	-	-
	1 HAp	1 wt %	-	-
	1.5 HAp	1.5 wt %	-	-
	0.3 TEP	-	0.3 ml	-
	0.6 TEP	-	0.6 ml	-
	0.9 TEP	-	0.9 ml	-
	0.3 DMTSP	-	-	0.3 ml
	0.6 DMTSP	-	-	0.6 ml
	0.9 DMTSP	-	-	0.9 ml

– Flowchart of MAPTMS/TMOS/HAp coatings on Ti6Al4V surfaces

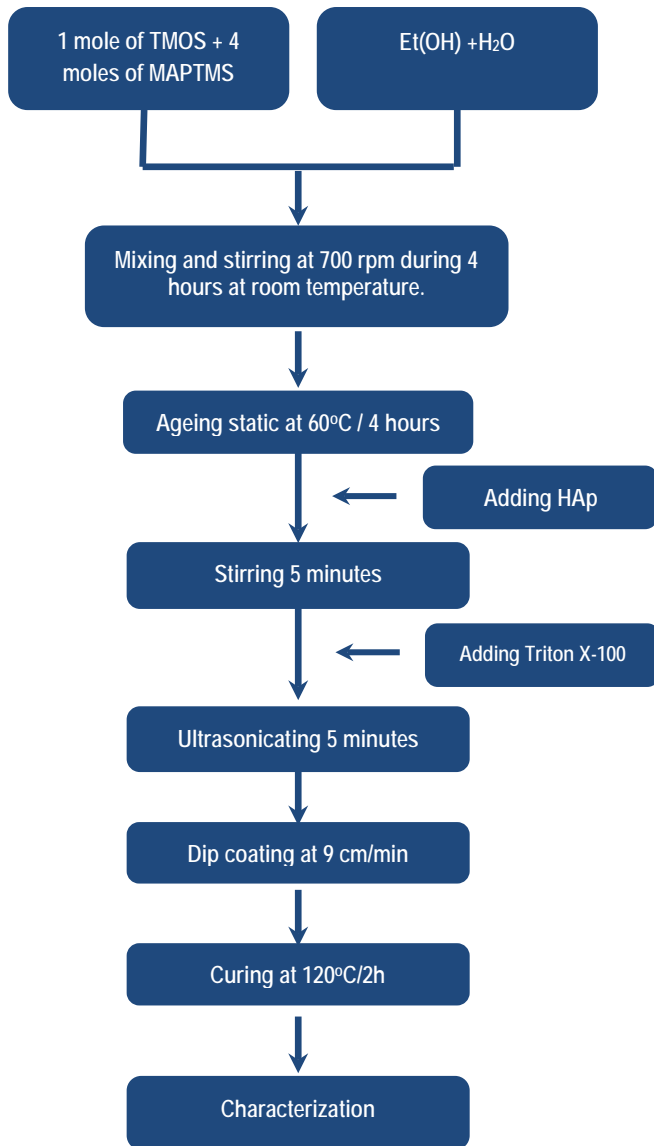
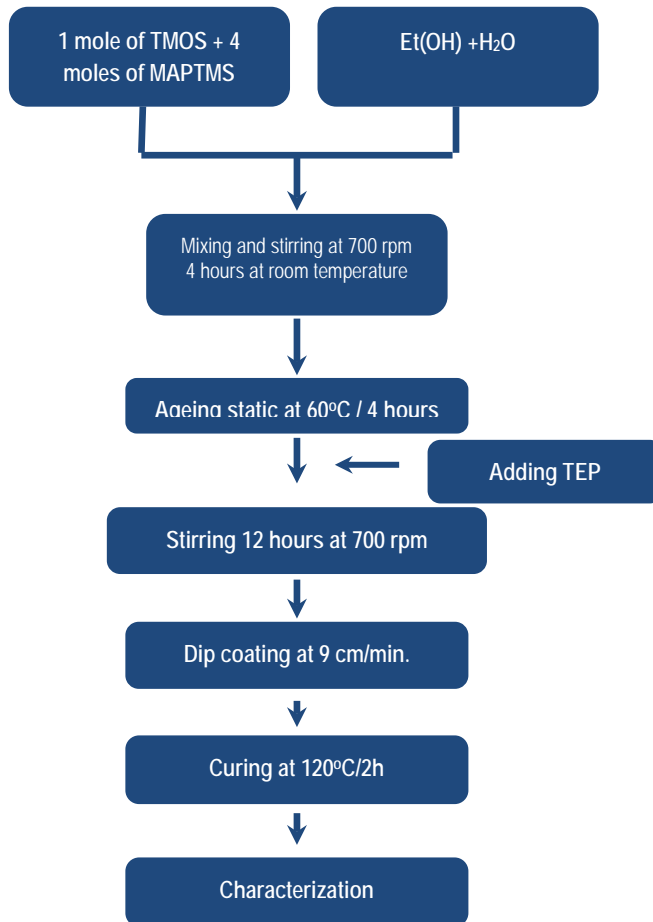


Fig. 3.9 Flowchart of the preparation of MAPTMS/TMOS/HAp coatings on Ti6Al4V via sol-gel process.

– Flowchart of MAPTMS/TMOS/TEP coatings on Ti6Al4V surfaces



**Fig. 3.10** Flowchart of the preparation of MAPTMS/TMOS/TEP coatings on Ti6Al4V via sol-gel process.

– Flowchart of MAPTMS/TMOS/DMTSP coatings on Ti6Al4V surfaces

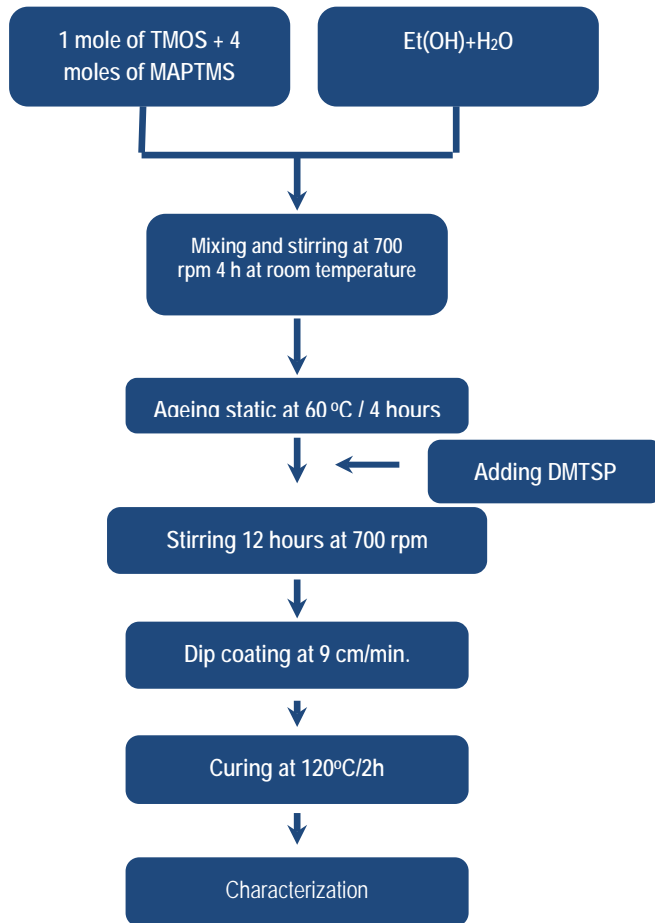


Fig. 3.11. Flowchart of the Preparation of MAPTMS/TMOS/ DMTSP coatings on Ti6Al4V via sol-gel process.

### 3.2.4 Characterization

#### 3.2.4.1 Fourier transforms infrared spectroscopy (FTIR)

The prepared sol samples were analyzed by Fourier transform infrared spectrometer (FTIR). Each sample was prepared by mixing about 0.5 ml of sol with 200 mg of Caesium iodide (CsI), which was subsequently pressed into pellet in an evacuated die. All the spectra were measured by using a Nicolet Magna 550 infrared spectrometer at room temperature, which covered the wave number range of 4,000–400  $\text{cm}^{-1}$ .

#### 3.2.4.2 Liquid-state nuclear magnetic resonance (NMR)

$^{29}\text{Si}$  and  $^{13}\text{C}$  NMR spectra of the liquid samples were recorded at 79.49 and 100.62 MHz, respectively, in a Bruker AVANCE-400 spectrometer. The external magnetic field was 9.4 T. The single-pulse NMR spectra were obtained after excitations with a  $\pi/2$  pulse length of 6  $\mu\text{s}$ , for  $^{29}\text{Si}$  and intervals between successive accumulations (recycle delay) of 5 s for each type of signal. NMR spectra were registered for  $^{13}\text{C}$  with a  $\pi/2$  pulse length of 5  $\mu\text{s}$  and a recycle delay of 10 s. The number of scans was 1600 in the case of  $^{29}\text{Si}$  and 128 for  $^{13}\text{C}$ . The  $^{29}\text{Si}$  and  $^{13}\text{C}$  chemical shift values are given relative to  $\text{Si}(\text{CH}_3)_4$ . The deconvolutions of the NMR spectra were carried out with the WINFIT program so that the different components, and their contributions, could be determined.

#### 3.2.4.3 Thermogravimetric analysis (DTA/TGA)

Thermogravimetric analysis of the various organic-inorganic hybrids in xerogel form was performed on a Mettler Toledo TGA/SDT A851. Samples of 5 mg crushed powder were put into an  $\text{Al}_2\text{O}_3$  crucible and the measurements were performed in the temperature range 23–900°C (heating rate 10°C/min) in air. The data was baseline corrected by carrying out a blank run and subtracting this from the plot obtained.

### 3.2.4.4 Attenuated total reflectance-infrared spectroscopy (ATR-IR)

The structural features of the cured hybrid coatings were characterized by attenuated total reflectance-infrared spectroscopy (ATR-IR) using a spectrophotometer Perkin Elmer, Model spectrum 100. The ATR-IR was recorded between 650 and 4000  $\text{cm}^{-1}$  with a resolution of 4  $\text{cm}^{-1}$  at room temperature. For each measurement 4 scans were collected.

### 3.2.4.5 Solid state nuclear magnetic resonance (NMR)

$^{29}\text{Si}$ ,  $^{13}\text{C}$  and  $^{31}\text{P}$  MAS NMR spectra of the solid samples were recorded at 79.49, 100.62 and 161.97 MHz respectively, in a Bruker AVANCE-400 spectrometer. The external magnetic field was 9.4 Tesla. All measurements were carried out at 20°C and the samples were spun around the magic angle of  $54.74^\circ$  with respect to the magnetic field at spinning rate of 10 kHz. The  $^{29}\text{Si}$  and  $^{31}\text{P}$  spectra were obtained with single pulse sequences after excitations with a  $\pi/2$  pulse lengths of 5  $\mu\text{s}$ , and intervals between successive accumulations (recycle delay) of 10s for both signals. Cross polarization and proton decoupling (CPMAS) NMR spectra were registered for  $^{13}\text{C}$  with a contact time of 1ms and a recycle delay of 10s. The numbers of scans were 400 in the case of  $^{29}\text{Si}$  and  $^{31}\text{P}$  and 600 for  $^{13}\text{C}$ . The  $^{29}\text{Si}$  and  $^{13}\text{C}$  chemical shift values are given relative to  $(\text{CH}_3)_4\text{Si}$ . The  $^{31}\text{P}$  chemical shift values are given relative to 85%  $\text{H}_3\text{PO}_4$  aqueous solution. The deconvolutions of the NMR spectra were carried out with the WINFIT program so that the different components, and their contributions, could be determined.

### 3.2.4.6 X-ray diffraction (XRD)

X-ray diffraction patterns of the MAPTMS/TMOS/HAp and MAPTMS/TMOS/TEP xerogels was analyzed using the same device and conditions mentioned in 3.1.2.2.

### 3.2.4.7 Scanning electron microscopy (SEM/EDX)

JEOL-JSM 840A Scanning electron microscope (SEM) coupled with Energy Dispersive X-ray analysis (EDX) were employed for the observation of morphology

and to determine the chemical composition of the prepared hybrid coatings. The samples were coated with ultra thin gold conductive layer to avoid the charging due to the non conductive nature of the studied samples.

### 3.2.4.8 Viscosity

The viscosity of different prepared sols was measured at room temperature at a shear rate of  $10 \text{ s}^{-1}$  at  $20 \text{ }^\circ\text{C}$  using a BOHLIN Rheometer equipped with a measuring plate of 40.4 mm and a gap of 0.150 mm.

### 3.2.4.9 Coating thickness

The thickness of the MAPTMS/TMOS/HAp, MAPTMS/TMOS/TEP, MAPTMS/TMOS/DMTSP films deposited onto Ti6Al4V substrates were measured by using a Dektak 6M-Veeco stylus profiler accompanied with Dektak 32 software. The coating thickness was measured on half coated samples. By a linear scanning (length of 1mm) was measured the difference or step produced between the uncoated and coated area on surface of the same. For statistical analysis three different areas of each film were studied and the results derived from coating thickness were expressed as mean values  $\pm$  standard deviation.

### 3.2.4.10 Wettability

The wettability of the MAPTMS/TMOS/HAp, MAPTMS/TMOS/TEP, and MAPTMS/TMOS/DMTSP films deposited onto Ti6Al4V substrates were determined by measuring the contact angle of distilled water (polar fluid) droplets on the surface of the films. The Sessile drop method was used for contact angle measurements using a Video-based Optical Contact Angle Measuring Instrument using a DSA 10 MK2, KRUSS, from Germany. A  $2 \text{ } \mu\text{l}$  fixed droplet of water was positioned on the surface; 3 drops per sample were applied. The drops were photographed immediately after positioning and images of drops were processed by the image analysis system, which calculated the contact angles from the shapes of the drops.

### 3.2.4.11 Confocal microscopy

The roughness was evaluated with an Optical Imaging Profiler Sensofar PLμ 2300 operating in confocal mode. Measurements were realized by using a confocal objective EPI 20X at a working distance of 4.5 with an numerical aperture of 0.45, which results in a spatial sampling of 0.8 μm and a rms resolution of <20nm.

Three different areas are selected on each sample to perform the measurements. On each area, eight roughness determinations have been done to obtain the Ra parameter, among others. Concretely, Ra is obtained from a line scanning of 80 μm. The Ra values here included are the medium value obtained as result of the 24 measurements performed on each sample.

### 3.2.5- In-vitro bioactivity

#### 3.2.5.1 Protein adsorption

To study the physiological behavior of the coated Ti6Al4V surfaces, protein adsorption onto these surfaces was studied. Fibrinogen was used as representative protein. Before incubation, the samples were rinsed with phosphate-buffered saline (PBS, pH=7.4) to rehydrate the surface and then transferred into wells of standard 6-well plates and 4 ml of 1 mg/ml fibrinogen solution in PBS was pipetted onto each surface (50 mM Tris/HCl, pH 7.4, 100 mM NaCl, 5mM MgCl<sub>2</sub>). Adsorption was allowed to proceed in an incubator for 1 h at 37°C.

Upon completion of adsorption, the samples were thoroughly rinsed with PBS 3 times and with dd water to remove unbound proteins (non-adsorbed) and salt residues then dried at 37 °C.

The amount of protein adsorbed to the films was determined by measuring the protein remaining in the solution by the Bradford method according to the manufacturer's protocols, and absorbance was measured using a well-plate reader at a wavelength of 595 nm. For Statistical analysis three samples of each hybrid powder was studied and the results derived from protein adsorption test were expressed as mean values ± standard deviation.

### – Tissue culture

In vitro studies were performed on coated and untreated Ti6Al4V substrates using normal human osteoblast (NHOst cells, Lonza, USA). Once culture was initiated the NHOst line was cultured at 37°C with 5% CO<sub>2</sub> in osteoblast basal medium (Lonza, USA) supplemented with 10% fetal calf serum, 1% gentamycin sulphate and 1% ascorbic acid. Cells were initiated and maintained as per the manufacturer's instructions.

#### 3.2.5.2 Neutral Red cell viability/cytotoxicity assay

To determine the effect of the different Ti6Al4V coatings on cell viability and determine substrate cytotoxicity the neutral red uptake assay was performed in the manner described by Repetto et al <sup>[120]</sup>. Ti6Al4V disks of 2 cm diameter and 0.4 cm thickness were coated with different organic-inorganic hybrids and sterilized by exposure to methanol. The discs were placed in six well tissue culture plates (Sarstedt Inc., USA) and 2500 cells/cm<sup>2</sup> were deposited on each substrate. Discs were incubated under normal conditions with refreshment of the media after three days. After seven days the medium was replaced with RPMI-1640 medium (Lonza, USA) containing 0.01% neutral red dye (Sigma-Aldrich, USA) and the plates incubated for 2 h under normal conditions. Discs were rinsed with PBS and an equal volume of de-stain solution (1% glacial acetic acid, 50% ethanol) were added. Plates were shaken for 20 min and absorbance at 540 nm was read by a micro-plate reader (Tecan, Switzerland). The experiment was done four times in triplicate and disks without cells were used to correct for dye adsorbed to disk coatings.

#### 3.2.5.3 Immunofluorescence

Osteoblast actin cytoskeleton and focal adhesion sites were visualized by staining after seven days on 0.9 mm disks seeded with 2500 cells/cm<sup>2</sup>. One unit of Alexa Flour 568 phalloidin (Invitrogen, USA) was used to stain f-actin. Monoclonal mouse anti-human vinculin clone hVIN-1 IgG1 (Sigma-Aldrich, USA) at a concentration of 1:1000 with Alexa Fluor 488 conjugated goat anti-mouse IgG (Invitrogen, USA) secondary at

a concentration of 1:1500 was used to visualize focal adhesion sites. Vectashield mounting solution (Vector Laboratories, USA) containing 4,6-diamidino-2-phenylindole was used to stain cell nuclei and applied before imaging with an Olympus DP71 fluorescence microscope.

### **3.2.5.4 Statistical analysis**

Cell viability/proliferation data was normalised and assessed using GraphPad Prism v.5, using a one way ANOVA, and Tukey's multiple pairwise comparison. The confidence level was 0.05 and the assumption of normality and constant variance was assessed in each case.

### **3.2.5.5 Corrosion behaviour**

The corrosion behaviour of the organic-inorganic hybrid/Ti6Al4V system in an electrochemical cell filled with Kokubo's solution was evaluated by applying electrochemical impedance spectroscopy (EIS) measurements using the same conditions mentioned in the 3.1.2.7.

## *Chapter (4)*

*Inorganic sol-gel derived thin films and Hydroxyapatite*

*Powders*



# Inorganic sol-gel derived thin films and Hydroxyapatite powders

## - Introduction

The bone tissue is a natural composite, composed of organic and inorganic materials. The inorganic solid is hydroxyapatite (HAp) while the organic one is collagen. The HAp has the formula  $\text{Ca}_{10}(\text{PO}_4)_6(\text{OH})_2$ , amounts to 70% of the total bone mass, with the remaining mass formed by organic matter "mostly collagen" and water <sup>[19]</sup>. The collagen molecules are bonded together forming fibrils, which bound together to form fibers. Between these fibers there are small interstitial empty spaces, where apatite nanocrystals are deposited. The HAp seems to be the most appropriate ceramic material for hard-tissue replacement. HAp ceramics do not exhibit any cytotoxic effects, show excellent biocompatibility with hard tissues, with skin and muscles tissues. For this reason, the most used calcium phosphate in implant fabrication is HAp, a biological active material with different forms, particles, films, coatings, fibers which has extensive biomedical applications <sup>[130]</sup>. Nano-sized HA powder has a high specific surface area and therefore exhibits enhanced activity toward chemical and biological interactions in the human body. HAp has been known to form in vitro and in vivo a bioactive bone-like apatite layer spontaneously on its surfaces <sup>[19,130]</sup>. The formed apatite layer acts as interface between the implant and tissue facilitating the formation of chemical and biological bond with the osseous tissue. Therefore, the essential prerequisite for a biomaterial to bond directly to living bone is the formation of an apatite layer on its surface when implanted in the body. As this layer is formed, the protein absorption onto the surface of such layer will trigger the osteoblasts, "new bone forming cells", to differentiate, reproduce, form new bone tissue.

The HAp can be synthesized by many methods <sup>[131,132]</sup>. The Sol-gel synthesis of HAp ceramics has attracted much attention because it offers a molecular-level mixing of the calcium and phosphorus precursors, which is capable of improving chemical homogeneity of the resulting HAp to a significant extent, in comparison with conventional methods such as solid state reactions, wet precipitation and hydrothermal synthesis <sup>[84-133]</sup>. The HAp synthesized by sol-gel will form strong chemical bonds with

bone in-vivo; all of these mentioned properties place the HAp into a class of biomaterials known as bioactive materials. Unfortunately brittleness limits its usage for load bearing applications. For that it can only be used as bone fillers and bone graft substitutes in orthopedics <sup>[134]</sup>.

The only exception where HAp is applied in dynamically loaded situations is the use of HAp as a coating material on metallic materials. When metallic materials are implanted in the human body, some of the consequences of in vivo degradation are the metal ion release from the surface of the implanted material and the harmful effect of the metal ion released which could escape into the surrounding tissue <sup>[135]</sup>. Thus the best implant metallic material will be the one exhibiting minimum ion release of less toxic ions and maximum biocompatibility. For this, the present work is aimed to design a multifunctional sol-gel derived hydroxyapatite coating on Ti-6Al-4V surface. This coating should enhance the implant surface bioactivity, as well as, avoid the metal ion release.

In the present part, triethylphosphite (TEP) has been chosen as phosphorus precursor because of its rapid hydrolysis. Subsequent interaction of hydrolyzed phosphite with Ca precursor as calcium nitrate tetrahydrate (CNT) will form HAp at relatively low temperature of 600°C using sol-gel process.

### **The aim of this chapter has been:**

- To prepare bioactive sol-gel derived HAp ceramic powders suitable for being used as reinforcement materials for organic-inorganic hybrid coatings.
- To prepare and characterize inorganic sol-gel derived HAp coatings on Ti6Al4V surfaces.
- To study the *in-vitro* bioactivity and corrosion protection behaviour of the resulting HAp-coatings.

### **4.1. Characterization of the sol-gel derived HAp powders**

The experimental techniques used to characterize the HAp powders prepared into this PhD thesis project have been the following:

- Thermal analysis (DTA/TG), to determine the optimum thermal treatment conditions to prepare HAp powders from the amorphous calcium phosphate (ACP) that was previously obtained by applying the sol-gel process.
- Fourier transforms infrared (FTIR), to study the functional groups in the thermally treated HAp powders.
- X-ray diffraction (XRD), to evaluate the crystallinity, crystal size, unit cell volume, lattice parameters and phases developed during the thermal treatment step.

### 4.1.1. Thermal analysis (DTA/TGA)

DTA/TGA is an excellent method for characterizing the materials obtained in this kind of studies and is a powerful tool to choose the proper thermal treatment temperatures for the prepared HAp powders. The differential thermal analysis (DTA) and thermogravimetry analysis (TGA) curves of the as prepared material are given in Figure 4.1.

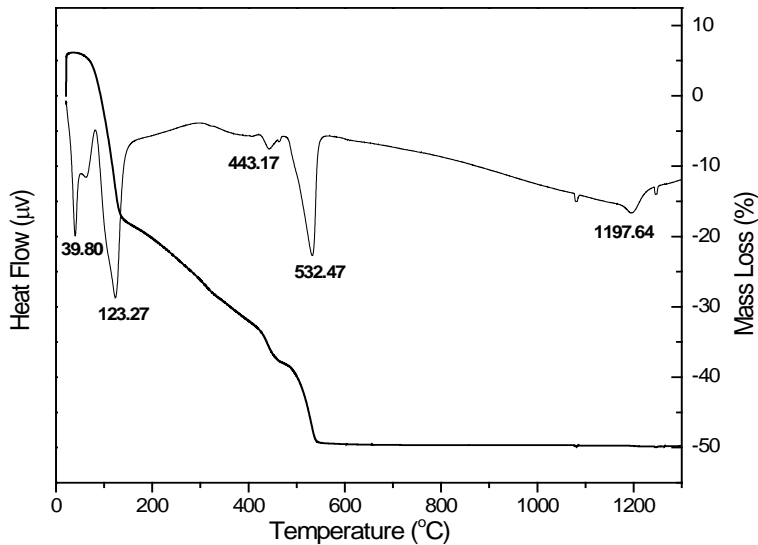


Fig. 4.1. DTA/TG of the as prepared S1 powder.

DTA was employed to determine the temperature at which the as-prepared powder, amorphous calcium phosphate (ACP), transforms to crystalline HAp. The first endothermic peak appeared at 38.8°C with the shoulder at 60°C is due to the evaporation of the absorbed water "residual moisture evaporation"<sup>[136]</sup>.

The two endothermic peaks at 123.27°C and 443.17°C can respectively be attributed to elimination of crystalline water in un-reacted calcium nitrate tetra hydrate  $\text{Ca}(\text{NO}_3)_2 \cdot 4\text{H}_2\text{O}$  and removal of  $\text{NO}_3^-$  ions as well as to the condensation "dehydration" of hydrogen phosphate ions ( $\text{HPO}_4^{2-}$ ) to form amorphous pyrophosphates ( $\text{P}_2\text{O}_7^{4-}$ ) which is a member of ACP that formed during processing of HAp synthesis<sup>[137-139]</sup>. The endothermic peak at 532.47°C is representative of the endothermic reaction indicating the crystallization of HAp. The last endothermic peak is observed at 1197.64°C is attributed to the decomposition of HAp<sup>[140]</sup>.

The TG curve of the as-prepared sample S1 is shown in Figure 4.1. The weight loss was complete at about 570°C and three discrete weight-loss regions occurred, the first region at 44-172°C with 25% weight loss which corresponds to elimination of adsorbed water indicated as endothermic peak at 38.8°C and shoulder at 60°C in the DTA diagram. The second weight loss region appeared at 172-479°C with 18% weight loss correspond to elimination of lattice water which indicated as endothermic peak in the DTA diagram at 443°C. The third weight loss observed at 479-570°C with a weight loss of 11% corresponds to the decomposition of the nitrate salts which is also indicated as an endothermic peak at 532°C in the DTA curve.

Depending on the DTA results, the studied samples were subjected to specific thermal treatments, in order to transform the as-prepared ACP into crystalline form. Table 4.1 shows the thermal treatment temperatures to which the prepared samples have been subjected. All the samples were subjected to the thermal treatment of 2 hours.

**Table 4.1.** Thermal treatment temperatures of the as received sample

Sample	Thermal treatment temperature (°C)	Time (hours)
S1	-	-
S6	600	2
S8	800	2
S12	1200	2

#### 4.1.2. Fourier transform infrared spectroscopy analysis (FTIR)

Fourier transform infrared spectroscopy (FTIR) is a widely used analytical technique for characterization of the functional groups within the structure of biomaterials such as HAp which IR active is. The most observed peaks are situated in the region of 900–1200  $\text{cm}^{-1}$  due to the presence of P–O groups of HAp. Theoretically, there are four vibrational modes present for phosphate ion:  $\nu_1$ (961  $\text{cm}^{-1}$ ),  $\nu_2$ (475–440  $\text{cm}^{-1}$ ),  $\nu_3$ (1190–976  $\text{cm}^{-1}$ ) and  $\nu_4$ (660–520  $\text{cm}^{-1}$ ), respectively. These modes are IR active and are used to characterize apatite structure <sup>[141]</sup>.

The FTIR spectra of the as-prepared and thermally treated samples are shown in Figure 4.2. The spectrum of the as prepared sample shows a very poorly defined broad band in the region where bands due to phosphate ions in the HAp should be present (Figure 4.2A). The intense broad band at 1342  $\text{cm}^{-1}$  and the sharp bands at 825  $\text{cm}^{-1}$  and 1631  $\text{cm}^{-1}$  along with the small peaks of 1049 and 1766  $\text{cm}^{-1}$  are related to the  $\text{NO}_3^-$  which comes from the starting precursor. As the temperature increases, the  $\text{NO}_3^-$  could decompose into gaseous oxide of nitrogen and, hence, the related absorption bands disappear as the temperature increase <sup>[141]</sup>. The bands at 740, 1083, 1164 and 555  $\text{cm}^{-1}$  indicate the presence of  $\text{P}_2\text{O}_7^{4-}$  in the as prepared sample dried at 80°C. These peaks also disappeared as temperature increased. The broad band at 3435  $\text{cm}^{-1}$  and the band at 914  $\text{cm}^{-1}$  assigned to  $\text{OH}^-$  stretching and bending of the lattice water both of which

are weakened, as the powder being thermally treated. All of these mentioned bands indicative of poorly crystalline or amorphous apatite structure (ACP).

The spectra of the samples S6, S8, S12 thermally treated at 600, 800 and 1200°C exhibit a decrease of the intensity of OH<sup>-</sup> band and disappearance of NO<sub>3</sub><sup>3-</sup> and P<sub>2</sub>O<sub>7</sub><sup>4-</sup> bands (Figures 4.2B-4.2D), indicating the transformation of ACP into crystalline form. This is confirmed by the appearance of new absorption bands in the 520-1500 cm<sup>-1</sup> range assigned to the major absorption modes of the PO<sub>4</sub><sup>3-</sup> groups, which are presents in the HAp.

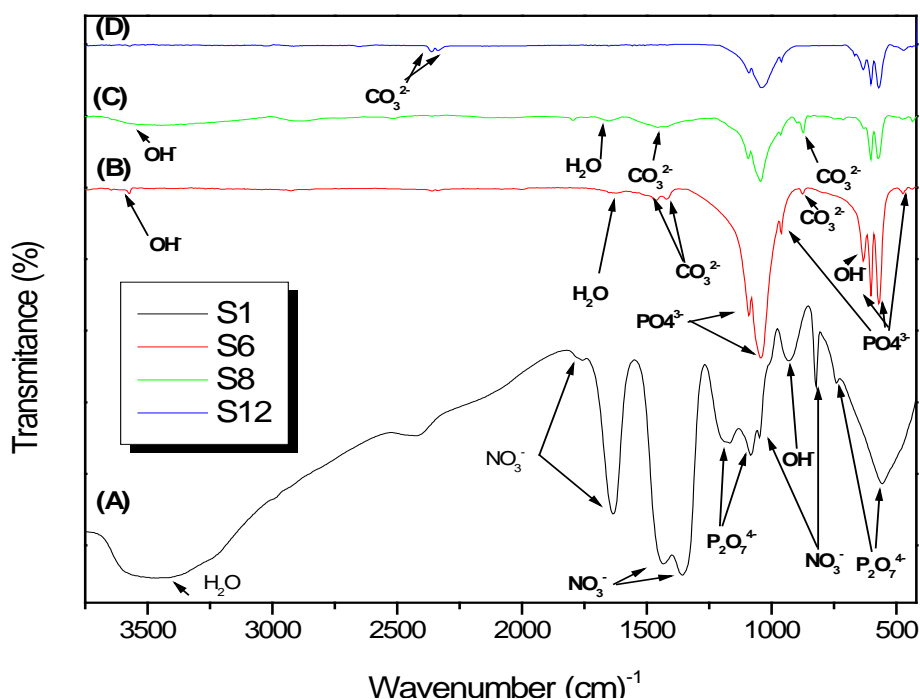


**Fig. 4.2.** FTIR spectra of the dried gel S1 and the powders thermally treated at different temperatures; 600°C/2h (S6), 800°C/2h (S8) and 1200°C/2h (S12).

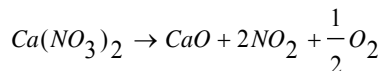
In the spectra of the sample S6 thermally treated at 600 °C, the bands at 474 and 570 and 608 cm<sup>-1</sup> are related to O–P–O bonds in PO<sub>4</sub><sup>3-</sup> groups (Figure 4.2B). These bands along with the small shoulders at 960 and 1091 cm<sup>-1</sup> and broad one at 1041 cm<sup>-1</sup> are related to PO<sub>4</sub><sup>3-</sup> group; indicate the formation of well-known typical FTIR pattern of HAp

[142]. Two small shoulders are observed at 3571 and 632  $\text{cm}^{-1}$  attribute to the absorption modes of  $\text{OH}^-$  stretching vibrations in HAp structure. The presence of the above mentioned absorption bands suggest the development of crystalline HAp at 600°C [143]. The water associated with HAp is present at 1631  $\text{cm}^{-1}$ . The small shoulder observed at 875  $\text{cm}^{-1}$  ( $\nu_2$ ) and the two weak peaks at 1465, 1419  $\text{cm}^{-1}$  ( $\nu_3$ ) are the indications of the presence of  $\text{CO}_3^{2-}$  groups in the lattice of HAp [144].

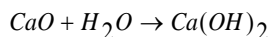
The incorporation of carbonate is a common phenomenon during the formation of biological apatite [145]. The carbonate substitution may result from  $\text{CO}_2$  in the atmosphere, dissolved in the solutions during preparation of the HAp. The  $\text{CO}_3^{2-}$  can easily replace  $\text{OH}^-$  (A sites) and  $\text{PO}_4^{3-}$  (B sites) at 1500–1545 and 1420–1470  $\text{cm}^{-1}$ , respectively to form carbonated HAp [145]. If the material is synthesized at high temperatures (800°C), the carbonate ion substitutes only the hydroxyl ion (A site), originating a type A carbonated HAp. For synthesis of HAp at relatively lower temperature (600°C), the substitution is less selective and both hydroxyl (A site) and phosphate ions (B site) are replaced [145].

In the spectrum of the S6 sample the two weak bands at 1465, 1419  $\text{cm}^{-1}$  ( $\nu_3$ ) and a small shoulder observed at 875  $\text{cm}^{-1}$  prove that the  $\text{CO}_3^{2-}$  groups were substituted for  $\text{PO}_4^{3-}$  groups, forming B-type carbonated apatite [145]. From biological point of view, the presence of a small amount of carbonate in the HAp structure is an advantage and has similarity to the natural bone mineral which contains 4–6% carbonate by weight [146].

So the carbonated HAp (C-HAp) is expecting to show higher bioactivity than that of HAp; this is due to the greater solubility. The  $\text{OH}^-$  band at 3563  $\text{cm}^{-1}$  is attributed to the surface hydroxyl ions of  $\text{Ca}(\text{OH})_2$  phase formed due to the chemical decomposition of the remaining calcium nitrate as follow:



The formed CaO is very reactive with water from the air and transforms to  $\text{Ca}(\text{OH})_2$  [147].



In the spectrum of the 800°C thermally treated sample S8 the bands characteristic of  $\text{PO}_4^{3-}$  groups appeared at 435, 570, 601  $\text{cm}^{-1}$  and small shoulders at 964, 1045 and 1091  $\text{cm}^{-1}$  (Figure 4.2C). The  $\text{CO}_3^{2-}$  peaks at 871  $\text{cm}^{-1}$  ( $\nu_2$ ) become more intense and the two bands at 1465, 1419  $\text{cm}^{-1}$  ( $\nu_3$ ) became broader than those of the sample S6 thermally treated at 600°C (Figure 4.2B), indicating that the CHAp is well formed <sup>[147]</sup>.

In the spectrum of the sample S12 thermally treated at 1200°C the band of  $\text{PO}_4^{3-}$  groups still are present at 570, 601, 632  $\text{cm}^{-1}$  and 960, 1041, 1091  $\text{cm}^{-1}$  (Figure 4.2D). These bands are characteristics of the HAp. The new carbonate bands which appear at 2320-2348  $\text{cm}^{-1}$  (combination of  $\nu_1+\nu_3$ ), 1467-1412 and 878  $\text{cm}^{-1}$  are observed which indicate that this sample contain carbonate.

The decomposition of  $\text{CaCO}_3$  is well known to occur at 580°C or higher temperatures, so the  $\text{CO}_3^{2-}$  bands expected to be absent in the spectra of the samples obtained at the present sintering temperatures (S6, S8, S12). However, the carbonate bands still evident in these spectra, which further proves the inclusion of  $\text{CO}_3^{2-}$  groups in the apatite structure.

### 4.1.3. X-ray Diffraction Analysis (XRD)

X-ray powder diffraction is a useful tool for determination and identification of crystalline phases. Two valuable structure parameters as crystallinity ( $X_c$ ) and the average crystallite size ( $L_c$ ) can be extracted from the X-ray diffraction peaks width <sup>[148]</sup>.

#### 4.1.3.1 Evaluation of Crystallinity

X-ray diffractometry (XRD) identifies the mineral phase and gives information about its crystallinity. As a general feature, a highly crystalline sample gives rise to narrow peaks and a poorly crystalline sample gives rise to broad peaks. "Crystallinity" refers to the degree of structural order in a solid. In a crystal, the atoms or molecules are arranged in a regular, periodic manner. In this respect means the degree of order within

the crystal lattice <sup>[149]</sup>. According to Landi et al, the fraction of crystalline phase ( $X_C$ ) can be calculated by using the following formula <sup>[150]</sup>:

$$X_C = 1 - \frac{V_{112/300}}{I_{300}}$$

### Where

$I_{300}$ : Intensity of peak diffracted from the (300) crystallographic planes of HAp.

$V_{112/300}$ : Intensity of the valley between the peaks of the planes (112) and (300) of HAp.

### 4.1.3.2 Crystallites Size by Scherrer's Equation.

The average crystallite size was calculated from the broadening in the XRD pattern. According to the Scherrer's equation <sup>[151]</sup>:

$$L_c = \frac{K\lambda}{\beta \cos \theta}$$

### Where

$L_c$ : Average crystallite size (nm).

K: Shape coefficient (value between 0.9 and 1.0).

$\lambda$ : Wave length of X -ray beam - Cu K $\alpha$  radiation ( $\lambda= 0.15406$  nm).

$\beta$ : Full width at half maximum (FWHM) of HAp (211).

$\theta$ , Diffraction angle

The conversion of  $\beta_{002}$  (rad-2 $\theta$ ) from  $\beta_{002}$  (degree-2 $\theta$ ) is obtained using the following formula. <sup>[148]</sup>.

$$\beta_{002}(\text{rad}) = \beta_{002}(\text{deg ree}) * \frac{\pi}{180}$$

The diffraction peak corresponding to the (002) was chosen for calculation of the crystalline size, as it is relatively sharper than the other peaks, this corresponds to the crystal growth following the c-axis of the HAp structure as reported <sup>[141]</sup>.

Figure 4.3 illustrates the XRD patterns of the aged gel S1, dried at 60°C and of the samples S6, S8, S12 thermally treated at 600, 800 and 1200°C for 2 h, respectively. It can be interpreted by the discussion that sharp reflection peak appears in the range of 31.8-40° 2θ for the thermally treated samples S6, S8, S12, representing the characteristic peak of HAp apatite phase (X-ray diffraction card No. JCPDS #(09-0432)).

The XRD pattern of the as-prepared sample S1 is mainly amorphous, and there is no obvious diffraction peaks observed. Since the as-prepared sample exhibited amorphous XRD so it is difficult to identify the diffraction peaks which correspond to the nitrate bands observed in the FTIR spectra of this sample. As the temperature increases several peaks appear, which ascribed to the diffraction peaks of the HAp phase.

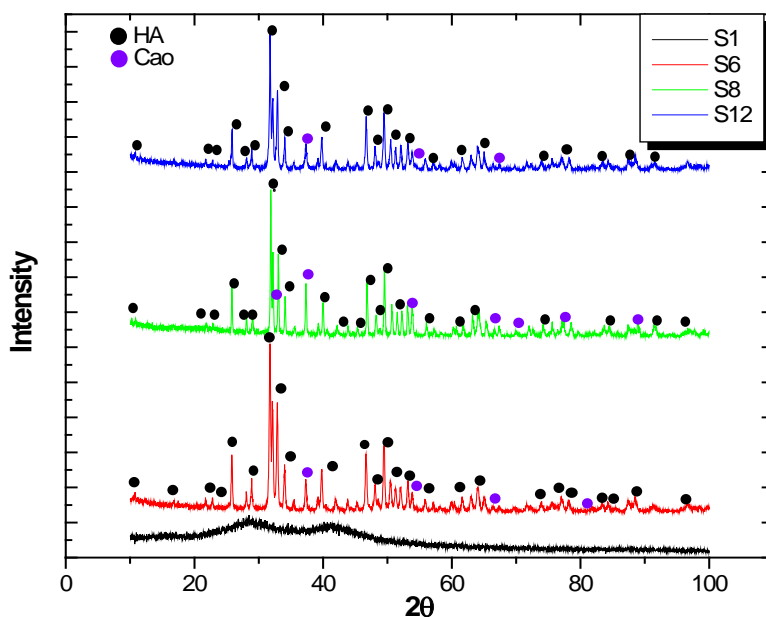


**Fig.4.3.** XRD patterns and developed phases of the dried gel S1 and the powders thermally treated at different temperatures; 600°C/2h(S6), 800°C/2h(S8) and 1200°C/2h(S12).

## CHAPTER 4

The XRD pattern of the sample S6, thermally treated 600°C, shows the crystalline phases developed. The pattern exhibits the existence of calcium oxide phase as traces, together with HAp as main phase. The presence of CaO within this is due to the remaining Ca (NO<sub>3</sub>)<sub>2</sub> in the CNT. The Ca (NO<sub>3</sub>)<sub>2</sub> can be directly transferred to CaO at the temperature of 600°C [133]. The degree of crystallinity calculated for sample S6 is 85% while the crystal size calculated was 40.7 nm.

The XRD pattern of the sample S8, thermally treated at 800°C, shows that the main developed phase still HAp besides a significant increase in the intensity of the characteristic peaks of CaO phase, when compared to the relative intensity of the peaks of HAp and CaO obtained in the sample S6. This indicates an increase in the amount of CaO with increasing the thermal treatment temperature from 600 to 800°C. Furthermore, this pattern exhibits the emergence of a new peaks characteristic of CaO. This peak is attributed to the further decomposition of calcium nitrate at high temperature.

The degree of crystallinity of sample S8 is 89%, which is greater than that obtained for the sample S6. Thus, the degree of crystallinity of HAp is increased as the temperature increase from 600 to 800°C (Table 4.2). Many authors reported that increasing the thermal treatment temperature results in the removal of residuals and further crystallization of HAp [88,152]. The sample S8 shows larger crystallite size (51 nm) than the one calculated for the sample S6 (40.7 nm). This performance is attributed to the grain growth phenomenon during thermal treatment.

**Table 4.2.** The degree of crystallinity of the powders thermally treated at different temperatures.

sample	Thermal treatment temperature (°C)	Degree of crystallinity%	Crystallite size (nm)
S6	600	85	40.7
S8	800	89	51
S12	1200	82	54

The XRD pattern of sample S12, thermally treated at 1200°C, shows that the main phase still HAp besides CaO as trace. The decrease in the amount of the CaO phase attributed to the consumption of such oxide to form calcium hydroxide which subsequently reacts with carbon dioxide to produce calcium carbonate. The newly formed  $\text{CO}_3^{2-}$  emerged as a new band at 2320-2348  $\text{cm}^{-1}$  within the FTIR spectrum of the sample S12. The degree of crystallinity of sample S12 is 82% as calculated by using Landi's equation <sup>[150]</sup>. The calculated crystal size found to be 54 nm, larger than those that were calculated for both S6 and S8 samples. The decrease in crystallinity degree is attributed to the decomposition of HAp at corresponding temperature 1200°C. The increase of the crystal size, when compared to samples S6 and S8, is attributed to an increase of ion migrations when increasing the temperature (Table 4.2).

The XRD data obtained provides further confirmation that the HAp powders are thermally stable up to 800°C, but suggests that there may be initial break down of the HAp into temperature approaching 1200°C (from XRD data). Thus it seems that temperatures up to 1200°C should be avoided when preparing the HAp coating/Ti6Al4V systems produced for Ti6Al4V implant. Figure 4.4 shows the Miller indices corresponding to HAp (X-ray diffraction card No. JCPDS #(09-0432). For comparison purposes in Table 4.3 are included the interplanar spacing ( $d$ , Å) and diffraction angle ( $2\theta^\circ$ ) at miller's indices ( $h k l$ ) for both, the standard HAp and the thermally treated samples S6, S8, S12.

For the peak located at  $2\theta$  equal to 25.87°, the characteristic reflection ( $hkl$ ) is (0 0 2) and for triplet peaks located at  $2\theta$  in the 31° to 32.90° range are (2 1 1), (1 1 2) and (3 0 0). As can be seen, there is a little deviation between these calculated values for S6, S8 and S12 samples and those values for standard XRD card No.(9-432), listed in Table 4.3.

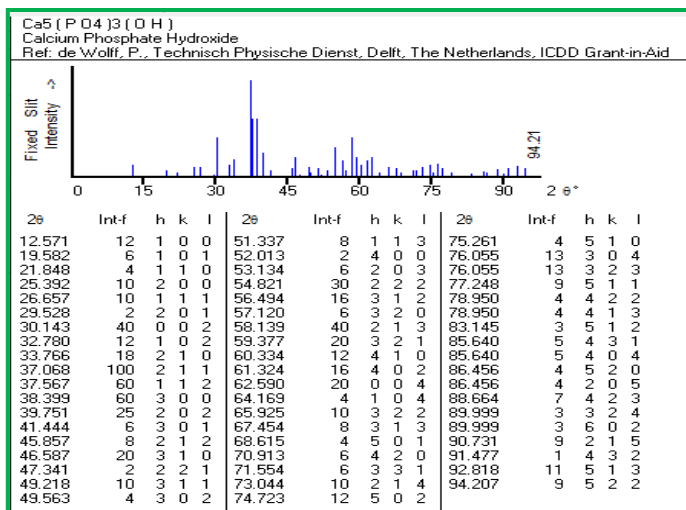


Fig. 4.4. X-ray diffraction card No. JCPDS #(09-0432)

Table 4.3 Comparison between PDF Card No.(9-432) (PCPDFWIN version 2.2, ICDD, JCPDS, 2001), and S6, S8, S12 in d Å (interplanar spacing) and 2θ° at h k l (Miller's indices).

JCPDS card No. (9-432)	0 0 2		2 1 1		1 1 2		3 0 0	
	d Å	2θ°						
S6	3.44	25.81	2.81	31.75	2.78	32.11	2.71	32.98
S8	3.44	25.81	2.80	31.88	2.77	32.19	2.70	33.04
S12	3.44	25.84	2.81	31.75	2.77	32.2	2.71	32.92

### 4.1.3.3 Lattice Parameters

The crystal structure of HAp can accommodate substitutions by various other ions for the PO<sub>4</sub><sup>3-</sup> and OH<sup>-</sup> groups. When the substituents are present simultaneously, they may affect the properties of the apatite crystallites [153]. The peaks of HAp were indexed based on hexagonal system and cell parameters were calculated using the (d) spacing of the indexed peaks. The size and the shape of the unit cell can be described by three vectors a, b and c these vectors define the unit cell and are called the crystallographic axes of the cell. They may also be describe in terms of their lengths (a,b,c) and the

# Inorganic sol-gel derived thin films and Hydroxyapatite powders

angles between them ( $\alpha$ ,  $\beta$ ,  $\gamma$ ). These lengths are the lattice constants or lattice parameters of the unit cell. For HAp calcium-phosphate bioceramics the crystal has hexagonal shape and the lattice parameters are characterized as follow:

$$a=b \neq c, \alpha=\beta=90, \gamma=120$$

The interplanar spacing ( $d$ ) for the sample was calculated according to Bragg's law<sup>[115]</sup>.

$$n\lambda = 2d \sin \theta$$

Where  $n$  is 1, and  $\lambda$  is 1.54 Å (Cu K $\alpha$ ).

The lattice parameters (a-axis and c-axis) of the sample were calculated from position of the proper diffraction lines. The samples S6, S8 and S12 were recognized by (JCPDS09-0432) by their miller's indices. The lattice parameters were determined through the (h k l) peak positions of apatite from XRD patterns according to the following equation<sup>[154]</sup>. The lattice constants of the HAp were also calculated from the X-ray data. Using the plane spacing formula for the hexagonal unit cell and simultaneously solving the equations resulting for the two highest angle peaks yields the lattice constants values a and b.

$$1/d^2 = 4/3 \left( \frac{h^2 + hk + k^2}{a^2} \right) + \frac{l^2}{c^2}$$

Where  $d$  is interplanar spacing, (h k l) are miller's indices and  $a$  and  $c$  lattice parameters. Lattice parameters were calculated by least-square method using diffraction peaks at (3 0 0) and (3 1 0) diffraction peaks for lattice parameter  $a$ . While lattice parameter  $c$  was calculated it from (2 1 1) and (1 1 2) diffraction peaks. The volume of the each unit cell was calculated by the following formula

$$V = \frac{\sqrt{3}}{2} a^2 \cdot c$$

## CHAPTER 4

Where  $V$  is the volume of unit cell (hexagonal),  $a$  and  $c$  are lattice parameters of unit cell. The refined lattice parameters of the HAp samples are in a good agreement with those previously reported [155,156]. The results of the lattice parameters calculations shown in Table 4.4 indicate that the lattice parameter  $a$  of the sample S8, thermally treated at 800°C, is smaller than that of the sample S6 thermally treated at 600°C. These results are in agreement with the results obtained by FTIR (Figure 4.3C).

The spectrum of the S8 sample shows that the phosphate ion is substituted for the carbonate ion (B-type CHAp). The  $\text{CO}_3^{2-}$  content is expected to cause a contraction in the  $a$ -axis due to its substitution for the larger  $\text{PO}_4^{3-}$  group [157]. These changes also appear logical considering that the ionic radius of  $\text{CO}_3^{2-}$  is smaller than that of  $\text{PO}_4^{3-}$ .

**Table 4.4.** Crystallographic (or lattice) parameters of S6, S8 and S12 samples calculated by using the least square method.

<b>S6</b>		<b>S8</b>		<b>S12</b>	
hkl = 3 0 0	d (Å) = 2.71 a (Å) = 9.38	hkl = 3 0 0	d (Å) = 2.70 a (Å) = 9.35	hkl = 3 0 0	d (Å) = 2.71 a (Å) = 9.38
hkl = 3 1 0	d (Å) = 2.26 a (Å) = 9.4	hkl = 3 1 0	d (Å) = 2.25 a (Å) = 9.36	hkl = 3 1 0	d (Å) = 2.26 a (Å) = 9.40
hkl = 2 1 1	d (Å) = 2.81 c (Å) = 6.93	hkl = 2 1 1	d (Å) = 2.80 c (Å) = 6.90	hkl = 2 1 1	d (Å) = 2.81 c (Å) = 6.95
hkl = 1 1 2	d (Å) = 2.78 c (Å) = 6.90	hkl = 1 1 2	d (Å) = 2.77 c (Å) = 6.87	hkl = 1 1 2	d (Å) = 2.77 c (Å) = 6.86
Average of lattice parameters a = 9.39      c = 6.91		Average of lattice parameters a = 9.358      c = 6.88		Average of lattice parameters a = 9.39      c = 6.90	
Unit cell volume (Å <sup>3</sup> ) V = 0.866 a <sup>2</sup> · c = 0.866 (9.39) <sup>2</sup> × (6.91) = 527.62		Unit cell volume (Å <sup>3</sup> ) V = 0.866 a <sup>2</sup> · c = 0.866 (9.35) <sup>2</sup> × (6.88) = 532.89		Unit cell volume (Å <sup>3</sup> ) V = 0.866 a <sup>2</sup> · c = 0.866 (9.39) <sup>2</sup> × (6.90) = 539.03	

The structure of prepared HAp samples can be described as a hexagonal unit cell with space group P63/m, with lattice parameters that are characteristic of standard

HAp,  $a=b=9.41 \text{ \AA}$  and  $c=6.88 \text{ \AA}$ . The unit cell volume of  $528.80 \text{ \AA}^3$  is in accordance with the database (JCPDS09-0432). All diffractograms of HAp samples presented nearly the same lattice parameters values like the standard one (Table 4.4). In addition these values are in good agreement with those reported for natural bone apatite  $a=9.419 \text{ \AA}$  and  $c=6.880 \text{ \AA}$  [158,159].

Analysis of the unit cell data suggests that there are minimal changes in the a-axis and c-axis after heating the HAp derived sol-gel at 600, 800, and  $1200^\circ\text{C}$ . Both the a and c values are within the range for the reported values for pure HAp ( $9.41 - 9.42 \text{ \AA}$  for the a-axis and  $6.87 - 6.88 \text{ \AA}$  for the c-axis). This performance again provides evidence to suggest that the Ca/P ratio must be close to the ideal 1.67 ratio [160].

### **4.2. *In-vitro* evaluation of functional properties of the resulting sol-gel derived HAp materials.**

An important effort of the present research has been devoted to evaluate two functional properties of the resulting sol-gel derived HAp materials: surface bioactivity and corrosion protection behavior.

This part of the study has been divided in two stages. One of them was devoted to evaluate the surface bioactivity of the resulting HAp powders. Another one was dedicated to evaluate the surface bioactivity and the corrosion protection behaviour of sol-gel derived HAp coatings prepared by dip-coating of sols on Ti6Al4V surfaces. Such sols were prepared by applying the same methodology used for obtaining the sol-gel derived HAp powders. The preparation methods used for obtaining powders and coatings have previously been described in the Experimental Part.

The main aim of these studies was to obtain multifunctional tailor-made thin films with pre-designed properties (bioactivity and corrosion protection) through the application of laborious interactive methodologies of approaching. These methodologies were based on applying iterative methods of preparation, changing for example the synthesis conditions and/or the thermal treatments for obtaining materials, in conjunction with the concurrence of characterization techniques and of behaviour evaluation of such materials, until obtaining new derived sol-gel coatings with the desired properties.

### - **Stage One: Immersion tests of HAp powders in Kokubo's simulated body fluid (SBF).**

Evaluation techniques applied in this part of the study:

- Inductive coupled plasma (ICP), to study the ion release and re-precipitation of  $\text{Ca}^{2+}$  and  $\text{PO}_4^{3-}$  ions from the nanocrystalline sol-gel derived powders for variable immersion time.
- Scanning electron microscopy/energy dispersive x-ray analysis (SEM/EDX), to study the surface morphologies and the chemical composition changes of HAp powders before and after immersion in SBF.
- Fourier transforms infrared (FTIR) after soaking in SBF, to study the functional groups changes after immersion in SBF.

### - **Stage Two: Immersion tests of the HAp coating/Ti6Al4V alloy system in Kokubo's simulated body fluid (SBF).**

Evaluation techniques applied in this part of the study:

- Surface characterization of the HAp-coatings/Ti6Al4V alloy system by SEM/EDX, before and after immersion in SBF.
- Study of the corrosion protection of HAp-coatings/Ti6Al4V alloy system in SBF, using electrochemical impedance spectroscopy (EIS).

#### **4.2.1. Bioactivity evaluation of the sol-gel HAp powders**

The bioactivity of artificial materials can be attributed to the formation of biologically active bone-like apatite layer. This apatite layer can be formed upon the surface of the sample when implanted in the body '*in-vivo*'. Kokubo et al indicted that the same layer could be reproduced in simulated body fluid (SBF) <sup>[161]</sup>.

Under normal conditions the SBF is supersaturated with respect to HAp. For that, once the apatite nuclei formed "nano-apatite seeds" on the surface of the substrate, the

apatite layer grows continuously by consuming calcium and phosphorus ions from the solution, with the result that the surface is covered with bone-like apatite layer.

Figure 4.5 shows a schematic representation of the bone-bonding mechanism of bioactive ceramics. It is known that most bioactive ceramics achieve the bonding with bone through the formation of apatite on their surface as shown in figure 4.5. This formed apatite has similar structure and composition to natural bone and is often called (Bone-like apatite). Osteoblasts can proliferate on the formed apatite, thereby leading to new bone formation and as a result the formed bone becomes in direct contact with the surface apatite on the bioactive material. Afterwards, a tight chemical bond is formed between the material and the surrounding bone [162]. Consequently, the essential requirements for an implant to exhibit bioactivity is the formation of bone-like apatite layer on its surface in a body environment. The same type of apatite could be formed in simulated body fluid (SBF) with inorganic ion concentration similar to that of human blood plasma which was proposed by Kokubo et al [161].

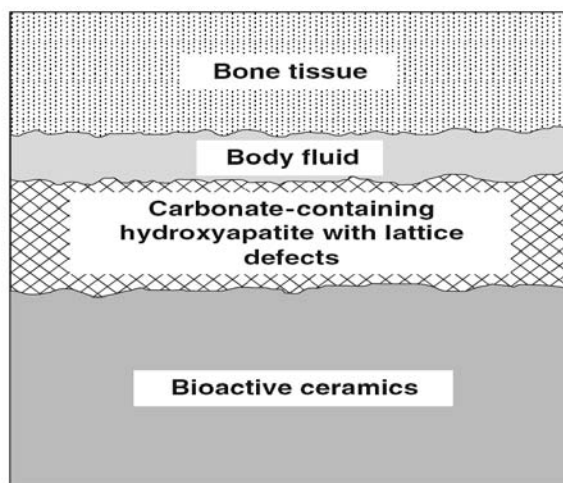


**Fig.4.5.** Bone-bonding mechanism of bioactive ceramics [162].

Immersion tests in Kokubo simulated body fluid (SBF) have been applied in the present study in order to evaluate the bioactivity of the HAp powders. During these immersion tests, the changes in concentration of the  $\text{Ca}^{2+}$  and  $\text{PO}_4^{3-}$  ions were determined for variable immersion time by applying inductively coupled plasma

technique (ICP). The changes in the concentration of both ions can constitute a valuable indicative of the dissolution and precipitation of apatite from SBF upon the surface of the sample produced during these immersion tests. Figure 4.6 shows that during the first 5 days in the simulated fluid it takes place an increase in the  $\text{Ca}^{2+}$  concentration accompanied by a decrease in  $\text{PO}_4^{3-}$ .

As the immersion time exceeds 5 days, the concentration of both ions decrease continuously. The initial increase, during the first 5 days, in the concentration of  $\text{Ca}^{2+}$  is due to the release of the  $\text{Ca}^{2+}$  from the samples surface into the SBF solution (Figure 4.6A). This accelerates the nucleation of apatite by increasing the ionic activity products of the apatite, i.e. it makes the solution more saturated with respect to the sample immersed in it. Once the apatite nuclei are formed, it grows continuously by consuming  $\text{Ca}^{2+}$  and  $\text{PO}_4^{3-}$  ions from the solution. Thus the concentration of both ions decreases with the time (Figures 4.6A y 4.6.B).

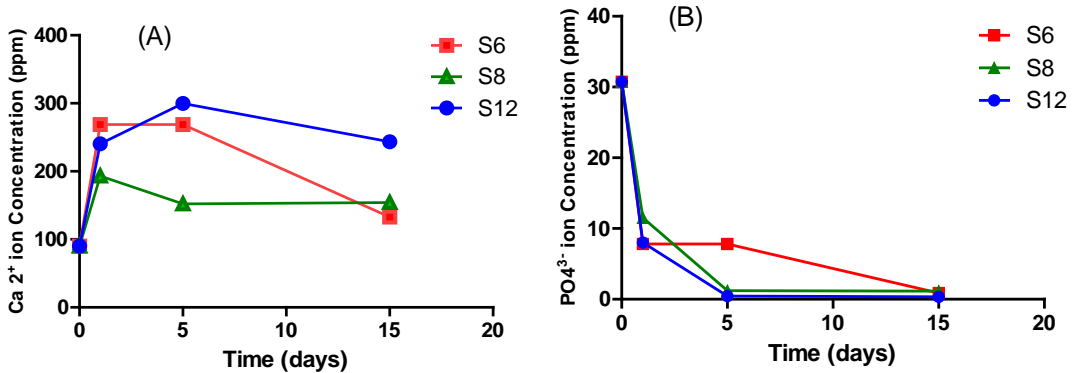
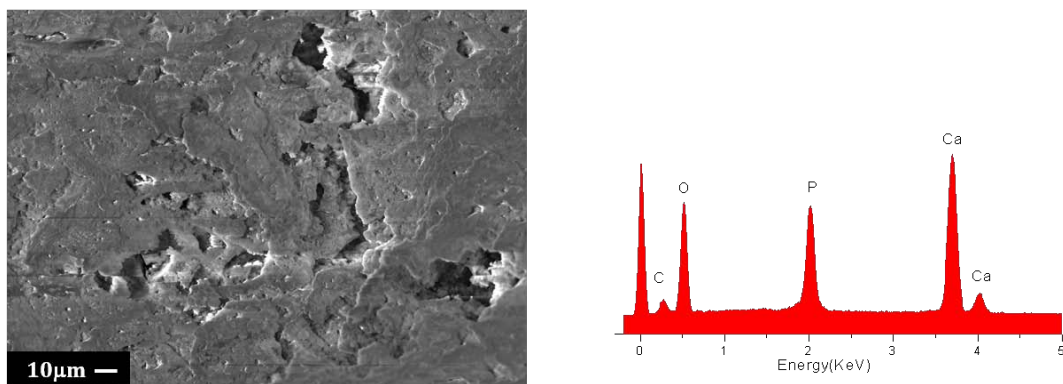


Fig. 4.6. (A)  $\text{Ca}^{2+}$  and (B)  $\text{PO}_4^{3-}$  concentrations in SBF during 15 days of immersion in SBF

In agreement with the view of Kokubo et al, the bioactivity of HAp containing materials can be accomplished by: (i) release of  $\text{Ca}^{2+}$  and  $\text{PO}_4^{3-}$  ions, and (ii) after saturation of the solution with both ions it will finally deposit apatite upon the surface of the samples "re-precipitation" [161].

This can be further explained as follows: The surface of the samples has negative charges due to the presence of the  $\text{OH}^-$  and  $\text{PO}_4^{3-}$  ions. Upon immersion in SBF, the sample starts to release the  $\text{Ca}^{2+}$  to the solution and results in an increase of the concentration of Ca ions in the solution. The released  $\text{Ca}^{2+}$  then attracted with the negative charges present upon the surface of the sample and forms Ca rich amorphous calcium phosphate (ACP). As a result of that mentioned, the surface becomes positively charged attracting the negative  $\text{PO}_4^{3-}$  and forming Ca-poor amorphous layer. The apatite is the more stable form of calcium phosphate members; for that the formed layer is a metastable which has to be crystallized through consumption of Ca and P ions from the solution results in concentration reduction of both ions in the SBF [162]. Another reason for the precipitation of these ions is the concentration gradients which promotes the precipitation of ions from the solution towards the substrate surface.

The surface morphology and EDX analysis of the 600°C thermally treated sample S6 before immersion in SBF are shown in Figure 4.7. The presence of pores upon the surface is attributed to the evaporation of ethanol and water during the heat treatment step. These pores could be useful as it can act as nucleating sites for the apatite precipitations. [163,164].



**Fig.4.7.** SEM micrographs and EDX spectra of the surface of the S6 sample before immersion in SBF.

The functional activity of cells in contact with the biomaterials is determined by the characteristics of the surface. For that such pores are valuable as they results in

“mechanical interlocking” which leads to mechanical bonding between the implant and the bone <sup>[164]</sup>.

After 15 days of immersion in SBF, the surface of the tablet S6 is completely covered with apatite precipitations (Figure 4.8). The corresponding EDX spectra show that the main composition of formed surface layer was calcium and phosphorus (Figure 4.8B). This Figure 4.8B shows the EDX spectrum obtained from the analysis of the sample S6 thermally treated at 600°C, after 15 days of immersion in SBF at 37.5°C

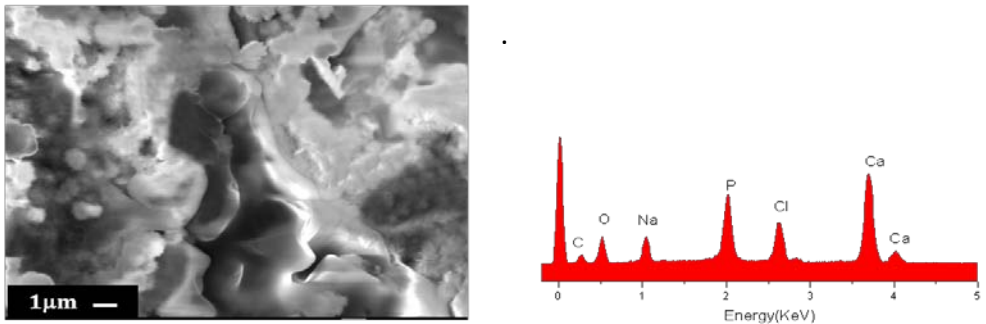


**Fig. 4.8.** SEM micrographs and EDX spectra of the surface of the S6 sample after immersion in SBF.

Even, being EDX a semi-quantitative analysis, these molar ratios indicates that the precipitates formed after SBF exposures should be apatite-like. The peaks corresponding to sodium and chloride are due to the presence of those elements in the SBF. The human bone also includes these elements, but is mainly made of apatite phase.

The surface morphology of the 800°C thermally treated sample S8 tablet after immersion in SBF for 15 days is shown in Figure 4.9A. The surface is covered with less precipitation of apatite-like “non-well developed apatite”. This is because the S8 sample exhibit lower dissolution than that of sample S6. Upon thermal treatment at 800°C the sample S8 becomes denser. The densification results in a lower dissolution of ions as it implies a decrease of the specific surface area exposed to the SBF solution. Despite the elemental analysis obtained by EDX analysis, the peaks corresponding to the main components of apatite (Ca, P and O) were identified (Figure 4.9B), with a Ca/P ratio of 1.55 ascribed to amorphous non-well developed apatite <sup>[165]</sup>. The spectrum also

exhibited peaks corresponding to Na, Mg and Cl, which are due to the presence of those elements in the SBF.

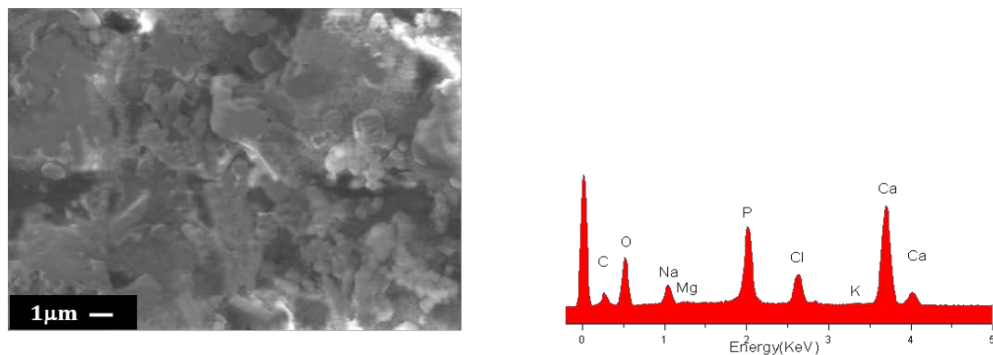


**Fig.4.9.** SEM micrographs and EDX spectra of the surface of the S8 sample after immersion in SBF

The surface morphology of the sample S12, thermally treated at 1200°C, after 15 days of immersion in SBF is shown in Figure 4.10. The surface exhibits precipitation upon its surface. The EDX analysis indicates that these precipitates have a Ca/P molar ratio that oscillates between 1.72 and 2.4 which indicates the precipitation of apatite-like.

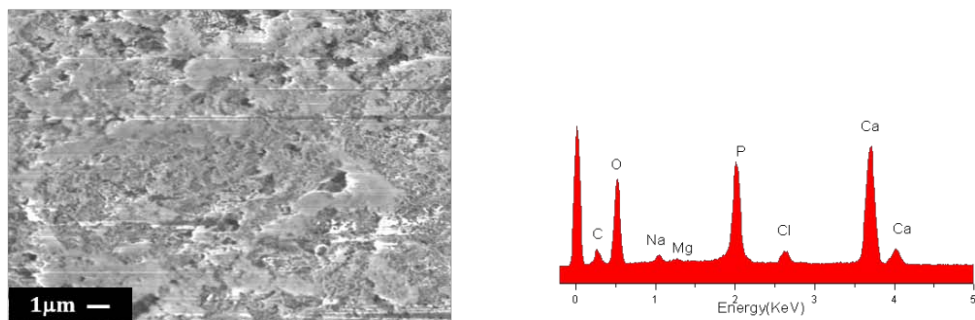


**Fig.4.10** SEM micrographs and EDX spectra of the surface of the S12 sample after immersion in SBF

The FTIR method is very sensitive to the vibration modes which are characteristic for molecular constituent groups permitting the identification of apatite precipitations. In-vitro tests were performed for all the obtained samples and the deposition of apatite-

like was followed by FTIR. Figure 4.11 shows the FTIR spectra of the prepared samples after 15 days of immersion in SBF.

The main functional groups in the spectra of the as prepared sample S1 exhibits characteristic of amorphous or poorly crystalline apatite precipitates (Figure 4.11A). The broad single band observed around  $1087\text{ cm}^{-1}$  is assigned to the vibration modes  $\nu_3$  corresponding to the P–O bonds in  $\text{PO}_4^{3-}$ . A small band is observed around  $869\text{ cm}^{-1}$  corresponds to the P–OH bond of pyrophosphate  $\text{HPO}_4^{2-}$  group

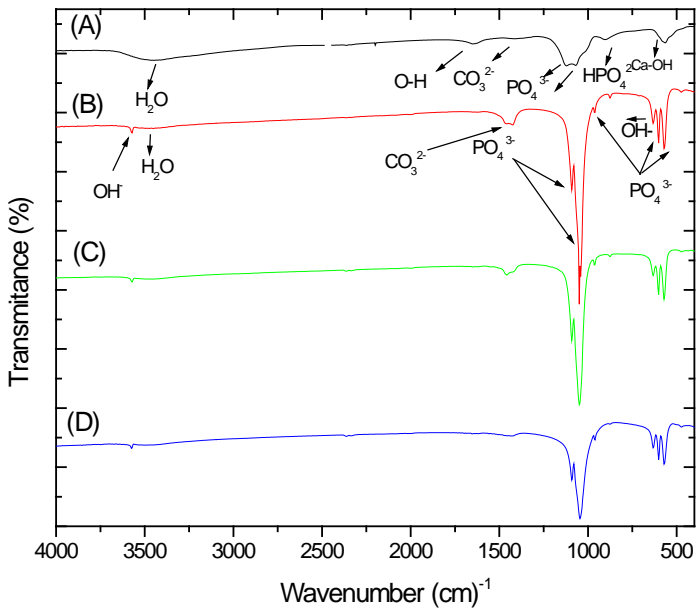


**Fig. 4.11** FTIR spectra of the dried gel S1 **(A)**, and the S6, S8 and S12 powders, thermally treated at 600 **(B)**, 800 **(C)**, and 1200°C **(D)**, after 15 days of immersion in SBF

A small shoulder observed around  $960\text{ cm}^{-1}$  corresponds to the  $\nu_1$  vibration mode of  $\text{PO}_4^{3-}$ . The band at  $1430\text{ cm}^{-1}$  is assigned to C–O stretching or the vibration mode  $\nu_3$  of  $\text{CO}_3^{2-}$ . The broadening nature of these characteristic bands is probably due to its amorphous nature, or to poorly crystallized precipitates of apatite. The broad single

bands observed at  $3436$  and  $1620\text{ cm}^{-1}$  are originate from O–H band stretching and bending of  $\text{H}_2\text{O}$  adsorbed molecular water, "water associated with HAp".

The main functional groups observed in the spectra of the thermally treated samples S6, S8 and S12 are  $\text{PO}_4^{3-}$ ,  $\text{CO}_3^{2-}$ ,  $\text{OH}^-$ , and  $\text{H}_2\text{O}$  exhibited characteristic features of crystallized precipitated stoichiometric HAp due to the precipitation of  $\text{Ca}^{2+}$  and  $\text{PO}_4^{3-}$  ions from SBF upon their surfaces.

The spectra of the sample S6 thermally treated at  $600^\circ\text{C}$  shows the typical bands of apatite precipitations (Figure 4.11B). The  $\text{PO}_4^{4-}$  bands were detected at  $470\text{ cm}^{-1}$  (vibration modes  $\nu_2$ ),  $570$  and  $601\text{ cm}^{-1}$  (vibration modes  $\nu_4$ );  $964\text{ cm}^{-1}$  (vibration modes  $\nu_1$ ),  $1049$  and  $1091\text{ cm}^{-1}$  (vibration modes  $\nu_3$ ). The  $\text{CO}_2^{3-}$  ion bands were visible at  $1434\text{ cm}^{-1}$  (vibration modes  $\nu_3$ ),  $1457\text{ cm}^{-1}$  (vibration modes  $\nu_4$  or  $\nu_3$ ) and  $875\text{ cm}^{-1}$ . The water associated with HAp is recognized through the broad spreading band at  $3432\text{ cm}^{-1}$ . The  $\text{OH}^-$  stretching vibration is observed at  $3569\text{ cm}^{-1}$ , and bending vibration ( $632\text{ cm}^{-1}$ ) is also apparent.

The spectra of the sample S8 thermally treated at  $800^\circ\text{C}$  (Figure 4.11) and the sample S12 thermally treated  $1200^\circ\text{C}$  (Figure 4.11D) thermally treated show the  $\text{PO}_4^{3-}$ ,  $\text{CO}_3^{2-}$ ,  $\text{OH}^-$  and  $\text{H}_2\text{O}$  bands. This indicates the precipitation of apatite upon the surface of the samples as confirmed with the ICP results. In comparison with the FTIR spectra before immersion, Figure 4.2, the observed bands after immersion, Figure 4.11, are sharper indicating the apatite precipitation on the surface of the samples after immersed in SBF for 15 days.

### **4.2.2. Evaluation of the surface bioactivity and the corrosion protection behaviour of the sol-gel derived HAp coatings**

Based on the previous part of study, we chose the thermal treatment conditions of  $600$  and  $800^\circ\text{C}/2\text{h}$  for thermal treatment of the HAp-coatings/Ti6Al4V alloy system to avoid the decomposition of the HAp which happen at  $1200^\circ\text{C}$  as confirmed by the DTA results.

The bioactivity of the HAp-coatings/Ti6Al4V thermally treated at  $600^\circ\text{C}/2\text{h}$  and  $800^\circ\text{C}/2\text{h}$  was evaluated by immersion of the coated HAp-Ti6Al4V discs in SBF for 15 days. The corrosion behaviour of the HAp-coatings/Ti6Al4V system in an electrochemical cell filled

with Kokubo's solution was evaluated by applying electrochemical impedance spectroscopy (EIS) measurements.

### - Immersion tests of HAp-coatings/Ti6Al4V alloy system in SBF

As it was mentioned in the above paragraphs, the bioactivity of artificial materials can be attributed to the formation of biologically active bone-like apatite layer. This layer can be formed upon the surface of the sample upon immersion in SBF solution <sup>[161]</sup>.

The SEM micrographs obtained for the surface of the HAp-coatings/Ti6Al4V before immersion in SBF are shown in Figures 4.12A and 4.12B. The surface of the sample thermally treated at 600°C/2h shows the presence of pores due to the evaporation of both, water and ethanol during thermal treatment (Figure 4.12A). While the surface of the sample thermally treated at 800°C/2h shows the presence of extensive cracks (Figure 4.12B) probably due to a thermal expansion coefficient mismatch between the coating and the Ti6Al4V substrates during cooling <sup>[166]</sup>.

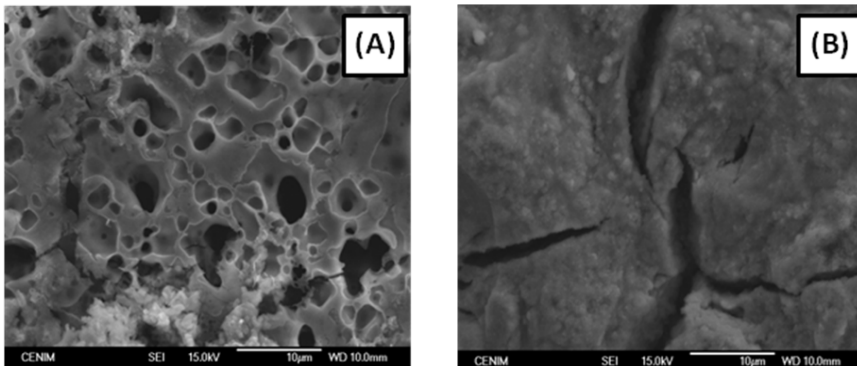


**Fig. 4.12** SEM micrographs obtained for the HAp-coatings/Ti6Al4V system thermally treated at (A) 600°C/2h, (B) 800°C/2h before immersion in SBF

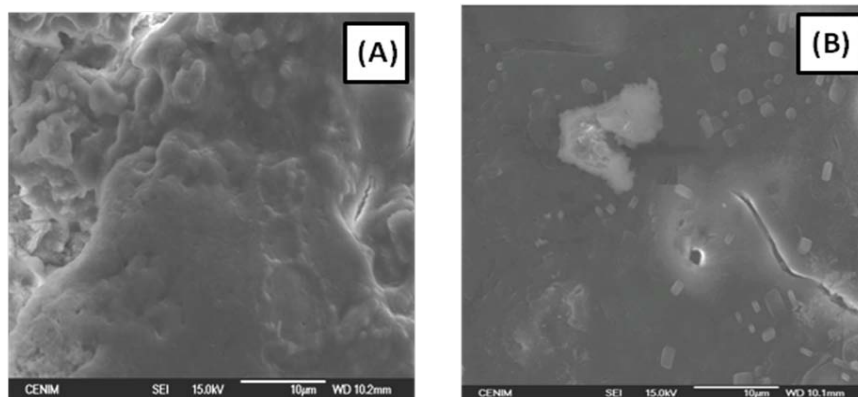


**Fig. 4.13.** SEM micrographs obtained for the HAp-coatings/Ti6Al4V system thermally treated at (A) 600°C/2h, (B) 800°C/2h after immersion in a SBF solution.

After 15 days of immersion in SBF the surface of both samples is covered with bone-like apatite layer which proved that both samples are bioactive. The surface of the sample thermally treated at 600°C/2h is completely covered with these precipitations from SBF (Figure 4.13A), while the surface of the sample thermally treated at 800°C/2h is not completely covered, as still some cracks are observed by SEM at the surface (Figure 4.13B). In this way the HAp coating is able to be a barrier against the aggressive SBF solution and to protect the Ti6Al4V alloy against corrosion.

### - **Interactions of SBF with the HAp-coating/Ti6Al4V alloy system. Corrosion protection behaviour**

Electrochemical impedance spectroscopy (EIS) was used for evaluating the barrier properties and the corrosion behaviour of the HAp-coatings/Ti6Al4V systems. Figures 4.14 and 4.15 show the evolution of the impedance plots with the immersion time in SBF for the HAp-coatings/Ti6Al4V systems thermally treated at 600°C/2h and 800°C/2h, respectively.

Figures 4.14A and 4.15A show the impedance data represented as Nyquist plots, where the imaginary part ( $Z''$ ) of the impedance vector  $Z(f)$  is represented in the complex plane against the real part ( $Z'$ ) of this vector, with the frequency ( $f$ ) as implicit variable <sup>[167]</sup>.

Figures 4.14B and 4.15B show the same impedance data in Bode representation. In the Bode diagrams the logarithm of the magnitude of the impedance vector ( $\log [|Z|]$ ) and the phase angle ( $\theta$ ) are plotted against the logarithm of frequency ( $\log [f]$ ) of the applied sinusoidal electric voltage signals <sup>[167]</sup>.

Electrochemical techniques are well suited to monitor changes over time of the interface between metal surfaces and aqueous solutions <sup>[167-174]</sup>. From EIS, information on the interface capacitance (thus oxide films, adsorption processes) and the interface resistance (charge transfer processes, dissolution of ions from metal alloys as for instance metallic implant materials) can be obtained <sup>[175]</sup>.

In addition, in studies of coated metals, information about the protector character of the coating can be also obtained <sup>[176]</sup>. In this case, the coating capacitance provides information on the thickness, porosity and the degree of surface coverage <sup>[177]</sup>. The coating capacitance value usually changes over the time in contact with aqueous solutions. The change depends on the barrier properties afforded by the coating against the ingress of water <sup>[177]</sup>. Finally, the coating resistance provides information about the ionic resistance of coating systems immersed in aqueous solutions. The changes of the ionic resistance with the immersion time are due to the penetration of the electrolyte through the intrinsic porous of the coating <sup>[177]</sup>. It is expected that all these concepts will be able to be extrapolated to the studies related with the corrosion behavior of coated metallic implants in contact with the simulated body fluids.

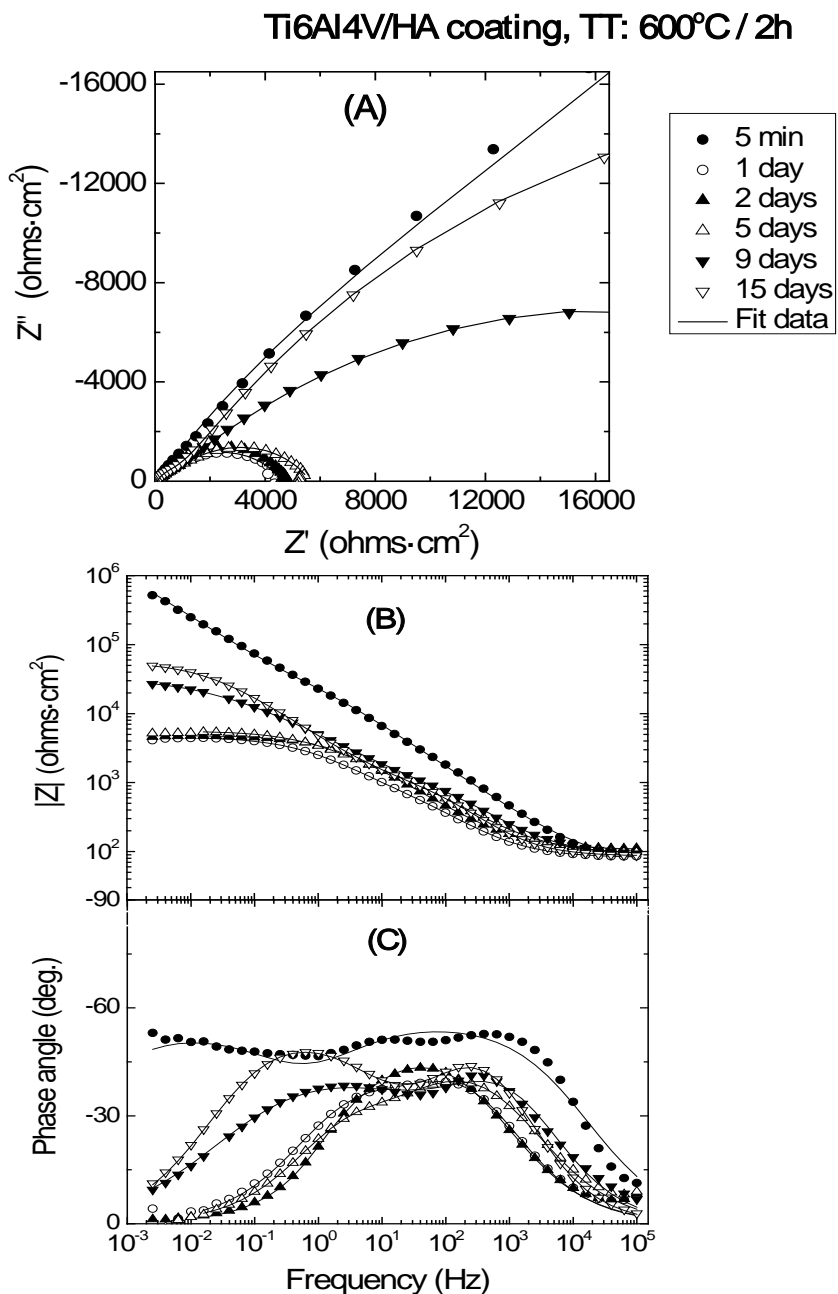


**Fig. 4.14** Evolution of the electrochemical impedance spectra with immersion time in SBF for samples S6 (HAP-coatings/Ti6Al4V alloy system thermally treated at 600°C/2h).

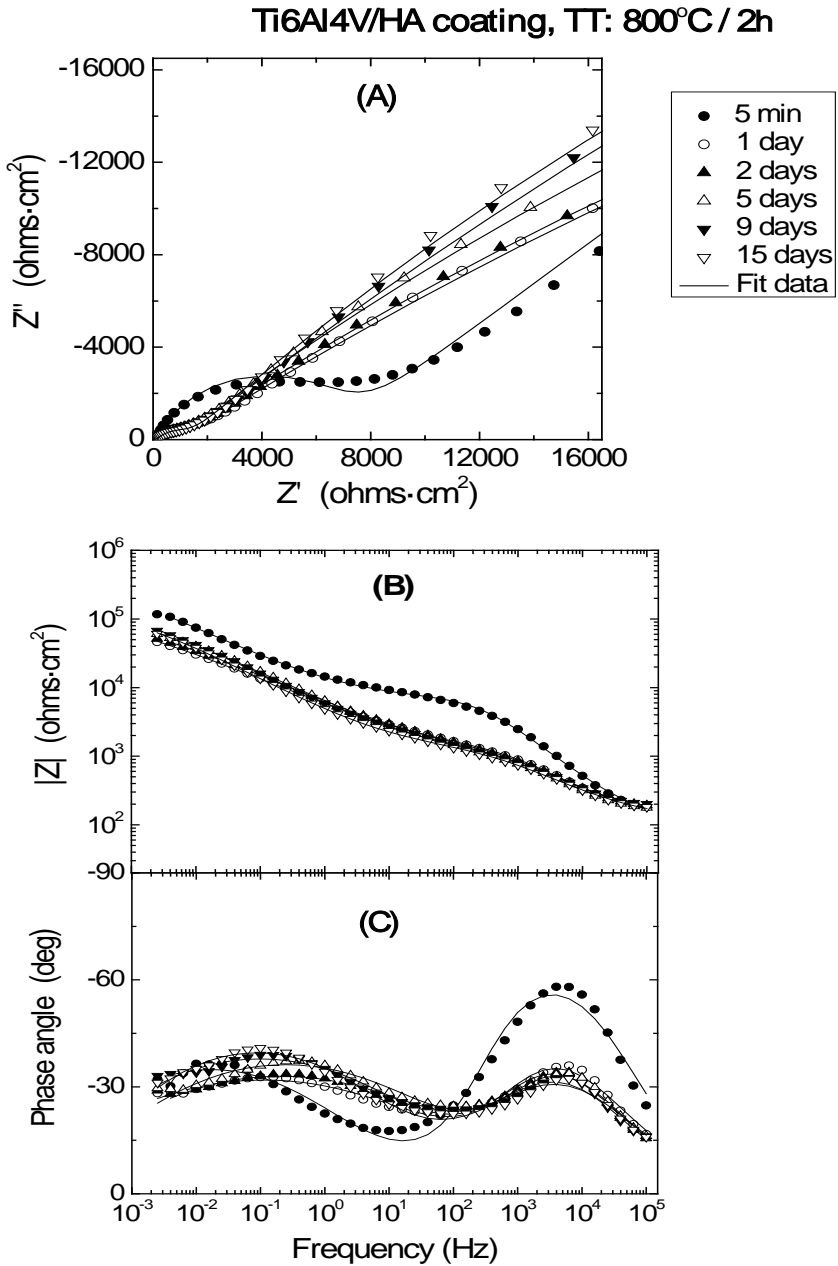


**Fig. 4.15** Evolution of the electrochemical impedance spectra with immersion time in SBF for sample: S8 (HAp-coatings/Ti6Al4V alloy system thermally treated at 800 °C, 2h)

- **Selection of the electrical equivalent circuit which describes the studied systems**

An interface undergoing an electrochemical reaction is typically analogous to an electronic circuit consisting of a specific combination of resistors and capacitors. Thus the electrochemical system can be described in terms of its equivalent circuit. The experimental impedance data can be modeled using complex non-linear least-square (CNLS) fit analysis and suitable electrical equivalent circuits (EECs).

Two equivalent circuits have been used for this study (Figure 4.16).

- The EEC showed in Figure 4.16A has been successfully used in a lot of researches related with the corrosion protection behavior of organic coatings on metal surfaces [\[177-180\]](#).
- The EEC showed in Figure 4.16B has been also used several times with providing also successful results [\[175-181\]](#).

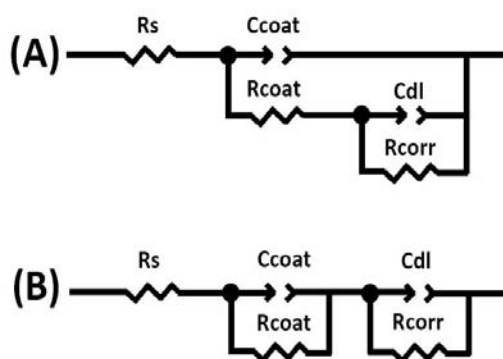


**Fig. 4.16** Electrical equivalent circuits used to analyze the experimental electrochemical impedance data

Following the notation of the ZView software, in both electrical equivalent circuits  $R_s$  represents the solution resistance of the bulk electrolyte.  $C_{coat}$  is the coating capacitance. Because of inhomogeneities in the coating,  $C_{coat}$  has to be implemented as a Constant Phase Element ( $CPE_{coat}$ ).  $R_{coat}$  is the coating pore resistance.  $R_{corr}$  represents to the corrosion resistance of the metal substrate and  $C_{dl}$  is the double layer

capacitance at the metal/electrolyte interface, both at the base of pores and perforations of the coating. Due to inhomogeneities in the coating and metal surface, this capacitance has also to be implemented as a CPEd. Mathematically, a CPE's impedance is given by the following equation <sup>[182]</sup>:

$$Z(\text{CPE}) = 1 / [T(j\omega)^{-P}]$$

Where

$j = \sqrt{-1}$ ,  $\omega$  is the angular frequency ( $\omega = 2\pi f$ ), and  $f$  is the frequency in Hz.

The CPE is defined by two parameters, CPE-T and CPE-P. CPE-T is a fit parameter and the exponential factor CPE-P is related with a non-uniform current distribution due to the surface roughness or other distributed properties, and varies between 0 and 1. The CPE reduces to a resistor for CPE-P = 0, to an infinite Warburg diffusion for CPE-P = 0.5 and to an ideal capacitor for CPE-P = 1.

Good fit results have been obtained by applying the electrical equivalent circuit showed in Figure 4.16A, to fit and simulate the experimental impedance plots obtained for the two systems selected for the present work, samples S6 (HAp/Ti6Al4V system) and S8 (HAp/Ti6Al4V system) (Figures 4.14 and 4.15). However, simultaneous agreement between calculated and measured impedance spectra does not necessarily mean that the circuit model is a unique representation of the spectra. One cannot assume the uniqueness of a circuit model merely on the basis of a good fit observed experimental spectrum <sup>[181]</sup>. Table 4.5 shows an example where the two equivalent circuits showed in Figure 4.16 provide very similar fit results when they are applied to the samples S8 (HAp/Ti6Al4V system), after 5 days of immersion in SBF. Table 4.5 also shows the chi-square ( $\chi^2$ ) values obtained with both equivalent circuits. The  $\chi^2$  parameter gives an estimation of the quality of the fitting results to the experimental impedance spectra. In all the tested samples the quality of the fitting results were also very good, independently of the two electrical equivalent circuits used for obtaining the fits, because the  $\chi^2$  obtained values were lower than  $10^{-3}$ . Nevertheless the equivalent circuit showed in Figure 4.16A gives to ambiguous values of the CPEd-n parameter when it is applied to the system thermally treated at 600°C/2h. Thus for 1 and 2 days of immersion

in solution the calculated values for CPE-P are equal to 9.268 and 1.933 respectively (Table 4.6). These results are very far from the range of values with a physical meaning ( $0.5 \leq \text{CPE-P} \leq 1$ ). In the case of the systems thermally treated at  $600^\circ\text{C}/2\text{h}$ , for 1 and 2 days of immersion in Kokubo solution, the relative error obtained for CPEdl-n values when applied to the equivalent circuit is also very bad (Table 4.6). On the other hand the equivalent circuit showed in Figure 4.16B provides very successful fitting results for all the experimental impedance plots obtained in this study. Thus this equivalent circuit was finally chosen for analyzing all the impedance data.

Table 4.5 Values obtained for the elements of the proposed equivalent circuits in Figure 4.15, applying CNLS fits of the ZView software on experimental impedance plots of the HAp-coatings/Ti6Al4V system. Sample S6 ( $600^\circ\text{C}/2\text{h}$ ). Immersion time in SBF: 5 days

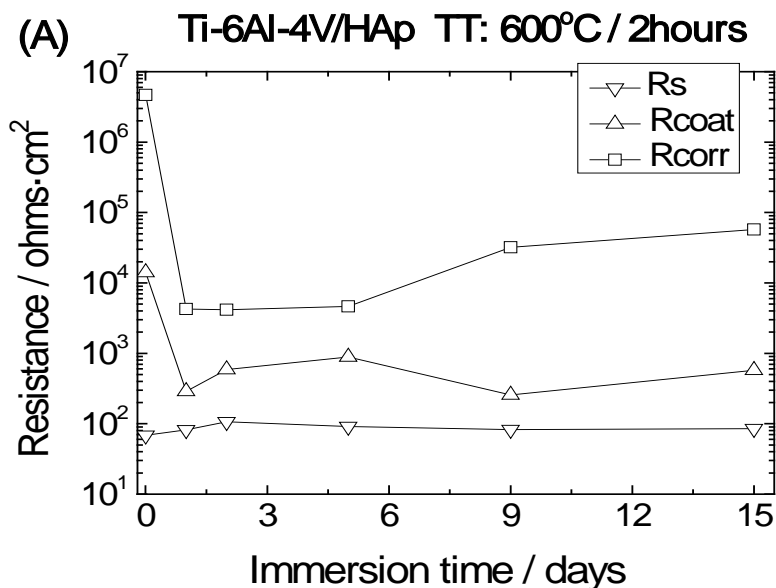
Element	EQUIVALENT CIRCUIT A		EQUIVALENT CIRCUIT B	
	Value	Error %	Value	Error %
Rs	138.8	2.47	126.6	2.33
Rcoat	1014	4.87	747.3	5.02
Ccoat-T	$2.32 \cdot 10^{-6}$	14.93	$3.36 \cdot 10^{-6}$	15.8
Ccoat-P	0.67	2.17	0.68	2.56
Cdl-T	$7.05 \cdot 10^{-5}$	0.85	$7.16 \cdot 10^{-5}$	0.79
Cdl-P	0.46	0.86	0.46	0.99
Rcorr	$1.47 \cdot 10^5$	4.77	$1.51 \cdot 10^5$	5.27
Chi-Squared ( $\chi^2$ )	0.0009		0.0011	

### - Interpretation of the results obtained

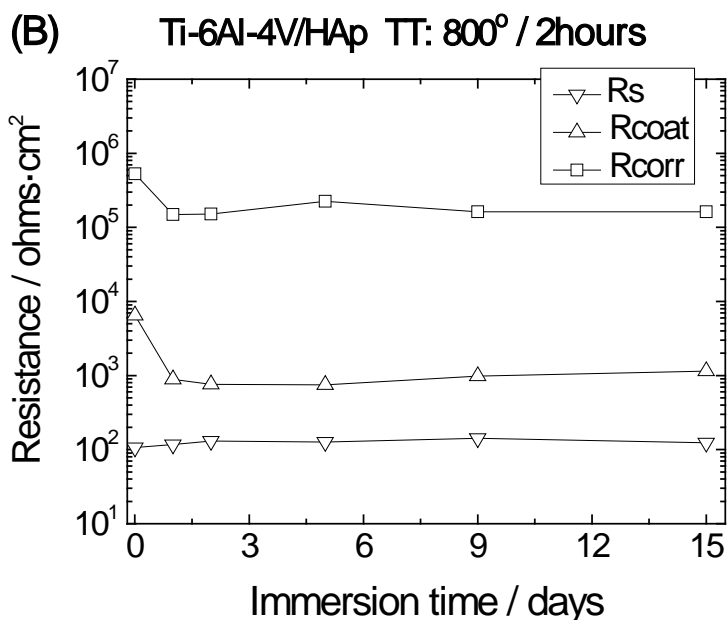
Besides of the evolution of the impedance plots of HAp-coatings/Ti6Al4V systems thermally treated at 600°C/2h and 800°C/2h as a function of the immersion times of samples in Kokubo solution, Figures 4.14 and 4.15 show the obtained plots by applying the equivalent circuit showed in Figure 4.16B. It can observe that these fit results are very satisfactory. On other hand obtained, Figures 4.14A and 4.15A show that for short immersion time (5 min) the Nyquist plots draw very open arcs. At the beginning of the immersion test, both samples show also high impedance modulus for all the tested domain of frequencies, such it can be observed in the Bode representation of the logarithm of the impedance magnitude against the logarithm of the frequency (Figures 4.14B and 4.15B). For this short immersion time both Figures show that for in the high frequencies range, the phase angle presents the highest values. High values of the phase angle at high frequencies are typically associated to barrier effects of coatings which are due to their dielectric properties.

Figure 4.17 and 4.18 show the values of the resistances ( $R_s$ ,  $R_{coat}$  and  $R_{corr}$ ) of the samples S6 (600°C/2h) and S8 (800°C/2h) for different immersion time in the SBF solution. These resistance values have been obtained from the experimental impedance plots by using CNLS fits of the ZView software and the equivalent circuit showed in Figure 4.16B. In both cases the  $R_s$  values are similar and remain without significant changes along the immersion time. For the HAp-coatings/Ti6Al4V systems obtained at 600°C/2h, the  $R_{coat}$  values shown a slight decrease due to the electrolyte inwards within the first day of immersion. After the first day the  $R_{coat}$  values showed small fluctuations, increasing slightly and then decreasing again after six days of immersion. These small fluctuations are associated with the changes observed in the  $R_{corr}$  values. In this case the  $R_{corr}$  values are sensitive to the changes occurring at the Ti6Al4V alloy/SBF interface at the base of the porous. After the first hours of immersion, the  $R_{corr}$  value decreases considerably which indicates that the electrolyte reaches the Ti6Al4V surface, in several microareas, and the activity in these microareas is a dominant effect. In these microareas, according to the passivity theory, in aqueous solution they have

simultaneously both active and passive surfaces and undergo a continuous process of partial dissolution and repassivation. Depending of the extent of surface in which the Ti6Al4V surface is in direct contact with the SBF, this process will be more or less important and will dominate the impedance response. For the sample thermally treated at 600°C/2h, this continuous process seems to be dominant along the next 5 days of immersion giving a result a constant value of 4.104 ohms.cm<sup>2</sup> within this period of time. After that, it is interesting observe that the values of the R<sub>corr</sub> parameter increase quickly and reach values closer to those observed at the beginning of the immersion tests (Figures 4.14A). This behaviour can be due to the blocking of the pores by the formation of precipitates from the solution which prevent further penetrations of the SBF impeding the growth of active microareas at the base of the HAp-coating pores.



**Fig 4.17.** Evolution of the R<sub>s</sub>, R<sub>coat</sub> and R<sub>corr</sub> values with immersion time in SBF of HAp-coatings/Ti6Al4V systems. Thermal Treatments: 600°C/2h.



**Fig. 4.18.** Evolution of the  $R_s$ ,  $R_{coat}$  and  $R_{corr}$  values with immersion time in SBF of HAp-coatings/Ti6Al4V systems. Thermal Treatments: 800°C/2h.

For the HAp-coatings/Ti6Al4V systems obtained at 800°C/2h, the  $R_{coat}$  values shown a slight decrease due to the electrolyte inwards within the first day of immersion and then a constant value of  $R_{coat}$  is attained (Figure 4.18), which shows a good stability of the coating along the immersion time. This stability is also reflected in the  $R_{corr}$  values obtained which follows the same trend. The  $R_{corr}$  slightly decreases upon exposure to the SBF and then remain almost constant along the immersion time (Figure 4.18). In this case, the slight decrease of both  $R_{coat}$  and  $R_{corr}$  values followed by a constant value within the immersion time (Figure 4.18), prove good stability and lower porosity of this coating when compared to the one obtained at 600°C for 2h. The high increase of the  $R_{corr}$  values observed in the samples coated at 600°C/2h is not here evidenced. Nevertheless the evolution of the Nyquist plots with the immersion time shows a slow decrease of the diameter of the arcs and the  $R_{corr}$  values of these samples, evidencing a best behaviour against corrosion during all the immersion tests in an aggressive solution such as the SBF. The morphology of the coatings plays an important role in the different behavior of these coatings. Since the coating obtained at 600°C/2h initially shows an intrinsic porosity with porous in the range of 1-2 micrometers diameter (Figure 4.12A)

and the coating obtained at 800°C shows a continuous layer with some cracks with a medium wide of half a micrometer and length of 8-10 micrometers (Figure 4.12B). In both cases, the inward of the SBF is allowed and thus the formation of HAp from the solution, which was one of the aims of this study. But the kinetic of this process is different in both cases, as reflected in the impedance results obtained. The porosity of the coating obtained at 600°C/2h favours a rapid ingress of the electrolyte and allows that the formation of the HAp into these pores occurs in a big extent than in the coating obtained at 800°C/2h. But on the other hand, due to this porosity the coating obtained at 600°C/2h shows a lesser barrier effect than the one provided for the coating obtained at 800°C/2h.

Table 4.6 shows the values obtained for the exponent P of the CPEdl of the equivalent circuits A and B applying the CNLS fits of the ZView software to the impedance experimental plots of HAp-Coatings/Ti6Al4V systems. The n values are directly related to the corrosion mechanisms. CPEdl would represent to the double layer capacitance of the metal/electrolyte interface at the base of pores and perforations of the coating. For the HAp-Coatings/Ti6Al4V samples thermally treated at 800°C/2h the P values are situated into the 0.41-052 range (Table 4.6).

These values are closer to those typically ascribed to diffusion mechanisms ( $P=0.5$ ), than to P values attributed to the electrochemical double layer capacitance ( $P=1$ ). From all the exposed above, it seems that the diffusion mechanisms through the pores and microcracks of the coating dominate on the activation processes and corrosion at the metal surface, preventing in this way the ion release from the metallic substrate to the SBF.3

**Table 4.6.** CPEDl-P values and % of relative error obtained with the equivalent circuits A and B applying CNLS fits from the ZView software on experimental impedance plots of samples S6 (600°C/2h) and S8 (800°C/2h), for variable immersion time in SBF

Immersion time in SBF	CPEDl-P values							
	Sample S6 (TT: 600°C / 2 hours)				(Sample S8) TT: 800°C / 2 hours			
	Equivalent Circuit A		Equivalent Circuit B		Equivalent Circuit A		Equivalent Circuit B	
	Value	Error %	Value	Error %	Value	Error %	Value	Error %
5 min	0.525	0.96	0.613	5.61	0.455	1.97	0.476	3.11
1 day	9.268	9.35	0.628	1.18	0.415	0.80	0.410	1.22
2 days	1.933	8.31-103	0.624	21.95	0.422	0.77	0.423	1.02
5 days	0.651	5.99	0.644	3.43	0.464	0.86	0.463	0.99
9 days	0.491	2.96	0.513	1.47	0.477	0.92	0.478	1.05
15 days	0.630	1.20	0.636	0.98	0.511	1.03	0.516	1.10

### Conclusions

Hydroxyapatite nano-crystalline coatings on Ti6Al4V alloy have been obtained by sol-gel route. The crystallite size and degree of crystallinity of the HAp sol-gel derived coatings strongly depends on the thermal treatment applied. Based on this knowledge, the prepared HAp sol-gel coating/Ti6Al4V systems were thermally treated during 2h at 600°C and 800°C, respectively. The obtained results showed that the prepared coatings are nanocrystalline HAp with little deviations from that present in the human bone. All the prepared HAp coating/Ti6Al4V systems showed good bioactivity upon immersion in SBF for fifteen days. In terms of corrosion protection, the HAp coating/Ti6Al4V systems thermally treated in the range 600-800°C exhibited good corrosion protection.



## ***Chapter (5)***

*Organic-inorganic hybrid sol-gel – Optimization of the  
synthesis processes of the hybrid matrix*



### Organic-inorganic hybrid sol-gel – Optimization of the synthesis processes of the hybrid matrix

#### - Introduction

The interest in developing (OI) organic-inorganic hybrid coatings is due to the unique properties derived from combining inorganic and organic components into a single system <sup>[183-189]</sup>. The organic-inorganic hybrids combine the properties of organic polymers (toughness, elasticity) with those of inorganic solids (hardness, chemical resistance). This type of material has many applications in diverse fields as optics, electronics, ionics, mechanics, energy, environment and biology <sup>[190,191]</sup>, separation, catalysis and sensing <sup>[192-196]</sup>, electrochemistry <sup>[197-202]</sup>, functional smart materials and corrosion protection coatings <sup>[124,203]</sup>, or biomaterials and biomedical applications <sup>[11, 205,206]</sup>. The sol-gel method has attracted intense and growing interest of the researchers because of its advantages over the other traditional preparation methods. This processing technique enables obtaining of high reactivity, better purity, improved control of the product structure and provides an easy, cost-effective, and excellent way to prepare the organic-inorganic hybrids <sup>[207,208]</sup>.

Organic–inorganic hybrid can be easily prepared at room temperature by hydrolysis and condensation of metal alkoxides of the type  $M(OR)_n$ , where M can be Si, Ti, Al, Sn, Zr, etc. This method comprises a chemical synthesis of materials having an oxide backbone and an additional organic component as a network modifier. Starting from hydrolysable molecular compounds, such as alkoxy compounds of silicon, for instance tetramethylorthosilicate (TMOS), the hydrolysis and condensation is induced by addition of water results in formation of an inorganic silica network.

The organic silane precursor, for instance  $\gamma$ -methacryloxypropyltrimethoxysilane (MAPTMS), contains organic groups which act as network modifiers. Due to the presence of these modifiers, the final silicon network gains different properties (e.g., hydrophobicity, flexibility or bioactivity) depending on the nature of the organic group used <sup>[209]</sup>. Figure 5.1 shows the polymerization reaction of the MAPTMS and TMOS mixture.

## POLYMERIZATION:

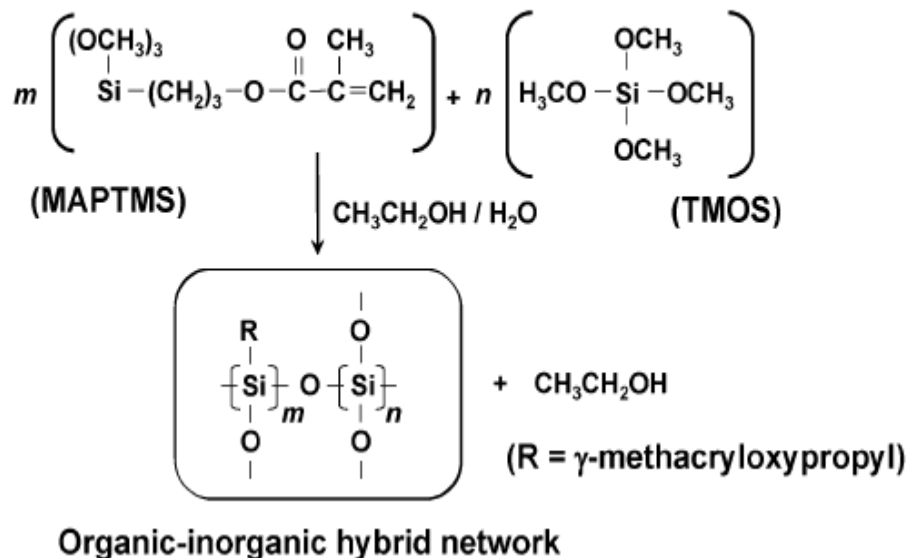


**Fig. 5.1** Schematic representation of the polymerization reaction of the MAPTMS and TMOS mixture producing a 3D organic-inorganic hybrid network.

As is known, hydrolysis and condensation of silane solution is a time-dependent process. A “workable” silane solution should contain a sufficient number of Si-OH groups for the subsequent condensations during silane surface treatment. Without sufficient hydrolysis, an oily silane film is obtained. Such film cannot provide corrosion protection due to the lack of a cross-linked structure and a good adhesion to substrates.

Figure 5.2 shows the structural differences between partially (Figure 5.2A), and fully condensed (Figure 5.2B) siloxane films. This difference could reflect the efficiency of the full condensed network in terms of corrosion protection. Thus the full condensed films are more effective in protecting the metal surfaces from being corroded.

## Organic-inorganic hybrid sol-gel– Optimization of the synthesis processes of the hybrid matrix

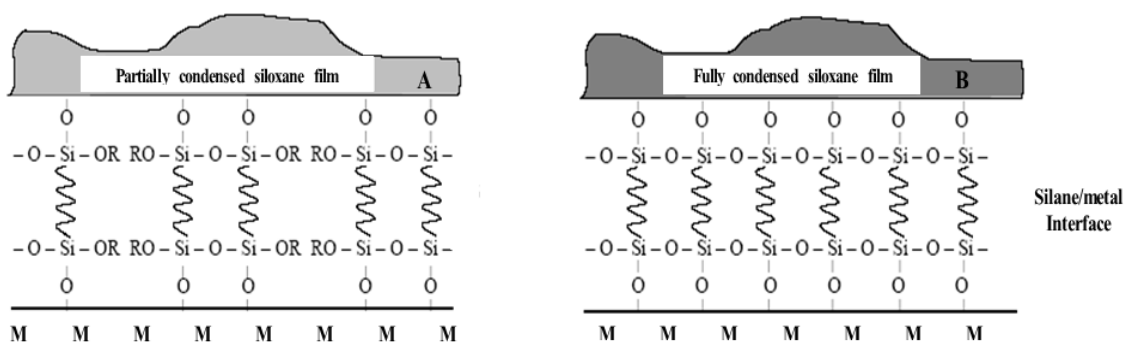


Fig. 5.2 Two-dimension schematic representation of the structure of a silane sol-gel film bonded onto a metal (M) substrate. (A) Partially condensed and (B) fully condensed.

### - Aim

Is to optimize the organic–inorganic hybrid preparation through studying the structural changes which take place during the hydrolysis and condensation processes of an MAPTMS/TMOS solution after the addition of water and ethanol. FTIR, liquid-state  $^{29}\text{Si}$  and  $^{13}\text{C}$  nuclear magnetic resonance (NMR) have been applied for this purpose.

Schematic representation of  $\gamma$ -methacryloxypropyltrimethoxysilane (MAPTMS) and tetramethoxysilane (TMOS) formula are shown in Figure 5.3. The MAPTMS (depicted in Figure 5.3A), is an organo-functional silane composed of a long backbone of carbon atoms with a silicon atom substituted with three  $-\text{O}-\text{CH}_3$  groups as head. The main organic fraction of the MAPTMS/TMOS hybrid coating is carried into the film by this molecule.

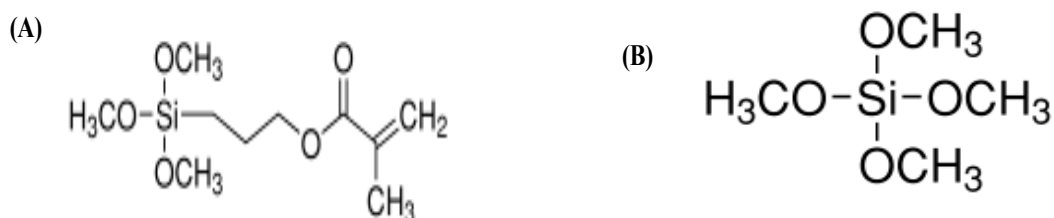


Fig. 5.3 Structural formula of (A) MAPTMS and (B) TMOS.

MAPTMS molecules contain one non-hydrolysable substituent linked to the silicon atom. The silicon/carbon bond is not hydrolysable and, therefore, it is stable in water at room temperature<sup>[128]</sup>.

The silicon-oxygen bonds can hydrolyse in presence of water, leading to the formation of Si-OH bonds. The hydroxyl groups are responsible for the chemical bonding to metal substrate, by means of condensation reaction with the hydroxides present on metal substrates. The MAPTMS molecules contain both alkoxide groups, which hydrolyse reacting with water, generate the sol-gel network and bond to the metal substrate, and organic functionalities which are embedded in the silane film and can polymerize and chemically interact with an organic coating.

TMOS (depicted in Figure 5.3B) is a simple molecule composed of a silicon atom bonded to four  $-O-CH_3$  groups. As a function of the hydrolysis condition, all the Si-(O-CH<sub>3</sub>) bonds can potentially hydrolyze and form Si-OH bonds. For this reason, TMOS is a sort of network former, owing to it promotes the formation of an inorganic network and inorganic domain of silica.

The inorganic phase is likely to be responsible of the improved barrier properties of the silane sol-gel films. Hydroxyl groups can interact with the metal substrate, leading to the formation of covalent bonds during film curing.

### **5.1 Fourier transform infrared spectroscopy (FTIR)**

The reaction between silanes species in liquid media occurs, in general, by sol-gel process in which hydrolysis and condensation of the silane groups take place. In particular, by mixing the two precursors (MAPTMS/TMOS) with H<sub>2</sub>O and ethanol at ambient temperature, the hydrolysis taking place in the solution must be considered. In this sense, the Fourier transform infrared spectroscopy (FTIR), is a rapid, nondestructive, and sensitive analytical method for identifying functional groups presented.

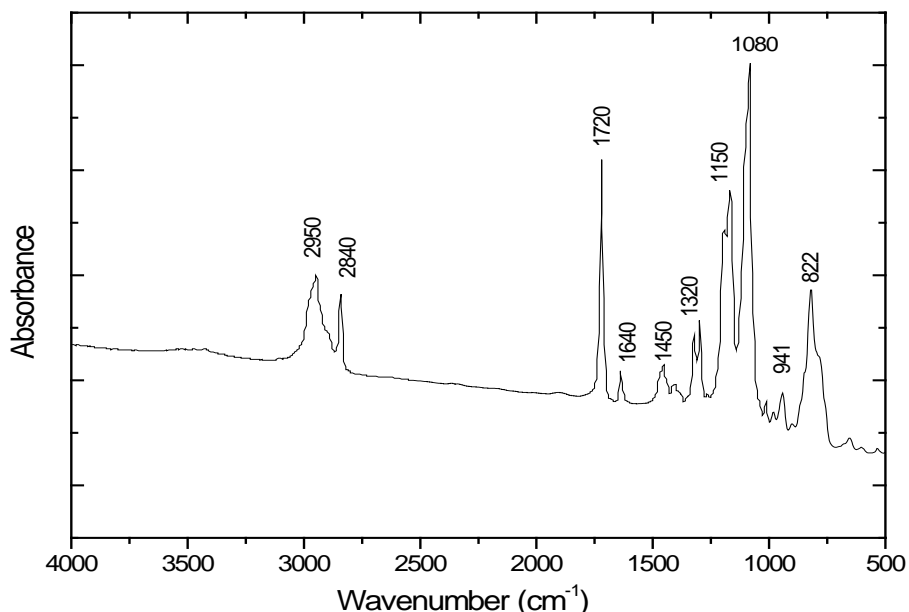


**Fig. 5.4.** FTIR spectrum of the MAPTMS/TMOS mixture in Et(OH)–H<sub>2</sub>O solvent system upon mixing.

The FTIR spectrum of the MAPTMS/TMOS upon mixing with Et (OH)/H<sub>2</sub>O solvent system can be seen in Figure 5.4. The corresponding band assignments are present in Table 5.1. The absorption bands around 2.950 and 2.840 cm<sup>-1</sup> are attributed to stretching vibrations of C–H bonds in alkyl and methoxy groups, respectively [210]. The band close to 1.720 cm<sup>-1</sup> is associated to the stretching vibrations of C=O carbonyl groups of MAPTMS, while that one at 1.640 cm<sup>-1</sup> is attributed to C=C groups of the methacrylate groups from the MAPTMS precursor [210-212]. The bands at 1.450 and 1.150 cm<sup>-1</sup> are attributed to deformation vibrations of C–H in CH<sub>2</sub> and CH<sub>3</sub> bonds [213]. The asymmetric and symmetric stretching vibrations of C–O of C–O–C bonds are attributed to bands at 1.320 and 1.300 cm<sup>-1</sup>, respectively [214]. Finally, the bands at 941 and 822 cm<sup>-1</sup> are assigned to the C=C vibrations of the C=C–C=O group, while that assigned to C–C–O skeleton vibration for pure ethanol appear at 1.090 cm<sup>-1</sup> [214]. All those bands (except the one at 2.840 cm<sup>-1</sup>) are related to the non hydrolysable

part of the MAPTMS/TMOS mixture and should appear in the FTIR spectra carried out after the hydrolysis process. The band at  $1.080\text{ cm}^{-1}$  is attributed to stretching vibrations of Si–O–C bonds. Other authors have also made the same attribution in different silanes [215,216].

This band is the one that is expected to be broken during the hydrolysis process. Presence of the very little band is assigned to Si–O–Si bonds at  $980\text{ cm}^{-1}$  indicates that certain condensation of the silane chains has taken place immediately upon mixing [217]. These bands prove the existence of condensation phenomena together with the hydrolysis one.

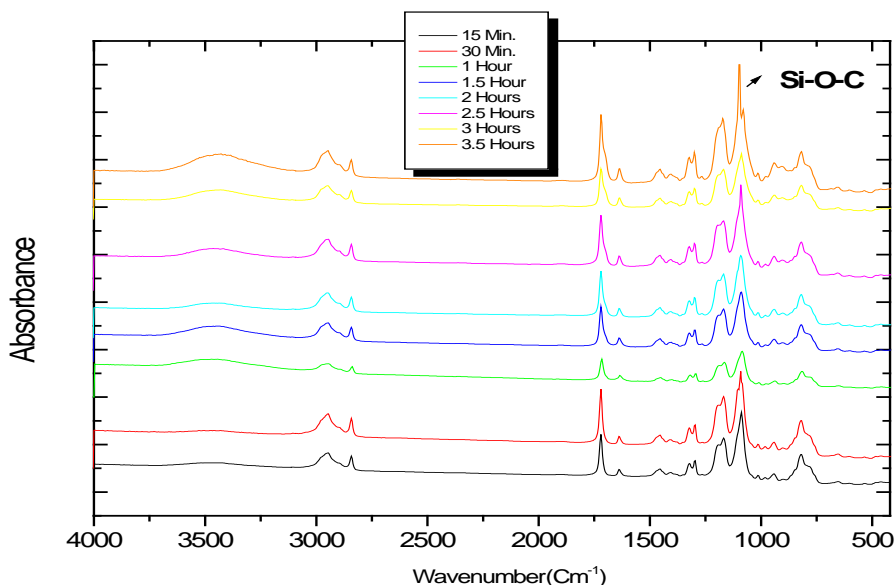
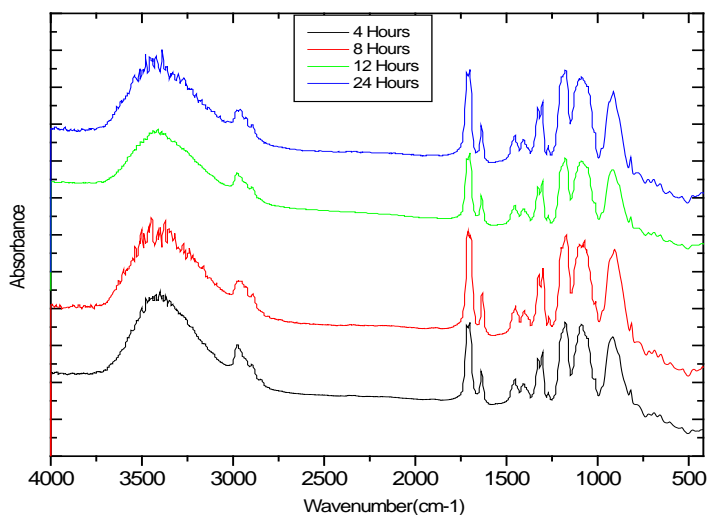


Fig. 5.5 FTIR spectra of the MAPTMS/TMOS mixture in Et(OH)/H<sub>2</sub>O solvent system. Hydrolysis time 15 min. - 3.5 h.

The FTIR spectra of the MAPTMS/TMOS aqueous mixture are shown in Figure 5.5, for hydrolysis time varying from 15 min up to 3.5 h. In these spectra it is clearly observed that the FTIR spectrum of 3.5 h is very similar to that after 1 min of mixing (Figure 5.4), which would indicate incomplete hydrolysis of the mixture.

As the hydrolysis time increases, 4 h of hydrolysis, the spectra change substantially (Figure 5.6), the band at  $2.840\text{ cm}^{-1}$ , associated with the methoxy group, which

appeared upon mixing (Figure 5.4), disappears for hydrolysis times of 4 h (Figure 5.6). This is indication of the completion of the reaction and allows establishing the beginning of optimal hydrolysis conditions at about 4 h. The same happens with the asymmetric stretching vibration of the Si–O–C, which appeared at  $1.080\text{ cm}^{-1}$  (Figure 5.4). This bond is the one that must be broken during the hydrolysis, and its absence in Figure 5.6A implies the end of the hydrolysis process<sup>[217]</sup>. This band disappeared and was replaced by two bands corresponding to Si–O–Si; results from the condensation process. Disappearance of the band of Si–O–CH<sub>3</sub> groups at  $2.840\text{ cm}^{-1}$  was also evidence together with the increase of a broad band at  $3.420\text{ cm}^{-1}$ , assigned to OH groups from Si–OH formed through hydrolysis<sup>[217]</sup>.



**Fig. 5.6** FTIR spectrum of the MAPTMS/TMOS mixture in EtOH–H<sub>2</sub>O solvent system. Hydrolysis time 4–24 h.

Figure 5.6 shows that for the hydrolysis time of 8 up to 24 h, the slight broadening of Si–O–Si bands results from a highly cross-linked network. It should be noted that the Si–O–Si band at higher frequencies  $1187\text{ cm}^{-1}$  is due to the formation of cyclic siloxane units. This band usually shifts in the high frequency direction when the silane films are

further cross linked. While the appearance of the Si-O-Si band at low frequency ( $1085\text{ cm}^{-1}$ ) is indicative of the formation of the long Si-O-Si chains.

**Table 5.1** Assignment of the FTIR peaks shown in Figures 5.4 and 5.6

Wavenumber (cm <sup>-1</sup> )	Group	References
2950	$\nu_{\text{as C-H}}$ (C-H)	[210]
2840	$\nu_{\text{s C-H}}$ (O-CH <sub>3</sub> )	[210]
1720	$\nu_{\text{s C=O}}$ (methacryloxy group)	[210-212]
1640	$\nu_{\text{C=C}}$ (methacryloxy group)	[210-212]
1450	$\delta\nu_{\text{CH}_2}$ (Si-R organic group)	[213]
1320	$\nu_{\text{as C-O}}$ (C-O-C)	[214]
1300	$\nu_{\text{s C-O}}$ (C-O-C)	[214]
1080	$\nu_{\text{as Si-O}}$ (Si-O-CH <sub>3</sub> )	[215,216]
1187	$\nu_{\text{as}}$ (Si-O-Si)	[217]
1085	$\nu_{\text{s}}$ (Si-O-Si)	[217]
3100-3600	$\nu_{\text{O-H}}$ (Si-OH)	[217]

## 5.2 Nuclear magnetic resonance (NMR)

### 5.2.1 <sup>29</sup>Si-NMR

Nuclear magnetic resonance (NMR) is a useful tool to study the silane hydrolysis. The NMR relaxation time measurements are sensitive to short range interactions and can be used to estimate the scale of miscibility of an organic–inorganic hybrid [218]. This is due to the good resolution and quantitative assignment of the NMR peaks of silane molecules in comparison with the FTIR analysis [219]. Liquid-state <sup>29</sup>Si and <sup>13</sup>C NMR have been applied to study the hydrolysis mechanism of the MAPTMS/TMOS mixture in Et(OH)/H<sub>2</sub>O solution. In the <sup>29</sup>Si NMR spectroscopy, the chemical shift of silicon is determined by the chemical nature of their neighbors, namely T, and Q structures [220]. A Q species is one in which the Si atom is capable of producing four siloxane bonds, which results from TMOS precursor, whereas a T species can only achieve three siloxane bonds and results from MAPTMS [183]. According to the nomenclature, four T signals of different nature can be present (T<sup>n</sup>, where n=0, 1, 2, or 3, respectively) [207]. Figure 5.7

shows a schematic representation of  $T^n$  silane structures.  $T^0$  appears in a spectral range from  $-37$  to  $-39$  ppm which is assigned to  $\text{RSi}(\text{OCH}_3)_3$  un-hydrolyzed species from MAPTMS.  $T^1$  occurs in the range defined between  $-46$  and  $-48$  ppm, assigned to condensed silicon units bearing only one bridging oxygen atom ( $\text{Si}-\text{O}-\text{Si}$ ),  $T^2$  is defined in the spectral range defined between  $-53$  and  $-57$  ppm which is assigned to doubly condensed silicon centers (two bridging oxygen atoms), and  $T^3$  is defined into the  $-61$  to  $-66$  ppm range, fully condensed silicon units (three bridging oxygen atoms) as sketched in Figure 4.22<sup>[220]</sup>.

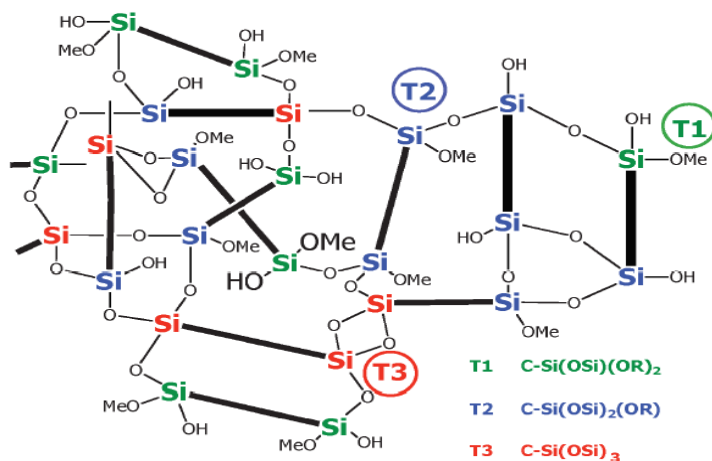


**Fig. 5.7** Schematic representation of  $T^n$  silane structures;  $n=1, 2,$  or  $3$

The  $^{29}\text{Si}$  spectra of MAPTMS/TMOS in  $\text{Et}(\text{OH})/\text{H}_2\text{O}$  solution are shown in Figure 5.7. Upon mixing of the two precursors (Figure 5.7A), the  $\text{RSi}(\text{OCH}_3)_3$  species from non-hydrolyzed MAPTMS ( $T^0$  units) give a well-detectable singlet signal at  $-42$  ppm. The appearance of mono-, di-, and tri-substituted siloxanes T species ( $T^1$  units at  $-50$  ppm,  $T^2$  units at  $-59$  ppm, and  $T^3$  units between  $-68$  and  $-71$  ppm) is a result of the self-condensation. These observations are in agreement with the FTIR results that showed the presence of condensed siloxane species at  $980\text{ cm}^{-1}$  upon mixing of the two precursors, indicated by the presence of the  $\text{Si}-\text{O}-\text{Si}$  band (Figure 5.4). The  $\text{Si}(\text{OCH}_3)_4$  unhydrolyzed species from TMOS were not detected in the  $^{29}\text{Si}$  spectra upon mixing of the

two precursors with H<sub>2</sub>O/ethanol, and this is because TMOS was used in small amount and easily hydrolyzed upon mixing.

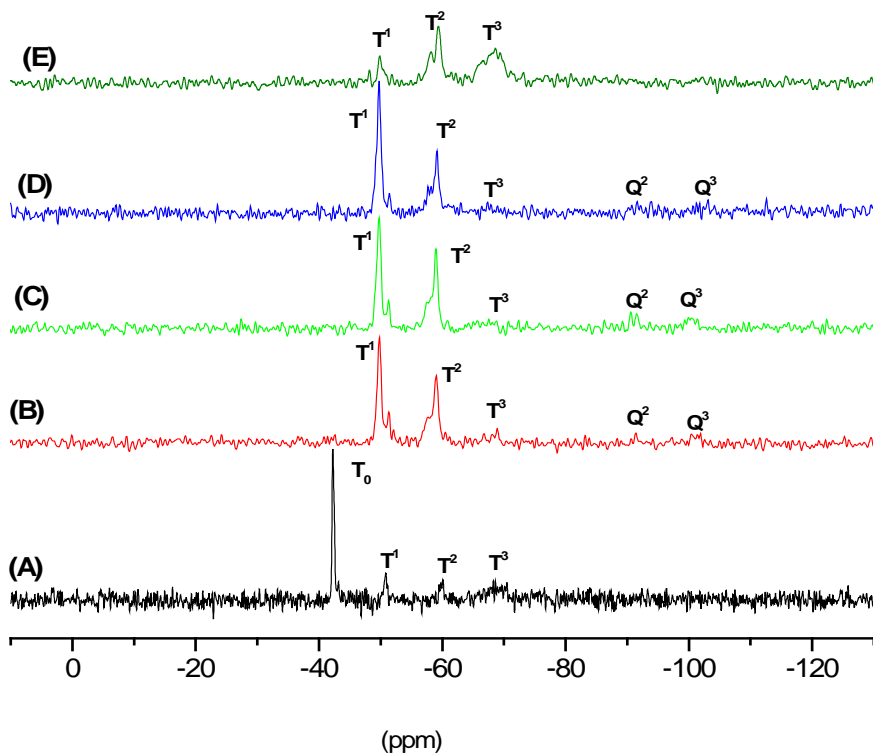


**Fig. 5.8** Liquid-state  $^{29}\text{Si}$  NMR spectra of MAPTMS/MOS mixture in Et(OH)/H<sub>2</sub>O solvent system. A upon mixing of MAPTMS and TMOS, B after 1 h, C after 2 h, D after 3 h, E after 4 h.

After 1 h of the reactive mixing, both the T<sup>1</sup> at 49.81 ppm and T<sup>2</sup> at 58 became clear and dominate the entire spectrum which indicates the progress of the hydrolysis process (Figure 5.8B). Also the T<sup>3</sup> of hydrolyzed MAPTMS and Q<sup>2</sup> and Q<sup>3</sup> of hydrolyzed TMOS appear as very small signals at 67.55, 91.78, and 101.66 ppm, respectively.

After 2 h of hydrolysis and up to 3 h (Figures 5.8C and 5.8D), there is not a significant change between these spectra and that of after 1 h and the concentrations of condensed T<sup>2</sup> and T<sup>1</sup> species units remain constant (Figure 5.8B).

After 4 h of hydrolysis, the T species in the form of T<sup>1</sup>, T<sup>2</sup>, and T<sup>3</sup> at -50, -58, and -68 ppm dominate the entire spectrum (Figure 5.8E). These results shed light upon three

important observations which indicate that 4 h was enough for the hydrolysis of the MAPTMS/TMOS mixture, in a similar way as the FTIR spectra has indicated. It can observe:

- The absence of unhydrolyzed TMOS,  $\text{Si}(\text{OCH}_3)_4$ , as it hydrolyzed very rapidly,
- The disappearance of the signal  $\text{T}^0$  corresponding to the initial unhydrolyzed MAPTMS (Figure 5.8A), and
- The appearance of the signal  $\text{T}^3$ , which corresponds fully to condensed silicon units with three siloxane bonds (three bridging oxygen atom) dominated all the spectrum of 4 h, (Figure 5.8E).

The  $^{29}\text{Si}$  NMR spectra provide the proportions of  $\text{T}^n$  species ( $n=1, 2$ , or  $3$ ), where  $\text{T}$  represents a Si atom oxygen bridged to another Si atoms. These allowed the quantification of the cross-linking degree within the silicate network. The  $\text{T}^1$ ,  $\text{T}^2$ , and  $\text{T}^3$  units arose from the self-condensation reactions only. The  $\text{T}^1$  units represented dimers or chain ends.  $\text{T}^2$  were associated with the linear siloxane sequences, and the  $\text{T}^3$  units witnessed about the appearance of three dimensional siloxane networks. In fact, the non-reacted silane molecules ( $\text{T}^0$  units) from MAPTMS gave a well detectable singlet signal at  $-42$  ppm (Figure 5.7A). This singlet disappeared from the spectrum after 1 h of reactive mixing, indicating beginning of the hydrolysis reaction. As it was expected from the FTIR results, the maximum of self-condensed products was observed after 4 h of reaction. The proportions of the T species in each hybrid system quoted in Table 5.2 were obtained from deconvolution of the  $^{29}\text{Si}$  NMR spectra with the WINFIT software. The spectra were deconvoluted into individual Gaussian line shapes, thus allowing a quantitative analysis of the spectra based on the peak areas of each species. From Figure 5.9, it can be seen that after 4 h of hydrolysis, the amount of  $\text{T}^3$  silicon content increased while that of  $\text{T}^2$  and  $\text{T}^1$  silicon content decreased in the matrix of the Si–O–Si structure. Thus hydrolysis was accompanied by a condensation reaction among the silanol groups to give oligomeric structures.

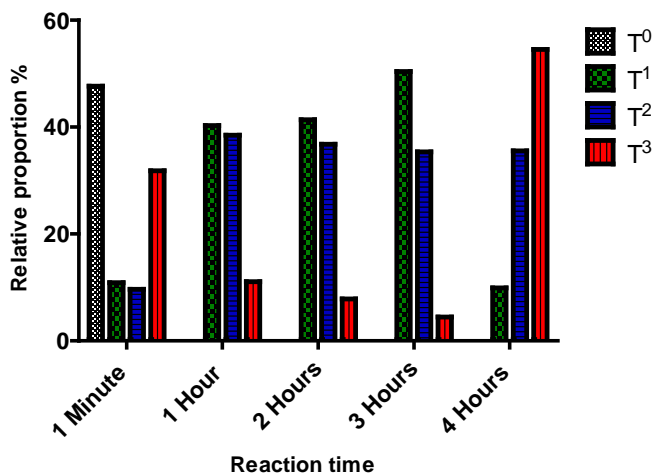


Fig. 5.9 Relationship of the signals, for species T<sup>0</sup>, T<sup>1</sup>, T<sup>2</sup>, and T<sup>3</sup> in the MAPTMS/TMOS hybrid.

Table 5.2 Relative proportions of T and Q species in the organic–inorganic hybrid materials from the <sup>29</sup>Si spectra in Figure 5.8.

Time in M	Relative <sup>a</sup> proportions (%)				Relative proportions <sup>b</sup> (%)		Ratio <sup>c</sup> (%)	
	T <sup>0</sup>	T <sup>1</sup>	T <sup>2</sup>	T <sup>3</sup>	Q <sup>2</sup>	Q <sup>3</sup>	T <sup>n</sup>	Q <sup>n</sup>
1	47.66	10.87	9.64	31.83	-	-	1	-
60	-	44.83	42.83	12.34	31.5	68.5	89.8	10.2
120	-	48.11	42.78	9.11	46.6	53.4	86	14
180	-	55.88	39.18	4.93	42.90	57.1	90	10
240	-	9.91	35.56	54.53	-	-	1	-

<sup>a</sup> Relative proportions (%): (each T species/total T species) · 100%.

<sup>b</sup> Relative proportions (%): (each Q species/total Q species) · 100%.

<sup>c</sup> Ratio (%):  $T_i = \{\text{total T species}/(\text{T species} + \text{Q species})\} \cdot 100\%$ ,  $Q_j = \{\text{total Q species}/(\text{T species} + \text{Q species})\} \cdot 100\%$ .

### 5.2.2 $^{13}\text{C}$ -NMR

The  $^{13}\text{C}$  NMR spectra of MAPTMS/TMOS in Et(OH)–H<sub>2</sub>O are shown in Figures 5.10 and 5.11. This mixture was hydrolyzed for 4 h in Et(OH)–H<sub>2</sub>O solution. In comparison with the  $^{29}\text{Si}$  NMR spectra, the patterns of the  $^{13}\text{C}$  NMR peak positions are significantly exhibiting multiple peaks. This suggests that there are several chemical compounds within the hybrid systems containing carbon-bonding structures. Peaks assignments for carbon-bonding types which can be attributed to the MAPTMS and TMOS precursors are given in Table 5.3.

The peaks from TMOS and MAPTMS in the  $^{13}\text{C}$  NMR spectra are in good agreement with earlier reports <sup>[221]</sup>. The hydrolysis of the MAPTMS/TMOS system was followed by the evolution of the peaks corresponding to the methyl groups attached to the silane and those liberated during the hydrolysis (CH<sub>3</sub>–OH and CH<sub>3</sub>–CH<sub>2</sub>–OH).

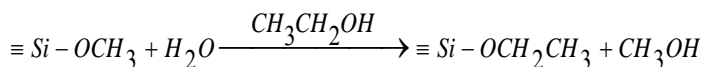
Upon mixing of the two silane precursors with Et(OH)/H<sub>2</sub>O solution, the peaks at 17.45 and 57.29 ppm are from ethoxy groups of ethanol and to CH<sub>3</sub>–C of MAPTMS <sup>[222]</sup> (Figs. 5.10A). The peaks at 48.97 are ascribed to un-hydrolyzed CH<sub>3</sub>–O–Si units of MAPTMS and TMOS.

The peak at 67.10 ppm is attributable to CH<sub>2</sub>–CH<sub>2</sub>–O units of MAPTMS while those that appear at 22.47 ppm are due to CH<sub>2</sub>–CH<sub>2</sub>–Si units of the same precursor. Finally, the peak at 9.18 ppm is attributed to Si–C of MAPTMS.

Up to 2 h of reaction, no changes can be detected (Figs. 5.10B, 5.10C, 5.11B and 5.11C). The spectra exhibit the same peaks corresponding to the carbon within the hybrid systems containing carbon-bonding structures.

After 3 h of hydrolysis, the spectra exhibit significant changes (Figs. 5.10D and 5.11D). The peak that appears at 49 ppm corresponds to the release of methanol as a result of the beginning of the condensation process. The emergence of this peak indicates the hydrolysis of the methoxy group in H<sub>3</sub>C–O–Si units from both precursors.

The hydrolysis of methoxy groups caused by water in ethanol contributed to the yielding of methanol as a reaction product that is seen in the liquid-state  $^{13}\text{C}$  NMR spectra <sup>[223]</sup>:



At the same time, during the hydrolysis of TMOS in ethanol, methoxy groups of TMOS are exchanged for alkoxy groups. This reaction is an equilibrium reaction and almost all of methoxy groups are exchanged for ethoxy groups. This gives well-developed bands at 17.62 and 57.26 ppm in the spectrum of 3 h hydrolysis (Figures 5.10D and 5.11D), corresponding to Si–O–CH<sub>2</sub>–CH<sub>3</sub> units, and methanol is released into the solution following the previous reaction. It has been reported<sup>[224]</sup> that the hydrolysis of solvents for silanes, such as water and ethanol, approach equilibrium rather than completion, due to the competition between silane hydrolysis and alcoholysis. In our study we also observed a similar phenomenon that gives well-developed bands at 17.62 and 57.26 ppm in the spectrum of 3 h hydrolysis (Figures 5.10D and 5.11D), corresponding to Si–O–CH<sub>2</sub>–CH<sub>3</sub> units.

After 4 h of hydrolysis, it takes place the disappearance of the methoxy groups of the initial silanes at 48.97 ppm and the concomitant formation of free methanol, as indicated by the peak growing at 49 ppm of the hydrolyzed mixture<sup>[225]</sup> (Figure 5.10 E). Thus the disappearance of the resonances assigned to the CH<sub>3</sub>–O–Si group is accompanied by the increase of the CH<sub>3</sub>–OH signal. All these facts can confirm that a time of 4 h is enough for the hydrolysis reactions to be completed.

These results indicated that the hydrolysable Si–O–CH<sub>3</sub> groups of both precursors were hydrolyzed and formed silanol groups that could be derived in Si–O–Si bonds due to subsequent condensation. This agrees well with the results obtained in <sup>29</sup>Si NMR spectra that showed that the hydrolysis was accompanied by a condensation reaction among the silanol groups to give oligomeric structures. The evidence of the presence of such structures was provided by the broadening of the different peaks in the <sup>13</sup>C NMR spectra.

## Organic-inorganic hybrid sol-gel– Optimization of the synthesis processes of the hybrid matrix

---

**Table 5.3** Peak assignments of  $^{13}\text{C}$  liquid state of both MAPTMS and TMOS according to peaks detected in (Figure 5.10).

MAPTMS (Aldrich)		TMOS (Aldrich)		Ethanol	
Nature of carbons	Ass.(ppm)	Nature of carbons	Ass.(ppm)	Nature of carbons	Ass.(ppm)
$\text{CH}_2\text{-}\underline{\text{C}}\text{H}_2\text{-O}$	67.10	$\underline{\text{C}}\text{H}_3\text{-O-Si}$	48.97	$\text{CH}_3\text{-}\underline{\text{C}}\text{H}_2\text{-OH}$	57.29
$\text{CH}_3\text{-O-Si}$	48.97			$\underline{\text{C}}\text{H}_3\text{-CH}_2\text{-OH}$	17.45
$\underline{\text{C}}\text{H}_2\text{-CH}_2\text{-Si}$	22.47				
$\underline{\text{C}}\text{H}_3\text{-C}$	17.45				
$\text{CH}_2\text{-Si}$	9.18				

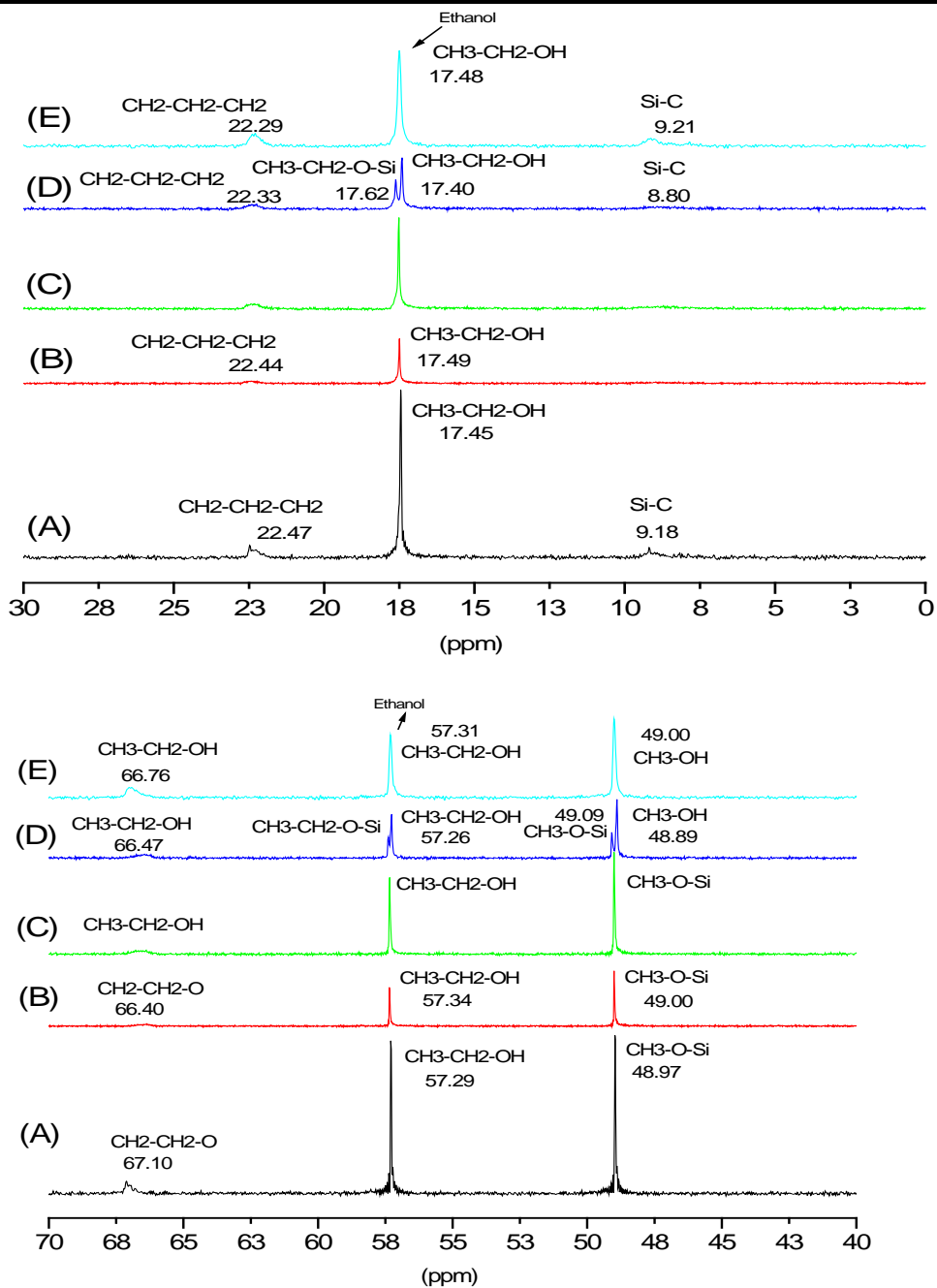


**Fig. 5.10** Liquid state  $^{13}\text{C}$  NMR spectra of prehydrolyzed MAPTMS/TMOS: (A) upon mixing of MAPTMS and TMOS; (B) after 1 hour; (C) after 2 hours; (D) after 3 hours, and (E) after 4 hours.

## Organic-inorganic hybrid sol-gel– Optimization of the synthesis processes of the hybrid matrix

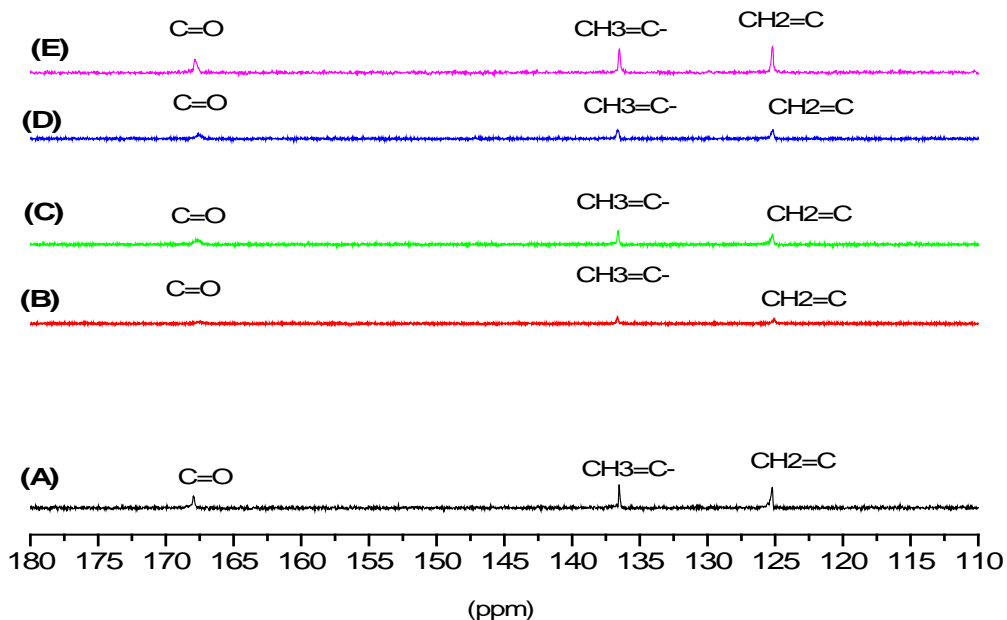


**Fig. 5.11** Liquid state <sup>13</sup>C NMR spectra of prehydrolyzed MAPTMS/TMOS: (A) upon mixing of MAPTMS and TMOS; (B) after 1 hour; (C) after 2 hours; (D) after 3 hours, and (E) after 4 hours.

### - Conclusions

In conclusion, the sol-gel reaction of the MAPTMS/TMOS system in Et(OH)/H<sub>2</sub>O solution was studied by FTIR and NMR. The aim of the study is to optimize the prehydrolysis times of both silanes and consequently their use as precursors for hybrid coating upon Ti6Al4V alloy. The early step of the condensation process was studied by collecting <sup>29</sup>Si NMR spectra. The quantitative analysis of the condensed species was calculated in terms of T<sup>1</sup>, T<sup>2</sup>, and T<sup>3</sup> silicon units. It could be concluded that the hydrolysis of the two silane precursors under the adopted synthesis strategy conditions is completed after approximately 4 h at room temperature. The quantitative analysis of NMR indicates the presence of self-condensation species after mixing the two precursors. The hydrolysis was accompanied by a condensation reaction between the silanol groups to give oligomeric structures.



## ***Chapter (6)***

*Organic-inorganic hybrid sol-gel thin films modified  
with Hydroxyapatite particles*



# Organic-inorganic hybrid sol-gel thin films modified with Hydroxyapatite particles

---

## Organic-inorganic hybrid sol-gel thin films modified with Hydroxyapatite particles

### - Introduction

Organic coatings are employed to protect metal surface from corrosion. They have the advantages of being mechanically flexible, but have poor abrasion and thermal resistance. The poor adhesion of the deposited films to the metal surface can provoke the delamination of the coatings and subsequent corrosion of metallic surface [226]. Inorganic sol-gel coatings could be an alternative to conventional organic coatings because they have excellent abrasion resistance and high density, but they are brittle and require high processing temperatures [72,227]. In contrast organic-inorganic hybrids prepared by sol-gel route are of great interest because they combine both organic and inorganic characteristics [185,188].

Organic-inorganic hybrids appear as an alternative for obtaining new materials with unusual features [191,228-230]. This is related to their diphasic structures, leading to multifunctional materials. The organic and inorganic components of the hybrid materials are combined together by chemical bond, making the interface of two parts not clear. In the organic-inorganic hybrid, the organic groups help the surface of the hybrid coating possess flexibility, and thus, less prone to cracking during heat treatment of the film. These features have been successfully exploited in last two decades in order to design a wide range of new multifunctional materials with tailored properties which can be potential useful for the development of ion selective membranes, electrochemical sensors, lithium-ion batteries, heterogeneous catalysts, corrosion protection coatings, etc. [83, 194-196, 231-233].

Figure 6.1 shows a simplified view of the reactions of hydrolytic deposition of silanes on inorganic or metal surfaces. The organic-inorganic films are normally obtained by dip-coating techniques where a stable thin film is obtained via immersion of metal substrate in an alcohol-water based silane solutions for few seconds. Such silane film is expected to act as a barrier against diffusion of corrosive species to the metal surface [234].

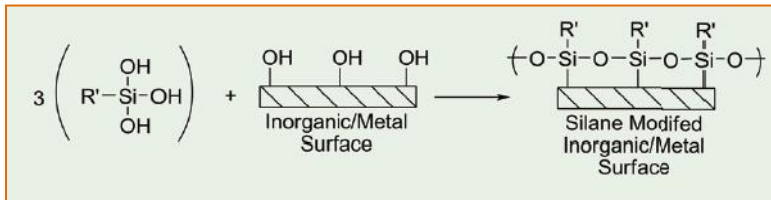


**Fig. 6.1** Simplified schematic of bonding mechanism between silane molecules and metal surface hydroxide layer.

The silanes contain hydrolysable alkoxy groups, which after hydrolysis are converted to hydrophilic silanol groups (Si-OH). When these groups become in contact with hydroxyl-covered metallic surfaces (Me-OH), upon curing, a condensation reaction takes place forming metallo-siloxane bonds (Me-O-Si) increasing adherence of the silanes to the metallic surface <sup>[235]</sup>. The excess of the Si-OH group present in the adsorbed structure forms a siloxane bonds (Si-O-Si), which inhibit the penetration of the corrosive agents such as water, oxygen, and chloride ions. Because the corrosion resistance of the organic-inorganic hybrid coatings prepared by sol-gel is based on its physical barrier properties, a homogenous crack-free material is required. Unfortunately, in both the hydrolysis and condensation reactions, a low molecular weight by-product such as alcohol is produced <sup>[236]</sup>. The drying process for the sol-gel material requires that the alcohol and water escape as the gel solidifies. Due to the evaporation of ethanol and water, small pores and pinholes are developed which provide paths for electrolyte to diffuse through the coating and corrode the metal substrate <sup>[237]</sup>. The combination of the sol-gel organic-inorganic hybrid films with the addition of HAp particles, bioactive ceramic, could be an efficient method to increase the barrier properties and bioactivity of the films. On one hand, such coating could act as a barrier avoiding the release of metal ions. On the other hand, HAp particles could make a bonding with the bone and may enhance the corrosion protection ability of the sol-gel coatings either by increasing the coating thickness or by having a pore blocking effect.

# Organic-inorganic hybrid sol-gel thin films modified with Hydroxyapatite particles

---

## - Aim

The aim of this chapter is to prepare and characterize new organic-inorganic coatings deposited onto Ti6Al4V substrates. These coatings were obtained by sol-gel method from mixtures of  $\gamma$ -methacryloxypropyltrimethoxysilane (MAPTMS) and tetramethoxysilane (TMOS) modifying the resulting organopolysiloxane matrix by dispersion of different amounts of inorganic hydroxyapatite (HAp) powders. Different contents of solid HAp particles have been dispersed in the starting MAPTMS/TMOS sol. The main aim of this modification is to overcome the drawbacks of voids formation during curing as a result of evaporation of water and ethanol during thermal treatment and to study the effect of HAp addition, as solid phosphorus precursor, incorporated in the siloxane network on the in-vitro bioactivity of the prepared hybrid films. The effect of the HAp incorporation on the structure, corrosion protection and bioactivity of these coatings has been studied.

## 6.1 Characterization

The experimental techniques used to characterize the studied samples are the following:

- Thermal analysis (TGA), to determine the optimum curing temperature of the deposited hybrid films,
- Attenuated total reflectance infrared (ATR-IR), to study the composition and functional groups in the coatings after curing ,
- Solid-state  $^{29}\text{Si}$ ,  $^{13}\text{C}$  ,  $^{31}\text{P}$  NMR for determining the nature of condensed species in the hybrid coatings after curing ,
- X-ray diffraction (XRD), to determine however the prepared films are amorphous or crystalline,
- Scanning electron microscope , SEM/EDX , to study the morphology and composition of the films deposited on Ti6Al4V alloy,
- Confocal microscope, to obtain information about the roughness and topographical structures,

- Viscometer, to calculate the viscosity of different prepared sols,
- Stylus profile-meter, to calculate the thickness of the hybrid films,
- Contact angle measurement, to characterize the wettability of the prepared hybrid films,
- Protein adsorption, for *in-vitro* evaluation of the biocompatibility in physiological environment,
- Neutral red uptake assay, to study the cell viability /toxicity and osteoblast cells proliferation,
- Immunofluorescence, to show the morphology of osteoblast cells attached to different hybrid coatings,
- Study of the bioactivity of MAPTMS/TMOS/HAp hybrid coatings on Ti6Al4V surfaces, assaying the precipitation of biomimetic bone-like apatite layer when the metal/sol-gel coating system is soaked in simulated body fluids (SBF) by using SEM/EDX,
- Study of the corrosion protection of MAPTMS/TMOS/HAp hybrid coatings on Ti6Al4V surfaces in SBF using electrochemical impedance spectroscopy (EIS).

### 6.1.1 Thermal Analysis (TGA)

The knowledge of the thermal behaviour of organic-inorganic materials is of great importance, in determining their best processing conditions. Thermal gravimetric analysis (TGA) is an important tool for thermal stability studies of materials. It allows determining the temperature range at which a heated sample undergoes a major conformational change by means of monitoring the thermal weight loss profile <sup>[79]</sup>.

Figure 6.2 shows TG curves (25-900°C temperature range) of MAPTMS/TMOS/HAp hybrid as a function of HAp content. It can be seen that all curves show three regions of weight loss. The initial weight loss (Region I), in all these samples, is considered to be the result of the elimination of the condensation by-products, ethanol and water <sup>[238]</sup>.

## Organic-inorganic hybrid sol-gel thin films modified with Hydroxyapatite particles

Figure 6.2 shows TG curves (25-900°C temperature range) of MAPTMS/TMOS/HAp hybrid as a function of HAp content. It can be seen that all curves show three regions of weight loss. The initial weight loss (Region I), in all these samples, is considered to be the result of the elimination of the condensation by-products, ethanol and water [239]. The second weight loss (Region II) above 350°C is due to the partial thermal degradation of organic matter in hybrids. The third weight loss stage (Region III) at 350-500°C is due to the complete burning of organics in the hybrid [240]. The TGA curves became flat at 600-900°C because the organic component had been completely removed, leaving behind only an inorganic SiO<sub>2</sub> and HAp component.

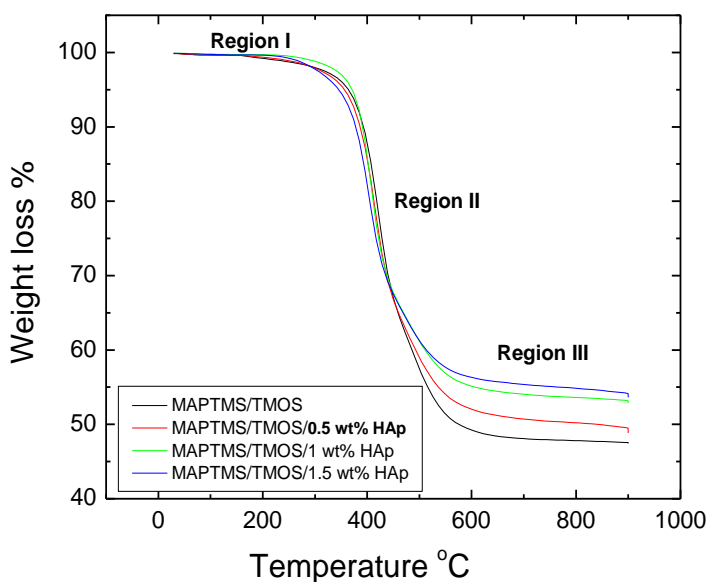


**Fig. 6.2** TG plots of the prepared MAPTMS/TMOS hybrids containing different amounts of HAp particles.

From the TGA data, (Table 6.1), it is clear that, as the HAp content increases, the weight loss decreases. In addition, HAp containing hybrid networks gave higher inorganic residues yield at 900°C of about 53.61, 51.21, 48.92 and 47.51 wt. % for the hybrid with 1.5, 1, 0.5 and 0 wt. % HAp. The residual char can be used as an indicator of thermal resistance. These results suggest that the thermal stability of the hybrid is

enhanced by HAp. This point to an enhancement of the thermal stability of the hybrid silane network.

Briefly, the thermal stability of the hybrid network can be improved because HAp particles into the network prevent the heat transfer to hybrid by acting as heat insulator. Other reason could be the enhancement of the cross-linking of the network by addition of HAp to the sol.

**Table 6.1.** Thermogravimetric results obtained for MAPTMS-TMOS with HAp.

<b>Sample</b>	<b>TGA</b>	
	<b>Weight loss % at</b>	<b>Residue % at 900 °C</b>
	<b>600°C</b>	
Control	50.81	47.51
0.5 wt % HAp	49.01	48.92
1 wt % HAp	44.91	51.21
1.5 wt % HAp	43.72	53.61

### **6.1.2 Attenuated Total Reflectance Infrared Spectroscopy (ATR-IR)**

The structural characterization of cured hybrid films was performed using ATR-IR spectroscopy. Figure 6.3 shows The ATR-IR spectra of the prepared MAPTMS/TMOS/HAp coatings on Ti6Al4V substrates. The ATR-IR band assignments for these films are presented in Table 6.2.

These spectra cover both low and high frequency regions. The low frequency region includes the vibrations characteristics of the silica network, namely the dominant band while those at higher frequencies are corresponding to the organic components within the hybrid. All hybrids present a characteristic band around 1,010  $\text{cm}^{-1}$  attributed to Si-O-Si group stretching vibrations, which are associated to the structural backbone of the hybrid material <sup>[83]</sup>.

The band at 2,957  $\text{cm}^{-1}$  may be ascribed to the C-H stretching absorptions of the  $\text{CH}_3$  residues <sup>[83]</sup>. The bands at 1,447  $\text{cm}^{-1}$  correspond to the symmetrical and asymmetrical  $\text{CH}_3$  deformational (umbrella) modes <sup>[83]</sup>. The stretching vibration of C=O group at 1,731  $\text{cm}^{-1}$  is attributed to the carboxyl of acrylate <sup>[83]</sup>.

## Organic-inorganic hybrid sol-gel thin films modified with Hydroxyapatite particles

The existence of these residues after a thermal treatment at 120°C during 2 hours indicates that the film still contains hydrocarbon units. These results confirm the presence of both organic and inorganic structures in the hybrid coatings. This indicates that the coating structure is formed by a silica network of Si–O–Si bonds interrupted in some points by organic groups.

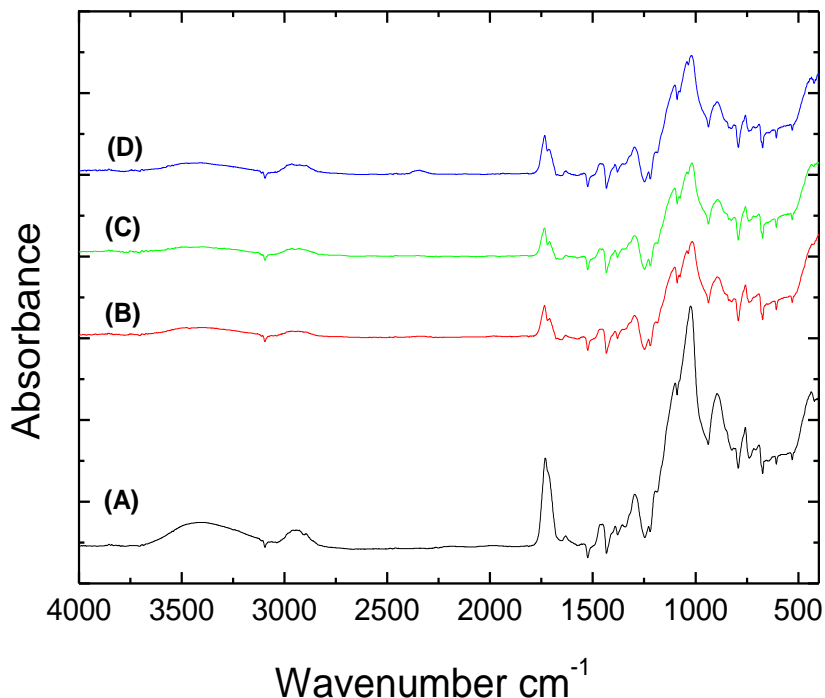


**Fig. 6.3** Representative ATR-IR absorption spectra of MAPTMS/TMOS/HAp-Ti6Al4V systems containing: (A) 0% wt. HAp; (B) 0.5 wt. % HAp ; (C) 1 wt. % HAp and, (D) 1.5 wt. % HAp, respectively.

In the ATR spectra of the HAp containing hybrid (Figures 6.3B - 6.3D) there is significant broadening and decrease in the intensity of the bands together with emergence of tiny shoulder at 1,045  $\text{cm}^{-1}$  corresponding to  $\text{PO}_4^{3-}$  stretching vibration [241]. The absence of component bands corresponding to Si-O-P in these spectra indicates no incorporation of phosphates into silica sites of the lattice. That, no reaction of the HAp particles with the hybrid matrix has been observed.

**Table 6.2.** Assignment of the ATR-IR bands in MAPTMS/TMOS/HAp-Ti6Al4V systems

Wavenumber ( $\text{Cm}^{-1}$ )	Assignment	References
3,100-3,600	$\nu_{\text{O-H}}$ (Si-OH groups)	[83]
2,957	$\nu_{\text{C-H}}$ (Si-R organic group) $\nu_{\text{C-H}}$ (-OCH <sub>2</sub> CH <sub>3</sub> )	[83]
1,447	$\delta_{\text{CH}_2}$ (Si-R organic groups)	[83]
1,731	$\nu_{\text{C=O}}$ (methacryloxy groups)	[83]
1,640	$\nu_{\text{C=C}}$ (methacryloxy groups)	[83]
1,010	$\nu_{\text{as Si-O}}$ (Si-O-Si in different environments) $\nu_{\text{Si-O}}$ (Si-OCH <sub>3</sub> groups)	[83]

### 6.1.3 Solid state Nuclear Magnetic Resonance (NMR).

Solid-state <sup>29</sup>Si, <sup>13</sup>C and <sup>31</sup>P NMR are suitable for determining the nature of the condensed species present in the hybrid films after curing at 120°C for 2 hours.

#### 6.1.3.1 Solid state <sup>29</sup>Si-NMR spectroscopy

Solid state <sup>29</sup>Si-NMR spectroscopy was used to measure the degree of condensation (extent of reaction) in the hybrid films. This technique affords significant information about the nature of the organosilica network regarding the cross-linkage of the polysiloxane chains [242]. In the <sup>29</sup>Si NMR, peak assignments are described in terms of T units, assignable to Si atoms surrounded by one (T<sup>1</sup>), two (T<sup>2</sup>) or three (T<sup>3</sup>) siloxane bonds, respectively [83]. These T units have been used to measure the degree of condensation (extent of reaction) in the xerogels as a function of the HAp content.

## Organic-inorganic hybrid sol-gel thin films modified with Hydroxyapatite particles

Four peaks for silica network units in the pure xerogel MAPTMS/TMOS (control) have been observed at -59.6 ppm ( $T^2$ ), -67.7 ppm ( $T^3$ ), -100.41 ppm ( $Q^3$ ) and, -111.22 ppm ( $Q^4$ ), respectively (Figure 6.4). Signals  $Q^3$  ( $Si(OSi)_3$ ) correspond to three hydroxyl groups and signals  $Q^4$  ( $Si(OSi)_4$ ) to four hydroxyl groups that took part in the condensation reactions, respectively [83].

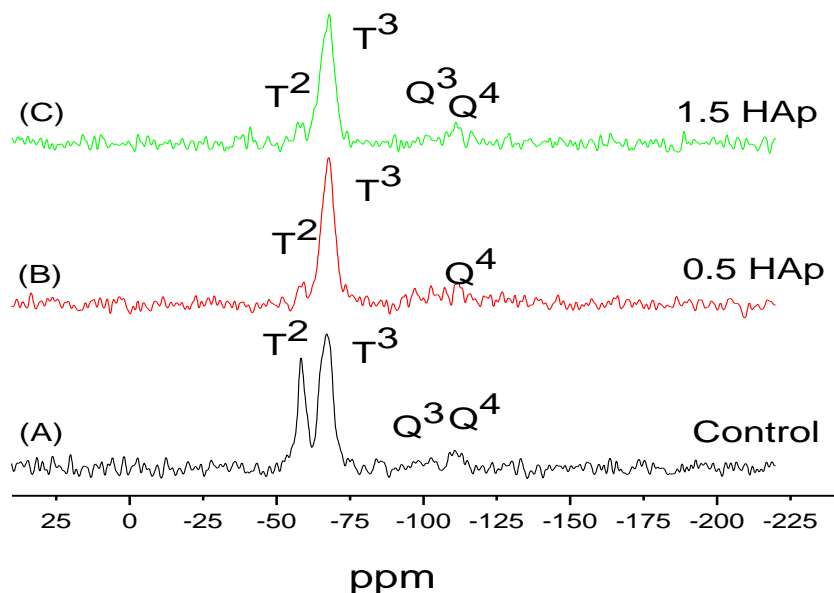


**Fig. 6.4** Solid state  $^{29}\text{Si}$  NMR spectra of MAPTMS/TMOS/HAp hybrids containing (A) 0% HAp; (B) 0.5 wt. % HAp and, (C) 1.5 wt. % HAp respectively

The MAPTMS monomer has trialkoxysilane functionality at each end group; it should form  $T^3$  species when condensed. While TMOS has tetraalkoxysilane units and upon condensation, it should result in  $Q^4$  species.

It is clear that  $^{29}\text{Si}$ -NMR spectra of the xerogel of the control sample (Figure 6.4A) and, the HAp containing xerogel (Figures 6.4B and 6.4C) evidencing that in both cases the T signals, due to the polymerization of the MAPTMS precursor, are much more intense than the Q signals, associated with the TMOS condensation.

The  $T^3$  signal is more intense than that corresponding to Si in  $T^2$  environments indicating a high degree of cross-linking in the organopolysiloxane matrix. That is, the network is dominated by  $T^3$  building blocks, accompanied by minor amounts of  $T^2$ ,  $Q^3$  and  $Q^4$  units.

Figure 6.5 shows the relationship of the signals, for species  $T^2$ ,  $T^3$ ,  $Q^3$ , and  $Q^4$  in the MAPTMS/TMOS hybrid with various content of HAp. The proportions of T and Q species in each xerogel system quoted in that Figure 6.5 and in Table 6.3 were obtained from deconvolution of the  $^{29}\text{Si}$ -NMR spectra with the WINFIT software. The spectra were deconvolved into individual Gaussian line shapes, thus allowing a quantitative analysis of the spectra based on the peak areas of each species. The results showed in Table 6.3 evidence that the HAp leads to higher degree of cross-linking in the organopolysiloxane matrix. The hybrid with HAp gave a larger fraction of  $T^3$  and  $Q^4$  than that from control sample. The relative intensity (in area) of  $T^3/T^2$  signals is 1.94, 9.96, and 11.77 for xerogels containing 0, 0.5 and 1.5 wt % HAp respectively.

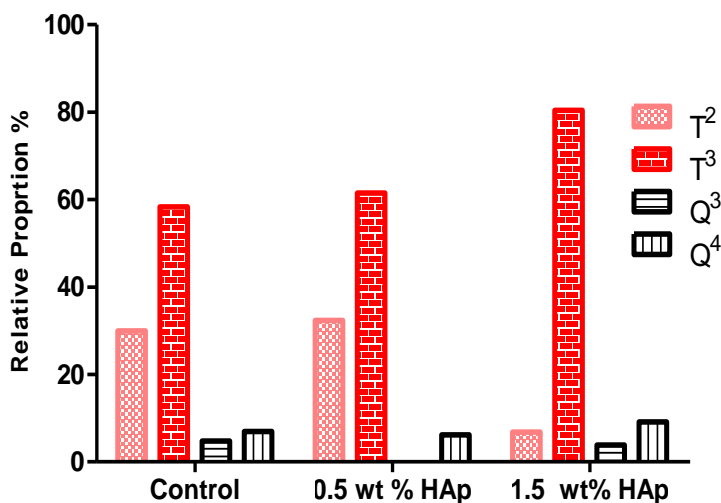


**Fig. 6.5.** Relationship of the signals, for species  $T^2$ ,  $T^3$ ,  $Q^3$ , and  $Q^4$  in the MAPTMS/TMOS hybrid with various content of HAp.

These results indicate that the addition of the HAp accelerated the condensation reaction, i.e. increasing the cross-linking density and, therefore, increasing the amount of fully condensed Si-O-Si structures.

# Organic-inorganic hybrid sol-gel thin films modified with Hydroxyapatite particles

**Table 6.3.** chemical shift  $\delta$  (ppm) and peak area (%) of T and Q units from deconvoluting the  $^{29}\text{Si}$ -NMR spectra.

Sample	$\delta$ (ppm) and peak area %					
	T <sup>0</sup>	T <sup>1</sup>	T <sup>2</sup>	T <sup>3</sup>	Q <sup>3</sup>	Q <sup>4</sup>
<b>Control</b>	-	-	-58.63 29.94	-66.97 58.35	-100.41 4.79	-111.22 6.93
<b>0.5 HAp</b>	-	-	-58.78 6.17	-67.60 61.49	-	-111.11 32.34
<b>1.5 HAp</b>	-	-	-57.90 6.83	-67.83 80.39	-101.91 3.84	-111.01 9.14

### 6.1.3.2 Solid state $^{13}\text{C}$ -NMR spectroscopy

The patterns of the  $^{13}\text{C}$ -NMR peak positions are significantly more complex (Figure 6.6). This suggests that there are several chemical compounds within the hybrid systems containing carbon-bonding structures.

In the  $^{13}\text{C}$ -NMR spectra of the MAPTMS/TMOS hybrids different signals have been observed at 17.5 ppm (C-CH<sub>3</sub>), 59.34 ppm (Si-O-CH<sub>3</sub>), 125.6 ppm (CH<sub>2</sub>=C), 136.2 ppm (CH<sub>3</sub>=C), 166.2 ppm (CH<sub>3</sub>=O) of the methacryloxy group, 9.7 ppm (Si-CH<sub>2</sub>) and 23.6 ppm (Si-CH<sub>2</sub>CH<sub>2</sub>CH<sub>2</sub>) (Figure 6.5A), appearing in all cases (both control and HAp containing hybrids) at similar chemical shift [83].

The  $^{13}\text{C}$ -NMR spectra of the HAp containing xerogel (Figures 6.6B and 6.6C) showed additional signal at 175.5 ppm. The revealed weak signal at 175.5 ppm, is assignable to carbonate ions of the carbonate HAp used [243].

The disappearance of the peak at 59.34 ppm corresponding to (Si-O-CH<sub>3</sub>), in the spectra of HAp containing hybrid indicate that the HAp addition catalyze the hydrolysis and breakdown of this unhydrolyzed bond to form condensed Si-O-Si units. This agrees with the results obtained from  $^{29}\text{Si}$ -NMR which showed the enhancement of the condensation after addition of HAp.

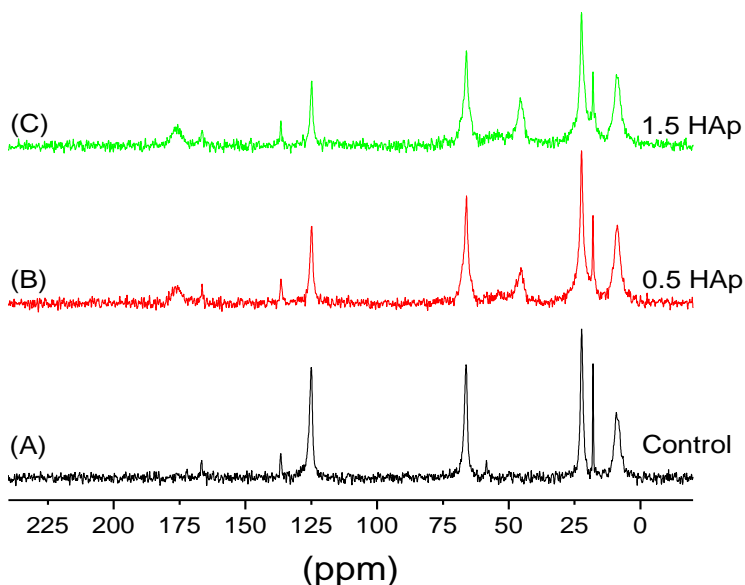


**Fig. 6.6** Solid state  $^{13}\text{C}$ -NMR spectra of MAPTMS/TMOS/HAp hybrids containing: (A) 0; (B) 0.5 wt. % HAp and, (C) 1.5 wt. % HAp, respectively.

### 6.1.3.3 Solid state $^{31}\text{P}$ -NMR spectroscopy

$^{31}\text{P}$ -NMR spectroscopy is a very powerful technique that could be used for determining the types of phosphorus species in the prepared hybrids.

Figure 6.7 shows the  $^{31}\text{P}$  Nuclear Magnetic Resonance ( $^{31}\text{P}$ -NMR) spectra of the MAPTMS/TMOS/HAp xerogel. The  $^{31}\text{P}$ -NMR spectra of hybrid containing HAp (Figures 6.7A and 6.7B) possess only a single signal at 2.9 ppm characteristic of crystalline HAp [244].

# Organic-inorganic hybrid sol-gel thin films modified with Hydroxyapatite particles

---

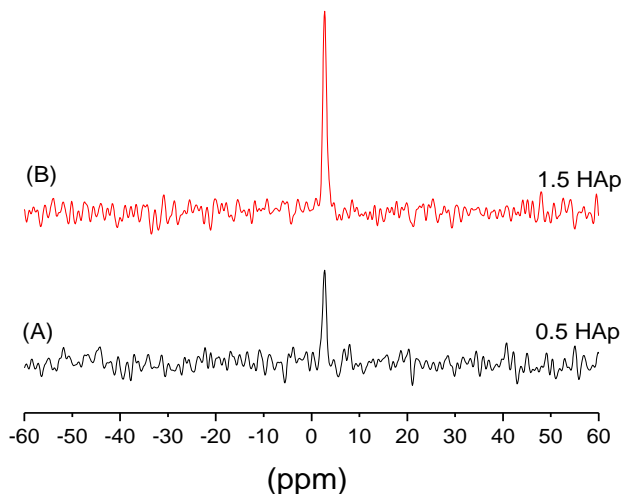


Fig. 6.7 Solid state  $^{31}\text{P}$  NMR spectra of MAPTMS/TMOS/HAp hybrid containing: (A) 0.5 wt. % HAp and, (B) 1.5 wt. % HAp respectively.

## 6.1.4 X-ray Diffraction (XRD)

Figure 6.8 shows the XRD patterns of MAPTMS/TMOS/HAp and pure HAp powder. The narrow peaks detected for pure HAp reveals a highly crystalline structure (Figure 6.8E). While for the MAPTMS/TMOS/HAp the XRD pattern is amorphous, as expected (Figures 6.7A-6.7D). This is because silane-based sol-gel chemistry consists primarily of hydrolysis and condensation reactions of alkoxy silane precursors that form amorphous glass-like materials as the reactions proceed <sup>[245]</sup>. In all XRD patterns of the prepared organic-inorganic hybrids there is only a broad band located at around  $2\theta=21^\circ$ , which is characteristic of amorphous silica <sup>[246]</sup>.

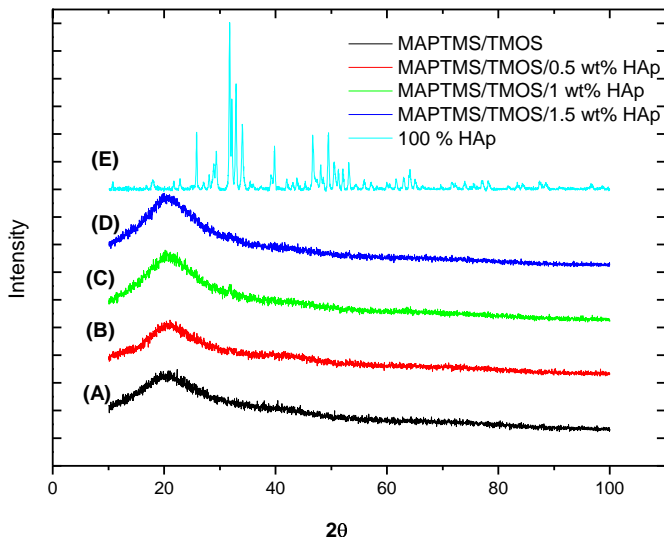


Fig. 6.8 Powder XRD patterns of pure HAp and hybrid sol-gel contain HAp.

### 6.1.5 Rheology

Rheology is concerned with the flow and deformation of materials experiencing an applied force. It is important to have a basic understanding of the viscosity of the sol as this is the criteria that govern the properties of the film being deposited. In general, within a few hours after preparation of the sol, the sol starts to form the network and as a result the viscosity increases.

Each sol composition i.e. MAPTMS/TMOS and MAPTMS/TMOS/HAp (0.5-1.5 wt %) was measured at a constant temperature of 20°C. This was repeated 3 times to allow a mean and standard deviation to be calculated.

The effect of the HAp additions on the viscosity of the MAPTMS/TMOS can be seen in Figure 6.9. The mean viscosity change +/- standard deviation (SD) was plotted as a function of different contents of HAp.

## Organic-inorganic hybrid sol-gel thin films modified with Hydroxyapatite particles

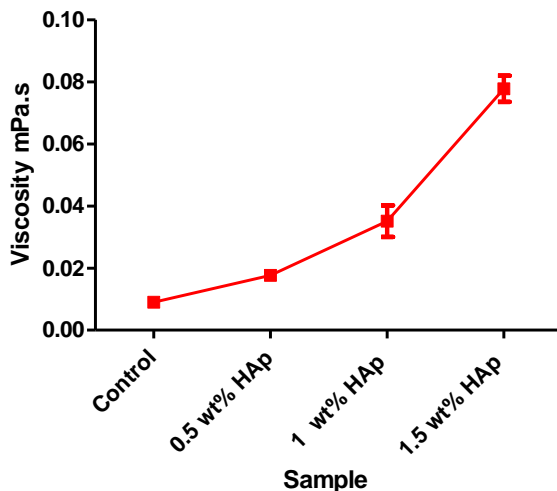


**Fig. 6.9** Viscosity changes of MAPTMS/TMOS sol measured with respect to different contents of HAp (mean +/- SD).

The control MAPTMS/TMOS sol showed viscosity value of  $0.009 \pm 0.0005$  mPa.s. For the HAp containing hybrids, the rheological behaviour was evaluated for fresh suspensions before dip-coating for different HAp powder loading (0.5-1.5 wt. %) relative to the amount of silane sol. As expected, an increase of the HAp content led to a noticeable increase in the sol viscosity ( $\eta$ ) and therefore these films are expected to give more thick films than the control one. The viscosity values are  $0.009 \pm 0.0005$ ,  $0.017 \pm 0.0007$ ,  $0.035 \pm 0.005$  and  $0.077 \pm 0.007$  mPa.s for control, 0.5 wt % HAp, 1 wt % HAp and 1.5 wt % HAp respectively (Table 6.4). The introduction of solid HAp particles in the sol reduced the flow ability of MAPTMS/TMOS sol and so resulted in more viscous sols.

Such increase in the viscosity is beneficial for the deposition of uniform and thicker films. Thus the increase of the sol viscosity is expected to lead to increase of the film thickness which could be beneficial for corrosion protection of the metal implant. The increase of viscosity could be also due to the enhancement of the polymerization of the sol upon addition of the HAp. These results agree will with the ATR-IR,  $^{29}\text{Si-NMR}$  and TGA results that showed enhancement of the cross-linking when HAp was added.

### 6.1.6 Film Thickness

For films which provide corrosion protection by barrier effect, the film thickness is an important parameter. The barrier properties afforded by the films reduce the diffusion of corrosive toxic species across it to the body. Thus, it is necessary to obtain the optimum thickness which allows a strong metal/film interface. Sometimes, if the thickness is higher than the optimum, the film can be easily detached from the metallic surface. Also an optimum viscosity and thickness provide a continuous and crack free sol-gel film onto the metallic surface.

The thickness of the films with and without HAp was measured using stylus profile-meter technique. Figure 6.10 shows the variation of coating thickness of the MAPTMS/TMOS/HAp coatings on Ti6Al4V as a function of the HAp content. The calculated values of films thickness can be seen in Table 6.4.

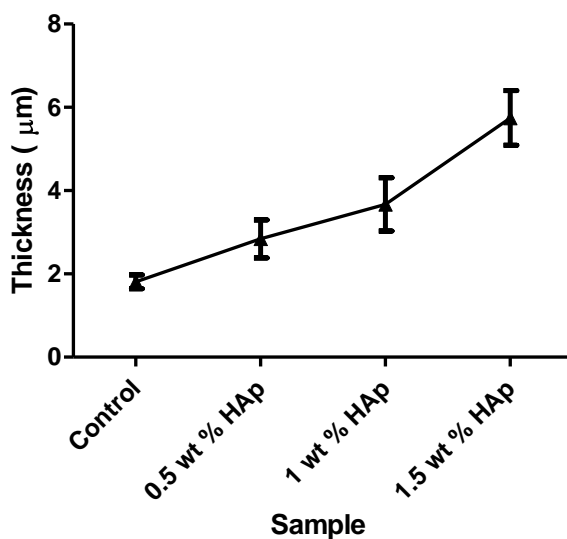


**Fig. 6.10** Thickness variation of MAPTMS/TMOS coatings deposited on Ti6Al4V at various HAp content.

This Table summarises the mean and standard deviation of data obtained for the coating thickness as a function of the HAp content. As expected, as a result of a viscosity increase, the coating thickness also increase as the content of HAp in the film does.

# Organic-inorganic hybrid sol-gel thin films modified with Hydroxyapatite particles

## 6.1.7 Wettability (Contact Angle)

Wettability of metallic biomaterial surfaces is one of the key factors that affect not only protein adsorption, cell attachment but also corrosion in living body. The degree of wetting is described by the contact angle  $\theta_c$ , the angle at which the liquid-gas interface meets the solid-liquid interface [247]. The surface hydrophilic or hydrophobic properties of the prepared hybrid films containing HAp were characterized by contact angle measurement. The contact angles of distilled water on the various coatings were measured by means of the sessile drop method. The overall mean contact angles, plus and minus the standard deviation for each of the films is shown in Table 6.4 and Figure 6.11.

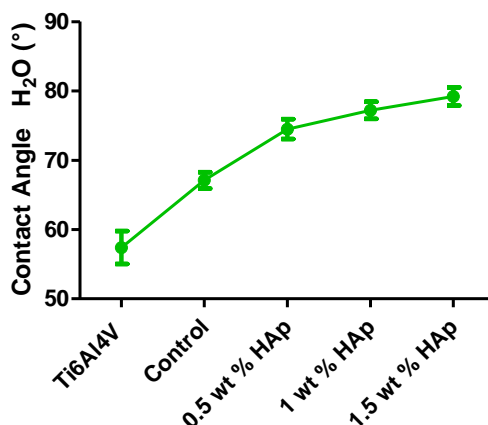


**Fig. 6.11** Variation of MAPTMS/TMOS coatings contact angle at various HAp content.

Table 6.4 represents the values of the contact angles ( $\theta$ ) and the respective standard deviations of the prepared hybrid films, using distilled water as a measuring liquid. The measured contact angles of the HAp containing films show wetting values lower than that of the control. The contact angles results for the prepared films are  $57.4 \pm 2.83$  for uncoated Ti6Al4V alloy,  $67.1 \pm 1.17^\circ$ , for MAPTMS/TMOS without HAp and,  $74.5 \pm 1.44^\circ$ ,  $77.2 \pm 1.23^\circ$  and  $79.2 \pm 1.30^\circ$  for MAPTMS/TMOS/HAp films contain 0.5, 1 and 1.5wt % HAp, respectively.

**Table 6.4** Viscosity of sol, contact angle and thickness of MAPTMS/TMOS-Ti6Al4V system in variation with the amount of HAp

<b>Surface</b>	<b>Contact Angle <math>\theta_{H_2O}</math> (°)</b>	<b>Viscosity mPa·s</b>	<b>Thickness (<math>\mu\text{m}</math>)</b>
<b>Ti6Al4V</b>	57.4± 2.83	-	-
<b>Control</b>	67.1 ± 1.17	0.009 ± 0.0005	1.80 ± 0.168
<b>0.5 wt % HAp</b>	74.5 ± 1.44	0.017 ± 0.0007	2.84± 0.457
<b>1 wt % HAp</b>	77.2 ± 1.23	0.035 ± 0.005	3.67 ± 0.639
<b>1.5 wt % HAp</b>	79.2 ± 1.30	0.077 ± 0.007	5.74± 0.655

All measurements carried out show that the contact angle values increase when the HAp content in the film increases. That is, the contact angles relations were as follows:

**MAPTMS/TMOS/HAp > MAPTMS/TMOS > uncoated Ti6Al4V**

This fact can be related to the higher organic content of the silane hybrid and with the increase of cross-linking of the siloxane network as HAp was added. These results are in agreement with the obtained <sup>29</sup>Si-NMR results. ATR results also agree with this fact since the ATR spectra showed that the Si-OH band located at 3100-3600 cm<sup>-1</sup> decreases in intensity in films with HAp. The surface must have optimum hydrophobicity to facilitate sufficient adsorption of the protein in its native form. The prepared film in this study are in range of 67.1 to 79.2°. These results indicate that the prepared films are in the optimum range of the contact angle 60-80°, which could be expected to lead to enhancement of the Ti6Al4V alloy surface as a metallic biomaterial<sup>[248]</sup>.

### **6.1.8 Scanning Electron Microscope (SEM/EDX)**

Figure 6.12 shows EDX and SEM micrograph of Ti6Al4V substrate before coating. The EDX analysis shows the presence of Ti, Al, and V from the alloy elements (Figure 6.12A). Figure 6.12B shows SEM micrograph of MAPTMS/TMOS coatings on Ti6Al4V, cured at 120°C for 2 hours. The SEM observations showed the formation of smooth, uniform, crack free and highly adherent protective film on the substrates that expect to lead to good corrosion resistance of Ti6Al4V alloys. The white points present on the surface could be condensed silica particles. The flexibility of such coating could be related to the high organic content of the coatings as confirmed by the EDX analysis of

## **Organic-inorganic hybrid sol-gel thin films modified with Hydroxyapatite particles**

---

the deposited film that shows the presence of carbon, oxygen, and silicon together with Ti, Al, from the substrate. The presence of the Ti, Al in the EDX reflects the micro-porous nature of the MAPTMS/TMOS film.

Figures 6.12C-6.12E show micrograph of Ti6Al4V substrate coated with MAPTMS/TMOS/HAp. The HAp particles seem to be well distributed all over the surface, even at high HAp content (1.5 wt %), as Figure 6.12E reveals. The EDX analysis of HAp containing films indicated the presence of calcium, phosphorus, oxygen, silicon and carbon. The almost disappearance of the Ti, Al in the EDX confirms the higher thickness of this film MAPTMS/TMOS-1.5wt% HAp when compared to the control (figure 6.12B). This is because at these EDX analysis conditions, the information obtained comes not only from the surface but also from an excited area which ranges from 1 to 1.5  $\mu\text{m}$  in deep. Thus, when the thickness of the analysed coating increases, the signal from the metallic substrate decrease.

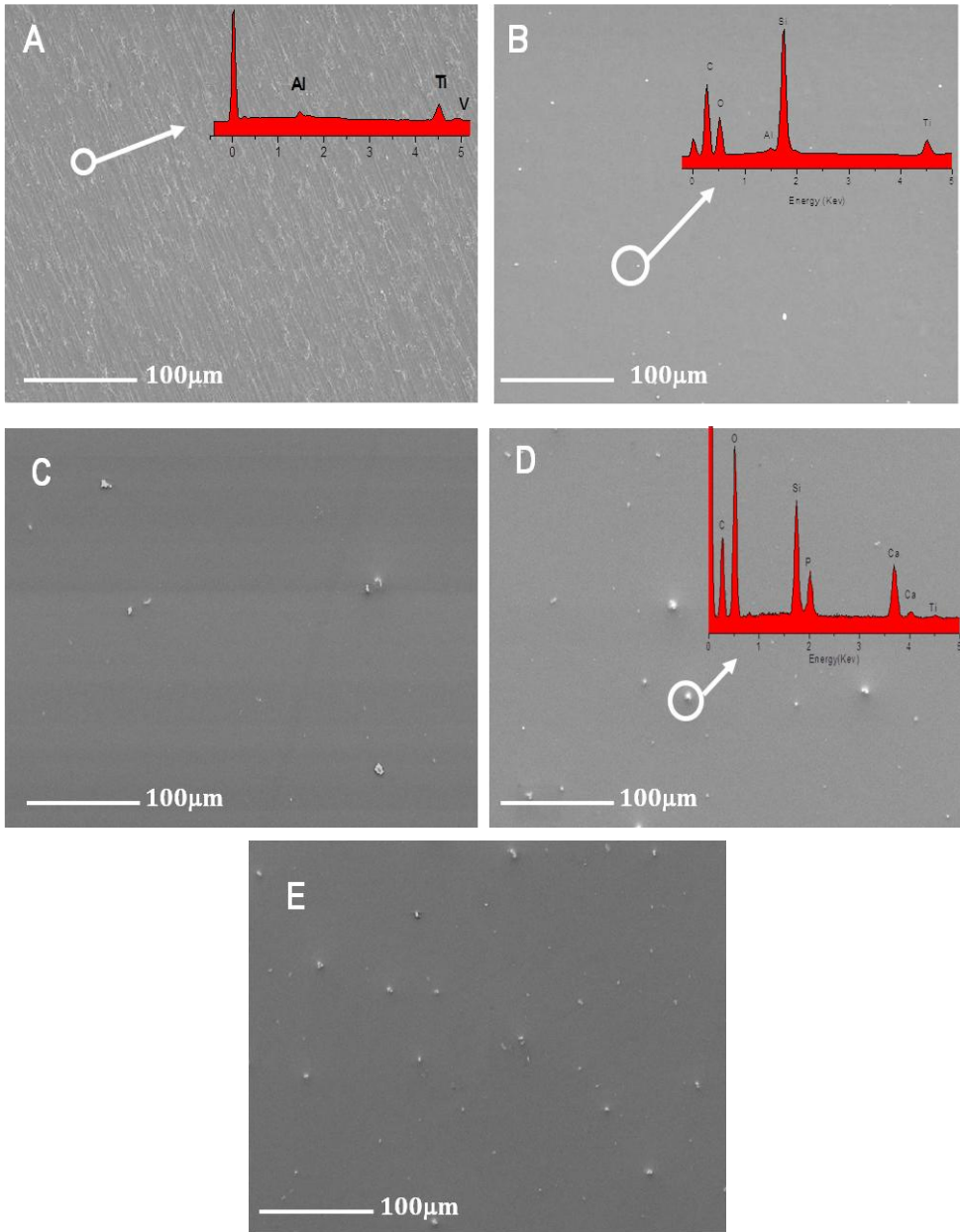


**Fig.6.12** SEM/EDX images for the prepared hybrid coatings deposited on Ti6Al4V substrates, un-coated (A) , and containing 0 wt % HAp (B); 0.5 wt % HAp (C); 1 wt % HAp (D) and, 1.5 wt % HAp (E) respectively.

# Organic-inorganic hybrid sol-gel thin films modified with Hydroxyapatite particles

## 6.1.9 Topography

The biocompatibility of the coated Ti6Al4V alloy which affects the cell and tissues response depends on the chemical composition of the surface and surface roughness [249-252]. Thus, the roughness of the film is critical factor which affect the implant fixation period and the fixation strength with the body tissue.

To obtain information about the roughness and topography, confocal microscopy was used to study the surface of the prepared hybrid films. The roughness parameters obtained are summarized in Table 6.5. These data have been obtained after deposition of a single layer of the hybrid films on the Ti6Al4V surfaces, in order to determine the effect of incorporation of HAp on the topography and roughness of the prepared films.

**Table 6.5** Surface roughness parameters for uncoated and hybrid coated/Ti6Al4V alloy

	<b>Ra (<math>\mu\text{m}</math>)</b>	<b>Rp (<math>\mu\text{m}</math>)</b>	<b>Rv (<math>\mu\text{m}</math>)</b>
<b>Ti6Al4V</b>	0.094 $\pm$ 0.018	0.467 $\pm$ 0.153	-0.361 $\pm$ 0.104
<b>Control</b>	0.162 $\pm$ 0.038	0.999 $\pm$ 0.666	-0.644 $\pm$ 0.198
<b>0.5% HAp</b>	0.163 $\pm$ 0.028	1.390 $\pm$ 0.911	-0.650 $\pm$ 0.155
<b>1% HAp</b>	0.165 $\pm$ 0.012	0.631 $\pm$ 0.150	-0.606 $\pm$ 0.103
<b>1.5% HAp</b>	0.275 $\pm$ 0.073	2.819 $\pm$ 0.957	-1.855 $\pm$ 0.606

3D images of the MAPTMS/TMOS and MAPTMS/TMOS/HAp coatings on Ti6Al4V substrates are shown in Figure 6.13. From the 3D image analysis of the MAPTMS/TMOS-Ti6Al4V system, Figure 6.13B, a Ra surface roughness value of 0.162  $\pm$  0.038  $\mu\text{m}$  was obtained. The slight increase of the Ra roughness value when compared with the uncoated alloy (0.094 $\pm$ 0.018  $\mu\text{m}$ ), Figure 6.13A, could be due to the evaporation of solvents during curing step at 120 $^{\circ}$ C/2h. This process may results in the formation of small peaks and valleys where the solvents evaporation took place.

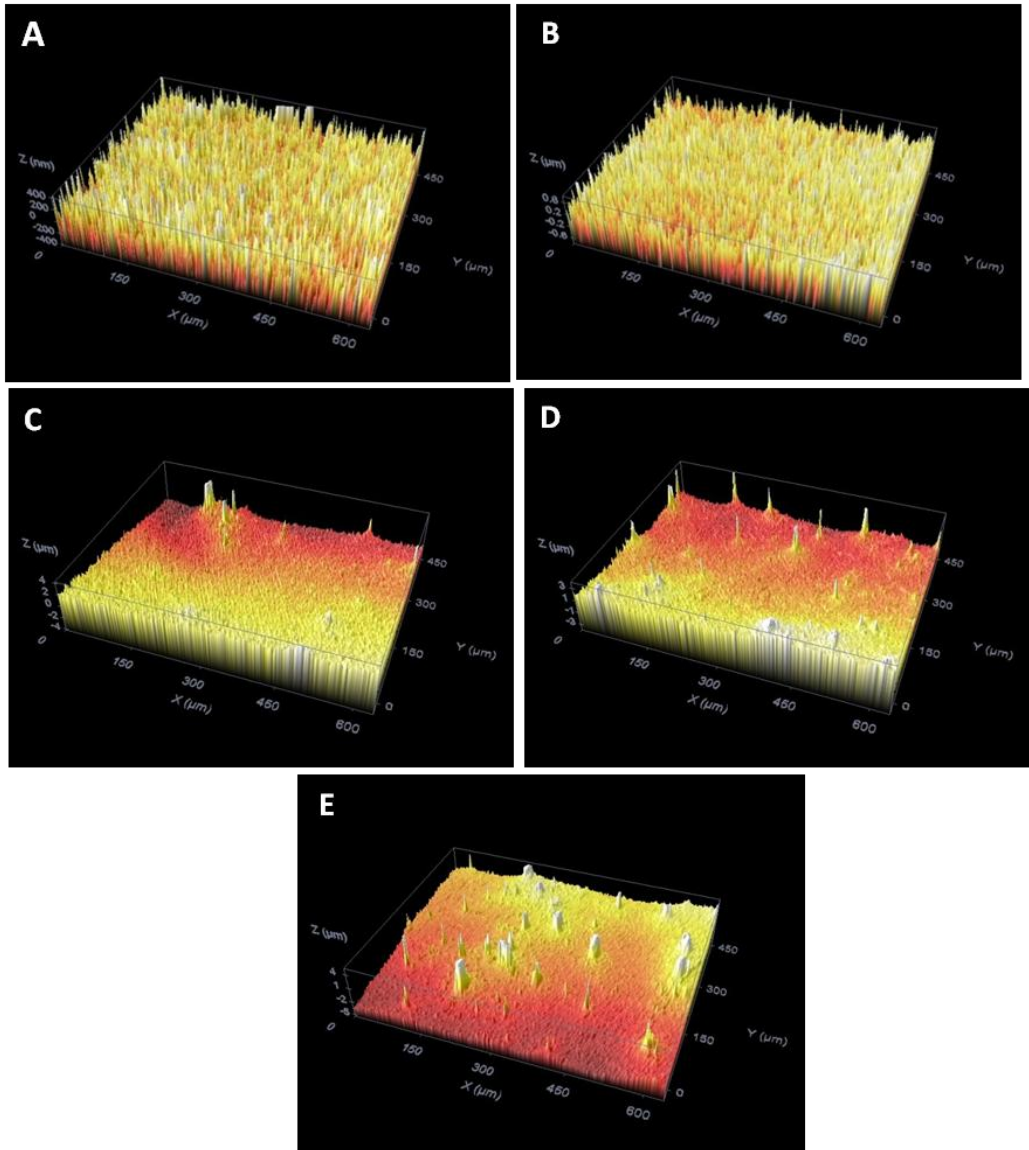


**Fig. 6.13** Confocal microscope three-dimensional images of the prepared hybrid coatings on Ti6Al4V and the uncoated Ti6Al4V surface.

# Organic-inorganic hybrid sol-gel thin films modified with Hydroxyapatite particles

---

Figures 6.13C-6.13E show topographic images taken on the MAPTMS/TMOS/HAp coatings on Ti6Al4V with 0.5, 1 and 1.5 wt % HAp respectively. These figures 6.13C-6.13E , shows some particles detectable at the surface which could be the HAp particles. The largest particles observed on the surface are likely to result from agglomeration of smaller particles in a heterogeneous manner in the sol-gel matrix. Further, there is a colour contrast in the image suggesting heterogeneity of the coating thickness.

The measured roughness values showed in Table 6.5 show that the increase of the HAp (0.5-1.5 wt %) content results in slight increase of the surface roughness. So it can be concluded that the surface roughness was affected and increased as the amount of HAp added. The roughness can be related to the sol viscosity, since higher sol viscosity corresponds to higher film roughness. From the obtained results, the roughness of the coating films increased owing to the high viscosity of the sols <sup>[253]</sup>. However, for the HAp containing films the formation of agglomerates could be an additional factor that leads to an increase of the surface roughness.

## 6.2 In-vitro bioactivity

The bioactivity of a material is accomplished through many steps. This includes formation of an amorphous Ca-P layer on the film surface and crystallization to carbonated HAp (c-HAp); then protein adsorption, cell proliferation and finally bone growth.

### 6.2.1 Protein adsorption

Based on Vroman effect, the adsorbed protein layer helps the biomaterial to be integrated in the biological system <sup>[45]</sup>. The more the protein adsorbed on an implant, the more cells can attach and proliferate <sup>[46,47]</sup>. For that, the protein adsorption is responsible for the biocompatibility of biomaterials. The study of protein adsorption to a material can be performed with a single protein, typically in a buffer solution <sup>[254,255]</sup>. Single proteins in buffer can be used to model fundamental aspects of protein adsorption or to study biological reactions of implant to one protein.

The interaction of prepared hybrid films on Ti6Al4V with single protein, fibrinogen in phosphate buffer saline (PBS), was studied to understand the behaviour of the prepared films with physiological environments. There are several proteins in human blood plasma but, we chose fibrinogen which is used as a standard to evaluate the biocompatibility of biomaterial <sup>[256]</sup>.

To evaluate the potential use of our materials for biomedical implants, we examined protein adsorption on the prepared surfaces. The main objective of this study is to evaluate adsorption processes as well as the amount of protein adsorbed on the different hybrid films/Ti6Al4V alloy using a phosphate buffer saline (PBS) with fibrinogen using the quantitative Bradford Protein assay.

### 6.2.1.1 Amounts of adsorbed fibrinogen

The chemical composition and surface charge of biomaterial surfaces strongly affect the protein adsorption behaviour <sup>[47]</sup>.

This is perhaps through interaction between the functional groups on the film surface and those of the protein itself. After immersion of the coated surfaces in 1 mg/ml fibrinogen solution in PBS, adsorption was allowed to proceed in an incubator for 1 h at 37°C

Absorbance was measured by reading the absorption of the aliquot solution, after removing the immersed samples, at a wavelength of 595 nm. Figure 6.14 shows the Bradford standard calibration curve of different protein concentration 0.2-1 mg/ml read at 595 nm. Based on this curve the amount of the adsorbed protein could be extracted by comparing the absorption values of the aliquot solution Figure 6.15. The measured absorbance values,  $0.57 \pm 0.004$ ,  $0.55 \pm 0.004$ ,  $0.51 \pm 0.000$ , and  $0.49 \pm 0.003$  for the aliquot solution after removing the uncoated alloy, control, and HAp containing films (0.5-1.5 wt %) respectively with the absorption values in the calibration curve.

# Organic-inorganic hybrid sol-gel thin films modified with Hydroxyapatite particles

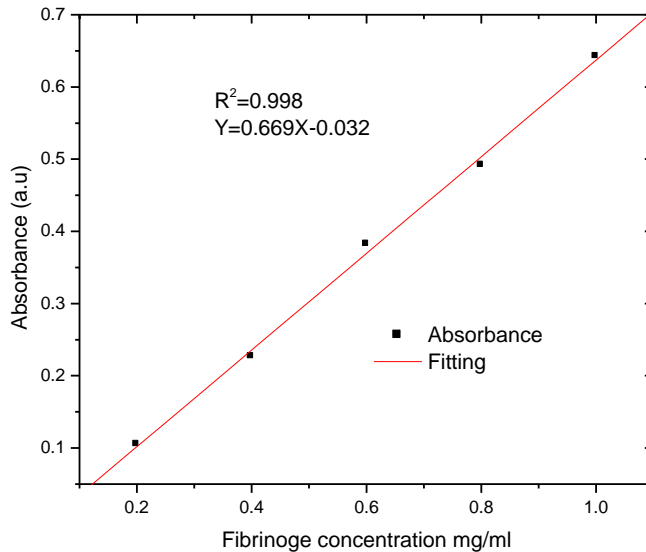


**Fig.6.14.** Bradford standard calibration curve of different protein concentration 0.2-1 mg/ml read at 595 nm

Figure 6.16 shows the calculated amounts of adsorbed fibrinogen onto prepared hybrid films were  $7.469 \pm 0.59$  and  $10.06 \pm 0.59 \mu\text{g}/\text{cm}^2$  for uncoated Ti6Al4V and control samples and  $15.49 \pm 0.07$  and  $17.62 \pm 0.40 \mu\text{g}/\text{cm}^2$  for 0.5 and 1.5 wt % HAp respectively. Thus the adsorbed fibrinogen amount is less on the un-coated sample and on the control film without HAp.

According to the popularly accepted understanding, electrostatic interactions are very important for protein adsorption [257].

The increase in the fibrinogen adhesion on the surface of MAPTMS/TMOS/HAp coatings on Ti6Al4V was likely due to the  $\alpha$ -C domains of fibrinogen, charged positively at pH 7.4. It has been reported that the protein adsorption on HAp is electrostatic in nature and two possible adsorption sites are involved and act as adsorption sites [257]. Thus in the HAp exist two sites where proteins bind to apatite. These two sites, positively charged surfaces (Ca sites,  $\text{Ca}^{2+}$ ) on HAp which can absorb negatively charged

proteins and negative charged sites (P sites,  $\text{PO}_4^{3-}$ ) which can absorb positively charged proteins [257].

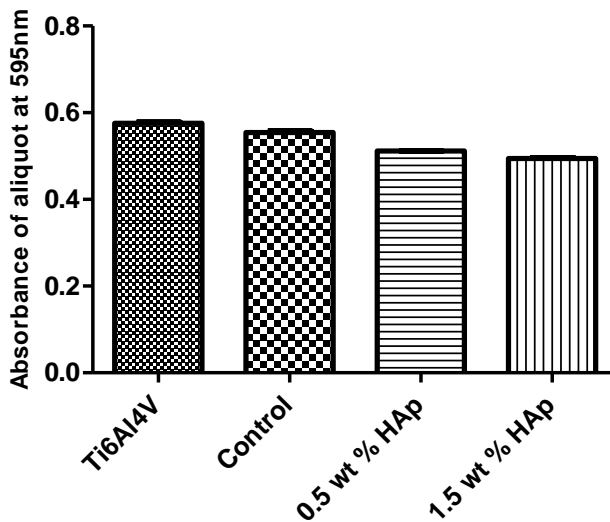


Fig.6.15 Absorbance read at 595 nm of aliquot solution after removing the surfaces .

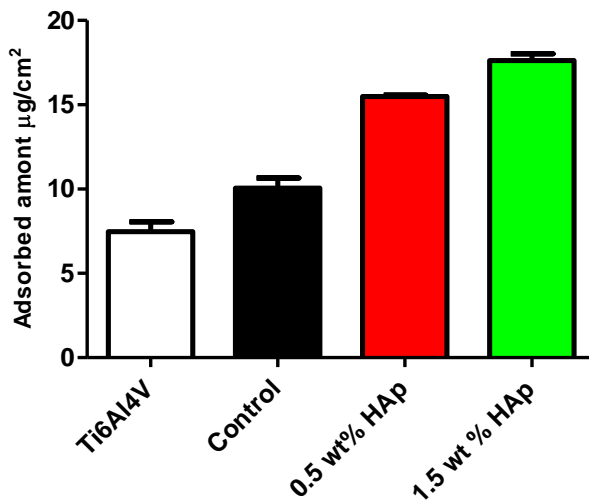


Fig.6.16 Amount of fibrinogen adsorbed on the prepared hybrid films

# Organic-inorganic hybrid sol-gel thin films modified with Hydroxyapatite particles

---

Because the,  $\text{Ca}^{2+}$  ions are positively charged, for that the fibrinogen could only bound to negative sites of the HAp surface,  $\text{PO}_4^{3-}$  (surface dominated by negatively charged oxygen (P-bound) by electrostatic attractive forces. For that it can conclude that the existence of HAp in the deposited films helps such surfaces to adsorb more fibrinogen amounts relative to those without HAp. Other reason could be the hydrophobicity of these surfaces relative to the other coatings.

The reason for the less adsorption of fibrinogen on the surface of the un-coated Ti6Al4V and control samples could be the wettability. Thus, the surface wettability also affected the adsorption of protein. This result is in agreement with Sigal et al and C. Perry et al who concluded that hydrophilic surfaces adsorb less protein <sup>[258,259]</sup>.

## 6.2.2 Osteoblast – film interactions

This part aims to study the effect of surface chemistry on attachment and proliferation of normal human osteoblast cells on the hybrid films prepared by sol-gel method. The initial attachment of osteoblast cells to surface of implants is fundamental for ensuring an early and successful osteointegration *in-vivo*. Enhanced cell responses to implant material are expected to benefit direct bone implant contact.

### 6.2.2.1 Osteoblast cytotoxicity/Viability

Measuring the interaction of implants with living cells is vital in the design and selection of surface modifications for bone implants. Thus cell growth and attachment are fundamental processes of wound healing and the integration of a biomaterial with tissue <sup>[260]</sup>. As such the influence of the different coatings on normal human osteoblast (NHOst) viability was evaluated *in-vitro* using the neutral red uptake assay <sup>[261-264]</sup>. Cell viability was determined by using neutral red uptake assay which based on the fact that the dye taken up by only the living cells. This assay could also give information about the trend of cell proliferation of normal human osteoblasts on the coated Ti6Al4V alloys. In a parallel experiment, the growth of the osteoblast on the coated surfaces was characterized by immunofluorescence staining of cell cytoskeleton.

Cell viability as assessed by the neutral red assay is shown in Figure 6.17. This Figure shows the amount of vital dye taken up by the cells as a measure of absorbance at 540 nm after 7 days of NHOst incubation on the bare Ti6Al4V, MAPTMS/TMOS and MAPTMS/TMOS/HAp coatings on Ti6Al4V.

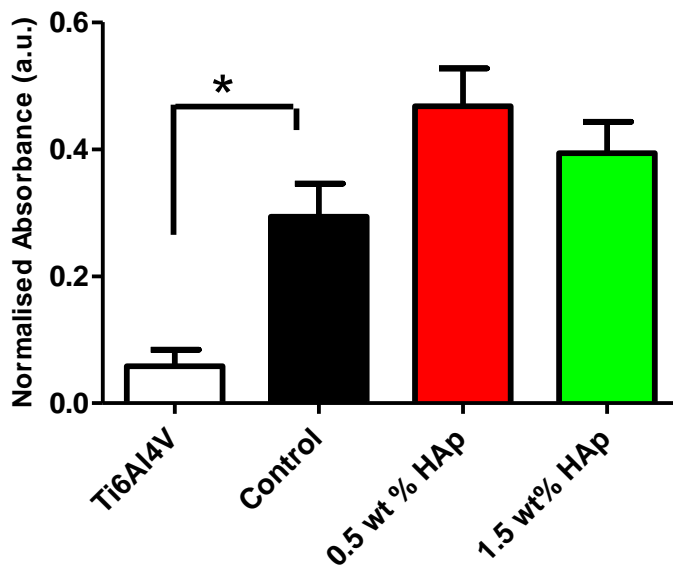


**Fig. 6.17** Neutral red proliferation/cytotoxicity assay for NHOst cultured on Ti6Al4V, MAPTMS/TMOS-Ti6Al4V and MAPTMS/TMOS/HAp-Ti6Al4V over a seven day period.

These results showed that the trend for NHOst cell proliferation was higher on MAPTMS/TMOS/HAp-Ti6Al4V with 0.5 wt % HAp, MAPTMS/TMOS/HAp-Ti6Al4V with 1.5 wt % HAp than on MAPTMS/TMOS-Ti6Al4V and uncoated Ti6Al4V systems. Proliferation of NHOst was slowest on the unmodified Ti6Al4V surface. All other substrates showed more growth.

The presence of growing cells on the surface of the un-coated alloy could be due to the ability of such alloy to form -OH group adsorbed on the oxide layer formed at ambient. Thus such -OH groups could be responsible for the little biocompatibility and growing of some cells on the uncoated alloy surface <sup>[265,266]</sup>.

The toxicity of the un-coated alloy seems to be higher with respect to the coated surfaces which could be the ion dissolution which has been demonstrated to adversely affect the healing of bone <sup>[267-269]</sup>. The Ti6Al4V alloy is generally considered as a

## Organic-inorganic hybrid sol-gel thin films modified with Hydroxyapatite particles

---

'standard material' for orthopaedic and dental implant applications. On the other hand, vanadium is cytotoxic and can initiate adverse tissue reactions which lead to the observed relatively higher cell cytotoxicity<sup>[270]</sup>.

In comparison to uncoated alloy and control samples, the MAPTMS/TMOS/HAp coated surfaces showed greater cell proliferation, as may be expected given its natural abundance in bone matrix, but results did not reach statistical significance. Thus, the level of viability of NH0st on the hybrid films containing HAp was not significantly higher than the other coated surfaces without HAp coated Ti6Al4V alloy.

Our results suggested that, modifying the silane with less than 1.5 wt % of bioactive HAp is enough to improve its bioactivity. The improvement in terms of the cell viability on the coated alloys in comparison to the bare metal may be due to the coating act as a physical barrier which inhibits the release of toxic metal ions into the growth medium. Low concentrations of these ions are considered toxic and a causative factor for cell death.<sup>[60]</sup> The less toxicity in the case of coated alloys confirmed the low metal ion release suggestion which is the consequence of the more dense films obtained upon addition of HAp as has been confirmed by <sup>29</sup>Si-NMR.

### 6.2.2.2 Osteoblasts adhesion

Osteoblast adhesion is important step in the acceptance of artificial implants by living body. The adhesion could be affected by the composition and the surface geometry. The adhesion of osteoblasts to the implant surface is a prerequisite for successful osteo-integration of the implant *in-vivo*. Cell adhesion can be divided into three sequential events: (a) cell attachment, (b) cell spreading and, (c) formation of focal adhesions and actin stress fibers<sup>[271]</sup>.

Focal contacts are formed at the leading edge of a migrating cell and often mature into focal adhesions, being the closest contacts between cells and implant surface. Vinculin is one of several proteins involved in the formation of a focal contact<sup>[271]</sup>. The ability of an adherent cell to attach and spread on a substrate can in part be assessed by looking at the morphology of the cell and its cytoskeleton.

In the attachment stage, osteoblast filopodia (smaller hair-like protrusions) explored, sense and extend over significant distances to find areas appropriate for attachment

on the substrate surface [272]. This first phase of cell–material interaction will influence the cells capacity to proliferate and differentiate [273]. The molecules responsible for these processes involve adhesion receptors such as integrins, the actin cytoskeleton and cytoskeletal associated proteins like vinculin.

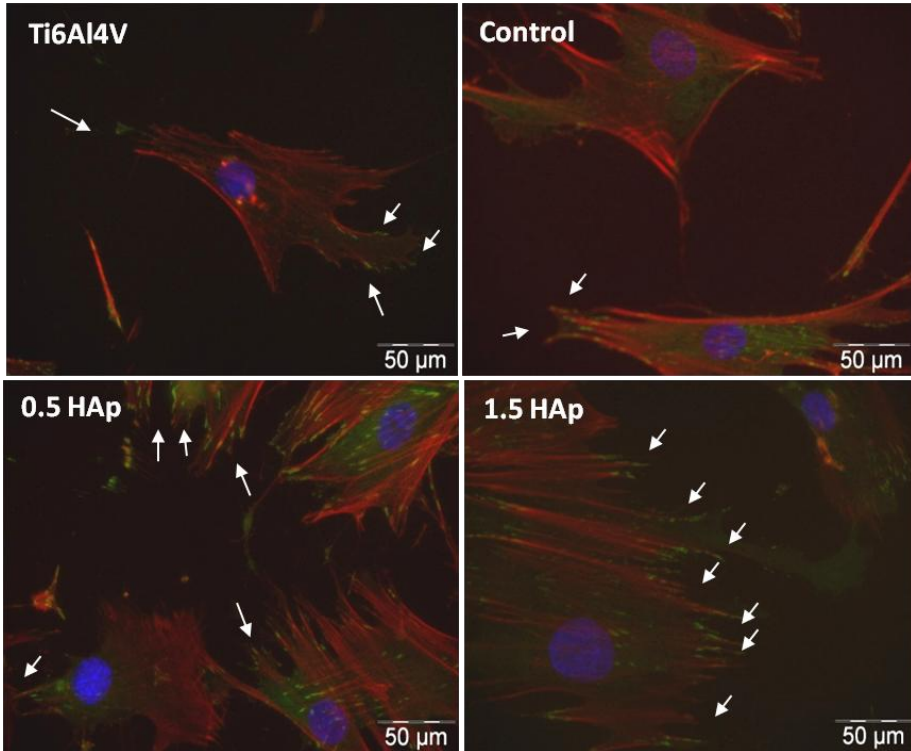


**Fig. 6.18** Fluorescence graphs of OB-cells growing on un-coated Ti6Al4V and coated surfaces. Vinculin: green; actin: red and, nuclei:blue respectively.

To further understand the nature of the interactions of osteoblasts with different substrates, the expression level of vinculin and the organization of actin filaments were determined by immunofluorescence technique. This technique is helpful for detecting the cell attachment and spreading driving force (integrins mediated formation of focal contacts of the cells with the surface and a dynamic rearrangement of the actin cytoskeleton). Immunofluorescence was conducted to observe these aspects of the osteoblasts cultured on the different substrates. Representative images are shown in Figure 6.18.

## Organic-inorganic hybrid sol-gel thin films modified with Hydroxyapatite particles

---

There were only a few cells observable under the fluorescence microscope on the uncoated surface. This was most likely to be due to the ion dissolution from the alloy in the culture medium which prevented cell attachment. The discouragement of cell adhesion on the surface was presumably due to the hydrophilic nature of the uncoated preventing protein adsorption. Ti6Al4V corrosion during cell culture could also be a contributing factor.

There were more cells on HAp containing films compared to uncoated substrate or MAPTMS/TMOS coatings on Ti6Al4V. In this respect the immunofluorescence images are in general agree with the neutral red uptake assay performed. In addition it was observed that osteoblasts on all the coated substrates showed a more substantial network of f-actin stress fibres than cells growing on the un-modified alloy.

### 6.2.3 Immersion in SBF

Surface bioactivity tests of the MAPTMS/TMOS/HAp hybrid coatings was assayed by soaking the coating/Ti6Al4V alloy in simulated body fluids (SBF) looking for precipitation of biomimetic HAp layers by using SEM/EDX.

Figure 6.19 shows SEM/EDX results of samples MAPTMS/TMOS and MAPTMS/TMOS/1.5HAp deposited on the surface of Ti6Al4V alloy, after 1 day of immersion in SBF solution. By comparing this SEM images with those obtained before the immersion tests in SBF (Figure 6.12), it can be observed that in both cases (control and HAp containing coatings) the surface is covered with precipitates from the SBF.

The EDX analysis of the MAPTMS/TMOS-Ti6Al4V systems shows the presence of Ca and P on these precipitates. The EDX also exhibited peaks corresponding to K, Na, Mg and Cl, which are due to the presence of those elements in the SBF. This behaviour is a proof of the efficiency of the prepared silane hybrid coatings for bone-like apatite precipitation.

After immersion of SBF, the siloxane film could be re-hydrolyzed, leading to the formation of Si-OH groups at the metal-solution interface. These silanol groups provide favourable nucleating sites for formation of the apatite; attract the calcium

and phosphate ions from the body fluid through electrostatic interactions and forms bone-like apatite layer on the surface [96, 97].

The reason why the bone-like apatite has been formed on the surface could be explained as follow; The SBF contains both phosphate and calcium ions. The high concentration of both calcium and phosphate ions in SBF, as well as the presence of silanol groups on the films most outer surface favours the heterogeneous nucleation of apatite on the surface of the studied hybrid films.

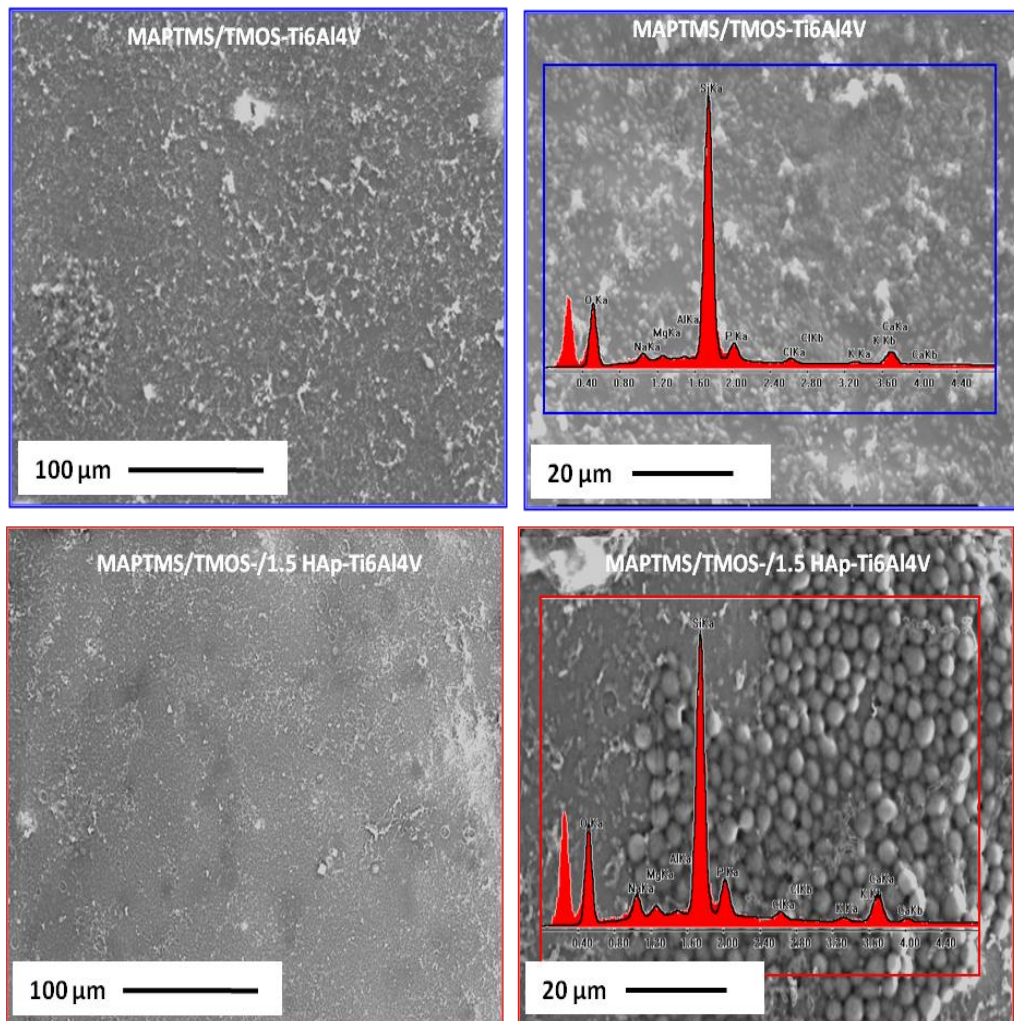


**Fig.6.19** SEM/EDX images for MAPTMS/TMOS and MAPTMS/TMOS/1.5 HAp.

## **Organic-inorganic hybrid sol-gel thin films modified with Hydroxyapatite particles**

---

Once apatite nuclei are formed, crystals of apatite grow spontaneously by consuming calcium and phosphate ions from the surrounding body fluid and form a layer of bone-like apatite. Then, with the immersion time, the apatite layer fully covers the surface. The modification of the MAPTMS/TMOS coatings with dispersions of HAp particles enhance the precipitation of bone-like apatite, as can be seen in (Figure 6.19). Thus on the surface of MAPTMS/TMOS/1.5HAp-Ti6Al4V system a well-developed bone-like apatite has been observed by SEM. The analysis of these precipitates by EDX also shows the presence of Ca and P. Thus the dispersions of HAp particles in the coating have behaved as preferential nucleation points for the precipitation of bone-like apatite from the SBF.

### **6.3 In vitro corrosion protection behaviour of the organic-inorganic hybrid sol-gel thin films modified with hydroxyapatite particles**

In vitro corrosion and protection studies of the MAPTMS/TMOS/HAp-Ti6Al4V system immersed in Kokubo's simulated body fluid (SBF) have been carried out by using electrochemical impedance measurements. Figure 6.20 shows impedance plots of three identical samples of a MAPTMS/TMOS/HAp-Ti6Al4V system after 24 hours of immersion in SBF. This system was formulated with 1wt % of HAp powder per 20 ml of 4:1 MAPTMS/TMOS sol. As we can see in the figure, the reproducibility of the experimental data obtained was quite acceptable.

In Figures 6.20 A and 6.20 B the impedance data have been represented in the complex plane as Nyquist plots, using two different scales. Figure 6.20A shows the Nyquist plots for the wide frequencies range. Figure 6.20 B shows a detail of the high frequency arcs. In Figure 6.20 C the variations of the logarithm of the impedance module and phase angle both against the frequency logarithm are displayed in format of Bode plots.

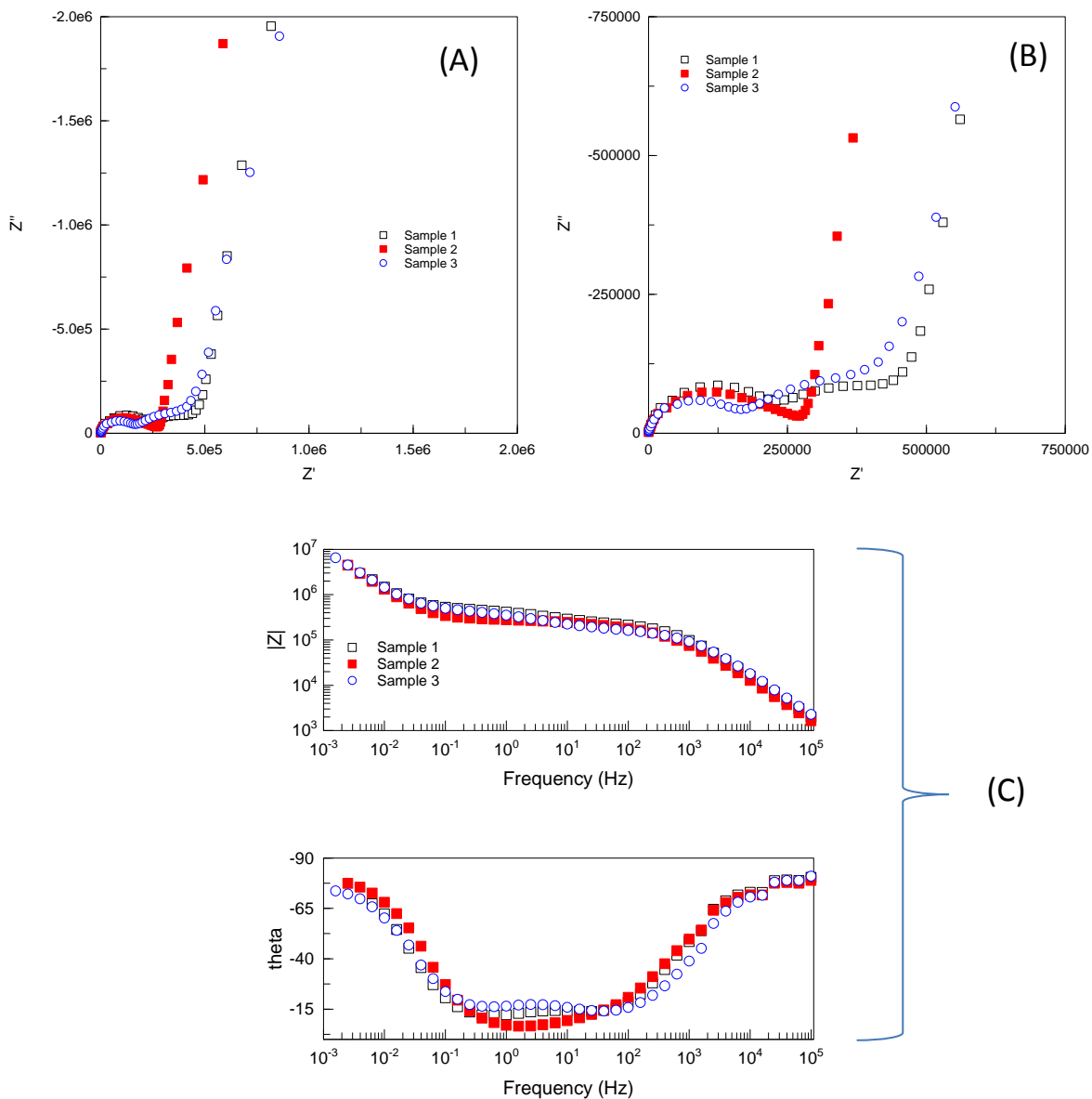


**Fig. 6.20** Nyquist plots, represented in two different scales [(A) and (B)] and, Bode plots (C) obtained for three identical samples of MAPTMS/TMOS/HAp system deposited on Ti6Al4V surfaces for a coating with a contain of 1 wt.% HAp powder. Electrolyte: SBF. Immersion Time: 1day.

## Organic-inorganic hybrid sol-gel thin films modified with Hydroxyapatite particles

Fig.6.21 show the experimental impedance plots and fit results obtained for one MAPTMS/TMOS/HAp-Ti6Al4V sample with an HAp content of 1 wt % per 20 ml MAPTMS/TMOS sol after 1 day of immersion in SBF. The fitting results were generated applying the equivalent circuit shown in figure 6.21 and using the fitting complex nonlinear least-squares (CNLS) techniques of the ZView software. The obtained data is shown in Table 6.6.

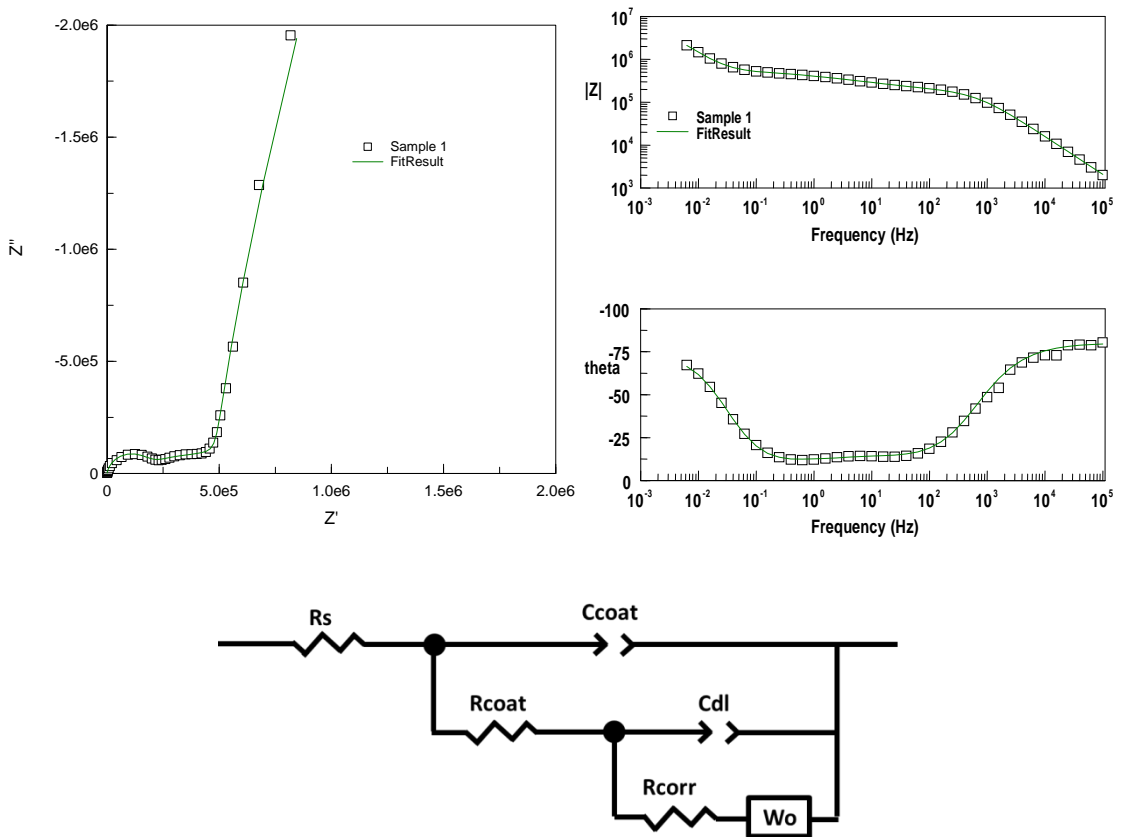


**Fig.6.21** Experimental impedance plots and fit results obtained for one MAPTMS/TMOS/HAp-Ti6Al4V sample. Hap content 1 wt % of 20 ml MAPTMS/TMOS sol. Immersion time in SBF: 1day.

**Table 6.6** . Values calculated with the Zview software for each one of the elements of the equivalent circuit to analyze the MAPTMS/TMOS/HAP-Ti6Al4V system. 1 wt % HAP/ silane content. Immersion Time SBF: 1day.

<b>Fit Results for sample 1</b>				
<u>Element</u>	<u>Freedom</u>	<u>Value</u>	<u>Error</u>	<u>Error %</u>
<b>Rs</b>	Free(±)	4.778	44.259	926.31
<b>Ccoat-T</b>		3.2576E-09	1.7995E-10	5.524
<b>Ccoat-P</b>		0.89135	0.0049198	0.55195
<b>Rcoat</b>		1.9095E05	6089.5	3.1891
<b>Cdl-T</b>	Free(±)	6.0991E-07	1.1093E-07	18.188
<b>Cdl-P</b>	Free(±)	0.55089	0.040994	7.4414
<b>Rcorr</b>	Free(±)	2.7073E05	36958	13.651
<b>Wo1-R</b>	Free(±)	2.362E05	60381	25.564
<b>Wo1-T</b>	Free(±)	2.081	0.61397	29.504
<b>Wo1-P</b>	Free(±)	0.47121	0.012012	2.5492
Chi-squared:			0.0016699	
Weighted sum of squares:			0.10687	

Good fitting results were obtained applying the equivalent circuit of Figure 6.21 to the values measured in the wide frequency range. This equivalent circuit proposed is mostly similar to those previously discussed in chapter 4. The only difference is that in this case, a Warburg diffusion element is incorporated into the equivalent circuit of figure 1.16A, in series with the  $R_{corr}$  element.  $W_o$  represents the finite length Warburg diffusion. It has been incorporated for the fitting of these HAp coating systems since in the response at LF (low frequencies) is more evident than in the other systems the presence of a diffusion component. In this research, however, rather than concentrating on behavior at LF, attention will be paid on the elements of the equivalent circuit which are directly related to the coating and the metal/coating interface. The physical meaning of these electrical elements was discussed in chapter 4 (Figures 4.16A and 4.16B). The chi-square values provide an estimation of the fitting quality. The chi-square values were lower than  $10^{-3}$ , proving the fitting quality for the

## Organic-inorganic hybrid sol-gel thin films modified with Hydroxyapatite particles

---

tested MAPTMS/TMOS/HAp-Ti6Al4V sample. The error values obtained for the calculated values of the electrical elements of this equivalent circuit are also low for all the tested samples.

Figure 6.22 shows, as an example, the evolution of impedance plots (Nyquist and Bode representations) with the immersion time in SBF of a MAPTMS/TMOS/HAp-Ti6Al4V sample whose sol-gel coating contains 1 wt % HAp per 20 ml of the MAPTMS/TMOS silane mixture.

The Nyquist plots have been represented at different magnifications, increasing the zoom of the HF region from the upper left plot to the lower right plot, to study in detail the evolution of the High-Frequency Arcs (HFAs).

Through a qualitative analysis of the impedance diagrams, valuable information about the intrinsic electrical properties of the coating and the protective properties of coatings in aqueous media can be obtained. Thus, from figure 6.22 information concerning the evolution of the coating properties with the immersion time can be obtained. Although the modulus of  $Z$  at lowest frequencies seems to be constant with the immersion time (see figure 6.22 C) the variation of the phase angle this the Bode plot, as well as, the variation in the shape of the Nyquist diagrams (figure 6.22 A, B) indicates that there is a evolution of the barrier properties afforded for this coating.

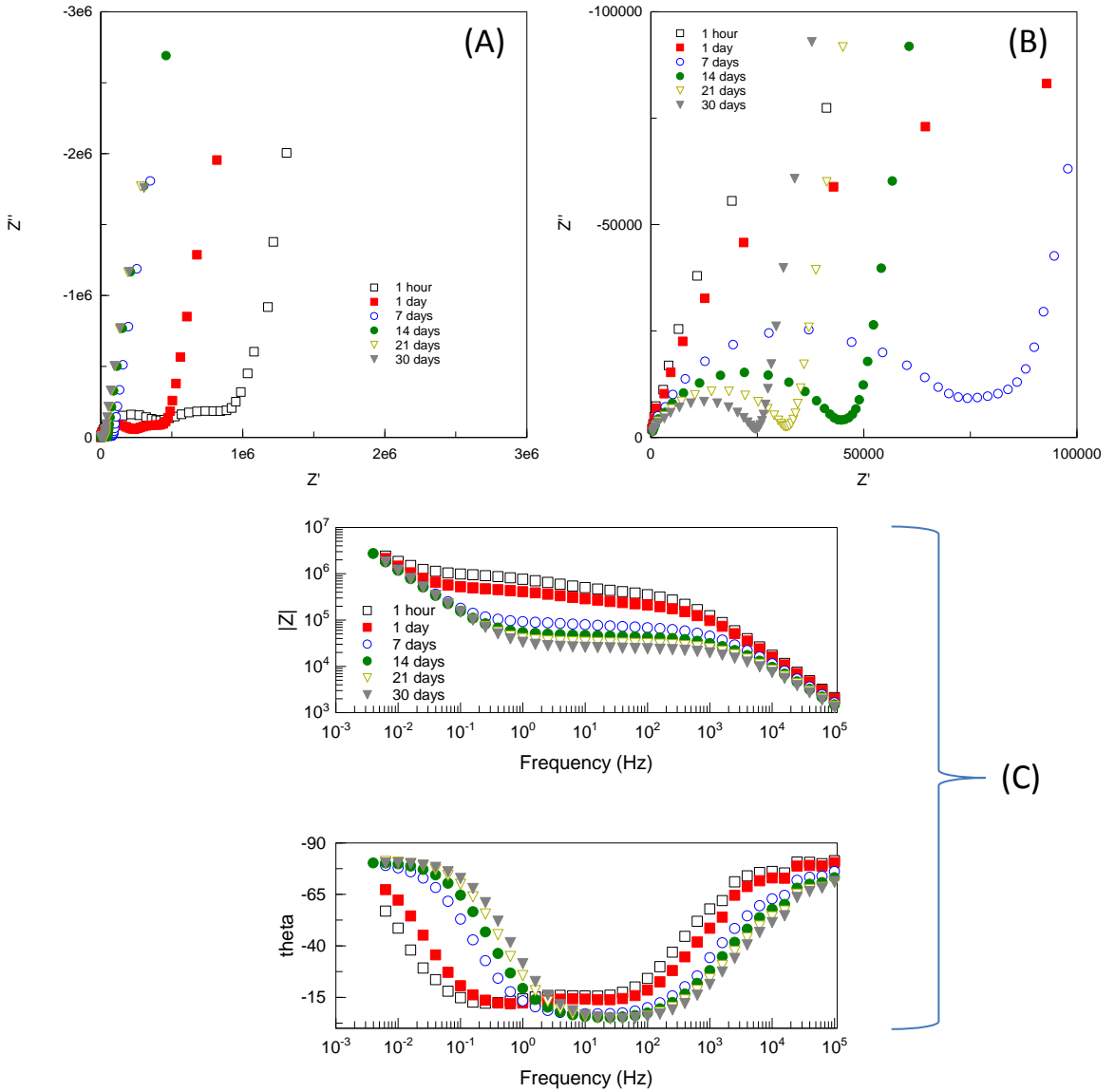


**Fig.6.22** Evolution with the immersion time of the Nyquist plots, represented in two different scales[(A) and (B)] and the Bode plots (C) obtained for the MPTMS/TMOS/HAp system deposited on Ti6Al4V surfaces for a coating with a contain of 1 wt.% HAp powder.

## Organic-inorganic hybrid sol-gel thin films modified with Hydroxyapatite particles

---

Figure 6.22 B showed that the diameter of the arc in the high frequency region (HF) of Nyquist diagrams was gradually decreasing with the immersion time in SBF. The chord located between the two cut-off points of this arc with the real axis of the complex plane coincides with the values of the ionic resistance ( $R_i$ ) of the electrolyte inside the pores of the coating. The decrease of  $R_i$  with the immersion time indicates that the coating slowly loses its barrier properties. The evolution with time of the  $R_{\text{coat}}$  and  $C_{\text{coat}}$  values calculated from the HFAs confirm this interpretation.

It is also interesting to note the changes that take place in the corresponding Bode plot (Figure 6.22C), which show a continuous slow decrease of the impedance modulus especially at medium frequencies. This behaviour is associated with a slow decrease of the corrosion resistance of the Ti6Al4V at the base of the pores at the metal/coating interface within the immersion time in the SBF solution. Finally, the diffusion process of electroactive species coming from the SBF solution going through the coating to the metal/coating interface and viceversa is more evident with the immersion time and it is reflected at lowest frequencies.

The quantitative analysis of these results has been done by ZView software. This commercial program is based on theoretical simulations with electrical equivalent circuits, fitting techniques and complex nonlinear least-squares (CNLS) methods. The equivalent circuit proposed in figure 6.21 displays accurate fitting plots for the HAP modified organic-inorganic hybrid coating/ Ti6Al4V system, as previously showed in table 6.6.

The evolution with the immersion time of the equivalent circuit parameters for the coating containing 1 wt % of HAp are shown in figure 6.23.

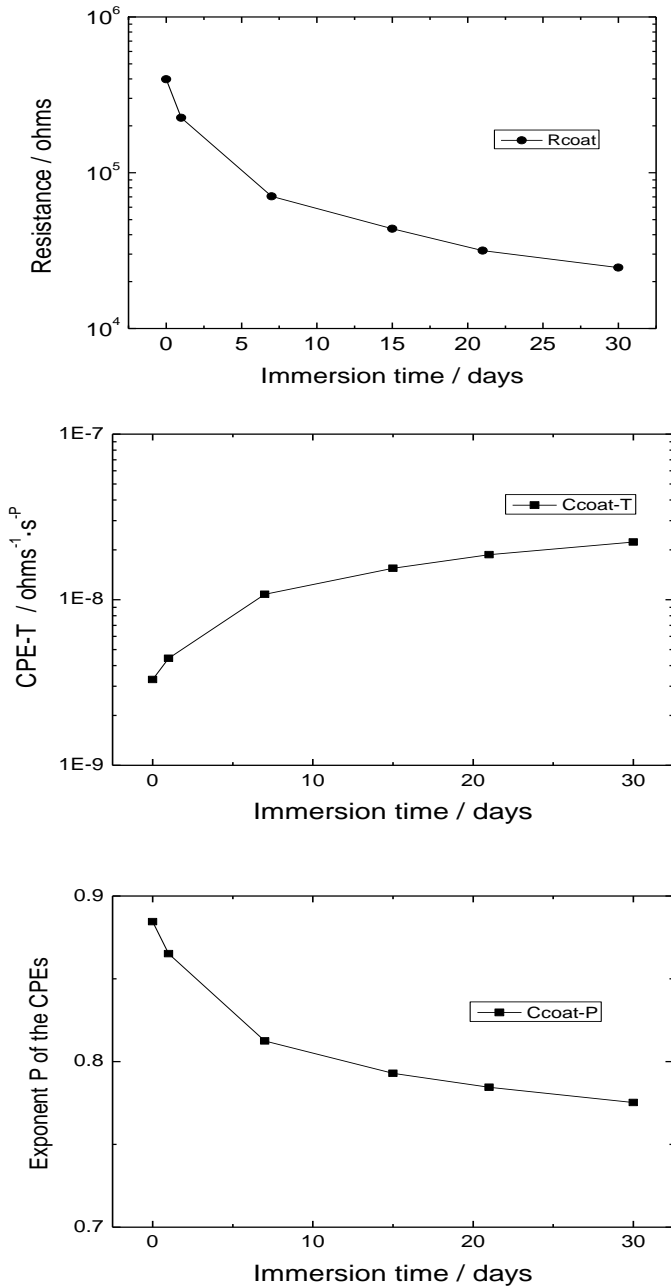


Fig.6.23 Evolution of the equivalent circuit parameters associated to the HFA with the immersion time in Kokubo solution of the MAPTMS/TMOS/HAp-Ti6Al4V system for a coating with a contain of 1 wt.% HAp powder.

## Organic-inorganic hybrid sol-gel thin films modified with Hydroxyapatite particles

---

Figure 6.23 shows: i) a continuous decrease of the ionic resistance of the coating pores ( $R_{\text{coat}}$ ) values with the immersion time in SBF, and ii) a continuous increase of the coating capacitance, correlated with the changes of CPE-T values and CPE-P. This behaviour is typically associated with the loss of the barrier properties and the increase of the water uptake in the coating with the immersion time.

To study the influence of the content (wt %) on the coatings impedance response, the behaviour of the coatings after one day of exposure has been compared. After the study of the evolution of the coatings with the immersion time, it is showed that one day of exposure is enough time to evaluate the barrier properties of the coatings without the interference of other processes like charge transfer, mass transport, etc. These processes become more important with the immersion time and thus can interact in higher degree with the proper evaluation of the barrier properties of the different coatings.

Figure 6.24 show the Nyquist plots, represented in two different scales [(A) and (B)] and, Bode plots (C) obtained for an uncoated Ti6Al4V sample and Ti6Al4V samples coated with MAPTMS/TMOS/HAp films containing different HAp powder percentages: 0 wt.% (blank sample), 0.5 wt.%, 1 wt.% and 1.5 wt.% respectively, after 1 day of immersion test in SBF.

Figure 6.24 C shows the same impedance data in Bode form. By comparing the impedance response obtained for the sol-gel coatings containing HAp in their organic-inorganic network with the impedance response of the blank samples (without HAp) it can be observed that the High-Frequency Arcs (HFAs) of the HAp free coatings intercept the real axis of Nyquist plots at lower  $Z'$  impedance values than the HFA obtained for the coatings containing HAp Figure 6.24 A and 6.24 B.

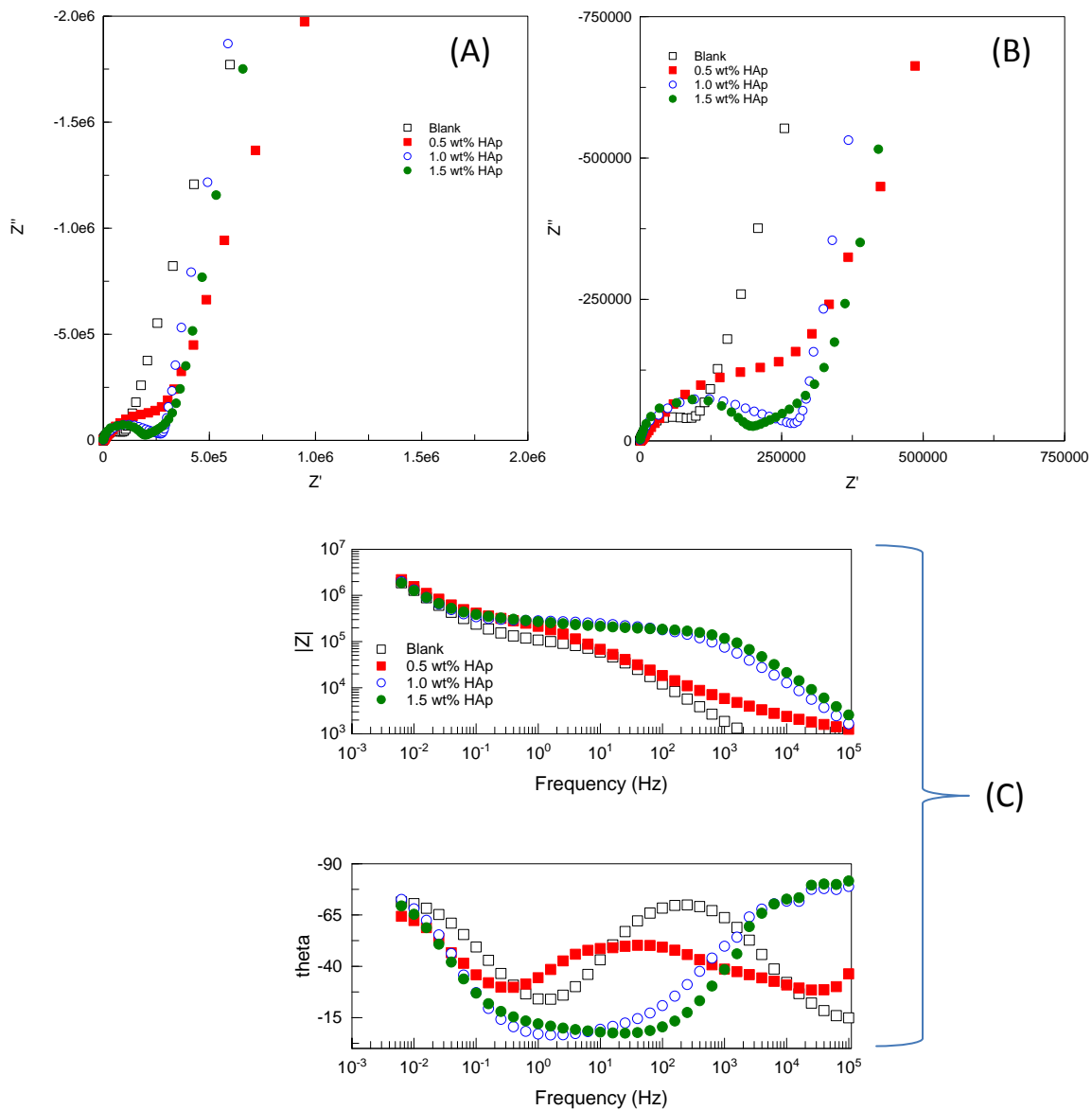


Fig 6.24 Nyquist plots, represented in two different scales [(A) and (B)] and, Bode plots (C) obtained for an uncoated Ti6Al4V sample and Ti6Al4V samples coated with MAPTMS/TMOS/HAp films containing different HAp powder percentages: 0 wt.% (blank sample), 0.5 wt.%, 1 wt.% and 1.5 wt.% respectively. Electrolyte: SBF. Immersion Time: 1day.

## Organic-inorganic hybrid sol-gel thin films modified with Hydroxyapatite particles

Table 6.7 shows the variations of resistance values ( $R_{HFA}$ ) and CPE parameters,  $(CPE-T)_{HFA}$  and  $(CPE-P)_{HFA}$ , associated to the impedance responses obtained for high frequencies as a function of the HAp content in the hybrid organic-inorganic network of the sol-gel coatings. For the MAPTMS/TMOS/HAp-Ti6Al4V systems,  $R_{HFA}$  and  $CPE_{HFA}$  are ascribed to the sol-gel coating resistance  $R_{coat}$ , and to the constant phase element of the sol-gel coating  $CPE_{coat}$ , respectively.

Table 6.7 Resistance values and CPE parameters associated to the high frequency arc (HFA) obtained for an uncoated Ti6Al4V sample and for MAPTMS/TMOS/HAp-Ti6Al4V systems with different HAp content. Electrolyte: SBF. Immersion time: 1day.

Sample	$R_{HFA}/\text{ohms}$	$(CPE-T)_{HFA} / \text{ohms}^{-1} \cdot \text{s}^{-p}$	$(CPE-P)_{HFA}$
Uncoated Ti6Al4V	$1.03 \cdot 10^7$	$1.19 \cdot 10^{-5}$	0.91
0 wt. % HAp coating	$1.14 \cdot 10^5$	$4.21 \cdot 10^{-7}$	0.82
0.5 wt. % . HAp sol-gel coating	$6.47 \cdot 10^5$	$1.25 \cdot 10^{-6}$	0.58
1 wt. % . HAp sol-gel coating	$1.99 \cdot 10^5$	$7.13 \cdot 10^{-9}$	0.84
1.5 wt. % HAp sol-gel coating	$1.84 \cdot 10^5$	$2.35 \cdot 10^{-9}$	0.89

The CPE-T values obtained from the high frequency arc (HFA) of the uncoated Ti6Al4V have the typical order of magnitude of the electrochemical double layer capacitance of a bare metal in contact with an aqueous solution. In this case, the constant phase element, CPE simulates a non-ideal behaviour of the capacitor due to the passive film formed onto the Ti6Al4V uncoated surface and  $R_{HFA}$  is the resistance associated with it. It is likely that also a complex mass transport mechanism intervenes in the system formed by corrosive medium (SBF)/dynamic passive film/Ti6Al4V alloy. Then the Nyquist diagrams can apparently present one single arc, possibly resulting to the superposition of several effects occurring at high-medium frequencies. The proximity between the various time constants causes semicircles and diffusion tails to interact to a varying degree, with a

masking or distortion of the single shapes, which complicates the plot of the diagrams, and thus obtaining properly the isolated values. Values close to 1 for the parameter  $(CPE-P)_{HFA}$  are indicating that the CPE behaves almost like a pure capacitor. In contrast with the results obtained for the uncoated Ti6Al4V alloy, the value of the CPE from the HFA for the MAPTMS/TMOS-Ti6Al4V system without HAp (blank sample) is two orders of magnitude lower than the CPEs found for the bare metal. This fact leads us to think that the physical meaning of this CPE is very different. Effectively, these values have the same order of magnitude of those typically expected for the capacitance of porous coatings of low thicknesses. On the other hand, the values of the capacitance associated to the HFA of the impedance plots obtained for coatings based on sol-gel organic-inorganic matrices modified with Hap, except the 0.5wt% Hap coating, are two magnitude orders lesser than those associated to the impedance HFA of the blank sample coating (i.e. 0 wt% HAp coating). The magnitude orders of these capacitances are usually associated to dielectric properties of dense thin films with good barrier properties. So it can be concluded, that in this case, the resistance  $R_{HFA}$  associated in parallel to this  $CPE_{HFA}$  corresponds to the resistance of the electrolyte inside the pores of the coating. Consequently, the HFA of the metal/coating systems are associated with two very important intrinsic electrical properties of the coating,  $C_{coat}$  and  $R_{coat}$ .

# Organic-inorganic hybrid sol-gel thin films modified with Hydroxyapatite particles

---

## Conclusions

In conclusion, after optimization of the preparation process of the silane matrix, a single layer system of Sol-gel derived MAPTMS/TMOS/HAp hybrids loaded with different content of HAp (0.5-1.5 wt %) were successfully deposited onto Ti-6Al-4V alloys, resulting in coatings with uniform and homogeneous particle distribution, without apparent defects. The influence of added HAp particles on the thermal behaviour, thickness, wettability, topography and morphology was studied. Results showed that, the hybrid films containing HAp particles exhibit a higher thermal stability, are thicker, and more hydrophobic than that of coatings without HAp. Solid-state multinuclear NMR and ATR-IR have been useful tools for studying the structural features and functional groups within the obtained films, and for providing information about the nature of formed species in the hybrid films after curing at 120°C for 2 hours. These techniques showed that the cross linking in the prepared hybrid was enhanced by addition of HAp.

The roughness of the coating films increased owing the formation of HAp agglomerates which could be an additional factor that leads to an increase of the surface roughness.

The effect of the incorporation of the HAp particles in the hybrid network on the in-vitro bioactivity of the resulting coatings has been assessed using fibrinogen adsorption test and osteoblast cytotoxicity/proliferation. The amount of protein adsorption increased as the content of HAp in the films increased. Thanks for the negatively charged  $\text{PO}_4^{3-}$  binding sites for the positively charged fibrinogen at pH 7.4. The cytotoxicity test showed little improvement, but not significant, of the cytotoxicity when these films contains HAp. The enhancement could be due to the efficiency of these coating to act as effective physical barrier, which inhibits the release of the toxic ions form the alloy to the cell culture medium. The better barrier properties are obtained for the coating containing 1wt% of HAp.



## ***Chapter (7)***

*Organic-inorganic hybrid sol-gel thin films modified with  
Triethylphosphite as phosphorous precursor*



**Organic-inorganic hybrid sol-gel thin films modified  
with Triethylphosphite as phosphorous precursor**

**- Introduction**

Sol-gel technique offers many advantages for the production of coatings that can be deposited on to materials including Ti6Al4V alloy as implant. The advantages of the sol-gel route include, it results in a homogenous product, it allows reduced firing temperatures, it results in a uniform structure, it is easily applied to complex structures, it has a low production and coating cost, it has a uniform shrinkage when heated and can rapidly dry without cracking <sup>[35-42]</sup>. This approach could enhance the surface characteristics of the Ti6Al4V alloy and improve host tissue bonding strength and corrosion resistance, whilst still maintaining the overall favorable mechanical properties of the bulk substrate, such as high strength and fracture toughness.

The organic–inorganic hybrids prepared by sol-gel route are very interesting due to their unique properties, which arise from the synergism between the properties of both components. The hydrolysis and condensation of the silanes results in polymeric structure exhibiting properties of chemical compatibility and flexibility able to accommodate other species <sup>[79-83]</sup>.

**- Aim**

A mixture of organofunctional alkoxy-silanes  $\gamma$ -methacryloxypropyltrimethoxysilane (MAPTMS), and tetramethylorthosilicate (TMOS) as inorganic precursor, with a molar ratio MAPTMS/TMOS of 4:1 using H<sub>2</sub>O-EtOH as solvent, was modified by adding triethylphosphite (TEP) in such a mixture. TEP was used as phosphorous precursor for the preparation of hybrid films for improvement of the corrosion protection and biocompatibility of the Ti6Al4V alloy. The effects induced by TEP content (0.3, 0.6 and 0.9 ml)/20ml in MAPTMS/TMOS sol on the physical, chemical, biological characteristics and corrosion resistance of the obtained films were studied.

The combination of silane precursors with phosphorus precursors could be an efficient method to increase the barrier properties and bioactivity of the films. This could be another way to overcome the problem of voids and pores that form during the curing of the film as a result of evaporation of water and ethanol. This coating could act as a barrier avoiding the release of metal ions from the metal to the surrounding tissue and the phosphate could help in making a bond with the bone by the adsorption of physiological proteins or enhance bone cells proliferation upon being in contact with the tissue and could enhance the corrosion protection ability of the sol-gel coatings.

## 7.1 Characterization

### 7.1.1 Thermal Analysis (TGA)

Thermal analysis was carried out in order to estimate the stability of the hybrid material after addition of TEP. The thermal stability is greatly affected by the structure, chemical composition. The thermal degradation profiles of MAPTMS/TMOS and MAPTMS/TMOS/TEP hybrid are shown in Figure 7.1.

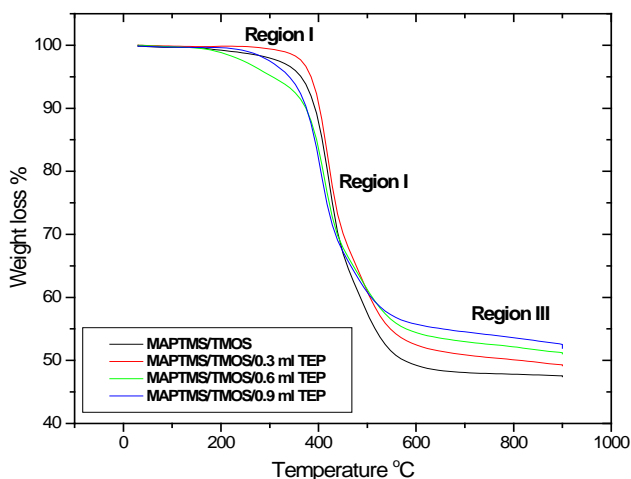


**Fig. 7.1** TG results of the prepared MAPTMS/TMOS hybrids containing different amounts of TEP

All the hybrids show three steps, with an initial weight loss (Region I). This weight loss is considered to be the result of the elimination of the condensation by-products ethanol

## Organic-inorganic hybrid sol-gel thin films modified with Triethylphosphite as phosphorous precursor

and water [239]. The second weight loss (Region II) above 350°C is due to the thermal degradation of elimination of organic matter in hybrids. The third weight loss stage (Region III) at 350-500°C is due to the complete burning of organics in the hybrid [240].

On the other hand, MAPTMS/TMOS/TEP with maximum content of TEP shows the highest thermal stability. However, the MAPTMS/TMOS hybrid shows the least thermal stability. The relative thermal stability data of studied hybrid materials was evaluated from these curves and is reported in Table 7.1.

The data from Table 7.1 shows that the weight loss was decreased with increasing the content of TEP. This because the phosphorus could act as a network former result in further cross-linking of the inorganic network in the hybrid.

**Table 7.1** Thermogravimetric results obtained for MAPTMS-TMOS with TEP

Sample	TGA	
	Weight loss % at 600°C	Residue % at 900°C
Control	50.81	47.51
0.3 ml TEP	47.57	49.21
0.6 ml TEP	46.63	53.18
0.9 ml TEP	44.29	53.63

The further cross-linking could limit the thermal conduction inside the hybrid material and thereby the kinetics of degradation. Apparently, enhancement of thermal stability of hybrids has been achieved by incorporation of phosphorus into the siloxane network. Thus, strong covalent bond Si-O-P could be formed in the network. In order to confirm this suggestion, ATR-IR of the prepared film has been accomplished.

### 7.1.2 Attenuated Total Reflectance Infrared Spectroscopy (ATR-IR)

ATR-IR spectroscopy was used to gain insight into the development of an organic-inorganic network and to study the influence of TEP addition on the structure of the siloxane network. Figure 7.2 shows The ATR spectra of the prepared

MAPTMS/TMOS/TEP coatings on Ti6Al4V substrates. The band assignments for this compound are presented in Table 7.2.

All spectra show the characteristic Si–O–Si absorption band of silica at  $1013\text{ cm}^{-1}$  and the characteristic absorption bands C–H stretching absorptions of the  $-\text{CH}_3$  residues at  $2926\text{ cm}^{-1}$ <sup>[83]</sup>. The bands at  $1454\text{ cm}^{-1}$  correspond to the symmetrical and asymmetrical  $-\text{CH}_3$  deformational (umbrella) modes<sup>[83]</sup>. The stretching vibration of C=O group at  $1738\text{ cm}^{-1}$  is attributed to the carboxyl of acrylate group of MAPTMS<sup>[83]</sup>. The presence of bands corresponding to inorganic silica together with organic groups indicates that after curing of the films at  $120^\circ\text{C}/2\text{hours}$ , the coatings are organic–inorganic in nature. Therefore the coating structure is formed by a silica network of Si–O–Si bonds interrupted in some points by organic groups. The band observed at  $3700\text{--}3150\text{ cm}^{-1}$  is characteristic of the stretching vibration of Si–OH<sup>[83]</sup>.

The spectra of pure MAPTMS/TMOS/TEP coatings on Ti6Al4V substrates show the emergence of new band at  $854\text{ cm}^{-1}$  (Figures 7.2B–7.2D), which correspond to the Si–O–P bending. This is a clear indication of the incorporation of phosphorus in the silica network<sup>[274]</sup>. The intensity of this band increased as the as the amount of TEP in the coating increased. From this observation and on the basis of the obtained ATR-IR spectra, the emergence of new bands corresponding to the Si–O–P indicates that the films are phosphosilicates that result from the formation of Si–O–P bond between silica and phosphate precursor.

At the same time, as the amount<sup>[83]</sup> of TEP in the hybrid increase, there is a consumption of the Si–OH located at  $3150\text{--}3700\text{ cm}^{-1}$ , which corresponds to the  $-\text{OH}$  stretching mode in Si–OH (i.e. silanol). The consumed  $-\text{OH}$  could be due to the hydrolysis of the TEP which might be explained by the following reaction:



The decreasing the amount of hydrophilic Si–OH bonds could allow the surface to possess more hydrophobic nature. These results indicate that the addition of the TEP accelerated the hydrolysis and condensation reactions through consumption of  $-\text{OH}$  groups. The intensities of the absorption bands corresponding to silanols (Si–OH) at

## Organic-inorganic hybrid sol-gel thin films modified with Triethylphosphite as phosphorous precursor

3150-3700  $\text{cm}^{-1}$  decrease, in the meanwhile, the ones to siloxane bonds (Si-O-Si) in the region of 1013  $\text{cm}^{-1}$  became broader.

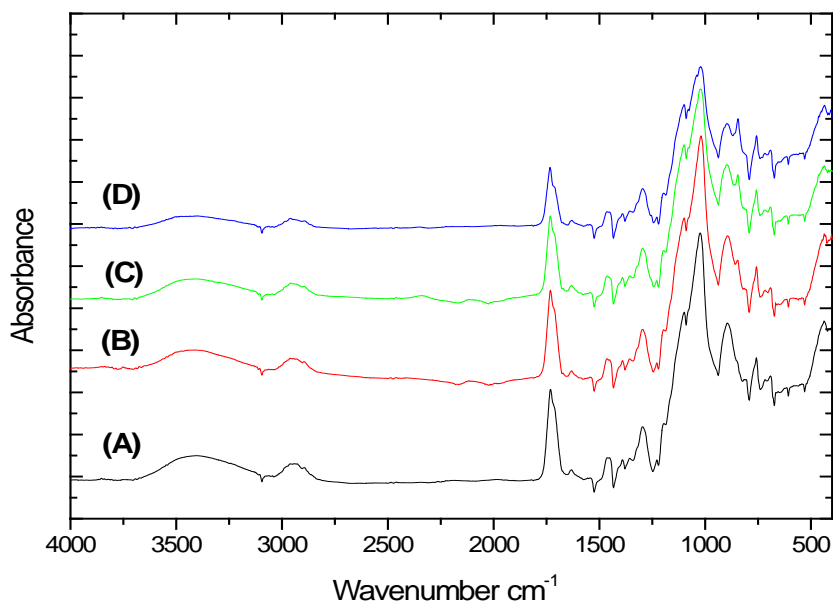


**Fig. 7.2.** Representative ATR-IR absorption spectra of MAPTMS/TMOS/TEP-Ti6Al4V systems containing: (A) 0 ml TEP; (B) 0.3 ml TEP; (C) 0.6 ml TEP and, (D) 0.9 ml TEP, respectively.

This indicates the occurrence of further cross-linking in the silane film. This agrees well with the results obtained from the TGA that showed enhancement of the thermal stability upon addition of TEP which could be due to improvement of the cross-linking.

**Table. 7.2** Assignment of the ATR-IR bands in MAPTMS/TMOS coatings on Ti6Al4V substrates reported by other authors .

Wavenumber (Cm <sup>-1</sup> )	Assignment	References
1,013	$\nu_{\text{as Si-O}}$ (Si-O-Si )	[83]
1,738	$\nu_{\text{C=O}}$ (methacryloxy groups)	[83]
2,957	$\nu_{\text{C-H}}$ (Si-R organic group)	[83]
3,150-3,700	$\nu_{\text{O-H}}$ (Si-OH groups)	[83]
1,454	$\delta_{\text{CH}_2}$ (Si-R organic groups)	[83]
854	P-O-Si bending	[274]

### 7.1.3 Solid state Nuclear Magnetic Resonance (NMR)

The structural characterization of the prepared hybrid with and without TEP was studied using solid-state <sup>29</sup>Si and <sup>13</sup>C NMR.

#### 7.1.3.1 <sup>29</sup>Si-NMR

Solid-state <sup>29</sup>Si-NMR measurements have been performed to gain further information about the structure of the inorganic side within the prepared organic-inorganic hybrid. This technique is useful in measuring the degree of condensation (extent of reaction) in the hybrid films. The <sup>29</sup>Si NMR spectra provide the proportions of T<sup>n</sup> (n=1; 2; or 3) species, where T represents a atom oxygen bridged to n Si atoms [83]. These allowed the quantification of the degree of cross-linking of the siloxane network.

Both xerogels, MAPTMS/TMOS and MAPTMS/TMOS/TEP, exhibited four peaks (Figures 7.3A-7.3C), with chemical shift of  $\delta = -59.6, -67.7, -100.41$  and  $-111.22$  ppm, corresponding to T<sup>2</sup>, T<sup>3</sup>, Q<sup>3</sup> and Q<sup>4</sup> resonances, respectively [83]. In the MAPTMS/TMOS/TEP gel the T<sup>2</sup> signal decrease in intensity as the content of the TEP in the gel increased (Figures 7.3B and 7.3C).

The proportions of T and Q species in each xerogel system quoted in Table 7.3 were obtained from deconvolution of the <sup>29</sup>Si NMR spectra with the WINFIT software. The spectra were deconvoluted into individual Gaussian line shapes, thus allowing a

## Organic-inorganic hybrid sol-gel thin films modified with Triethylphosphite as phosphorous precursor

quantitative analysis of the spectra based on the peak areas of each species. The Table shows the chemical shift  $\delta$  (ppm) and peak area (%) of T and Q units from deconvoluting the  $^{29}\text{Si}$ -NMR spectra. The present results suggested that the presence of TEP enhance the condensation process of silicates.

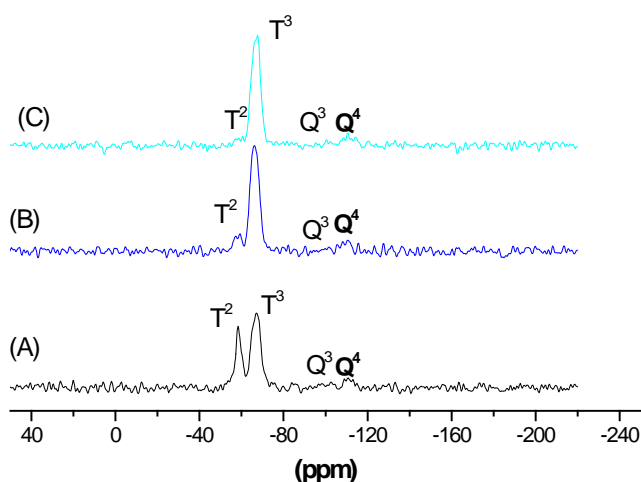


**Fig. 7.3** Solid state  $^{29}\text{Si}$ -NMR spectra of MAPTMS/TMOS containing: (A) 0 ml of TEP; (B) 0.3 ml of TEP, and (C) 0.9 ml of TEP

Figure 7.4 shows the relationship of the signals, for species  $\text{T}^2$ ,  $\text{T}^3$ ,  $\text{Q}^3$ , and  $\text{Q}^4$  in the MAPTMS/TMOS hybrid with various content of TEP. These results show it is clear that the TEP leads to higher degree of cross-linking in the organopolysiloxane matrix. In this way the increase of the cross-linking density provokes an increase of the amount of fully condensed Si-O-Si structures in the films.

The hybrid with TEP gave a larger fraction of  $\text{T}^3$  and  $\text{Q}^4$  than that from control sample. The relative intensity (in area) of  $\text{T}^3/\text{T}^2$  signals is 1.94, 7.66 and 16.15 for, xerogels containing

0.3 and 0.9 ml of TEP respectively. Indicating that, the 0.9 ml TEP containing xerogel presents a highest cross-linking degree.

**Table. 7.3.** chemical shift  $\delta$  (ppm) and peak area (%) of T and Q units from deconvoluting the  $^{29}\text{Si}$ -NMR spectra

Sample	$\delta(\text{ppm})$ and peak area %					
	T <sup>0</sup>	T <sup>1</sup>	T <sup>2</sup>	T <sup>3</sup>	Q <sup>3</sup>	Q <sup>4</sup>
Control	-	-	-58.63 29.94	-66.97 58.35	-100.41 4.79	-111.22 6.93
0.3 TEP	-	-	-58.05 10.26	-66.34 78.68	-100.42 2.43	-109.71 8.63
0.9 TEP	-	-	-58.50 5.13	-66.91 82.85	-101.19 2.56	-111.24 9.47

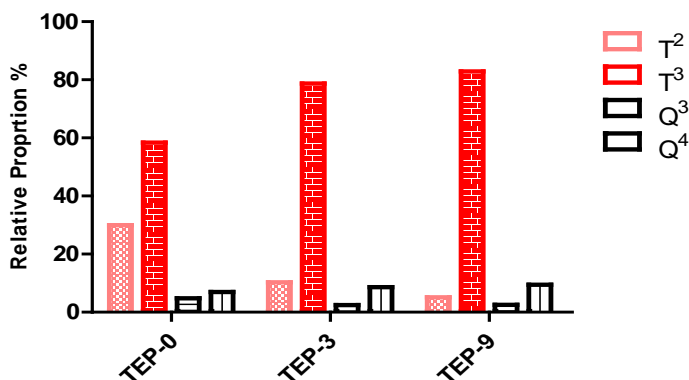


**Fig. 7.4.** Relationship of the signals, for species T<sup>2</sup>, T<sup>3</sup>, Q<sup>3</sup>, and Q<sup>4</sup> in the MAPTMS/TMOS hybrid with various content of TEP.

These results agree well with those obtained from the ATR, where it was observed that the presence of P in the hybrid led to broadening of the ATR bands and decrease of the Si-OH silanol bands corresponding to uncondensed species in the film.

### 7.1.3.2 $^{13}\text{C}$ -NMR

The structure of the organics present in the hybrid material was analyzed by using of the solid state  $^{13}\text{C}$ -NMR. The  $^{13}\text{C}$ -NMR spectrum of the MAPTMS/TMOS xerogel displayed signals at 17.5 ppm ( $\text{C}-\underline{\text{C}}\text{H}_3$ ), 59.34 ppm ( $\text{Si}-\text{O}-\underline{\text{C}}\text{H}_3$ ), 125.6 ppm ( $\text{CH}_2=\underline{\text{C}}$ ), 136.2 ppm ( $\text{CH}_3=\underline{\text{C}}$ ) and 166.2 ppm ( $\text{CH}_3=\text{C}$ ) (Figure 7.5A) which are ascribed to the methacryloxy groups. Signals at 9.7 ppm ( $\text{Si}-\underline{\text{C}}\text{H}_2$ ) and 23.6 ppm ( $\text{Si}-\underline{\text{C}}\text{H}_2\text{CH}_2\text{CH}_2$ ) appearing in all cases (control and TEP containing hybrids) at similar chemical shift <sup>[83]</sup>.

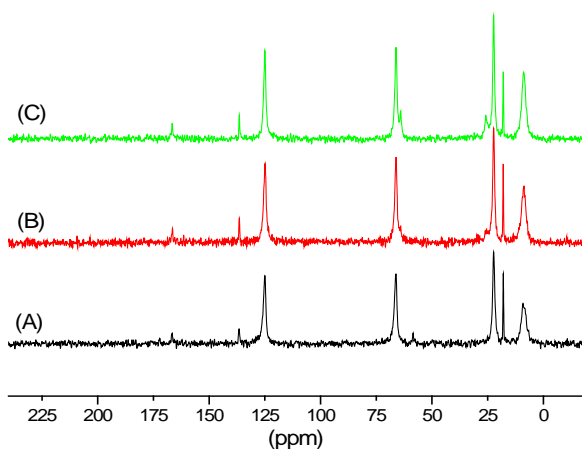


**Fig. 7.5.** Solid state  $^{13}\text{C}$ -NMR spectra of MAPTMS / TMOS containing **(A)** 0 **(B)** 0.3 ml TEP **(C)** 0.9 ml TEP.

In the  $^{13}\text{C}$  NMR spectra of the TEP containing xerogel, Fig.7.5 B-C , two tiny peaks emerged at 26.1 and 64.4 ppm corresponding to  $\underline{\text{C}}\text{H}_3-\text{CH}_2-\text{O}$  and  $\text{CH}_3-\underline{\text{C}}\text{H}_2-\text{O}$  created as a result of hydrolysis of the TEP <sup>[83]</sup>.

### 7.1.4 Scanning Electron Microscope (SEM/EDX)

Figure 7.6A shows SEM micrograph of MAPTMS/TMOS coatings on Ti6Al4V substrates cured at 120°C for 2 hours. The SEM observations showed the formation of smooth, uniform, crack free and highly adherent protective film on the substrates that expect to lead to good corrosion resistance of Ti6Al4V alloys. The white points present on the surface could be condensed silica particles. The EDX analysis shows the presence of carbon, oxygen, silicon together with titanium and aluminium from the substrate (Figure 7.6B). The presence of Ti and Al indicates the existence of micro-pores in the deposited MAPTMS/TMOS film on the surface of the Ti6Al4V alloy.

Figures 7.6C-7.6E show micrographs of the MAPTMS/TMOS/TEP coatings on Ti6Al4V substrates. The films cover continuously the Ti6Al4V surface. EDX analysis of these films indicated the presence of phosphorus, carbon, oxygen and silicon. This confirms the incorporation of the phosphorus in the siloxane matrix which agrees well with the results obtained by the ATR-IR. The disappearance of the Ti, Al in the EDX spectra could be due to the good coverage and further densification of the deposited MAPTMS/TMOS/TEP films on the Ti6Al4V substrate.

# Organic-inorganic hybrid sol-gel thin films modified with Triethylphosphite as phosphorous precursor

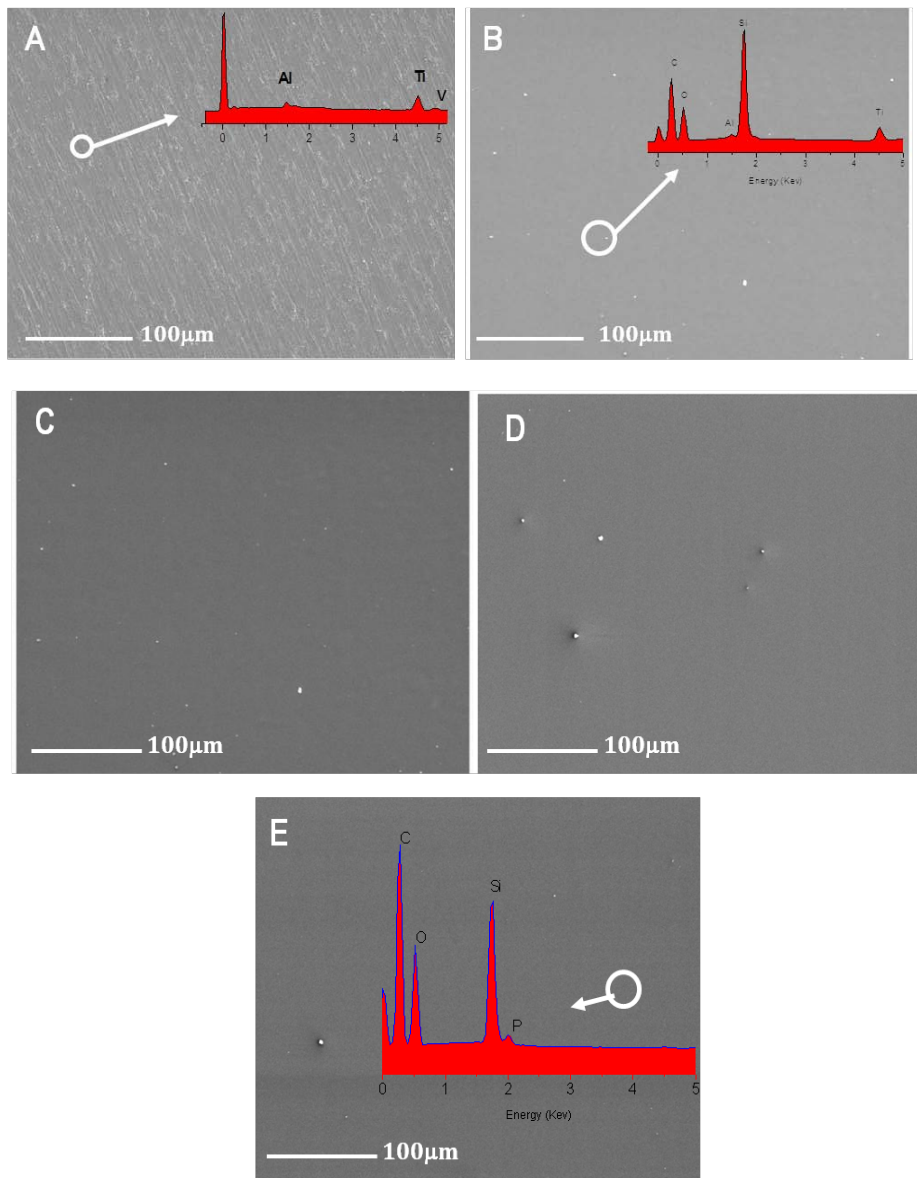


**Fig.7.6** SEM micrographs and EDX analysis of the prepared hybrid coatings deposited on Ti6Al4V substrates, un-coated (A) , and containing 0 ml of TEP (B); 0.3 ml of TEP (C) ; 0.6 ml of TEP (D) 0.9 of TEP (E) .

### 7.1.5 Phase separation problem with higher TEP content

Figure 7.7 show SEM micrograph of the MAPTMS/TMOS/TEP-Ti6Al4V coated surface at different magnifications. Figures 7.7A and 7.7C show micrographs of the MAPTMS/TMOS/TEP system containing 5 ml of TEP and Figures 7.7B and 7.7D show micrographs of the same system containing 10 ml of TEP. The features observed suggest that these hybrid sol-gel materials might have phase separation, indicating that the TEP was not well mixed and not properly incorporated into the MAPTMS/TMOS matrix for high TEP concentrations.

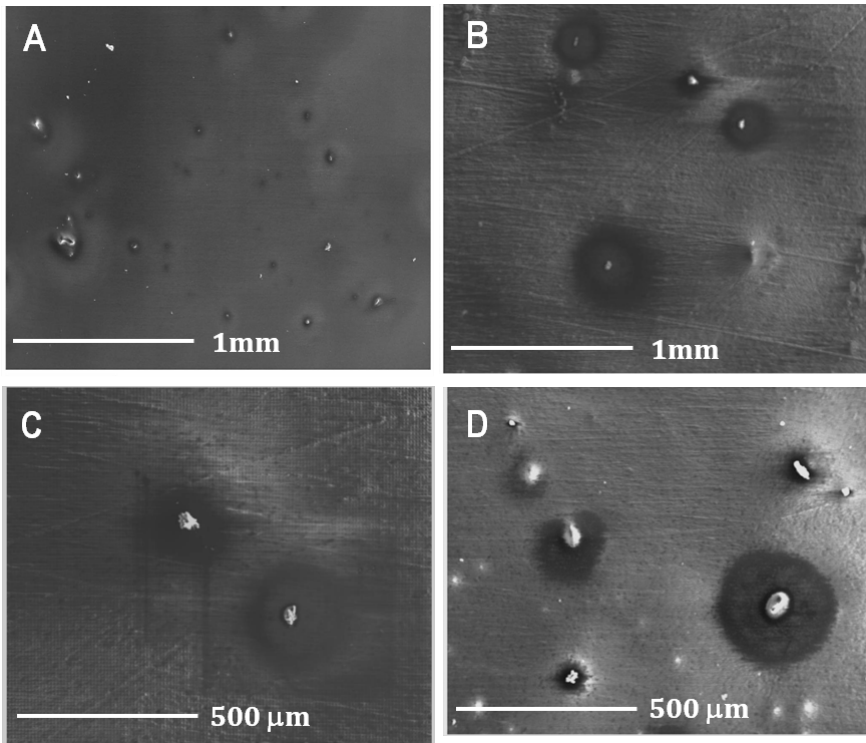


**Fig. 7.7** SEM micrographs and EDX analysis of the prepared MAPTMS/TMOS/TEP-Ti6Al4V system containing (A) 5 ml of TEP; (B) 10 ml of TEP; (C) 5 ml of TEP, and (D) 10 ml TEP.

### 7.1.6 Rheology

The effect of the different content of TEP on the viscosity of the MAPTMS/TMOS sol can be seen in Figure 7.8. This Figure shows the mean viscosity change +/- its standard deviation versus different contents the TEP in the sol. The control MAPTMS/TMOS sol (0 ml of TEP) showed viscosity ( $\eta$ ) values of  $0.009 \pm 0.0005$ . For the TEP containing hybrids,  $\eta$  slightly increase with the TEP content, from  $0.011 \pm 0.0008$  to  $0.013 \pm 0.0007$  for sols containing 0.3 and 0.9 ml of TEP respectively (Table 7.4). These increases in the viscosity with the TEP content can be related to two phenomena: the developing of a stronger network due to an increase in the interactions between phosphorus and silica in the formed network chains and/or the enhancement of the polymerization of the sol upon addition of the TEP. These results are in agreement with the ATR,  $^{29}\text{Si}$ -NMR and TGA results that also showed enhancement of the polymerization. This indicates the enhancement of the silica condensation, which consequently leads to higher viscosity compositions after TEP addition.

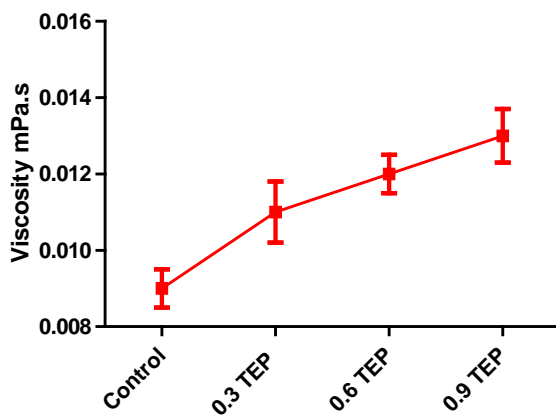
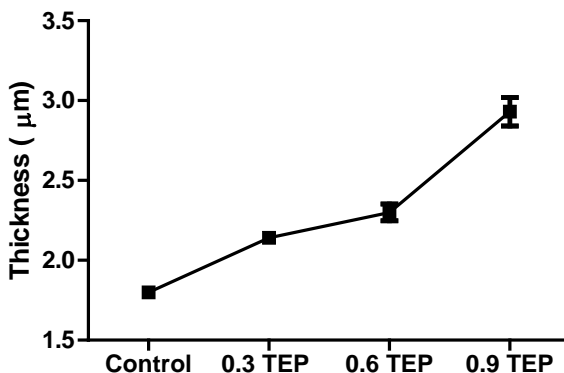


Fig. 7.8 Change of MAPTMS/TMOS sol viscosity as a function of TEP content.

### 7.1.7 Film Thickness

Figure 7.9 represents the thickness variation of the MAPTMS/TMOS/TEP coatings on Ti6Al4V substrates as a function of TEP content. In Table 7.4 are shown the Ra thickness values of MAPTMS/TMOS/TEP films, which are represented in Figure 7.9. As Figure 7.9 shows, the thickness of the films increase as the content of TEP does. This

could be due to the increase of the sol viscosity after addition of the TEP to the MAPTMS/TMOS sol.



**Fig. 7.9** Variation of the thickness of the MAPTMS/TMOS/TEP coatings deposited on Ti6Al4V surfaces as a function of TEP content.

### 7.1.8 Wettability (Contact Angle)

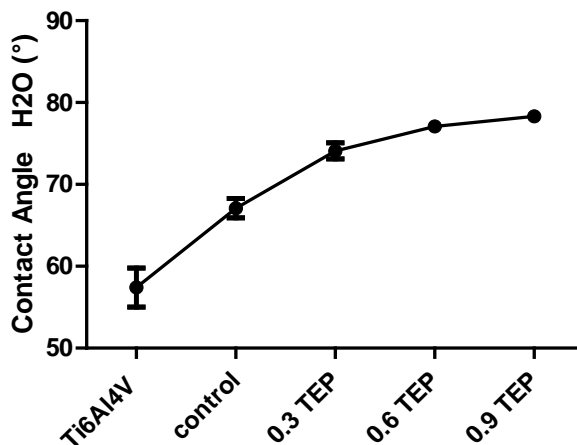
Contact angle measurement is a technique for wettability analysis and is directly related to surface energy and tension. Contact angle describes the shape of a liquid droplet resting on a solid surface. When drawing a tangent line from the droplet to the touch of the solid surface, the contact angle is the angle between the tangent line and the solid surface. The measurement of the contact angle provides information regarding the bonding energy of the solid surface and the surface tension of the droplet.

Figure 7.10 displays the contact angle of the MAPTMS/TMOS/TEP coatings deposited on Ti6Al4V surfaces as a function of TEP content. In Table 7.4 are summarized the contact angles values ( $\theta$ ) and their respective standard deviations of the prepared hybrid films. The measurements were performed using distilled water as a measuring liquid.

The contact angle slightly increases by increasing the TEP content into the hybrid matrix. This point to a decrease of wettability as the concentration of TEP increases. This could be related to the fact that the TEP increases the cross-linking density; increasing the content of hydrophobic Si-O-Si units in the film and as a result the hydrophobicity of the

## Organic-inorganic hybrid sol-gel thin films modified with Triethylphosphite as phosphorous precursor

coating can be increased. These results are in agreement with the  $^{29}\text{Si}$ -NMR and ATR-IR results.



**Fig. 7.10** Contact angle values of the MAPTMS/TMOS/TEP coatings deposited on Ti6Al4V surfaces as a function of TEP content.

**Table 7.4** Viscosity of sol, contact angle and thickness of MAPTMS/TMOS coatings on Ti6Al4V substrates as a function of TEP content.

Surface	Contact Angle $\theta$ H <sub>2</sub> O (°)	Viscosity	Thickness ( $\mu\text{m}$ )
Ti6Al4V	57.4 ± 2.83	-	-
Control	67.1 ± 1.17	0.009 ± 0.0005	1.80 ± 0.017
0.3 TEP	78.1 ± 0.97	0.011 ± 0.0008	2.14 ± 0.019
0.6 TEP	82.1 ± 0.48	0.012 ± 0.0005	2.30 ± 0.052
0.9 TEP	85.3 ± 0.41	0.013 ± 0.0007	2.93 ± 0.090

### 7.1.9 Confocal microscopy

The roughness of the surface of the coated Ti6Al4V was assessed by confocal microscopy. Figure 7.11 depicts the morphology of uncoated and coated alloys. Figure 7.11-Ti6Al4V shows the scan obtained of the uncoated alloy. The Ra roughness parameters of the prepared coatings are summarized in Table 7.5. The 3D image analysis of the control film showed Ra surface roughness values of  $0.165 \pm 0.012 \mu\text{m}$ .

**Table 7.5** Surface roughness parameters for uncoated and hybrid coated/Ti6Al4V alloy.

	<b>Ra (<math>\mu\text{m}</math>)</b>	<b>Rp (<math>\mu\text{m}</math>)</b>	<b>Rv (<math>\mu\text{m}</math>)</b>
<b>Ti6Al4V</b>	0.094±0.018	0.467±0.153	-0.361±0.104
<b>Control</b>	0.165±0.012	0.631±0.150	-0.606±0.103
1 TEP	0.137±0.018	0.565±0.140	-0.488±0.103
2TEP	0.133±0.018	0.580±0.154	-0.569±0.095
3 TEP	0.129±0.016	0.577±0.199	-0.484±0.098

This increase of Ra roughness values when compared with uncoated alloy ( $0.094 \pm 0.018 \mu\text{m}$ ) could be due to the evaporation of solvents during drying. Although, there are not significant variations between the Ra values of these surfaces, it seems that there is a slight decrease of Ra when the TEP contain increase. This shows that the surface becomes slightly smooth. This can be explained by the fact that by increasing the TEP content, the density of the films is increased and so the film becomes less porous.

# Organic-inorganic hybrid sol-gel thin films modified with Triethylphosphite as phosphorous precursor

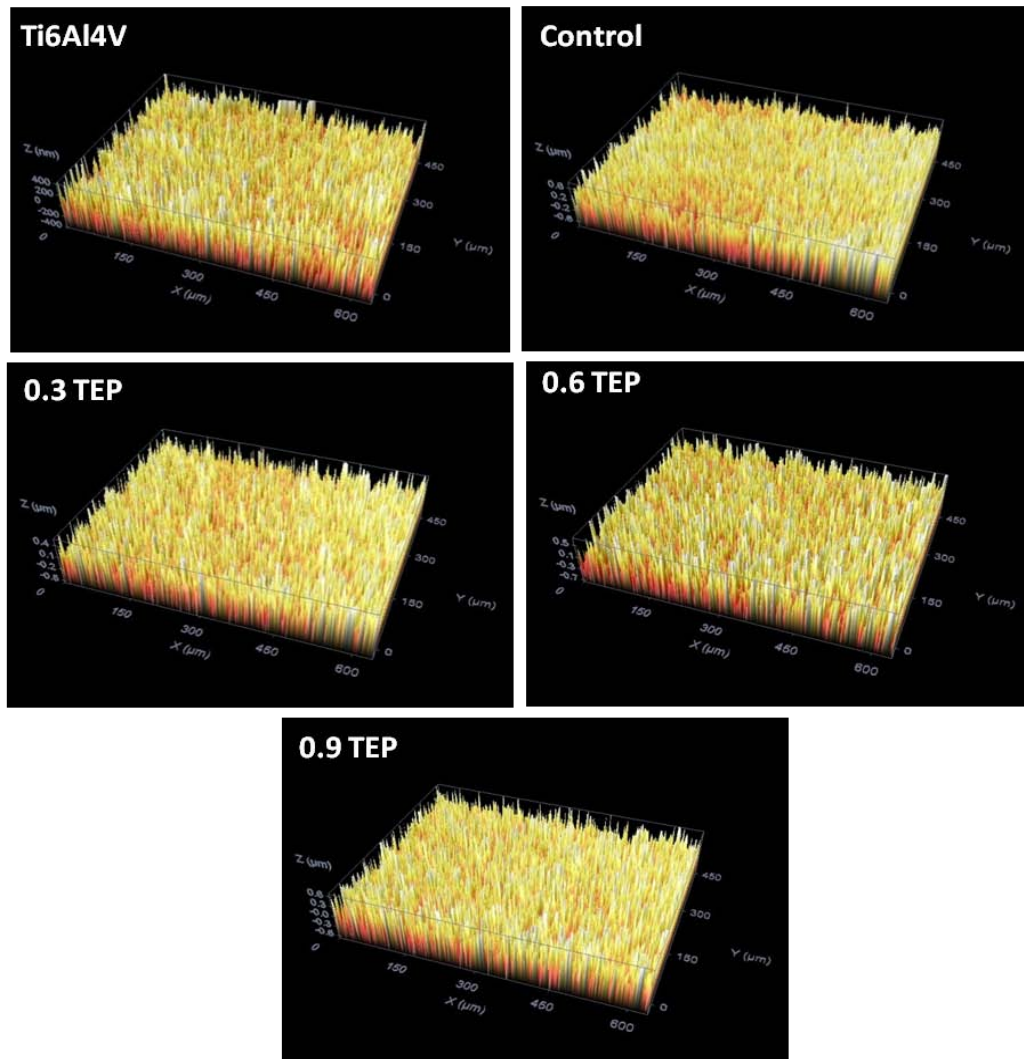


**Fig. 7.11** Confocal microscope three-dimensional images of the TEP hybrid coatings on Ti6Al4V and the uncoated Ti6Al4V surface.

## 7.2 In-vitro Bioactivity

### 7.2.1 Bradford protein assay

To evaluate the potential use of prepared coatings for biomedical implants, fibrinogen adsorption on the surface of the prepared films is examined. After immersion of the coated surfaces in 1 mg/ml fibrinogen solution in PBS, adsorption was allowed to proceed in an incubator for 1 h at 37°C. Absorbance was measured by reading the absorption of the aliquot solution at a wavelength of 595 nm after removing the immersed samples.

Figure 7.12 shows the Bradford standard calibration curve of different protein concentration 0.2-1 mg/ml read at 595 nm. Based on this curve the amount of the adsorbed protein could be extracted by comparing the absorption values of the aliquot solution after removing the uncoated alloy, control and MAPTMS/TMOS/TEP (0.3-0.9) respectively with the absorption values in the calibration curve.

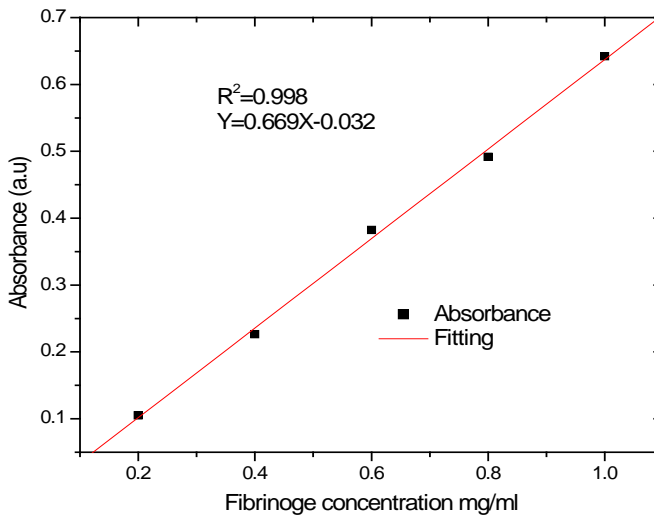


**Fig.7.12** 595 nm Bradford method standard calibration curve.

### 7.2.1.1 Amounts of adsorbed fibrinogen

The amount of fibrinogen adsorbed onto different surfaces is shown in Figure 7.14. Greater amount of protein was adsorbed onto TEP containing films compared with the control and uncoated Ti6Al4V alloy over the same incubation time. The chemical composition of the substrate surface strongly affects the protein adsorption process, as has been documented <sup>[47]</sup>.

This could be explained with the fact that protein adsorption onto implant surface is limited by the availability of binding sites. According to the popularly accepted understanding, electrostatic interactions are very important for protein adsorption <sup>[257]</sup>.

Based on this curve the amount of the adsorbed protein could be extracted by comparing the absorption values of the aliquot solution Figure 7.13. The measured absorbance values,  $0.57 \pm 0.004$ ,  $0.55 \pm 0.004$ ,  $0.50 \pm 0.003$ ,  $0.417 \pm 0.00057$  for the aliquot solution after removing the uncoated alloy, control, and TEP containing films (0.3, 0.9 TEP) respectively with the absorption values in the calibration curve.

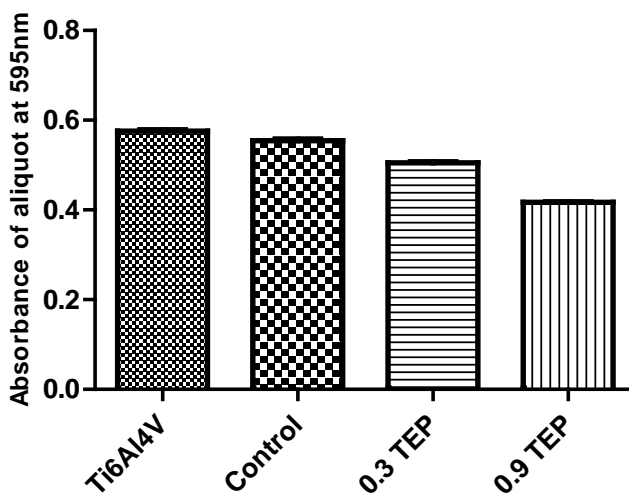


**Fig.7.13** Absorbance read at 595 nm of aliquot solution after removing the surfaces.

Figure 7.14 shows the calculated amounts of adsorbed fibrinogen onto prepared hybrid films. The adsorbed amount were  $7.469 \pm 0.59$  and  $10.06 \pm 0.59 \mu\text{g}/\text{cm}^2$  for uncoated Ti6Al4V and control samples and  $16.24 \pm 0.38 \mu\text{g}/\text{cm}^2$  for samples containing 0.3 ml of TEP and  $27.28 \pm 0.072 \mu\text{g}/\text{cm}^2$  for samples containing 0.9 ml of TEP. Thus the phosphorous incorporation leads to enhancement of protein adsorption. The reason could be the presence of P binding sites for protein adsorption <sup>[257]</sup>.

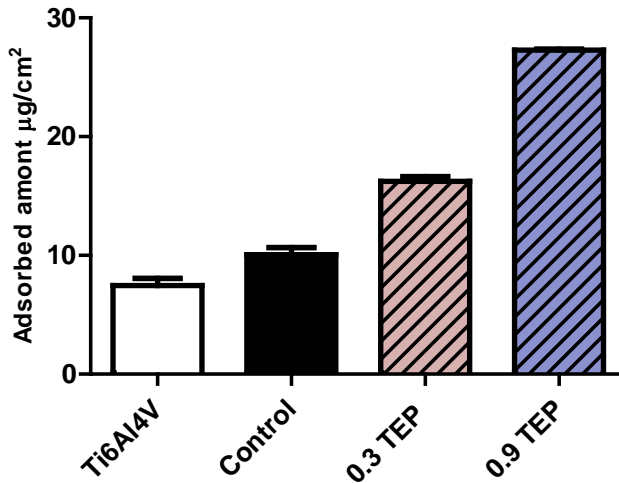


Fig.7.14.Amount of fibrinogen adsorbed on the prepared hybrid films.

## 7.2.2 Osteoblast – film interactions

### 7.2.2.1 Osteoblast cytotoxicity/viability

The effects on the NHOst of coatings surface with and without TEP were qualitatively evaluated *in-vitro* using the neutral red assay. Four different substrates (uncoated Ti6Al4V, MAPTMS/TMOS-Ti6Al4V, MAPTMS/TMOS/0.3TEP-Ti6Al4V and MAPTMS/TMOS/0.9TEP-Ti6Al4V) were tested over 7 days of exposure. Significant differences between the samples with TEP and those without could be observed, Figure 7.15. One can see in this Figure the amount of vital dye taken up by the cells as a measure of absorbance at 540 nm after seven days on the different tested surfaces.

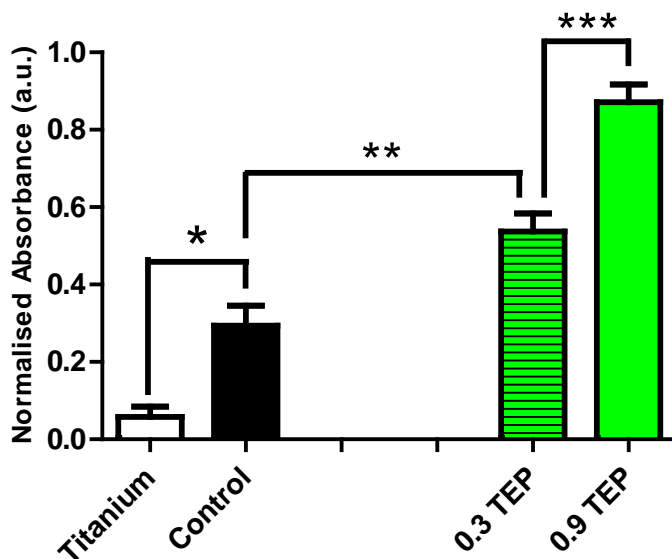


Fig. 7.15 Neutral red cytotoxicity assay for NH0st cultured on Ti6Al4V, MAPTMS/TMOS-Ti6Al4V and TEP containing hybrids (0.3-0.9 ml TEP) over a seven day period.

These results showed that the trend for NH0st cell viability was highest on MAPTMS/TMOS/TEP-Ti6Al4V, then MAPTMS/TMOS-Ti6Al4V and finally on the uncoated Ti6Al4V. Proliferation of NH0st was slowest on the unmodified Ti6Al4V surface with all other substrates showing significantly more growth.

The toxicity of the un-coated alloy seems to be higher with respect to the coated surfaces. On one hand, this could be due to the toxicity of vanadium and aluminum that released from the alloy and can initiate cell toxicity and adverse tissue reactions as been reported [270]. On the other hand, the less cytotoxicity on the coated surfaces, because the coating could act as a physical barrier inhibiting the ion release to the culture medium.

Performance was best on the films with TEP, with both hybrids performing significantly better than the uncoated Ti6Al4V alloy and MAPTMS/TMOS-Ti6Al4V samples. The films with 0.9 ml of TEP performed significantly higher than all of the other substrates. These findings showed that the TEP is more effective and resulted in more cells viability at 7

days. The low cytotoxicity observed in the case of 0.9 TEP containing films confirmed the low metal ion release suggestion.

For biomaterials, the surface topography, composition, surface energy and wetting properties, could also affect the osteoblast adhesion and proliferation. Since there is no great variation between the measured roughness values of uncoated or coated alloys, the effect of roughness is neglected. Other factor could be the wettability which found to be decreased as the TEP content increased. The decrease of wettability of the prepared films found to be in the optimum range for cell attachment <sup>[248]</sup>. Other factor could be the composition, the effect of phosphorous on the cell proliferation and consequence densification of the film maybe obvious. Therefore, these results suggest that presence of phosphorous in the coatings promotes osteoblast cell adhesion on the sol-gel coatings. This in agreement with J. FIKE who concluded that, the phosphate treatment increases osteoblast behaviour in-vitro <sup>[275]</sup>.

Cell adhesion and subsequent cell proliferation on prepared films is also determined by the protein adsorption to these materials. In comparison with the results obtained by the fibrinogen protein adsorption assay, after placement of the implant into a biological environment a protein film adsorbs through which the cell attachment occurs. These results also in agreement with the results obtained by Zanchetta P et al., who concluded that osteoblasts often show a higher adhesion degree on hydrophobic surfaces <sup>[276]</sup>.

The obtained result suggests that the prepared hybrid coatings with and without TEP are biocompatible and non-toxic for surface modification.

### 7.2.2.2 Osteoblasts adhesion

Immunofluorescence was conducted to observe these aspects of the osteoblasts cultured on the different films and representative imagery is shown in Figure 7.16. There only a few cells were observable under the fluorescence microscope on the uncoated and MAPTMS/TMOS surfaces. This was most likely to be due to the ion dissolution from the alloy in the culture medium which prevented cell attachment. There were more cells on the MAPTMS/TMOS/TEP-Ti6Al4V system with 0.9 ml of TEP content which shows the highest number of observed cells.

## Organic-inorganic hybrid sol-gel thin films modified with Triethylphosphite as phosphorous precursor

The immunofluorescence imagery is in agreement with the performance of viability/cytotoxicity assay. In addition it was observed that osteoblasts on all the TEP containing substrates showed a more substantial network of f-actin stress fibres and the expression of vinculin by the osteoblasts than cells growing on the bare alloy or MAPTMS/TMOS coated Ti6Al4V alloy. MAPTMS/TMOS/TEP-Ti6Al4V system with 0.9 ml of TEP has shown to have the most developed network of focal adhesion sites.

The presence of phosphorous in the coatings seems to enhance cell attachment and spreading. Phosphorus plays a key role in biochemical pathways in the body, such as energy production, cell division and is known to activate osteoblast function. The phosphorus has been reported to be important for cell division and could stimulate the spreading of the osteoblasts on the surfaces and stimulate cellular metabolic activity and osteoblast proliferation. [275-277]

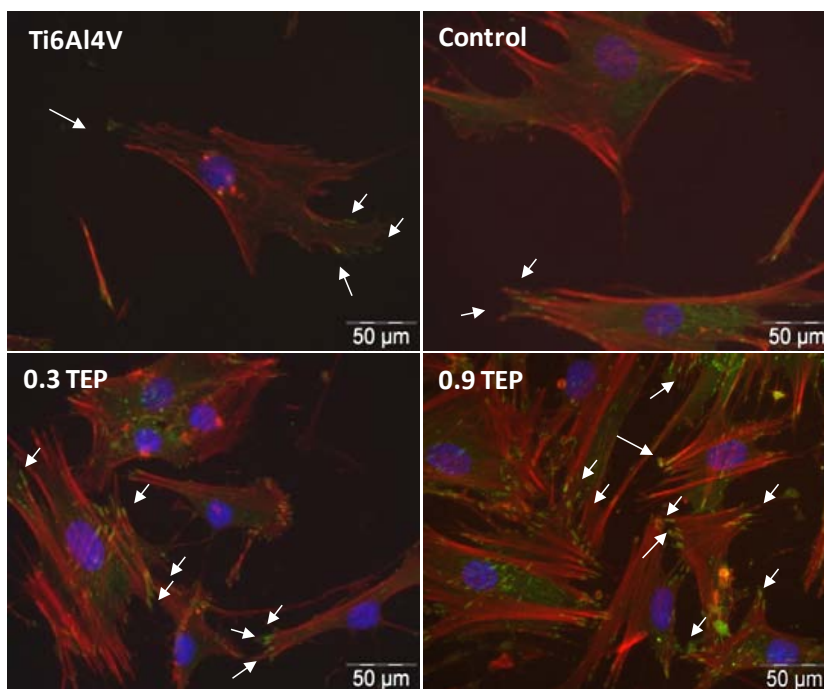


**Fig. 7.16** Fluorescence graphs of OB-cells growing on: un-coated Ti6Al4V and coated surfaces; vinculin (green), actin (red) and nuclei (blue).

In conclusion, the research of the actin skeleton is an established method for indirect cell adhesion tests. The number of focal adhesion sites also indicates increased adhesion [271,272]. As such the number of focal adhesion sites indicate that cell adhesion on the surfaces with highest content of TEP is superior to that of all other substrates.

These findings showed that the TEP is more effective and resulted in more cells at seven days. This confirms the results from the previous neutral red uptake assay. Our results demonstrate that organic-inorganic hybrid coating based on silane and phosphorus precursors can significantly improve the proliferation of osteoblast cells and reduce the cytotoxicity of the Ti6Al4V substrate.

### 7.2.3 Immersion in SBF

Surface bioactivity tests of the MAPTMS/TMOS/TEP hybrid coatings were assayed by immersion in SBF for 1 day. Figure 7.17 shows SEM micrographs and EDX analysis obtained after 1 day of immersion in SBF solution of the MAPTMS/TMOS/0.9 TEP system deposited on the Ti6Al4V alloy.

The surface morphology of the alloy after soaking shows precipitation from the SBF. The EDX analysis shows the presence of both calcium and phosphorus which indicates the formation of bone like apatite after immersion in SBF.

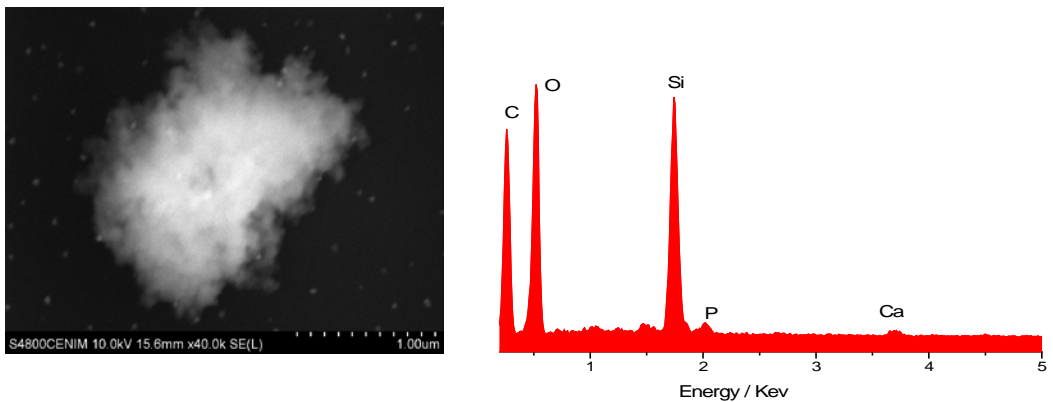


**Fig.7.17** SEM micrographs and EDX analysis of MAPTMS/TMOS/0.9 TEP –Ti6Al4V system.

### 7.3 In vitro corrosion protection behaviour of the TEP modified organic–inorganic hybrid coatings on Ti6Al4V alloy

In vitro corrosion and protection studies of the MAPTMS/TMOS/TEP-Ti6Al4V system immersed in Kokubo's simulated body fluid (SBF) have been carried out by applying the methodology of testing and analysis of results described in chapters 4 and 6. Figure 7.18 shows the electrochemical impedance spectroscopy (EIS) results of the MAPTMS/TMOS/TEP-Ti6Al4V system evaluated after immersion in SBF at different immersion times. This system is formulated with a volumetric ratio of 0.9 ml of TEP against 20 ml of MAPTMS/TMOS sol. In Figure 7.18 the impedance data in the complex plane (i.e. Nyquist plots) (A) and the variations of the logarithm of the impedance module (B) and phase angle (C) both against the frequency logarithm (Bode plots) is displayed.

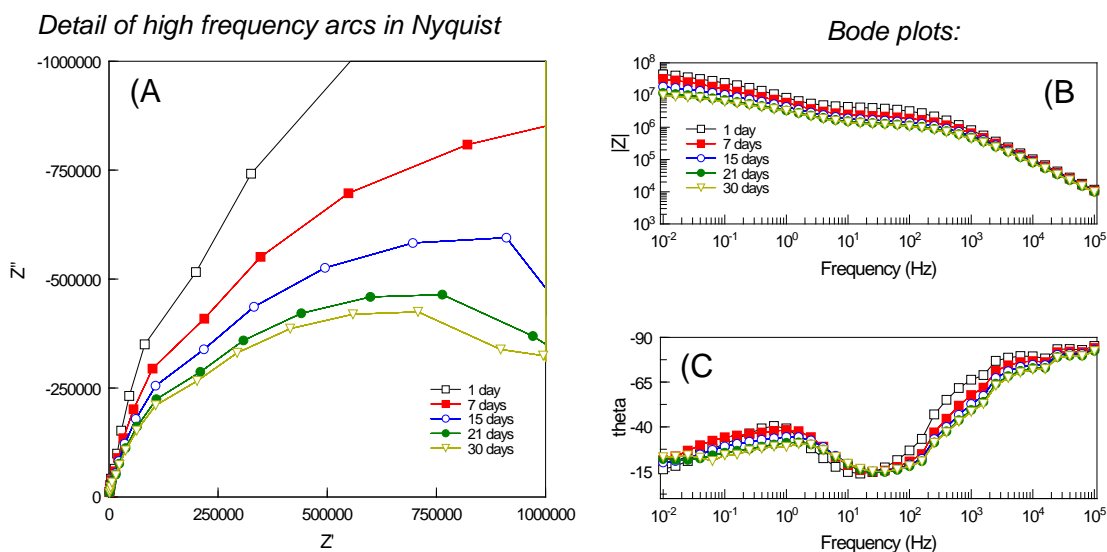


Fig.7.18. Evolution of the impedance plots of the MAPTMS/TMOS/TEP-Ti6Al4V system (0.9 ml/20 ml of TEP/silane ratio) as a function of the immersion time in SBF.

Through a qualitative analysis of the impedance diagrams, valuable information about the intrinsic electrical properties of the coating and the protective properties of coatings in aqueous media can be obtained. Thus, from Figure 7.18A is showed that the diameter of the arc in the high frequency region (HF) of Nyquist diagrams was gradually decreasing with the immersion time in SBF. The chord located between the two cut-off points of this arc with the real axis of the complex plane coincides with the values of the ionic resistance ( $R_i$ ) of the electrolyte inside the pores of the coating. The decrease of  $R_i$  with the immersion time indicates that the coating slowly loses its barrier properties.

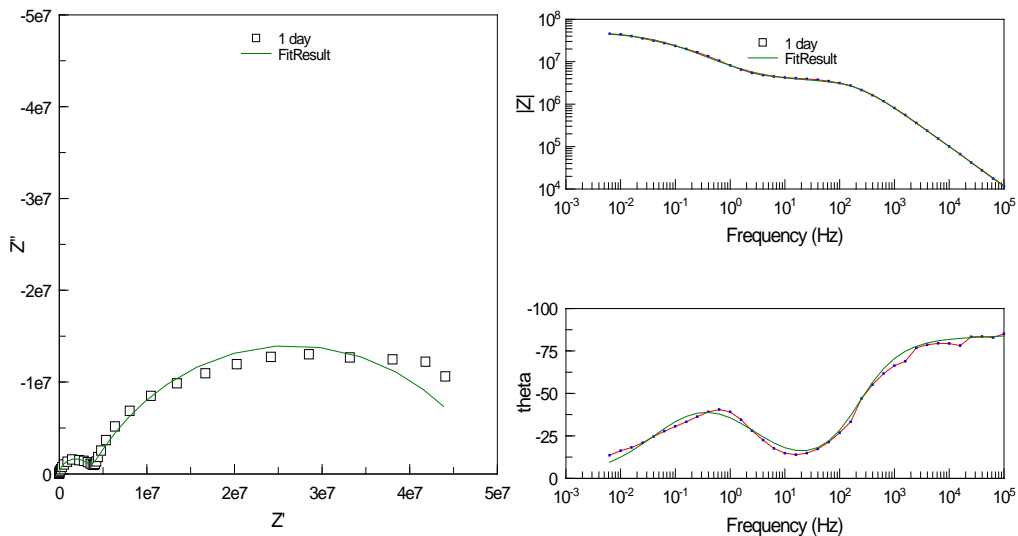
It is also interesting to note the changes that take place in the corresponding Bode plot (Figure 7.18B), which show a continuous slow decrease of the impedance modulus especially at low frequencies. This behaviour is associated with a slow decrease of the corrosion resistance of the Ti6Al4V at the base of the pores at the metal/coating interface within the immersion time in the SBF solution.

The quantitative analysis of these results has been done by ZView software. This commercial program is based on theoretical simulations with electrical equivalent circuits, fitting techniques and complex nonlinear least-squares (CNLS) methods. The equivalent circuit used in chapters 4 and 6 (Figure 4.16 (A, B)) displays also accurate fitting plots for the TEP modified organic-inorganic hybrid coating/ Ti6Al4V system.

Figure 7.19 shows, as an example, the impedance plots obtained experimentally after 24 hours of immersion in Kokubo solution for two identical samples of the MAPTMS/TMOS/TEP-Ti6Al4V system. The fitting results generated applying the equivalent circuit of figures 4.16 (A, B) have been also plotted in this figure. Table 7.6 shows the fitting values calculated for each one of the elements of the equivalent circuit used.

# Organic-inorganic hybrid sol-gel thin films modified with Triethylphosphite as phosphorous precursor

**sample 1:**



**sample 2**

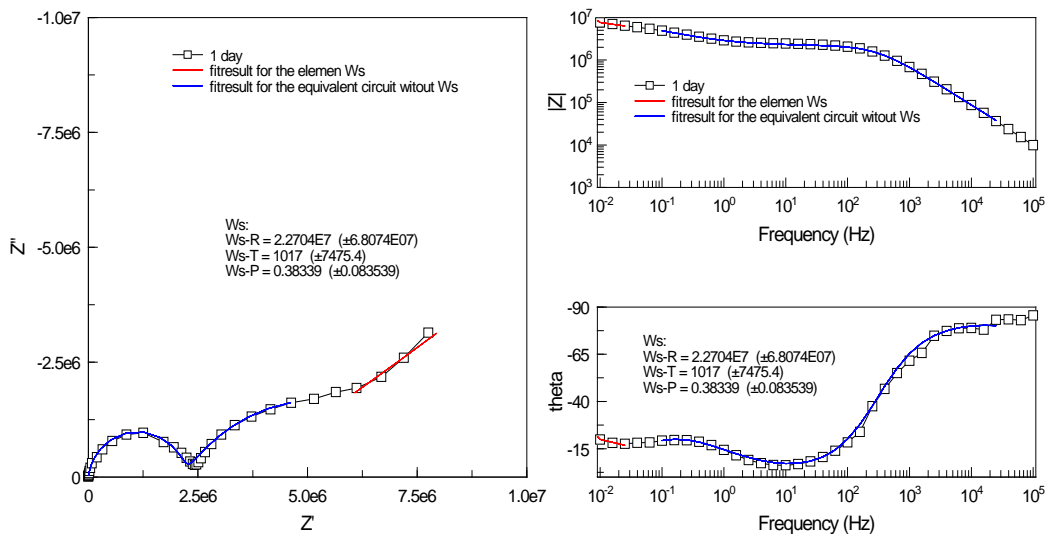


**Fig.7.19** Experimental impedance plots and fit results obtained for two MAPTMS/TMOS/TEP-Ti6Al4V samples. TEP/silane ratio = 0.9 ml/20 ml. Immersion time in SBF: 1day.

## CHAPTER 7

**Table 7.6.** Values calculated with the Zview software for each of the equivalent circuit elements for the MAPTMS/TMOS/TEP-Ti6Al4V system.  
TEP/silane ratio = 0.9 ml/20 ml. Immersion Time SBF: 1day.

<b>Fit Results for sample 1</b>				
<u>Element</u>	<u>Freedom</u>	<u>Value</u>	<u>Error</u>	<u>Error %</u>
<b>Rs</b>	Free(±)	-131.6	411.28	312.52
<b>Ccoat-T</b>	Free(±)	3.5544E-10	2.0266E-11	5.7017
<b>Ccoat-P</b>	Free(±)	0.92654	0.0053686	0.57942
<b>Rcoat</b>	Free(±)	3.5803E+06	71980	2.0104
<b>Cdl-T</b>	Free(±)	4.606E-08	1.0497E-09	2.279
<b>Cdl-P</b>	Free(±)	6.9318	0.012708	1.8333
<b>Rcorr</b>	Free(±)	4.6002E+07	1.386E06	3.0129
Chi-squared:			0.0056495	
Weighted sum of squares:			0.37852	

<b>Fit Results for sample 2</b>				
<u>Element</u>	<u>Freedom</u>	<u>Value</u>	<u>Error</u>	<u>Error %</u>
<b>Rs</b>	Free(±)	-561.5	369.13	65.74
<b>Ccoat-T</b>	Free(±)	7.8166E-10	6.045E-11	7.7335
<b>Ccoat-P</b>	Free(±)	0.87688	0.0069469	0.79223
<b>Rcoat</b>	Free(±)	1.07E+06	29301	2.7384
<b>Cdl-T</b>	Free(±)	1.3083E-07	4.8659E-09	3.7193
<b>Cdl-P</b>	Free(±)	5.7775	0.016861	2.9184
<b>Rcorr</b>	Free(±)	1.2576E+07	8.38E-05	6.6671
Chi-squared:			0.0042556	
Weighted sum of squares:			0.25108	

## Organic-inorganic hybrid sol-gel thin films modified with Triethylphosphite as phosphorous precursor

---

By applying this methodology, satisfactory results are obtained. But also, like in the case of the impedance results shown in chapter 6, it is noted that, in general, the reproducibility of the ionic resistance of the coating and the charge transfer resistance of the metal/electrolyte interface were affected by the uncertain character of macroscopic failures. In contrast, good reproducibility was obtained for the coating capacitance values, which depend almost exclusively on changes occurring at the microscopic level.

The unfitting values obtained for the circuit component  $R_s$  (Table 7.6) are due to the fact that its true value is masked by the  $R_{coat}$  and  $R_{corr}$  values, which are usually many orders of magnitude greater than those of the resistance of the electrolyte,  $R_s$ .

Figure 7.20 shows the evolution of the equivalent circuit parameters during the immersion tests in Kokubo solution for the MAPTMS/TMOS/TEP-Ti6Al4V system, (results shown in figures 7.18 (A, B, C)). These results have been calculated according to the methodology above mentioned. It can be observed that the  $R_{coat}$  and  $R_{corr}$  values change mostly within the first 5 days of immersion, and then these values stay almost constant, within reasonable magnitude margins along the 25 days of immersion in the SBF, which is an aggressive solution with a high salt content. According to these results, it can be concluded that, these coatings have interesting protective properties, despite their low thicknesses ( $< 3 \mu\text{m}$ ). The low values found for the parameter  $T$  of the CPE,  $C_{coat-T}$  (next to  $10^{-10} \text{ ohms}^{-1} \cdot \text{s}^{-P}$ ), measured at the beginning of the immersion test in the SBF, indicate that: (i) it is correct to associate the arc of high frequencies of the Nyquist diagrams to the intrinsic properties of the coating ( $R_{coat}$  and  $C_{coat}$ ); (ii) the equivalent circuit selected to evaluate these results is also correct, and (iii) the values found for  $C_{coat-T}$  are indicating that the coating integrity is suitable and that this coating presents good dielectric properties (insulator). The slow evolution of this parameter with the immersion time indicates that the water uptake in the coating is low. This behaviour is associated with good barrier properties, good stability and good protective properties of these sol-gel coatings against the corrosive aqueous medium (SBF) and thus against corrosion. The values of the second parameter that defines this CPE, the exponent  $P$  ( $C_{coat-P}$ ), are close to 1 and also decrease slowly with the immersion time, indicating

that the chemical properties of these coatings remain stable during the immersion tests. Concerning the parameter Cdl-T, the values obtained are within the range of the typical values assigned to the electrochemical double layer on this metallic alloys, which indicates that the equivalent circuit selected is correct and that therefore the middle-frequency arc can be associated to the corrosion processes of the metallic substrate at the base of the coating pores. This process is described by the association in parallel of the Rcorr/Cdl electrical elements in the equivalent circuit. The values of the parameter Cdl-P are lower than 1 and quite close to 0.5 (Figure 7.20), being 1 the expected value for an ideal capacitor. Due to this fact, these values of Cdl-P could be associated to diffusion processes. However, diffusion processes typically take place at very low frequencies, so instead of diffusion processes, it seems correct to associate the middle-frequency arc of these samples to the electrochemical double layer at the base the coating pores at the metal/coating interface.

# Organic-inorganic hybrid sol-gel thin films modified with Triethylphosphite as phosphorous precursor

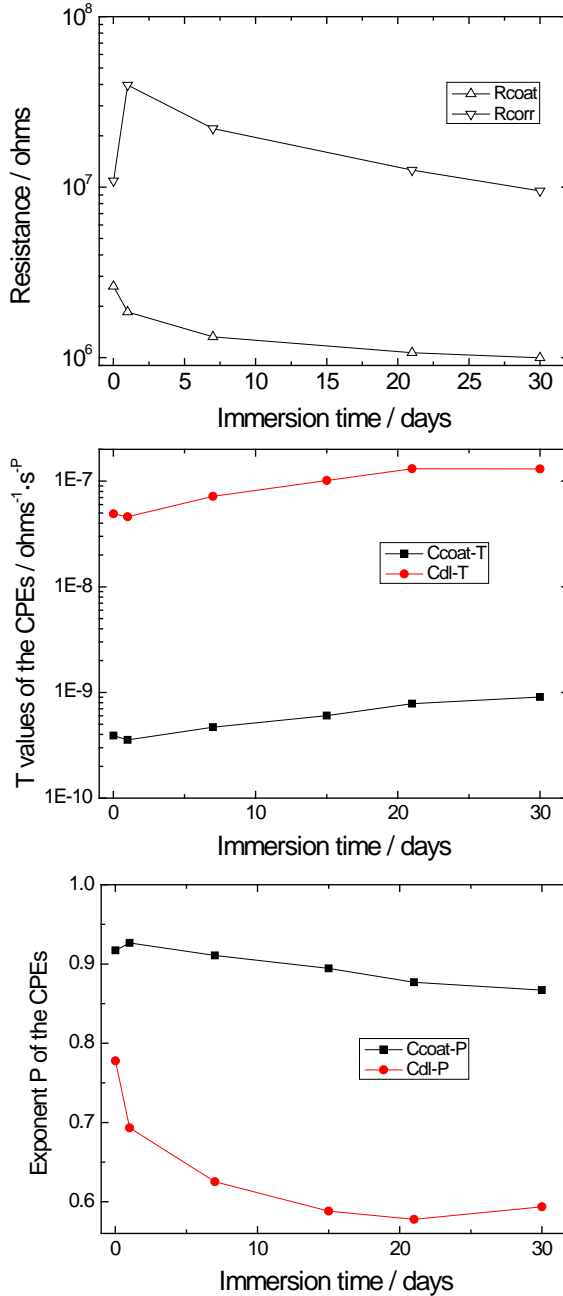


**Fig.7.20** Evolution of the equivalent circuit parameters during the immersion tests in Kokubo solution for the MAPTMS/TMOS/TEP-Ti6Al4V system. Formula: 0.9 ml of TEP for 20 ml of silanes mixture.

Actually, at the lowest frequencies, the impedance plots of the MAPTMS/TMOS/TEP-Ti6Al4V system immersed in Kokubo simulated body fluid (SBF) show some deviation with respect to the theoretical results generated by the equivalent circuit used in chapters 4 and 6 (Figures 4.16). These deviations can be due to the beginning of diffusion phenomena developed in finite thickness layers with transmissive boundary conditions<sup>[177]</sup>. These phenomena can be quantified by adding in the equivalent circuit a new element called finite-length Warburg diffusion,  $W_s$  (Figure 7.21). The impedance of the electrical element  $Z_w$  is governed by the following equation:

$$Z_w = R \cdot \tanh(j \cdot T \cdot \omega)^p / (j \cdot T \cdot \omega)^p$$

Parameters:  $W_s$ -R,  $W_s$ -T,  $W_s$ -P

$J = -1$

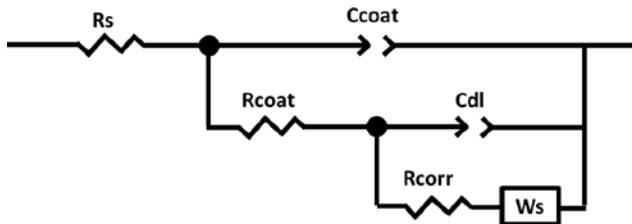


**Fig.7.21.** General electrical equivalent circuit of metal/sol-gel coating system in contact with an aqueous electrolyte, taking in account the short circuit terminus  $W_s$ , associated to diffusion phenomena in finite length layers.

This element is also known as a Generalized Finite Warburg element (GFW). It is an extension of another more common element, the Finite-Length Warburg (FLW).

To use the FLW equation in the ZView software it is necessary to set  $W_s$ -P = 0.5 and set its freedom to 'fixed'.

The FLW is the solution of the one-dimensional diffusion equation of a particle, which is completely analogous to wave transmission in a finite-length RC transmission line.

In the diffusion interpretation the parameter  $W_s$ -T is governed by the following relation:

## Organic-inorganic hybrid sol-gel thin films modified with Triethylphosphite as phosphorous precursor

$$W_s-T = d^2 / D$$

Where

$d$  is the effective diffusion thickness

$D$  is the effective diffusion coefficient.

In a first approach, it can be considered that the values of effective diffusion thickness and coating thickness coincide.

The GFW is similar to this, but for it the square root becomes a continuously varying exponent  $W_s-P$  such that  $0 < W_s-P < 1$ .

If the data exhibits only the high frequency ( $45^\circ$  slope) behavior and not the transition to low frequency behavior, either  $W_o-R$  or  $W_o-T$  must be set as Fixed(X) in the control work fit parameters of the ZView software menu. Alternately, a CPE can be used in this situation.

This version of the Warburg element is terminated in a finite resistance. At very low frequencies,  $Z'$  approaches  $W_s-R$  and  $Z''$  goes to zero.

The representation in the complex plane of the equation  $Z=R \cdot \tanh(j \cdot T \cdot \omega)^P / (j \cdot T \cdot \omega)^P$  plots in the first quadrant a curve similar to the fourth part of the Bernoulli's lemniscate (Figure 7.22)

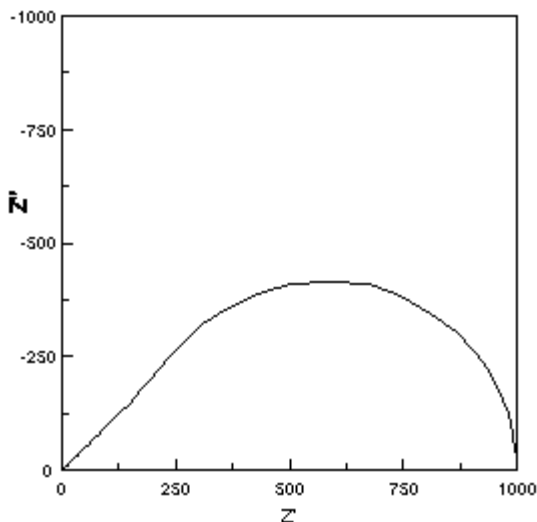


**Fig.7.22.** Graphics produced in the complex plane by the equation  $Z=R \cdot \tanh(j \cdot T \cdot \omega)^P / (j \cdot T \cdot \omega)^P$  for:  $W_s-R = 1000$ ;  $W_s-T = 0.1$ ;  $W_s-P = 0.5$ . The frequency of the  $Z''$  maximum is at  $\omega_{max} = 2.53/W_s-T = 25.3$  rad/sec = 4.03 Hz.

Figure 7.23 Shows the Bode plots obtained after 24 hours of immersion in SBF for a bare Ti6Al4V alloy sample and for Ti6Al4V alloy samples coated with organic-inorganic films formulated with different concentrations of TEP: 0 ml (blank sample), 0.3 ml, 0.6 ml and 0.9 ml respectively added to a mixture of 20 ml of silanes (molar ratio of MAPTM/TMOS = 4:1).

The strong dependence of the impedance response versus frequency of these tested samples makes difficult to represent the results in format of Nyquist diagrams into a single chart. For this, it is necessary to represent these Nyquist impedance plots by using different scales, in order to make possible the analysis in detail the diagram regions at low and high frequencies.

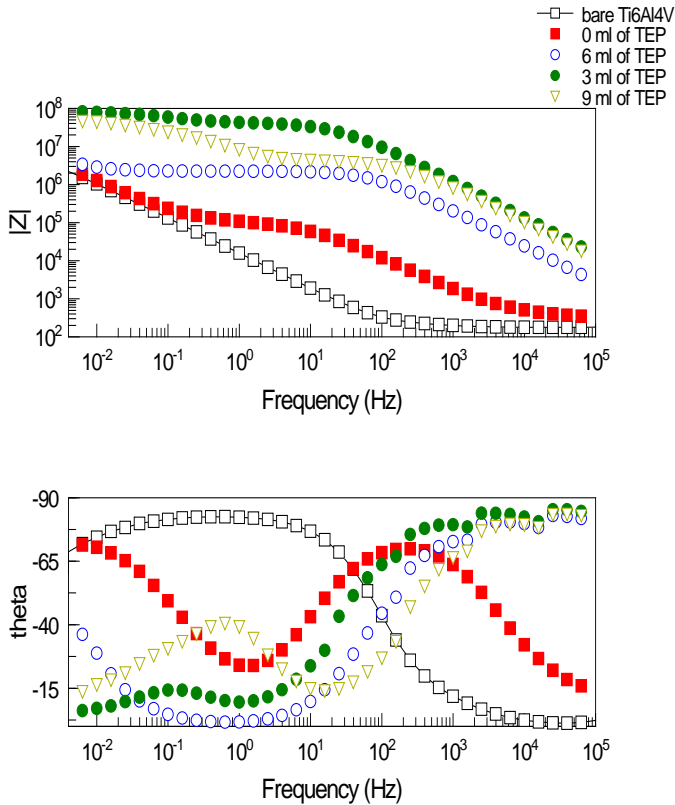


**Fig.7.23** Bode plots recorded for uncoated and coated Ti6Al4V alloy with hybrid sol-gel films with different contents in TEP: 0 ml (blank sample), 0.3 ml, 0.6 ml and 0.9 ml respectively. Electrolyte: SBF. Immersion Time: 1day.

## Organic-inorganic hybrid sol-gel thin films modified with Triethylphosphite as phosphorous precursor

Figure 7.24 shows the same impedance data represented in the above Figure 7.23, but now these data are represented in Nyquist plots format. It can be clearly observed in Figure 7.24A that the higher impedance values in the entire domain of measured frequencies correspond to those coatings which contain 0.6 and 0.9 ml of TEP respectively. The Figure 7.24B shows the high-frequency arcs of the coatings and a detail of the impedance plots of those samples that have the lower impedance values which are the samples based on coatings that contain 0 and 0.3 ml of TEP respectively.

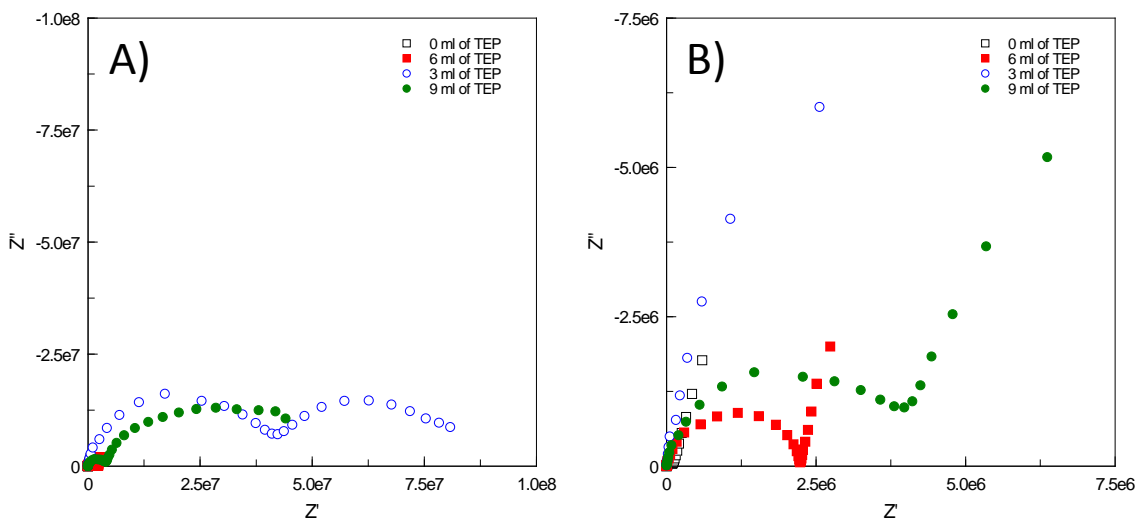


**Fig. 7.24.** Representation in two different scales of the Nyquist plots of samples of Ti6Al4V hybrid films coated with sol-gel with different contents in TEP: 0 ml (blank sample), 0.3 ml, 0.6 ml and 0.9 ml respectively. Electrolyte: SBF. Immersion Time: 1day.

Table 7.7 shows the values for the different elements of the equivalent circuit. These values were obtained from the impedance plots shown in Figures 7.23 and 7.24. The CPE-T values obtained from the high frequency arc (HFA) of the uncoated Ti6Al4V have the typical order of magnitude of the electrochemical double layer capacitance of a bare metal in contact with an aqueous solution. As previously commented in chapter 6, CPE simulates a non-ideal behaviour of the capacitor due to the passive film formed onto the

Ti6Al4V uncoated surface and  $R_{HFA}$  is the resistance associated with it. Values close to 1 for the parameter  $(CPE-P)_{HFA}$  are indicating that the CPE behaves almost like a pure capacitor. In contrast with the results obtained for the uncoated Ti6Al4V alloy, the value of the CPE from the HFA for the MAPTMS/TMOS-Ti6Al4V system without TEP (blank sample) is two orders of magnitude lower than the CPEs found for the bare metal. This fact leads us to think that the physical meaning of this CPE is very different. Effectively, these values have the same order of magnitude of those typically expected for the capacitance of porous coatings of low thicknesses. On the other hand, the values of the capacitance associated to the HFA of the impedance plots obtained for coatings based on sol-gel organic-inorganic matrices modified with TEP are two or three magnitude orders lesser than those associated to the impedance HFA of the blank sample coating (i.e. 0 ml TEP coating). The magnitude orders of these capacitances are usually associated to dielectric properties of dense thin films with good barrier properties. So it can be concluded, that in this case, the resistance  $R_{HFA}$  associated in parallel to this  $CPE_{HFA}$  corresponds to the resistance of the electrolyte inside the pores of the coating. Consequently, the HFA of the metal/coating systems are associated with two very important intrinsic electrical properties of the coating,  $C_{coat}$  and  $R_{coat}$ . From these parameters it is possible to obtain the values of the polymer dielectric constant or relative permittivity ( $\epsilon_r$ ) and the conductivity of the electrolyte  $\sigma_i$ .

**Table 7.7** CPE and resistance values associated to the high frequency arc (HFA) for MAPTMS/TMOS/TEP-Ti6Al4V systems with different content in TEP. Electrolyte: SBF. Immersion time: 1day.

Sample	$(CPE-T)_{HFA} / \text{ohms}^{-1} \cdot \text{s}^{-P}$	$(CPE-P)_{HFA}$	$R_{HFA}/\text{ohms}$
Uncoated Ti6Al4V	$1.19 \cdot 10^{-5}$	0.91	$1.03 \cdot 10^7$
0 ml TEP coating	$3.97 \cdot 10^{-7}$	0.83	$1.10 \cdot 10^5$
0.3 ml TEP coating	$1.77 \cdot 10^{-9}$	0.90	$2.18 \cdot 10^6$
0.6 ml TEP coating	$2.30 \cdot 10^{-10}$	0.94	$3.45 \cdot 10^7$
0.9 ml TEP coating	$3.63 \cdot 10^{-10}$	0.92	$3.59 \cdot 10^6$

## Organic-inorganic hybrid sol-gel thin films modified with Triethylphosphite as phosphorous precursor

---

In addition, the evaluation of these two parameters at different immersion times in the corrosive media is very useful to obtain the evolution of the protective properties of the coatings. Thus, following these criteria above exposed, it can be concluded, that the MAPTMS/TMOS/TEP coatings with lower values of  $C_{coat-T}$  and higher values of  $R_{coat}$  are those which afford the best protection. Table 7.8 shows that, for 24 hours of immersion in SBF, the coatings containing 0.6 and 0.9 ml of TEP are the coatings that afford the best corrosion protection behaviour.

### Conclusion

The experimental results show that phosphorus can be successfully used to act as a network former together with silicon by the formation of Si–O–P bonds. The results of the ATR-IR analysis indicated the formation of phosphosilicate network. In addition the SEM analysis confirms the formation of a transparent and homogenous film which covers continuously the metallic surface. The incorporation of phosphorus in the siloxane network resulted in an increase of sol viscosity due to an enhancement of the cross-linking and polymerization, as confirmed by the NMR results. The incorporation of phosphorus at molecular level resulted in enhancement of in-vitro protein adsorption and also osteoblast cytotoxicity/proliferation have been improved. These results reflect the importance of phosphorus for cell division and could stimulate the spreading of the osteoblasts on the surfaces and stimulate cellular metabolic activity and osteoblast proliferation.



## ***Chapter (8)***

*Organic-inorganic hybrid sol-gel thin films modified with  
Dimethylsilylphosphite as phosphorous precursor*



**Organic-inorganic hybrid sol-gel thin films modified with Dimethylsilylphosphite as phosphorous precursor**

**- Introduction & Aim**

In this chapter, sol–gel processing was used to prepare an organic-inorganic hybrid coating on Ti6Al4V alloy, via incorporation of a liquid phosphorus precursor, dimethylsilylphosphite (DMTSP), which had previously shown promise when mixed with silane hybrid with regards to corrosion protection and biological properties, as mentioned in chapter 7.

Organic–inorganic hybrid coatings were prepared using again the MAPTMS/TMOS system modifying this time the organic-inorganic matrix by adding in its network phosphorous atoms using DMTSP as phosphorous precursor. Like the TEP, the use of DMTSP allowed the introduction at a molecular level of P into a siloxane network. The formulated hybrid coatings were subjected to the same preparation procedures as the MAPTMS/TMOS/TEP mentioned in chapter 7 and variable amounts of DMTSP.

**8.1 Characterization**

The experimental techniques used to characterize the studied samples are the following:

- Thermal analysis (TGA), to determine the optimum curing temperature of the deposited hybrid films,
- Attenuated total reflectance infrared (ATR-IR), to study the composition and functional groups in the coatings after curing ,
- Solid-state <sup>29</sup>S- NMR for determining the nature of condensed species in the hybrid coatings after curing ,
- Scanning electron microscopy , SEM/EDX , to study the morphology and composition of the films deposited on Ti6Al4V alloy,
- Contact angle measurement, to characterize the wettability of the prepared hybrid films,
- Neutral red uptake assay cell viability /toxicity and osteoblast cells proliferation,

- Immunofluorescence, to show the morphology of osteoblast cells attached to different hybrid coatings,
- Study of the corrosion protection of MAPTMS/TMOS/DMTSP hybrid coatings on Ti6Al4V surfaces in SBF using electrochemical impedance spectroscopy (EIS) technique.

### 8.1.1 Thermogravimetric analysis (TGA).

Thermal stability plays an essential role in determining the proper curing temperature of the deposited hybrid films. Thermal decomposition behaviour of MAPTMS/TMOS hybrid modified with DMTSP (22-900°C) is shown in Figure 8.1.

There were three distinct weight loss stages in the TGA curves of all hybrids. The first weight loss takes place at 30–223°C, which can be assigned either to the removal of the residual water and/or water from remnant silanol groups <sup>[239]</sup>. At the second stage, the weight loss region of 223–439°C corresponded to the burning of the organic components in the hybrid <sup>[218]</sup>. The third stage happened between 439 and 679°C, which was associated with further decomposition of organic components. Over 640°C, no weight loss is observed, indicating that all the organic part has been eliminated from the silica matrix <sup>[240]</sup>.

In comparison with the TGA curve of the pure hybrid MAPTMS/TMOS, the MAPTMS/TMOS/DMTSP has higher thermal stability. Thus, the weight loss decreased as the amount of DMTSP in the hybrid increased.

From the inorganic yield, Table 8.1, it is clear that the hybrid containing DMTSP has higher thermal stability which reflected in production of higher amount of residues at 900°C. This could be an indication of the further improvement in the network formation in case of the DMTSP containing hybrids.

These results suggest that the thermal stability of hybrid is enhanced by incorporation of DMTSP. This is consistent with one or more of a number of possibilities. One of them is that the higher silica content in the hybrid with DMTSP can enhance thermal stability <sup>[278]</sup>.

# Organic-inorganic hybrid sol-gel thin films modified with Dimethylsilylphosphite as phosphorous precursor

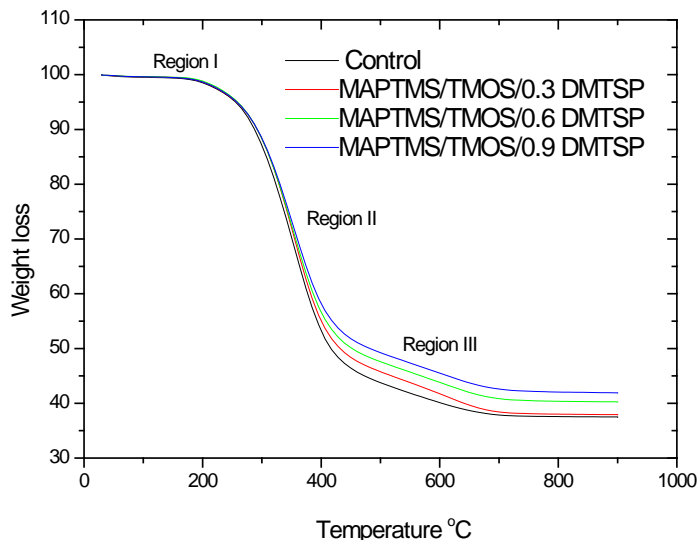


**Fig. 8.1** TG results of the prepared MAPTMS/TMOS hybrids containing variable amounts of DMTSP

In comparison with the control hybrid without DMTSP. Other possibilities to explain this thermal behaviour could be due to the stronger interaction between the organic and inorganic phases in systems modified with DMTSP <sup>[279]</sup> and/or the higher degree of cross-linking of these systems. The phosphorus from DMTSP molecule could act as a network former. These suggestions could be explained further by help of ATR-IR and NMR techniques.

**Table 8.1** Thermogravimetric results obtained for MAPTMS-TMOS with DMTSP

Sample	TGA	
	Weight loss % at	Residue % at 900°C
	600°C	
Control	60.3	37.5
0.3 DMTSP	58.3	37.8
0.6 DMTSP	56.1	40.29
0.9 DMTSP	54.72	41.8

### 8.1.2 Attenuated total reflectance infrared (ATR-IR)

Attenuated total reflectance infrared spectroscopy has been used to gain insight into the development of an organic–inorganic network and to elucidate the structural changes present as the DMTSP precursor was introduced into the hybrid networks. To reveal the interactions between the siloxane network and DMTSP, ATR-IR spectra of pure siloxane and siloxane/DMTSP hybrid coatings were acquired, and shown in Figure 8.2.

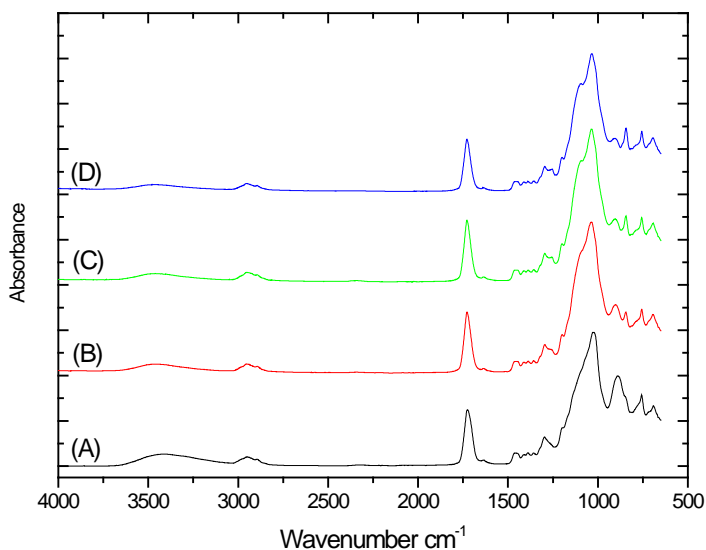


Fig. 8.2 ATR-IR spectra of the MAPTMS/TMOS/ DMTSP -Ti6Al4V system for coatings containing different content of DMTSP. (A) 0ml (B) 0.3ml DMTSP (C) 0.6ml DMTSP(D) 0.9ml DMTSP

The most resolved bands are attributed to the vibration frequencies between  $1032\text{ cm}^{-1}$  correspond to the siloxane bond (Si–O–Si) [83]. The band of  $2938\text{ cm}^{-1}$  is attributed to the  $\text{-CH}_2\text{-}$  asymmetric stretching vibration [83]. The C=O absorption from the MAPTMS precursor appears strongly at  $1732\text{ cm}^{-1}$  [83]. All spectra in Figure 8.2 show characteristic peak of -OH (at  $3405\text{ cm}^{-1}$ ) [83]. The control sample showed the Si-OH bands at  $917\text{ cm}^{-1}$  which decreased in intensity as DMTSP content increased (Figure 8.2A). This could show the hydrophobicity increase as the amount of DMTSP in the hybrid increased [280].

The spectra of the DMTSP containing films showed additional bands at  $1069\text{ cm}^{-1}$  stretching and bending at  $833\text{ cm}^{-1}$  (Figures 8.2B-8.2D) that can be ascribed to Si-O-P bands [274]. These results suggested that DMTSP was successfully incorporated and bonded with siloxane in the hybrid network.

For further information about the effect of addition of DMTSP on the structure of the formed films, NMR analysis of the obtained xerogels have been analyzed using  $^{29}\text{Si}$  –NMR solid state  $^{29}\text{Si}$ .

### 8.1.2.1 $^{29}\text{Si}$ -NMR

$^{29}\text{Si}$ -NMR spectroscopy affords significant information about the nature of the organosilica network regarding the cross-linking and to quantify the proportions of the condensed silicate species. In other words, the  $^{29}\text{Si}$ -NMR can determine relative concentrations of  $\text{Q}^n$  and  $\text{T}^n$  species in the organic-inorganic hybrid and the influence of the DMTSP on the condensation of the inorganic silica in this siloxane network. The  $^{29}\text{Si}$  NMR spectra of the prepared MAPTMS/TMOS/DMTSP system are shown in Figure 8.3. The chemical shift of a silicon atom in siloxane network is referred to use the traditional terminology  $\text{Q}^n$  and  $\text{T}^n$  where the superscript corresponds to the number of oxygen bridge to other silicon atoms [83].

In the spectre of the control sample, four peaks have been observed at  $-59.6$ ,  $-67.7$ ,  $-100.41$  and  $-111.22$  ppm (Figure 8.3A), corresponding to the units  $\text{T}^2$ ,  $\text{T}^3$ ,  $\text{Q}^3$  and  $\text{Q}^4$  respectively.

In the spectra MAPTMS/TMOS/DMTSP there are a decrease in the intensity of the peak located  $-59.6$  ( $\text{T}^2$ ), together with increase of that at  $-67.7$  ppm ( $\text{T}^3$ ) as the content of DMTSP increased (Figures 8.3B and 8.3C). These indicate the cross-linking have been enhanced by addition of DMTSP in the hybrid. Since the DMTSP incorporation gave greater peaks for the bridges, the addition of DMTSP promoted the condensation of the silanol groups of the mixture. The hybrid with DMTSP gave a larger fraction of  $\text{T}^3$  and  $\text{Q}^4$  than that from control sample. The relative intensity (in area) of  $\text{T}^3/\text{T}^2$  signals is 1.94, 8.12 and 16.27 for xerogels containing 0.3 and 0.9 ml DMTSP respectively, indicating that the 0.9 DMTSP containing xerogel presents a highest cross-linking degree.

DMTSP containing films showed the highest degree of cross-linking which could be due to the higher silicon content of these films, as the DMTSP precursor contain silicon atom bind to phosphorus

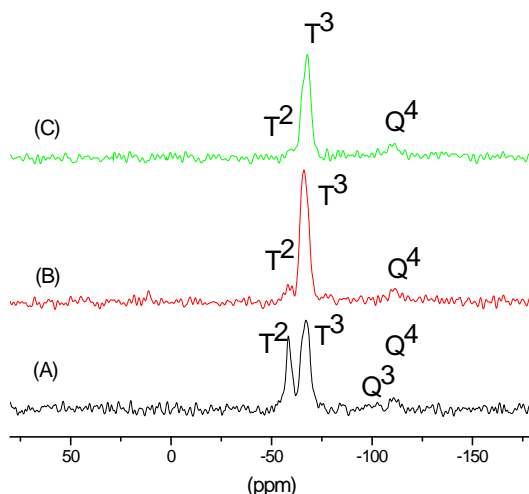


**Fig. 8.3.** Solid state  $^{29}\text{Si}$ -NMR spectra of MAPTMS / TMOS containing (A) 0ml (B) 0.3ml DMTSP (C) 0.9ml DMTSP

### 8.1.3 Energy dispersive X-ray (EDX) and Scanning Electron Microscope (SEM)

Scanning electron microscope (SEM) was used to study the morphology of the prepared hybrid coatings. The SEM observations of the surface morphology and appearance of the prepared hybrid films are presented in Figures 8.4A-8.4D.

All films showed the formation of a uniform, homogeneous, crack free and highly adherent protective film on the substrates that should lead to a good corrosion resistance of Ti6Al4V alloys coated with the organic–inorganic hybrid coatings.

The EDX spectra of the MAPTMS/TMOS-Ti6Al4V system showed the presence of elements from the substrate (Ti and Al) which could reflect the porosity of such coating (Figure 8.4A).

# Organic-inorganic hybrid sol-gel thin films modified with Dimethylsilylphosphite as phosphorous precursor

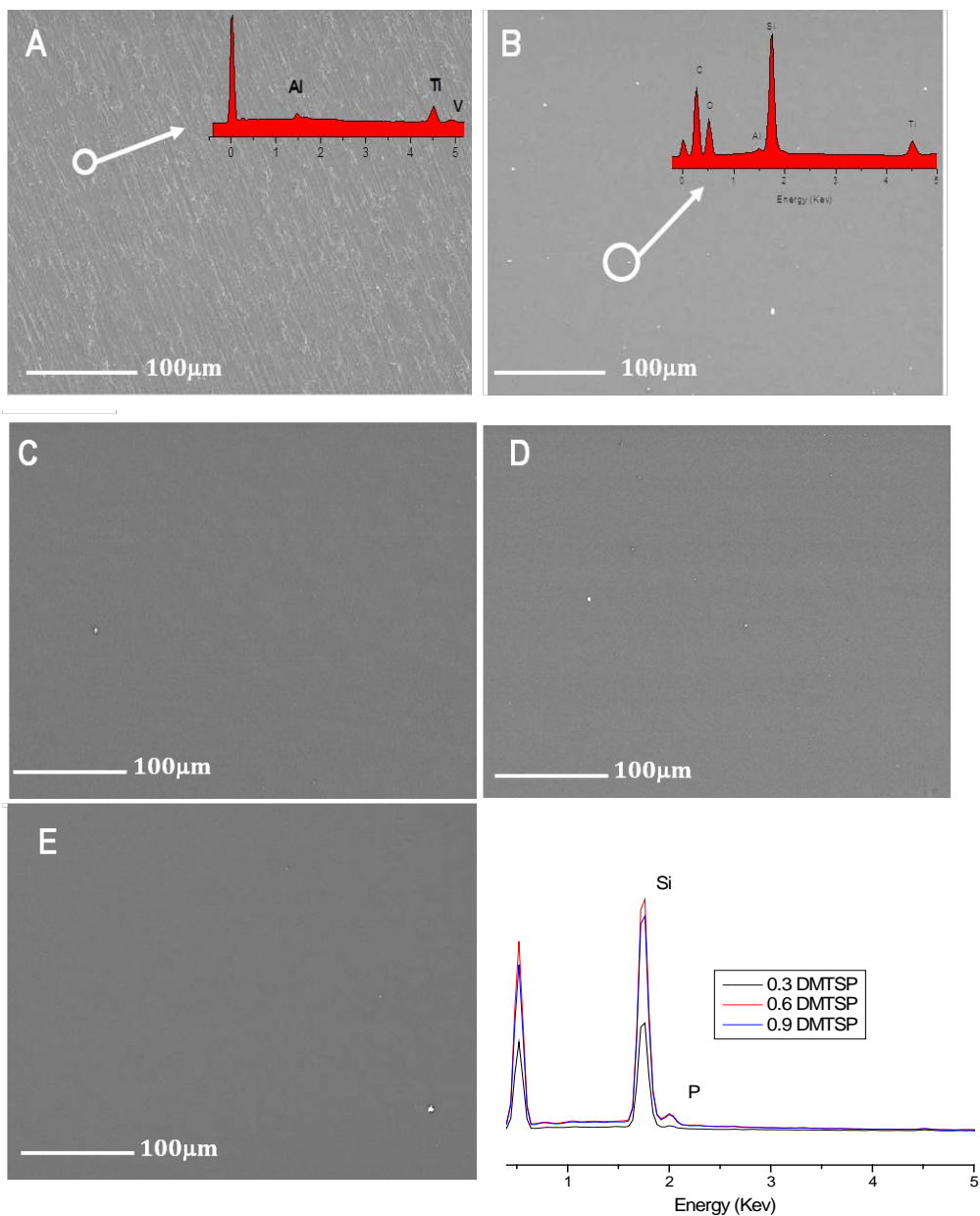


**Fig.8.4** SEM/EDX images for the prepared hybrid coatings deposited on Ti6Al4V substrates, un-coated (A) , and containing 0 ml DMTSP (B); 0.3 ml DMTSP ( C); 0.6 ml DMTSP (D) and, 0.9 ml DMTSP (E) respectively.

The EDX spectra of the MAPTMS/TMOS/DMTSP-Ti6Al4V systems show the phosphorus which confirms the incorporation of the DMTSP in the hybrid films (Figure 8.4C-D). No elements from the alloy surface have been detected in EDX spectra, which indicate the effectiveness of such coating in coverage of the whole substrate surfaces.

### 8.1.4 Contact angle

The sessile drop method has been used to evaluate the water contact angle of all prepared films. It appears that the films containing DMTSP films are slightly hydrophobic with respect to the control film. The measured values are  $67.1 \pm 1.17$ ,  $75.3 \pm 1.72$ ,  $76.0 \pm 0.28$  and  $79.3 \pm 0.46$  for the control film, and those containing 0.3-0.9 ml DMTSP respectively. The contact angle shows a slight increase, as the amount of DMTSP does. This indicates that the incorporation of DMTSP in the hybrids slightly decrease the wettability of the hybrids. Such variation of the wettability could affect the cellular response to these films. This in agreement with the results obtained by ATR-IR and  $^{29}\text{Si}$ -NMR, the decrease of the Si-OH bands was correlated with the reduction of the wettability of the DMTSP containing hybrid films.

## 8.2 In-vitro bioactivity

### 8.2.1 Cytotoxicity /viability

The formation of an implant-tissue interface depends on the physico-chemical properties and the cell biocompatibility of an implant material. Biocompatibility involves two different aspects, biological safety and bio-functionality <sup>[281]</sup>. The analysis of biological safety includes testing of the cytotoxicity which could be accomplished using the Neutral red uptake assay as mentioned <sup>[115]</sup>. On the other hand, the surface of a biomaterial is the major parameter influencing in its bio-functionality. Initial cell attachment to a material surface determines the subsequent processes like cell adhesion, spreading, morphology, migration, proliferation and differentiation <sup>[282, 283]</sup>.

## Organic-inorganic hybrid sol-gel thin films modified with Dimethylsilylphosphite as phosphorous precursor

The influences of DMTSP incorporation in the MAPTMS/TMOS films on the proliferation of NHOst have been studied by neutral red uptake assay. Figure 8.5 shows the osteoblast cytotoxicity/ viability on the un-coated and coated Ti6Al4V alloy after 7 days culture.

At the 7 days culture interval, the absorbance values for uncoated surfaces were lower, while coated surfaces registered higher absorbance values. On the other hand, cell vitality was seemingly enhanced by the coated surfaces, as evident by the increase in absorbance values. The proliferation of osteoblasts on the coated film was higher than those of un-coated one after 7 days in culture. However, the proliferation of osteoblasts on the hybrid films containing DMTSP was comparable to that of the un-coated and control film. The cell viability tendency on the DMTSP containing film increased as the content of DMTSP in the hybrid increased. This result indicates of better performance tendency of cells adhered to the DMTSP containing film than that to the control sample and uncoated substrate.

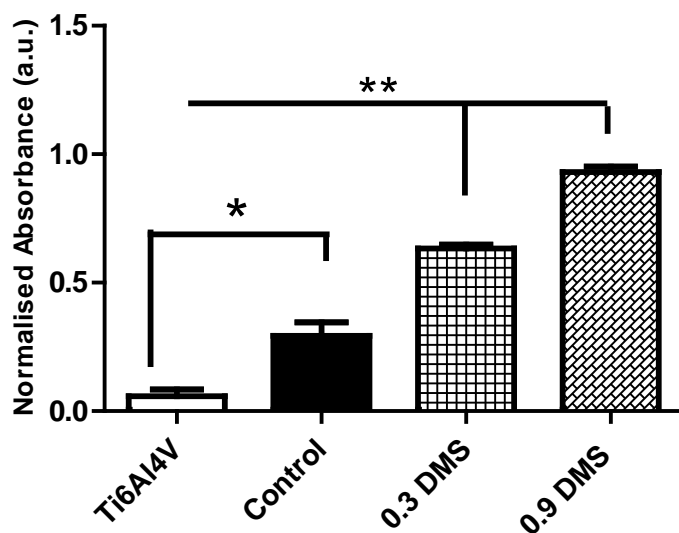


**Fig. 8.5.** Neutral red proliferation/cytotoxicity assay for NHOst cultured on un-coated Ti6Al4V, MAPTMS/TMOS-Ti6Al4V system (control) and hybrids containing DMTSP (0.3 and 0.9 ml) over a 7 day period.

This result suggests that the presence of phosphorus in the coating may be helpful in improving cell growth and in turn osteointegration. In comparison with the HAp and TEP containing hybrids, mentioned in chapter 6 and 7, the DMTSP containing films showed the highest degree of cross-linking which could be due to the higher silicon content of these films, as the DMTSP precursor contain silicon atom bind to phosphorus. This could make the DMTSP containing film show the best biological performance as it contain more silicon but the same phosphorus both of which are important for the biological performance and cell proliferation.

Film composition could be another factor, which determines the functional activity of cells in contact with a biomaterial. Thus, as a result of further cross-linking of the films upon addition of DMTSP, the toxic ions from the alloy will not release to the culture medium and in turn result in better viability of osteoblasts on these films.

### 8.2.2 Cell adhesion

Cell adhesion has influence on the proliferation and differentiation of bone cells, as well as on the osseointegration of bone-implant and so is of critical importance for biocompatibility of the material <sup>[284]</sup>. It is known that the cell adhesion and further spreading on the surface of the substrate is the first phase of the interaction between cells of the organism and the implant; therefore, the quality of the first phase is of critical importance for biocompatibility of the material.

The cell morphology on the prepared hybrid films with and without DMTSP were analyzed using fluorescence microscopy (Figure 8.6). The figure shows the morphology of adherent cells cultured for 7 days on the uncoated and coated Ti6Al4V substrates with various coating compositions.

Our in-vitro study showed that osteoblasts spread both on the surface of uncoated Ti6Al4V and on the Ti6Al4V coated with MAPTMS/TMOS and MAPTMS/TMOS/DMTSP films. The cell on the surfaces of the DMTSP containing films has more focal adhesion contacts/vinculin compared with the uncoated or control sample.

The formation of more focal adhesion contacts on the surfaces containing DMTSP (Figures 8.6) indicates that osteoblast-like cells were highly activated with strong adhesion on these films. On the other hand, fewer focal adhesions were exposed with assembled

vinculin formed in the cells on the un-coated or control film (Figure 8.6). Thus, the actin stress fibers and focal adhesions were not completely formed in the cells adhering on the films without DMSTP. Thus, osteoblasts growing on the uncoated substrates created less mature focal contacts than osteoblasts growing on the coated films.

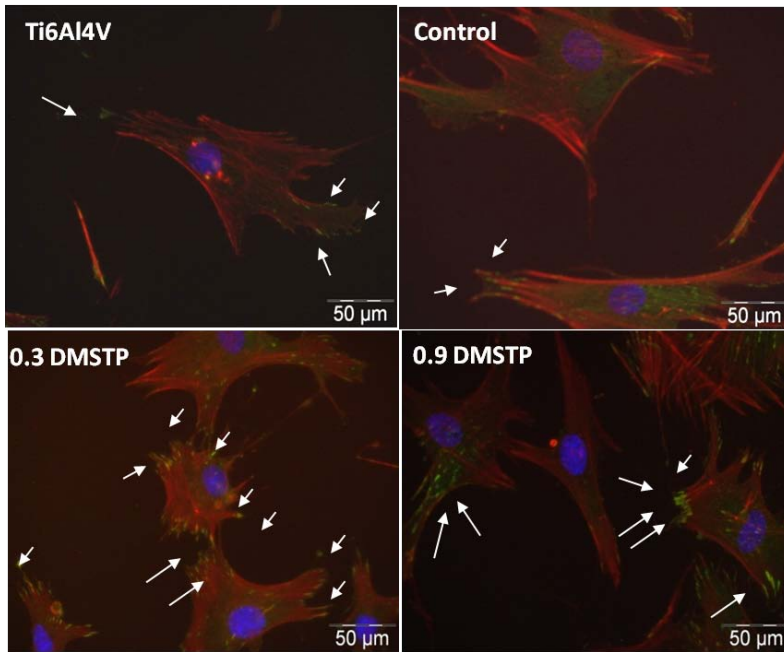


**Fig. 8.6** Fluorescence graphs of OB-cells growing on un-coated Ti6Al4V and coated surfaces for vinculin (green), actin (red) and nuclei (blue).

Our results are in agreement with previously published observations. It has been repeatedly reported that cell adhesion and proliferation depends on surface chemistry and, varies with surface composition rather than general surface properties like wettability [285-290]. Thus, cell proliferation on these surfaces was different depending primarily on the film composition rather than on wettability.

In our study we detected that the osteoblasts' cells more effectively adhere on the surface of phosphorus containing films, mixed at molecular level, than on the films without phosphorus or phosphorus mixed at particle level (Hap containing films chapter 6). The results obtained suggest that the composition of the films plays an important role

at different stages of interaction between osteoblasts and the substrate surface. There were greater numbers of cells on samples with silane/DMTSP coating (Figure 8.6), which would be explained by better cell viability.

### **8.3. *In vitro* corrosion protection behaviour of the DMTSP modified organic–inorganic hybrid coatings on Ti6Al4V alloy**

*In vitro* corrosion and protection studies of the MAPTMS/TMOS/DMTSP-Ti6Al4V system immersed in Kokubo's simulated body fluid (SBF) have been carried out by electrochemical impedance measurements. Figure 8.7 shows impedance plots of three identical samples of a MAPTMS/TMOS/DMTSP-Ti6Al4V system after 24 hours of immersion tests in SBF. This system was formulated with a volumetric ratio of 0.6 ml of DMTSP per 20 ml of 4:1 MAPTMS/TMOS sol. The reproducibility of the experimental impedance data obtained was quite acceptable. In Figures 8.7 A and 8.7 B the impedance data have been represented in the complex plane as Nyquist plots, using two different scales. Figure 8.7A shows the Nyquist plots for the wide frequencies range. Figure 8.7B shows a detail of the high frequency arcs. In Figure 8.7C the variations of the logarithm of the impedance module and phase angle both against the frequency logarithm are displayed in format of Bode plots. The symbols of these plots represent the experimental data, while the lines represent the modeled data obtained using the equivalent circuit shown in Figure 8.7D. Table 8.2 shows the results obtained by applying such equivalent circuit to the fitting complex nonlinear least-squares (CNLS) techniques of the ZView software to analyze these experimental impedance data.

Good fitting results were obtained by using the equivalent circuit of Figure 8.7D to the values measured in a wide frequency range. The physical meaning of the electrical elements of this equivalent circuit was discussed in chapter 4 (Figures 4.16A and 4.16B). The chi-square values provide an estimation of the fitting quality. The chi-square values were lower than  $10^{-3}$ , proving the fitting quality for all the tested MAPTMS/TMOS/DMTSP-Ti6Al4V samples. The error values obtained for the calculated values of the electrical elements of this equivalent circuit are also low for all the tested samples.

# Organic-inorganic hybrid sol-gel thin films modified with Dimethylsilylphosphite as phosphorous precursor

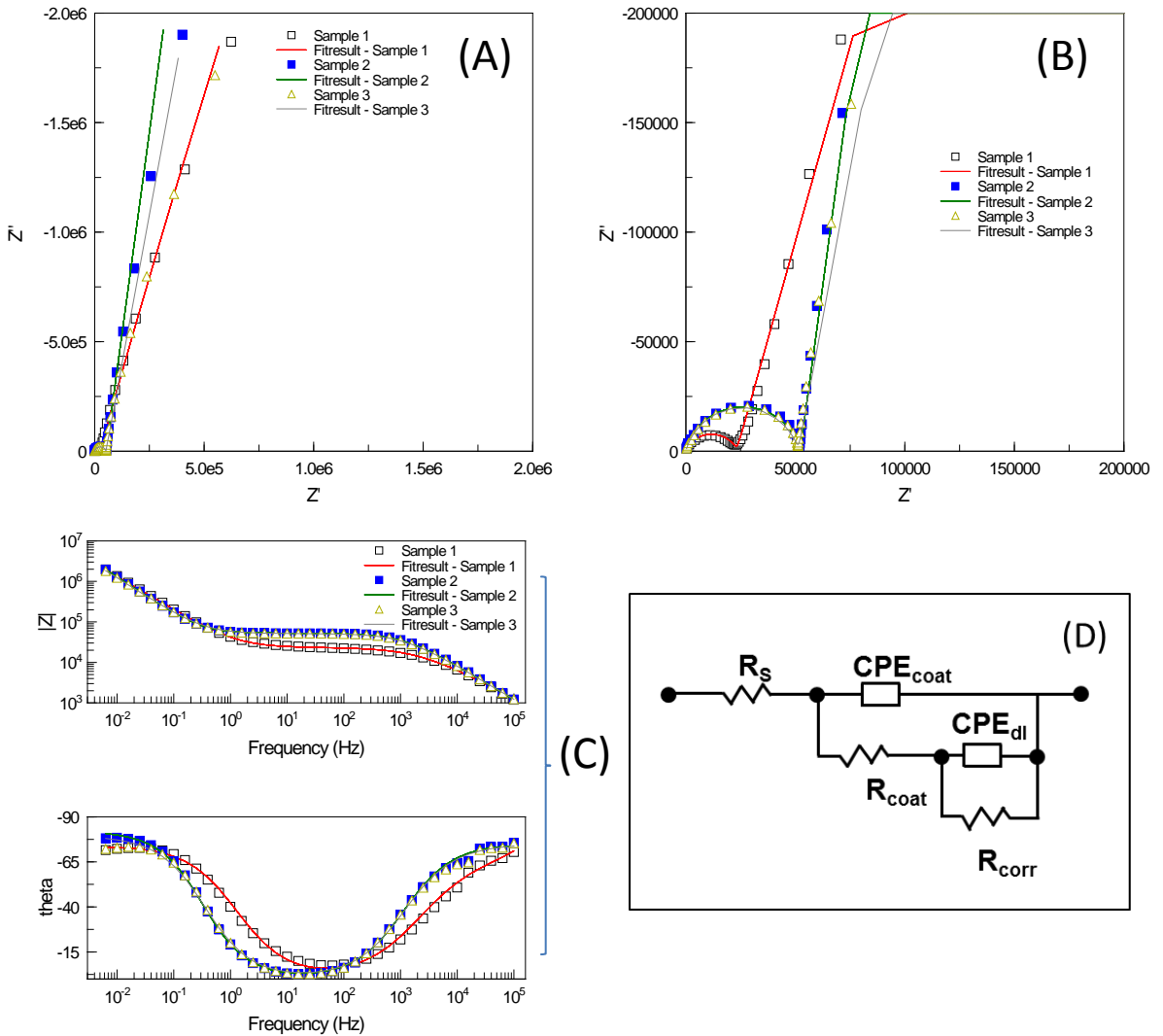


**Fig.8.7** Experimental impedance plots and fit results obtained for three identical samples of MAPTMS/TMOS/DMTSP-Ti6Al4V. DMTSP/silanes ratio = 0.6 ml/20 ml. Immersion time in SBF: 1day.

**Table 8.2** Values obtained for the electrical elements of the equivalent circuit shown in Figure 8.7

Samples: MAPTMS/TMOS/DMTSP-Ti6Al4V.

DMTSP /silanes = 0.6 ml/20 ml; Immersion time in SBF: 1day.

Electrical Element	Sample 1	Sample 2	Sample 3
$R_s/\Omega$	174.90 ± 44.00	17.74 ± 21.19	2.57 ± 31.75
$C_{coat-T}/\Omega^{-1}\cdot s^{P1}$	$3.68\cdot 10^{-8} \pm 3.24\cdot 10^{-9}$	$1.05\cdot 10^{-8} \pm 4.18\cdot 10^{-10}$	$1.16\cdot 10^{-8} \pm 6.73\cdot 10^{-10}$
$C_{coat-P1}$	0.74 ± 0.01	0.84 ± 0.01	0.84 ± 0.01
$R_{coat}/\Omega$	$2.36\cdot 10^5 \pm 2.43\cdot 10^2$	$5.23\cdot 10^5 \pm 2.60\cdot 10^2$	$5.15\cdot 10^5 \pm 3.81\cdot 10^2$
$C_{dl-T}/\Omega^{-1}\cdot s^{P2}$	$7.42\cdot 10^{-6} \pm 6.94\cdot 10^{-8}$	$9.84\cdot 10^{-6} \pm 7.22\cdot 10^{-8}$	$9.50\cdot 10^{-6} \pm 1.03\cdot 10^{-7}$
$C_{dl-P2}$	0.83 ± 0.01	0.91 ± 0.01	0.88 ± 0.01
$R_{corr}/\Omega$	$1.28\cdot 10^8 \pm 1.71\cdot 10^8$	$1\cdot 10^{20} \pm 1\cdot 10^{20}$	$1\cdot 10^{20} \pm 1\cdot 10^{20}$
<b>Chi-Squared</b>	0.0028773	0.0014146	0.0028864
<b>Weighted Sum of Squares</b>	0.19278	0.094776	0.19339

The electrical performance of the DMTSP sol-gel coatings is very different to that observed for the blank coating. Figure 8.8 A and 8.8 B show the Nyquist impedance plots (in two different scales), obtained for MAPTMS/TMOS/DMTSP-Ti6Al4V systems with different content in DMTSP and for an uncoated Ti6Al4V sample and, after 1 day of immersion test in SBF. Figure 8.8 C shows the same impedance data in Bode form. By comparing the impedance response obtained for the sol-gel coatings containing phosphorus in their organic-inorganic network with the impedance response of the blank samples (phosphorus-free sol-gel coatings) it can be observed that the High-Frequency Arcs (HFAs) of the DMTSP sol-gel coatings intercept the real axis of Nyquist plots at lower  $Z'$  impedance values than the HFA obtained for the blank coating Figure 8.8 A and 8.8 B.

# Organic-inorganic hybrid sol-gel thin films modified with Dimethylsilylphosphite as phosphorous precursor

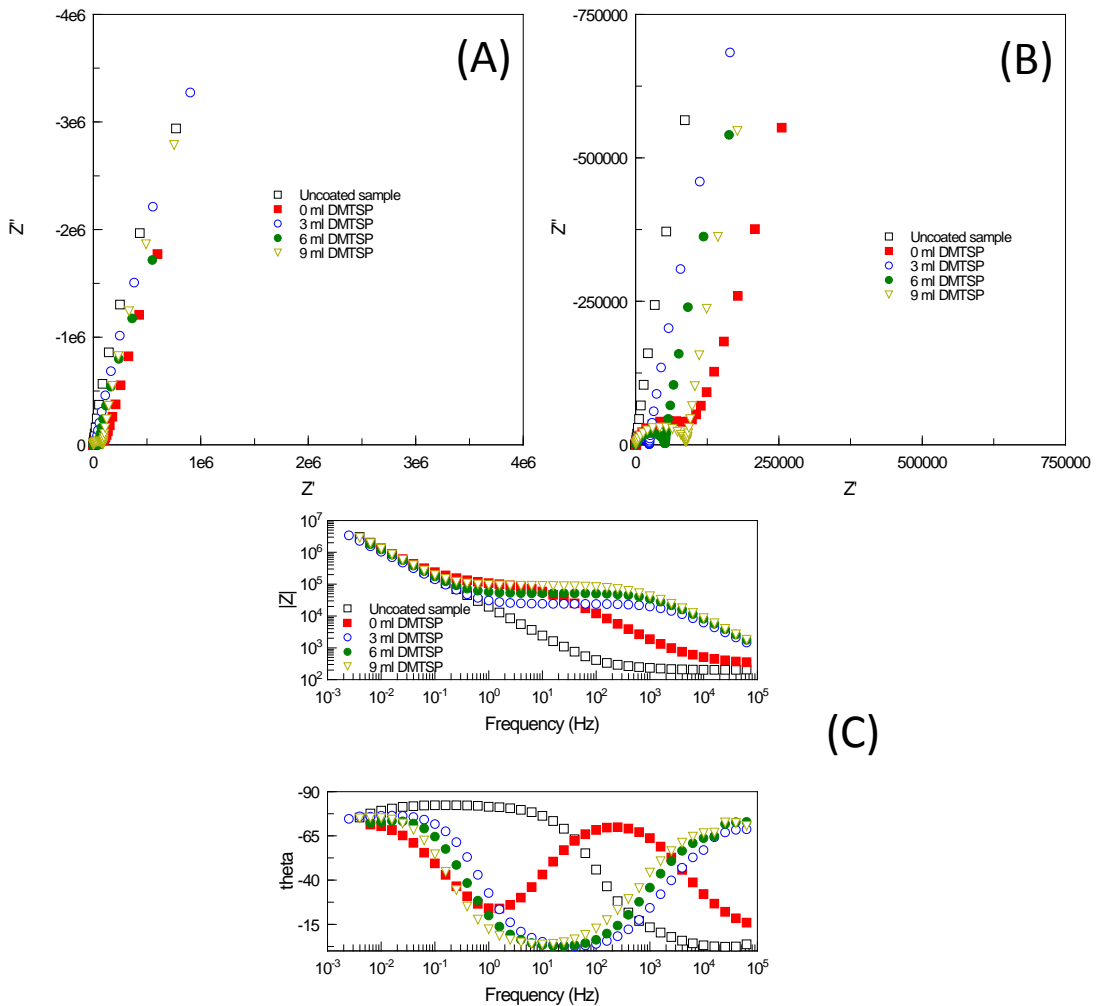


**Fig.8.8** Nyquist plots, represented in two different scales[(A) and (B)] and, Bode plots (C) obtained for an uncoated Ti6Al4V sample and Ti6Al4V samples coated with DMTSP sol-gel thin films with different DMTSP contents: 0 ml (blank sample), 0.3 ml, 0.6 ml and 0.9 ml respectively. Electrolyte: SBF. Immersion Time: 1day

Table 8.3 shows the variations of resistance values ( $R_{HFA}$ ) and CPE parameters,  $(CPE-T)_{HFA}$  and  $(CPE-P)_{HFA}$ , associated to the impedance responses obtained for high frequencies as a function of the phosphorous content in the hybrid organic-inorganic network of the sol-gel coatings. The  $R_{HFA}$  values and  $CPE_{HFA}$  parameters are showed in this table for comparison purposes. The physical meaning of these parameters has been discussed in chapter 7.3 (see Table 7.7 and its comments). For the MAPTMS/TMOS/DMTSP-Ti6Al4V systems,  $R_{HFA}$  and  $CPE_{HFA}$  are ascribed to the sol-gel coating resistance  $R_{coat}$ , and to the constant phase element of the sol-gel coating  $CPE_{coat}$ , respectively.

The  $R_{coat}$  and  $(CPE-T)_{coat}$  values obtained for the DMTSP sol-gel coatings are one order of magnitude lower than the  $R_{coat}$  values for the blank samples (0 ml DMTSP sol-gel coatings), as clearly shows Table 8.3 . These differences indicate that the DMTSP sol-gel coatings have higher porosity degree and lower dielectric constant than the phosphorous-free blank sol-gel coatings. Higher porosity means lesser barrier properties, but lower dielectric constant suggests that the intact areas of the coating are a better barrier against the water up-take.

**Table 8.3** Resistance values and CPE parameters associated to the high frequency arc (HFA) obtained for an uncoated Ti6Al4V sample and for MAPTMS/TMOS/DMTSP-Ti6Al4V systems with different DMTSP content. Electrolyte: SBF. Immersion time: 1day.

Sample	$R_{HFA}/ohms$	$(CPE-T)_{HFA} / ohms^{-1} \cdot s^{-P}$	$(CPE-P)_{HFA}$
<b>Uncoated Ti6Al4V</b>	$1.03 \cdot 10^7$	$1.19 \cdot 10^{-5}$	0.91
<b>0 ml DMTSP coating</b>	$1.14 \cdot 10^5$	$4.21 \cdot 10^{-7}$	0.82
<b>0.3 ml DMTSP coating</b>	$2.46 \cdot 10^4$	$1.60 \cdot 10^{-8}$	0.82
<b>0.6 ml DMTSP coating</b>	$5.31 \cdot 10^4$	$1.27 \cdot 10^{-8}$	0.83
<b>0.9 ml DMTSP coating</b>	$8.67 \cdot 10^4$	$1.36 \cdot 10^{-8}$	0.82

## Organic-inorganic hybrid sol-gel thin films modified with Dimethylsilylphosphite as phosphorous precursor

Figures 8.9 and 8.10 show the evolution of impedance plots (Nyquist and Bode representations) with the immersion time in SBF of a MAPTMS/TMOS/DMTSP-Ti6Al4V sample whose sol-gel coating was formulated with a ratio of DMTSP 0.9 ml per 20 ml of the MAPTMS/TMOS silane mixture.

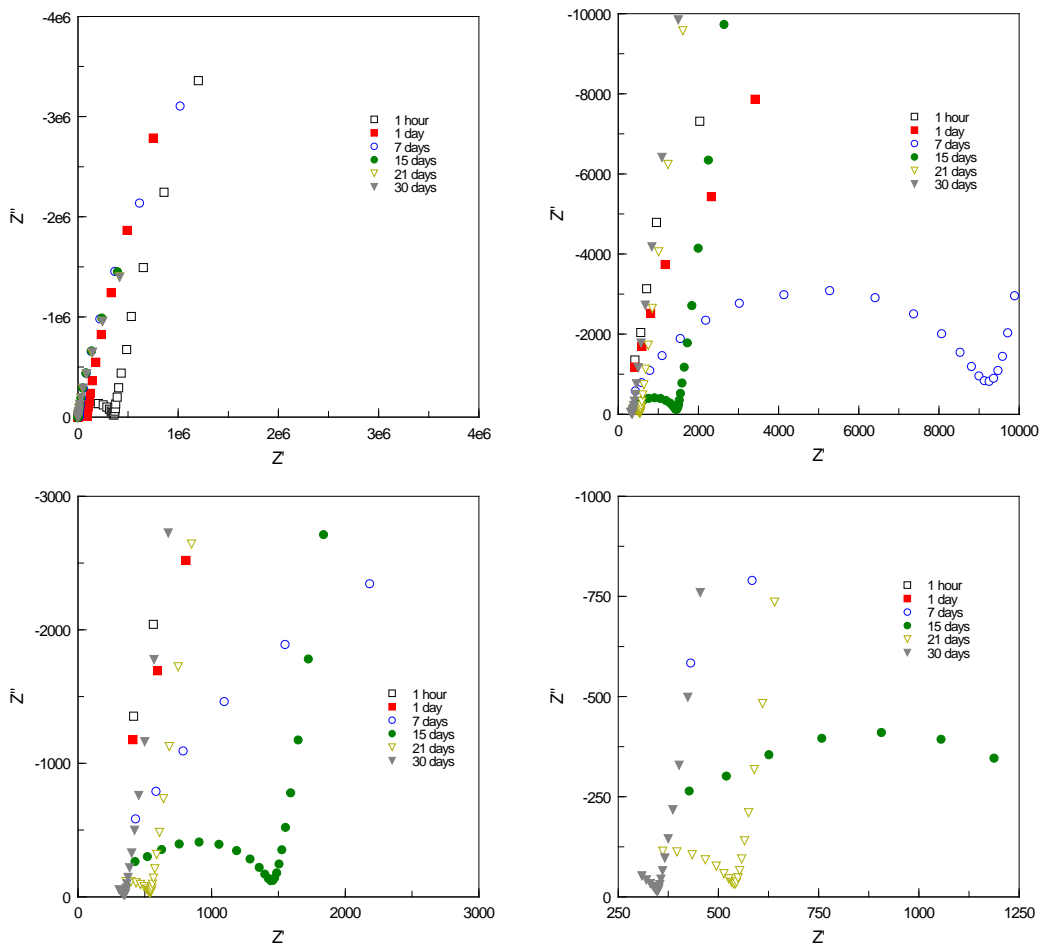


**Fig.8.9** Evolution of the Nyquist plots with the immersion time in Kokubo solution for a MAPTMS/TMOS/DMTSP-Ti6Al4V system. DMTSP/silanes ratio = 0.9 ml/20 ml.

The Nyquist plots have been represented at different magnifications, increasing the zoom of the HF region from the upper left plot to the lower right plot, to study in detail the evolution of the High-Frequency Arcs (HFAs). The impedance plots show that the values of the impedance modulus continuously decrease within the immersion time, reaching its lowest values after 30 days in SBF. This behaviour is ascribed to the gradual loss of the barrier properties of the coating and the water uptake which such a coating undergoes during the immersion test in the SBF. The evolution with time of the  $R_{\text{coat}}$  and  $C_{\text{coat}}$  values calculated from the HFAs confirm this interpretation.

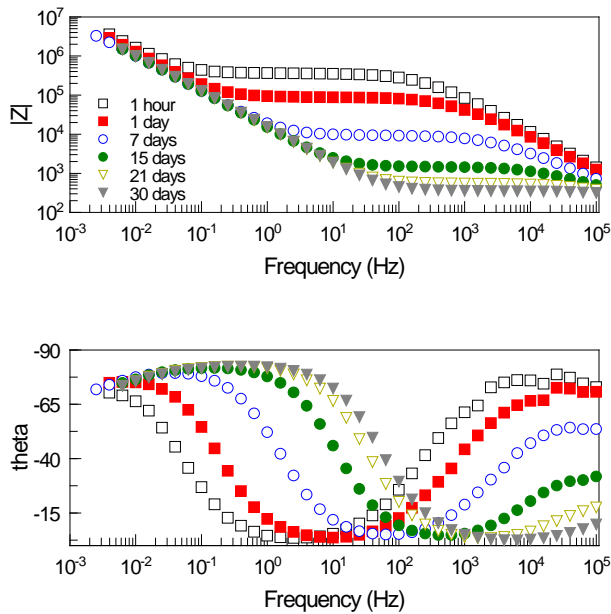


**Fig.8.10** Evolution of the Bode plots with the immersion time in Kokubo solution for a MAPTMS/TMOS/DMTSP-Ti6Al4V system. DMTSP /silanes ratio = 0.6 ml/20 ml.

( $R_{\text{coat}}$ ) values with the immersion time in SBF, and ii) a continuous increase of the coating capacitance, correlated with the changes of CPE-T values and CPE-P. This behaviour is typically associated to the loss of the barrier properties and the increase of the water uptake in the coatings. The order of magnitude of the CPE-T values obtained from the Low-Frequency Arcs (LFAs) are indicating that this LFAs are due to the association in parallel of an electrochemical double layer capacitor ( $C_{\text{dl}}$ ) and an ion-electron charge

## Organic-inorganic hybrid sol-gel thin films modified with Dimethylsilylphosphite as phosphorous precursor

---

transfer resistor ( $R_{corr}$ ), situated both at the metal/solution interface into the base of the pores of the sol-gel coating in contact with SBF. The values of the parameters  $R_{corr}$ , Cdl-T and Cdl-P remain stable during the 30 days of immersion in SBF. Cdl-P presents values close to 1, which indicates that  $C_{dl}$  behaves approximately, as a pure capacitor. It is worth remembering that all Ti6Al4V samples were polished before being coated with the MAPTMS/TMOS/DMTSP sol. Cdl-P values close to 1 are also indicating that the surface of the metal substrate located at the base of the pores beneath the sol-gel coating remains flat and free of corrosion products during the 30 days of the immersion test in SBF. The high values found for  $R_{corr}$  support this interpretation.

All results obtained by applying the electrochemical impedance spectroscopy technique and presented in the previous paragraphs are very promising. However, the low values found for the  $R_{coat}$  parameter of these DMTSP sol-gel coatings can suggest that these sol-gel formulations will not be suitable for the development of coatings with high barrier properties when exposed for long time to immersion tests in SBF.

The low barrier properties for long time could be potentially dangerous from the standpoint of corrosion protection. A logical way to overcome this drawback can be the development of strategies which consist in applying coating systems with gradient properties based on the deposition of multilayer coatings. Such systems that the outer layer of the coating system in contact with the SBF possesses high bio-active performance and the inner layer of the coating in contact with the metal substrate retains its barrier properties (inert behaviour) throughout all the period of long term immersion tests .

The barrier mechanism of the corrosion protection coatings is opposite to the bio-active mechanism of those coatings based on biomimetic performance. Thus, it is not possible to optimize both mechanisms in the same coating. For this reason multilayered coatings are needed for the approach of our study, in which the most external layer is bioactive and the internal film is chemically inert.

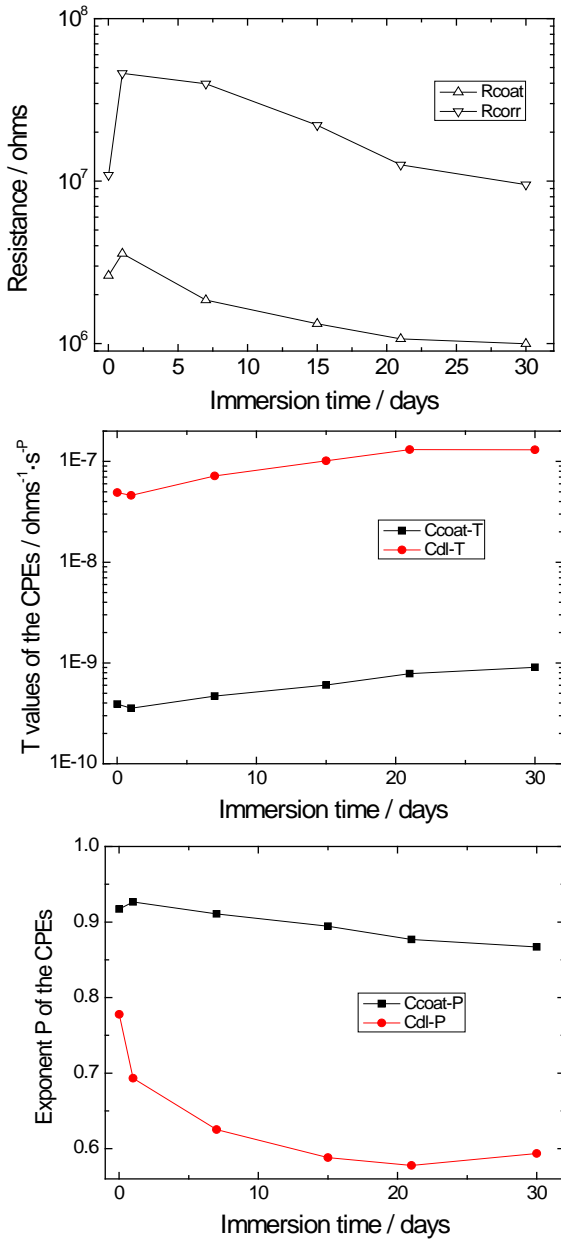


**Fig.8.11** Evolution of the equivalent circuit parameters with the immersion time in Kokubo solution of the MAPTMS/TMOS/DMTSP-Ti6Al4V system. Formula: 0.9 ml of DMTSP per 20 ml of silanes mixture.

## Organic-inorganic hybrid sol-gel thin films modified with Dimethylsilylphosphite as phosphorous precursor

---

Figure 8.12 shows the experimental results of the impedance plots obtained for an uncoated Ti6Al4V sample and two MAPTMS/TMOS/DMTSP-Ti6Al4V systems based on 1 and 2 coats respectively. The formulation of the topcoat for the system based in two sol-gel coats had a DMTSP/silanes ratio equal to 0.6 ml/20 ml. The innercoat of the two coats system was formulated with a MAPTMS and TMOS mixture with a 4:1 MAPTMS/TMOS molar ratio which provided a barrier effect to the system. The formulation of the one coat system was identical to that sol-gel topcoat. The impedance plots were recorded after 1day of immersion in SBF.

In Figures 8.12 A and 8.12 B the impedance data are represented in Nyquist diagrams by using two different scales for the impedance values. Figure 8.12 shows the complete impedance Nyquist plot for the entire tested frequencies domain. Figures 8.12B zooming a detail of the low frequency response of the tested samples in this study. Finally in Figure 8.12C the impedance plots were displayed by using the Bode representation.

The analyses of these experimental impedance plots were carried out using the equivalent circuit showed in Figure 8.7 D. Fitting complex nonlinear least-squares (CNLS) techniques available in the ZView software were used again for such a study. Table 8.4 shows the values obtained for each electrical element of the equivalent circuit. The application of two coats improves notably the barrier properties of the MAPTMS/TMOS/DMTSP-Ti6Al4V systems which reach  $R_{coat}$  values of  $3.90 \cdot 10^6$  ohms, comparable to those obtained for the MAPTMS/TMOS/TEP-Ti6Al4V systems based in the use of a single coat.

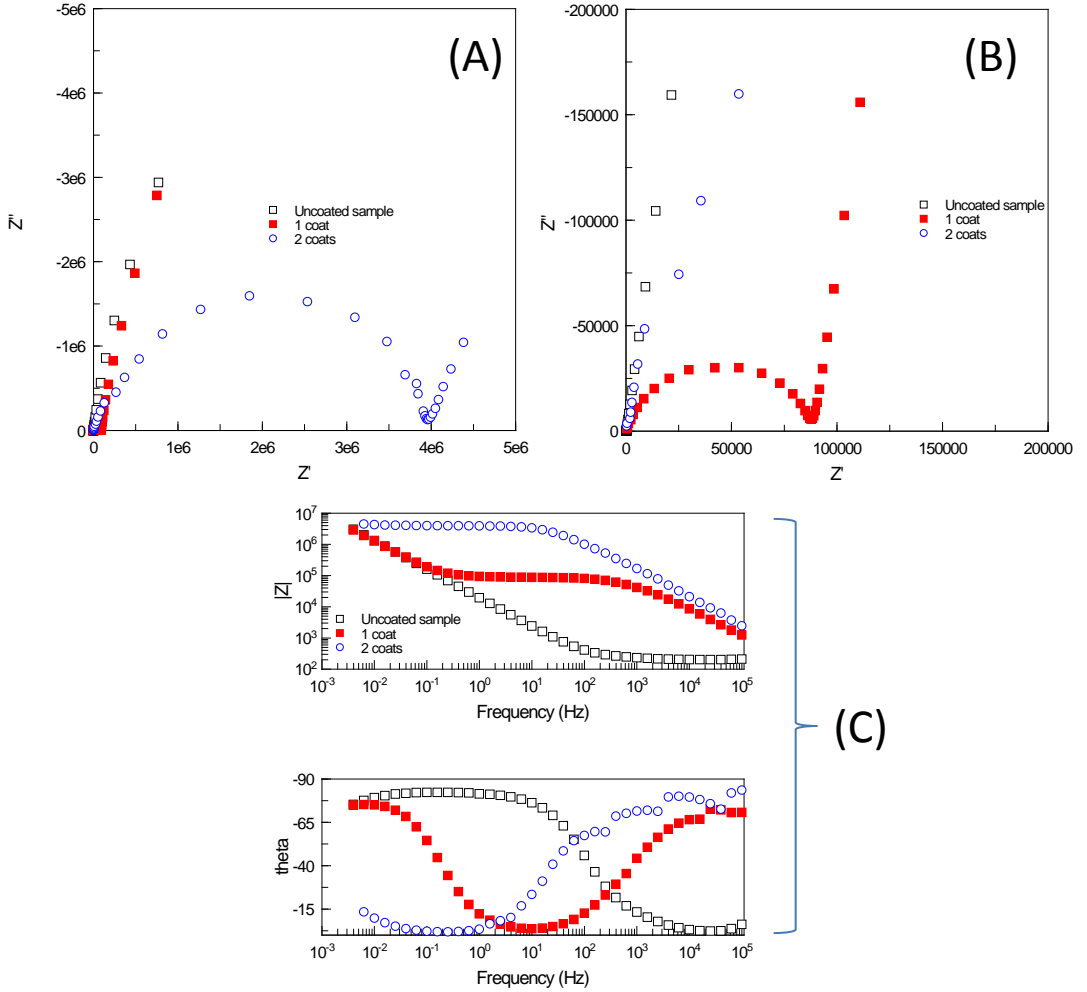


**Fig.8.12** Impedance plots obtained for an uncoated Ti6Al4V sample and for two MAPTMS/TMOS/DMTSP-Ti6Al4V systems based on 1 and 2 coats respectively. DMTSP/silanes ratio = 0.9 ml/20 ml. Immersion time in SBF: 1day.

# Organic-inorganic hybrid sol-gel thin films modified with Dimethylsilylphosphite as phosphorous precursor

---

**Table 8.4** Calculated values for each element of the equivalent circuit of an uncoated Ti6Al4V sample and of two MAPTMS/TMOS/DMTSP-Ti6Al4V systems based on 1 and 2 coats respectively. Immersion time in SBF: 1 day. (DMTSP/silane ratio = 0.9 ml/20 ml).

## Bare Ti6Al4V sample

Rs (CPE-Rp)

Rs = 244.9 ( $\pm 1.9042$ )

CPE-T =  $9.4795E-6(\pm 2.3278E-08)$

CPE-P =  $0.91454(\pm 0.00071167)$

Rp =  $2.5399E7(\pm 1.8004E06)$

## MAPTMS/TMOS/DMTSP-Ti6Al4V systems

### **HFA for 1 coat:**

Rs (CPE-Rp)

Rs = 37.68 ( $\pm 34.82$ )

CPE-T =  $1.36E-8 (\pm 7.5806E-10)$

CPE-P =  $0.81962 (\pm 0.0051829)$

Rp =  $86653 (\pm 1068.9)$

### **LFA for 1 coat:**

Rs (CPE-Rp)

Rs = 88402 ( $\pm 288.69$ )

CPE-T =  $9.6584E-6 (\pm 2.5721E-08)$

CPE-P =  $0.90699 (\pm 0.0011832)$

Rp =  $3.0449E7 (\pm 1.479E06)$

### **HFA for 2 coats:**

Rs (CPE-Rp)

Rs = -228.8 ( $\pm 156.17$ )

CPE-T =  $3.303E-9 (\pm 1.9178E-10)$

CPE-P =  $0.8643 (\pm 0.0060804)$

Rp =  $3.902E6 (\pm 93302)$

### **LFA for 2 coats:**

Rs (CPE-Rp)

Rs =  $3.9406E6 (\pm 8695.7)$

CPE-T =  $1.0313E-5 (\pm 4.2816E-07)$

CPE-P =  $0.76344 (\pm 0.015456)$

Rp =  $4.1164E7 (\pm 3.5347E07)$

### Conclusion

The incorporation of DMTSP in the organic-inorganic hybrid based on MAPTMS/TMOS lead to emergence of Si-O-P and  $\text{PO}_4^{-3}$  both of which indicate that the DMTSP has been mixed at molecular level and successfully incorporated in the network. Denser films have been obtained after incorporation of DMTSP, thus these films with DMTSP could act as an effective physical barrier. Again the presence of phosphorus at molecular level, results in enhancement of the osteoblast cytotoxicity /viability and adhesion.

## ***Chapter (9)***

*Comparison between functionalities of prepared Organic-inorganic hybrid sol-gel thin films*



## Comparison of functionalities of the O-I hybrid coatings /Ti6Al4V

### 9.1 Biological Protein adsorption:

To evaluate the potential use of prepared coatings for biomedical implants, fibrinogen adsorption on the surface of the prepared films is examined. After placement of the implant into a biological environment a protein film adsorbs before cell attachment occurs. Thus, high capacity of protein adsorption is an important property of implant surfaces for biomedical applications. Researches demonstrated that cell adhesion and survival could be modulated by protein pre-adsorption on the scaffold. The more the protein is adsorbed in a scaffold, the more cells can attach and survive.

According to the popularly accepted understanding, electrostatic interactions are very important for protein adsorption, and P sites, are necessary to perform as bridge between coated surfaces and proteins [254]. In neutral biological fluid, fibrinogen would be positively charged and would combine with  $\text{PO}_4^{3-}$  by electrostatic attractive forces. The prepared hybrid coatings in the present study showed enhancement of protein adsorption after modification of the silane matrix with HAp or TEP, both of which could provide binding sites for fibrinogen due to the incorporation of P sites in the siloxane network.

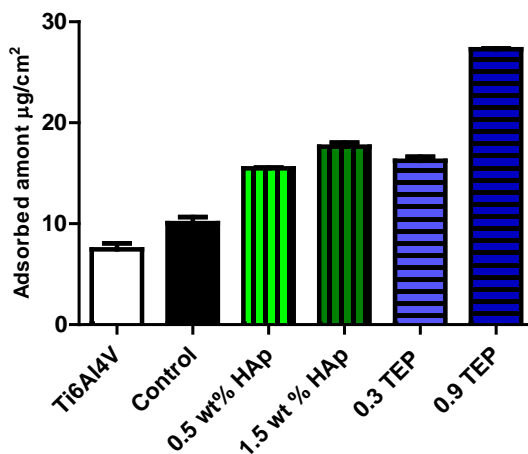


Fig.9.1.Amount of fibrinogen adsorbed on the prepared hybrid films

Figure 9.1 compares the amount of fibrinogen adsorbed on the prepared hybrids films. Hybrid films prepared with TEP, as phosphorous precursor, seem to be more effective in terms of the amount of adsorbed fibrinogen, as Figure 9.1 shows. Moreover, in the hybrid films containing TEP, the increase of TEP content from 0.3 to 0.9 ml per 20ml of MAPTMS/TMOS sol produces an increase of the adsorbed fibrinogen of  $10 \mu\text{g}/\text{cm}^2$ .

This proves that the P sites created by the incorporation of TEP in the siloxane network are effective sites to attract and combine fibrinogen.

Comparing the hybrid sol-gel films containing HAp or TEP, both used as phosphorous precursor, the TEP results to become more efficient phosphorous precursor in terms of fibrinogen adsorption. The reason is that in the case of HAp containing films, the presence of the P sites is concentrated in the points and/or surface areas where the HAp particles are distributed into the matrix, while in the case of TEP containing films; P sites exist at molecular level, providing more attaching sites with a better and more homogeneous distribution into the matrix.

These results suggest that incorporation of phosphate could effectively enhance the protein adsorption, and hybrid sol-gel films containing TEP showed better performance compared with hybrid sol-gel films containing HAp. These results, lead us to expect that the DMTSP, used as phosphorous precursor, could be also more effective than HAp in terms of protein adsorption ability.

### 9.2 Cytotoxicity /viability

Qualitative cell adhesion Data from four repeats, 3 replicates within each repeat, showed that the presence of phosphorus at molecular level is more effective in terms of cytotoxicity/viability and cell adhesion. Figure 9.2 shows the results obtained in the in-vitro evaluation using the neutral red assay. The evaluation was performed for NHOst cultured on un-coated Ti6Al4V, MAPTMS/TMOS-Ti6Al4V system (control) and hybrids containing HAp (0.5 and 1.5 wt %) , TEP and DMTSP (0.3 and 0.9 ml) respectively over a 7 day period. In this context, the organic-inorganic hybrid films modified by HAp, TEP and DMTSP showed enhancement of the cell adhesion and proliferation. Significant differences between the samples containing 0.9 TEP and 0.9 DMTSP and those without can be observed. The toxicity of the un-coated alloy seems to be higher with respect to the coated surfaces. On one hand, the toxicity of

vanadium and aluminium that released from the alloy can initiate cell toxicity and adverse tissue reactions as been reported [270]. On the other hand, the less cytotoxicity on the coated surfaces is due to the barrier effect afforded by coatings, inhibiting the ion release to the culture medium.

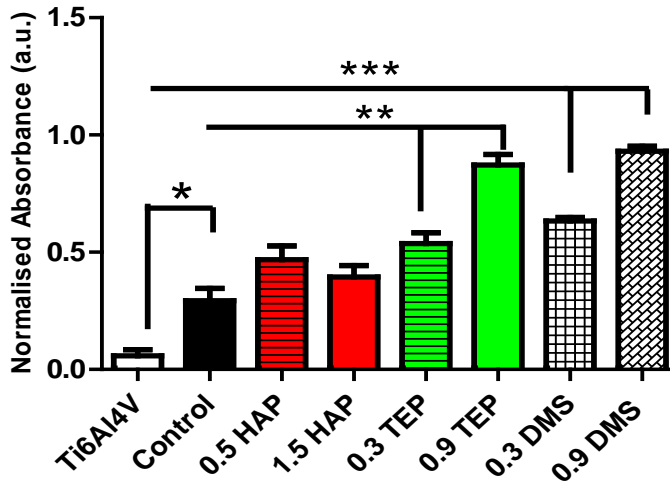


**Fig. 9.2.** Neutral red proliferation/cytotoxicity assay for NHOst cultured on un-coated Ti6Al4V, MAPTMS/TMOS-Ti6Al4V system (control) and hybrids containing HAp (0.5 and 1.5 wt%) , TEP and DMTSP (0.3 and 0.9 ml) respectively over a 7 day period

The best biological behaviour has been obtained by adding DMTSP to the hybrid during preparation. The reason could be the composition, denser films have been obtained, the DMTSP containing films showed highest degree of cross-linking. Thus, as a result, the ion release is more inhibited and this results in better viability of osteoblast on these films. Other reason could be way in that the phosphorus is incorporated which has been reported to be important for cell division and could stimulate the spreading of the osteoblasts on the surfaces and stimulate cellular metabolic activity and osteoblast proliferation. [275,276]

### 9.3 Osteoblasts adhesion

To further understand the nature of the interactions of osteoblast with the different surfaces obtained in this study, the expression level of vinculin and the organization of actin filaments were determined by immunofluorescence technique. For comparison purposes, representative images obtained of OB-cells growing on uncoated Ti6Al4V and coated surfaces are showed in Figure 9.3. The figure shows the morphology of adherent cells cultured for 7 days on the uncoated and coated Ti6Al4V substrates with various coating compositions. The coating compositions are indicated in the upper left part of each image.

Our *in-vitro* study showed that osteoblasts spread both on the surface of uncoated Ti6Al4V and coated substrates. The cell on the surfaces of the phosphorus containing films has more focal adhesion contacts /vinculin compared with the uncoated or control sample.

The formation of more focal adhesion contacts indicates that osteoblast cells were highly activated with strong adhesion on these films. On the other hand, fewer focal adhesions were exposed with assembled vinculin formed in the cells on the un-coated or control film. Thus, osteoblasts growing on the uncoated substrates created less mature focal contacts than osteoblasts growing on the phosphorus containing films.

Our results are in agreement with previously published observations. It has been repeatedly reported that cell adhesion and proliferation depends on surface chemistry and, varies with surface composition rather than general surface properties like wettability [285-290]. Thus, cell proliferation on these surfaces was different depending primarily on the film composition rather than on wettability.

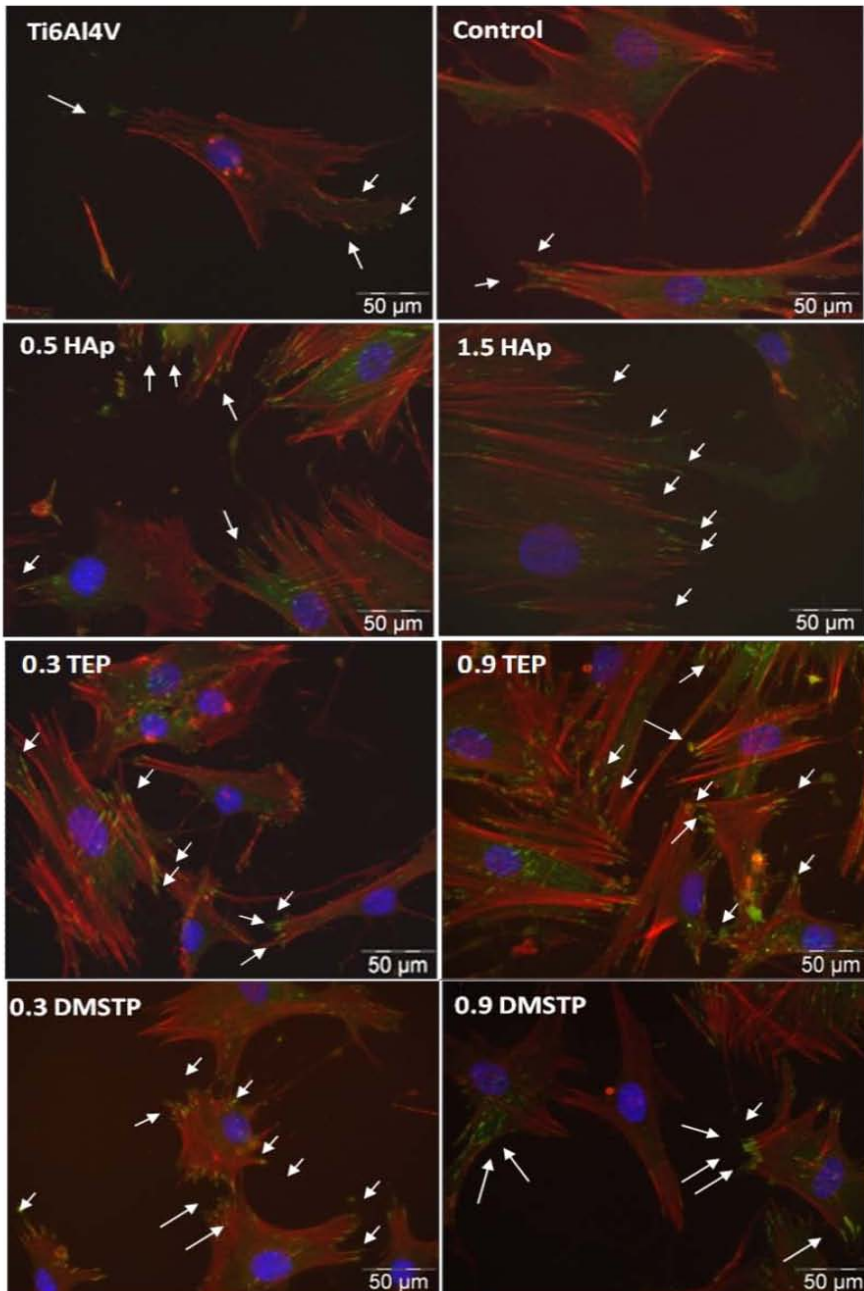


**Fig. 9.3** Fluorescence graphs of OB-cells growing on un-coated Ti6Al4V and coated surfaces for vinculin (green), actin (red) and nuclei (blue).

#### 9.4 Comparison of corrosion protection behaviour of the organic-inorganic hybrid sol-gel thin films

To evaluate the barrier properties afforded for the studied systems, the quantitative analysis of the impedance response by fitting with an adequate equivalent circuit is a valuable tool, as has been discussed in previous chapters.

Thus, to compare the studied coatings, the evolution of the equivalent circuit parameters associated to the HFA during the immersion tests in Kokubo solution is shown in Fig.9.4. For each coating systems, the formulation providing the best performance has been selected. The coatings compared are the HAp hybrid sol-gel (MAPTMS/TMOS/HAp-Ti6Al4V) system with 1 wt % HAp, and MAPTMS/TMOS/TEP-Ti6Al4V, MAPTMS/TMOS/DMTSP-Ti6Al4V systems with 0.9 ml of TEP and DMTSP per 20 ml of silanes mixture, respectively.

A comparison of the results reveals that the worst performance is obtained for the hybrid sol-gel containing DMTSP. Although this system starts with an  $R_{\text{coat}}$  value similar to that of the HAp hybrid coating and a CPE-T slightly higher, then with the immersion time there is a continuous decrease of the ionic resistance of the coating pores ( $R_{\text{coat}}$ ) values and a continuous increase of the coating capacitance, correlated with changes of the CPE-T values and CPE-P. This behaviour is associated to the loss of the barrier properties and the increase of water uptake in these coatings containing DMTSP.

In contrast, in the case of TEP containing hybrid sol-gel films, it can be observed that the  $R_{\text{coat}}$  and  $R_{\text{corr}}$  change mostly within the first 5 days of immersion and then these values stay almost constant, within reasonable magnitude margins along the 25 days of immersion in the SBF. According to this noticed results, it can be concluded that, the TEP containing films have interesting protective properties despite their low thickness  $<3\mu\text{m}$ .

At the same time, the slow evolution of the  $C_{\text{coat-T}}$  parameter with the immersion time indicates that the water uptake in the coating with TEP is low which reflect the good barrier properties, stability and good protective behaviour of the TEP containing films against the aggressive SBF solution.

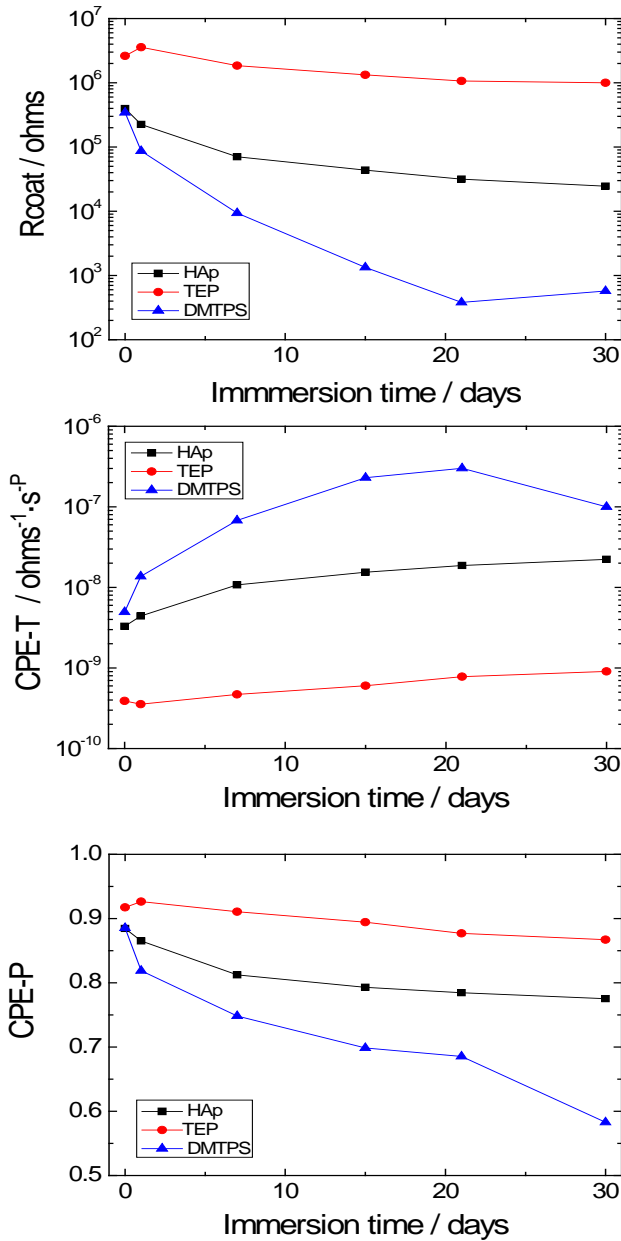


**Fig.9.4** Evolution of the equivalent circuit parameters associated to the HFA during the immersion tests in Kokubo solution for the MAPTMS/TMOS/HAp-Ti6Al4V system with 1 wt % HAp and MAPTMS/TMOS/TEP-Ti6Al4V system and MAPTMS/TMOS/DMTSP-Ti6Al4V system Formula: 0.9 ml of TEP and DMTSP for 20 ml of silanes mixture.

The values of the second parameter  $C_{coat-P}$  are close to 1 and decreases slowly with the immersion time, which provides an evidence of the chemical stability of these coatings during immersion test.

Finally, in the case of HAp containing hybrid sol-gel films, the similar behaviour like that of the TEP containing films have been observed, but the values of the  $C_{coat-P}$  are close to 1 but less than those measured in case of TEP containing films.

This comparison indicates that, in general, the best corrosion protection behaviour has been observed in case of TEP containing films, then HAp containing films and finally the DMTSP containing films.

## *General Conclusions*



### Conclusions:

The following conclusions can be drawn from the present work:

- **Inorganic HAp onto Ti6Al4V substrate:**
  - Hydroxyapatite coatings on Ti6Al4V alloy have been obtained by sol-gel route.
  - The obtained results show that all the prepared samples have crystal structure and composition like hydroxyapatite, with little deviations from that present in the human bone.
  - The bioactivity of the studied samples is found to be closely related to the thermal treatments applied. That is, the bioactivity decreases as the temperature of the thermal treatment increase.
  - The corrosion behaviour of the resulting HAp coatings in SBF has been studied by electrochemical impedance spectroscopy (EIS). The HAp coated Ti6Al4V alloy displayed good bioactivity when soaked in the SBF and acceptable corrosion protection behaviour.
- **The preparation conditions of the MAPTMS/TMOS sol have been optimized using FTIR and NMR techniques.**
- Hydrolysis and condensation of silane solution is a time-dependent process. A “workable” silane solution should contain a sufficient number of Si-OH groups for the subsequent condensations during silane surface treatment. Without sufficient hydrolysis, an oily silane film is obtained. Such film cannot provide corrosion protection due to the lack of a cross-linked structure and a good adhesion to substrates.
  - The hydrolysis of the two silane precursors MAPTMS and TMOS under the adopted synthesis strategy conditions is completed after approximately four hours at room temperature.

- **Organic–inorganic hybrid coating onto Ti6Al4V substrate.**
- Three different coatings have been prepared MAPTMS/TMOS/HAp, MAPTMS/TMOS/TEP and MAPTMS/TMOS/DMTSP.
- FTIR-ATR and NMR results demonstrate formation of Si-O-Si and Si-O-P bridges within the hybrid films in the case of TEP and DMTSP containing hybrids. While in the case of HAp containing hybrids, the solid ceramic HAp exists as inert dispersed particles in the films.
- All hybrid films show an increase in their thermal stability due to interactions between the inorganic P and Si in case of TEP and DMTSP containing hybrids while in case of HAp containing hybrids the thermal stability also increase because the inorganic HAp could act as heat insulator.
- In terms of network densification and cross-linking, all hybrids coatings containing HAp, TEP or DMSTP result in a more cross-linked network. The highest cross-linking degree is obtained by DMTSP.
- In biological study using fibrinogen, the presence of P binding sites at molecular level in case of using liquid precursor make the TEP containing hybrids more effective in amount of protein adsorbed than HAp containing hybrids.
- In cytotoxicity, all the prepared containing phosphorus coatings showed the enhancement of cell proliferation and adhesion relative to the uncoated or MAPTMS/TMOS hybrid. The great improvement has been obtained when mixing liquid precursors of phosphorus DMTSP or TEP with those of MAPTMS/TMOS. The best cellular proliferation obtained when using MAPTMS/TMOS/DMTSP-Ti6Al4V system. This behavior could be due to two reasons: (i) the silicon content is higher and (ii) presence of phosphorus at molecular level, both of which are important for cell division and proliferation.

## CONCLUSIONS and FUTURE WORK

---

- There was always a correlation between the cross-linking degree and biological performance of the prepared films. Again the best biological cellular proliferation has been obtained with the highest cross-linked films containing DMTSP.
- The corrosion behavior in SBF of the three organic-inorganic hybrid coating/Ti6Al4V systems has been studied by electrochemical impedance spectroscopy (EIS). The MAPTMS/TMOS/TEP hybrid sol-gel film provides the best barrier properties when soaked in the SBF for 30 days.

The most relevant finding to emerge from this Thesis is that the organic-inorganic hybrid coating which shows the best bioactivity and corrosion behavior is the coating based on MAPTMS/TMOS/DMTSP, achieving the desired properties and thus multifunctionality, aim of this Thesis.

The work presented in this thesis is part of a larger programme looking at the possibility of using organic-inorganic hybrids for improvement of the Ti6Al4V surface as the materials of choice for bone repair and replacement. Applicable metallic implants must undergo in-vivo testing to deduce whether or not the material is suitable for biomaterials applications. As in-vitro testing cannot replicate the complex environment of the human body.

The results of this thesis have generated several findings which need further investigation:

- a) The ion dissolution rate from the different coatings and/or metallic substrate to the culture media containing osteoblast cells needs to be measured and requires further measurements.
- b) The obtained *in-vitro* results are of prediction of the *in-vivo* performance of prepared materials. All of this needs more research, including *in-vivo* experimentation, to produce a viable product.



## *List of Figures*



## LIST OF FIGURES

---

### List of Figures

<b>Fig.1.1.</b> Biocompatibility depending on a variety of system parameters-----	2
<b>Fig.1.2.</b> Types of natural grafts, allograft heart valves (A) skin graft (B) -----	3
<b>Fig.1.3.</b> A typical hip implant with titanium femoral (A) dental Implant-----	3
<b>Fig.1.4.</b> Polymeric biomaterials, contact lens (A), sutures (B) -----	5
<b>Fig.1.5.</b> HIP alumina and zirconia ceramics as orthopaedic implants-----	6
<b>Fig.1.6.</b> Schematic representation of the crystal structure of HAp-----	7
<b>Fig 1.7.</b> (A) Natural and (B) artificial hip joints-----	10
<b>Fig.1.8.</b> Schematic representation of the bone structure-----	13
<b>Fig.1.9</b> Arrangement of HAp and collagen in the formation of bone-----	13
<b>Fig.1.10.</b> Representative diagram of osteoblast cells-----	15
<b>Fig.1.11.</b> Reaction steps during the corrosion of a metal in liquid environment -----	17
<b>Fig.1.12.</b> Components of Ti based hip implant-----	18
<b>Fig.1.13.</b> Schematic diagram of a sol-gel spin-coating process-----	20
<b>Fig.1.14.</b> Schematic representation of the formation of bonds between the substrate and the sol-gel-----	21
<b>Fig 1.15.</b> Schematic diagram of a sol-gel spin-coating process-----	21
<b>Fig.1.16.</b> Two-dimension schematic representation of the structure of a silane bonded to a metal -----	23
<b>Fig.1.17.</b> Representative diagram of bioactivity mechanism of silane–metal coatings	26
<b>Fig.1.18.</b> Schematic of a differential thermal analysis-----	29
<b>Fig.1.19.</b> Diagram of a Thermo-Gravimetric Analysis Instrument-----	30
<b>Fig.1.20.</b> Schematic diagram for determining Bragg's law-----	31
<b>Fig.1.21.</b> Schematic diagram of an IR Instrument-----	32
<b>Fig.1.22.</b> Schematic drawing to show the contact angle-----	33
<b>Fig.1.23.</b> Schematic diagram of the profilometer stylus-----	34
<b>Fig.1.24.</b> Diagram illustrating how the scanning electron microscope works-----	35
<b>Fig.1.25.</b> A block diagram of the instrumentation used to make the EIS measurements-----	39
<b>Fig.1.26.</b> Simple equivalent circuit with one time constant-----	40
<b>Fig.1.27.</b> Nyquist plot with impedance vector-----	40
<b>Fig.1.28.</b> .Bode plot with one time constant-----	41
<b>Fig.1.29.</b> Purely Capacitive Coating-----	44
<b>Fig.1.30.</b> Typical Bode and Nyquist Plot for a perfect coating-----	44
<b>Fig.1.31.</b> The Randles cell equivalent circuit-----	45
<b>Fig.1.32.</b> Typical Bode and Nyquist Plot for a corroding bare metal-----	45
<b>Fig.1.33</b> Typical Bode and Nyquist Plot for a corroding coated metal-----	46
<b>Fig.1.34.</b> Equivalent Circuit for a porous Coating-----	47
<b>Fig.3.1.</b> Flow chart of the Preparation of HAp coatings on Ti6Al4V via sol-gel process	54

## LIST OF FIGURES

---

<b>Fig 3.2.</b> Static SBF test in plastic container at constant temperature 37°C-----	<b>56</b>
<b>Fig.3.3.</b> Schematic representations of $\gamma$ -methacryloxypropyltrimethoxysilane (MAPTMS)-----	<b>59</b>
<b>Fig.3.4.</b> Schematic representations of tetramethoxysilane (TMOS) -----	<b>59</b>
<b>Fig. 3.5.</b> Schematic representation of Triethyl phosphite (TEP) -----	<b>60</b>
<b>Fig.3.6.</b> Schematic showing the chemical process that is taking place as TEP is hydrolyzed-----	<b>60</b>
<b>Fig.3.7.</b> Schematic representation of Dimethylsilylphosphite (DMTSP) -----	<b>61</b>
<b>Fig 3.8.</b> Dip coater used for deposition of sol-gel layer upon Ti6Al4V surface-----	<b>63</b>
<b>Fig.3.9.</b> Flowchart of the preparation of MAPTMS/TMOS/HAp coatings on Ti6Al4V	<b>65</b>
<b>Fig.3.10.</b> Flowchart of the preparation of MAPTMS/TMOS/TEP coatings on Ti6Al4V	<b>66</b>
<b>Fig.3.11.</b> Flowchart of the Preparation of MAPTMS/TMOS/ DMTSP coatings on Ti6Al4V-----	<b>67</b>
<b>Fig. 4.1.</b> DTA/TG of the as prepared S1 powder-----	<b>76</b>
<b>Fig.4.2.</b> FTIR spectra of the dried gel S1 and the powders thermally treated-----	<b>79</b>
<b>Fig.4.3.</b> XRD patterns and developed phases of the prepared samples-----	<b>83</b>
<b>Fig.4.4.</b> X-ray diffraction card No. JCPDS #(09-0432) -----	<b>86</b>
<b>Fig.4.5.</b> Bone-bonding mechanism of bioactive ceramics-----	<b>91</b>
<b>Fig.4.6.</b> (A) $\text{Ca}^{2+}$ and (B) $\text{PO}_4^{3-}$ concentrations in SBF during 15 days of immersion in SBF-----	<b>92</b>
<b>Fig.4.7.</b> SEM /EDX of the surface of the S6 sample before immersion in SBF-----	<b>93</b>
<b>Fig.4.8.</b> SEM micrographs and EDX spectra of the surface of the S6 sample after immersion in SBF-----	<b>94</b>
<b>Fig.4.9.</b> SEM micrographs and EDX spectra of the surface of the S8 sample after immersion in SBF-----	<b>95</b>
<b>Fig.4.10</b> SEM micrographs and EDX spectra of the surface of the S12 sample after immersion in SBF-----	<b>95</b>
<b>Fig.4.11</b> FTIR spectra of the prepared samples after 15 days of immersion in SBF	<b>96</b>
<b>Fig.4.12</b> SEM micrographs obtained for the HAp-coatings/Ti6Al4V before immersion in SBF-----	<b>98</b>
<b>Fig.4.13.</b> SEM micrographs obtained for the HAp-coatings/Ti6Al4V after immersion in a SBF-----	<b>99</b>
<b>Fig.4.14</b> Evolution of the electrochemical impedance spectra of S6-----	<b>101</b>
<b>Fig.4.15</b> Evolution of the electrochemical impedance spectra of S8-----	<b>102</b>
<b>Fig.4.16</b> Electrical equivalent circuits used to analyze the experimental electrochemical impedance data-----	<b>103</b>
<b>Fig.4.17.</b> Evolution of the $R_s$ , $R_{coat}$ and $R_{corr}$ values with immersion time in SBF of HAp-coatings/Ti6Al4V systems. Thermal Treatments: 600°C/2h-----	<b>107</b>
<b>Fig.4.18.</b> Evolution of the $R_s$ , $R_{coat}$ and $R_{corr}$ values with immersion time in SBF of HAp-coatings/Ti6Al4V systems. Thermal Treatments: 800°C/2h-----	<b>108</b>

## LIST OF FIGURES

<b>Fig.5.1.</b> Schematic representation of the polymerization reaction of the MAPTMS and TMOS mixture producing a 3D organic–inorganic hybrid network	<b>112</b>
<b>Fig.5.2.</b> Two-dimension schematic representation of the structure of a silane sol-gel film bonded onto a metal (M) substrate. (A) Partially condensed and (B) fully condensed-----	<b>113</b>
<b>Fig.5.3.</b> Structural formula of (A) MAPTMS and (B) TMOS-----	<b>113</b>
<b>Fig.5.4.</b> FTIR spectrum of the MAPTMS/TMOS mixture in Et(OH)–H <sub>2</sub> O solvent system upon mixing-----	<b>115</b>
<b>Fig.5.5.</b> FTIR spectra of the MAPTMS/TMOS mixture in Et(OH)/H <sub>2</sub> O solvent system. Hydrolysis time up to 3.5 h-----	<b>116</b>
<b>Fig.5.6.</b> FTIR spectrum of the MAPTMS/TMOS mixture in EtOH–H <sub>2</sub> O solvent system Hydrolysis time up to 24 h-----	<b>117</b>
<b>Fig.5.7.</b> Schematic representation of T <sup>n</sup> silane structures; n=1, 2, or 3-----	<b>119</b>
<b>Fig.5.8.</b> Liquid-state <sup>29</sup> Si NMR spectra of MAPTMS/MOS mixture in Et(OH)/H <sub>2</sub> O solvent system. A upon mixing of MAPTMS and TMOS, B after 1 h, C after 2 h, D after 3 h, E after 4 h-----	<b>120</b>
<b>Fig.5.9.</b> Relationship of the signals, for species T <sup>0</sup> , T <sup>1</sup> , T <sup>2</sup> , and T <sup>3</sup> in the MAPTMS/TMOS hybrid-----	<b>122</b>
<b>Fig.5.10.</b> Liquid state <sup>13</sup> C NMR spectra of prehydrolyzed MAPTMS/TMOS: (A) upon mixing of MAPTMS and TMOS; (B) after 1 hour; (C) after 2 hours; (D) after 3 hours, and (E) after 4 h-----	<b>126</b>
<b>Fig.5.11.</b> Liquid state <sup>13</sup> C NMR spectra of prehydrolyzed MAPTMS/TMOS: (A) upon mixing of MAPTMS and TMOS; (B) after 1 hour; (C) after 2 hours; (D) after 3 hours, and (E) after 4 h-----	<b>127</b>
<b>Fig.6.1</b> Simplified schematic of bonding mechanism between silane molecules and metal surface hydroxide layer-----	<b>129</b>
<b>Fig.6.2</b> TG plots of the prepared MAPTMS/TMOS hybrids containing diferent amounts of HAp particles-----	<b>132</b>
<b>Fig.6.3</b> Representative ATR-IR absorption spectra of MAPTMS/TMOS/HAp-Ti6Al4V systems containing: (A) 0% wt. HAp; (B) 0.5 wt. % HAp ; (C) 1 wt. % HAp and, (D) 1.5 wt. % HAp, respectively-----	<b>134</b>
<b>Fig.6.4</b> Solid state <sup>29</sup> Si NMR spectra of MAPTMS/TMOS/HAp hybrids containing (A) 0% HAp; (B) 0.5 wt. % HAp and, (C) 1.5 wt. % HAp respectively-----	<b>136</b>
<b>Fig.6.5.</b> Relationship of the signals, for species T <sup>2</sup> , T <sup>3</sup> , Q <sup>3</sup> , and Q <sup>4</sup> in the MAPTMS/TMOS hybrid with various content of HAp-----	<b>137</b>
<b>Fig.6.6</b> Solid state <sup>13</sup> C-NMR spectra of MAPTMS/TMOS/HAp hybrids containing: (A) 0; (B) 0.5 wt. % HAp and, (C) 1.5 wt. % HAp, respectively-----	<b>139</b>
<b>Fig.6.7</b> Solid state <sup>31</sup> P NMR spectra of MAPTMS/TMOS/HAp hybrid containing: (A) 0.5 wt. % HAp and, (B) 1.5 wt. % HAp respectively-----	<b>140</b>
<b>Fig. 6.8</b> Powder XRD patterns of pure HAp and hybrid sol–gel contain HAp-----	<b>141</b>
<b>Fig.6.9</b> Viscosity changes of MAPTMS/TMOS sol measured with respect to different	

## LIST OF FIGURES

contents of HAp (mean +/- SD) -----	142
<b>Fig.6.10</b> Thickness variation of MAPTMS/TMOS coatings deposited on Ti6Al4V at various HAp content-----	143
<b>Fig.6.11</b> Variation of MAPTMS/TMOS coatings contact angle at various HAp content-----	144
<b>Fig.6.12</b> SEM/EDX images for the prepared hybrid coatings deposited on Ti6Al4V substrates, un-coated (A) , and containing 0 wt % HAp (B); 0.5 wt % HAp (C); 1 wt % HAp (D) and, 1.5 wt % HAp (E) respectively-----	147
<b>Fig.6.13</b> Confocal microscope three-dimensional images of the prepared coatings /Ti6Al4V-----	149
<b>Fig.6.14.</b> Bradford standard calibration curve of different protein concentration 0.2-1 mg/ml read at 595 nm-----	152
<b>Fig.6.15</b> Absorbance read at 595 nm of aliquot solution after removing the surfaces	153
<b>Fig.6.16</b> Amount of fibrinogen adsorbed on the prepared hybrid films-----	153
<b>Fig.6.17</b> Neutral red viability/cytotoxicity assay for NHOst cultured on Ti6Al4V, MAPTMS/TMOS-Ti6Al4V and MAPTMS/TMOS/HAp-Ti6Al4V over a seven day period-----	155
<b>Fig. 6.18</b> Fluorescence graphs of OB-cells growing on un-coated Ti6Al4V and coated surfaces. Vinculin: green; actin: red and, nuclei:blue respectively-----	157
<b>Fig.6.19</b> SEM/EDX images for MAPTMS/TMOS and MAPTMS/TMOS/1.5 HAp-----	159
<b>Fig.6.20</b> Nyquist plots, represented in two different scales [(A) and (B)] and, Bode plots (C) obtained for three identical samples of MAPTMS/TMOS/HAp system deposited on Ti6Al4V surfaces for a coating with a contain of 1 wt.% HAp powder. Electrolyte: SBF. Immersion Time: 1day-----	161
<b>Fig.6.21</b> Experimental impedance plots and fit results obtained for one MAPTMS/TMOS/HAp-Ti6Al4V sample. HAp content 1 wt % of 20 ml MAPTMS/TMOS sol. Immersion time in SBF: 1day-----	162
<b>Fig.6.22</b> Evolution with the immersion time of the Nyquist plots, represented in two different scales[(A) and (B)] and, the Bode plots (C) obtained for the MAPTMS/TMOS/HAp system deposited on Ti6Al4V surfaces for a coating with a contain of 1 wt.% HAp powder-----	165
<b>Fig.6.23</b> Evolution of the equivalent circuit parameters associated to the HFA with the immersion time in Kokubo solution of the MAPTMS/TMOS/HAp-Ti6Al4V system for a coating with a contain of 1 wt.% HAp powder-----	167
<b>Fig.6.24</b> Nyquist plots, represented in two different scales [(A) and (B)] and, Bode plots (C) obtained for an uncoated Ti6Al4V sample and Ti6Al4V samples coated with MAPTMS/TMOS/HAp films containing different HAp powder percentages: 0 wt.% (blank sample), 0.5 wt.%, 1 wt.% and 1.5 wt.% respectively. Electrolyte: SBF. Immersion Time: 1day-----	169

## LIST OF FIGURES

<b>Fig.7.1</b> TG traces of the prepared MAPTMS/TMOS hybrids contain various amounts of TEP-----	<b>174</b>
<b>Fig.7.2.</b> Fig. 6.3 Representative ATR-IR absorption spectra of MAPTMS/TMOS/TEP-Ti6Al4V systems containing: (A) 0 ml TEP; (B) 0.3 ml TEP; (C) 0.6 ml TEP and, (D) 0.9 ml TEP, respectively-----	<b>177</b>
<b>Fig.7.3</b> Solid state <sup>29</sup> Si-NMR spectra of MAPTMS/TMOS containing: (A) 0 ml of TEP; (B) 0.3 ml of TEP, and (C) 0.9 ml of TEP-----	<b>179</b>
<b>Fig.7.4.</b> Relationship of the signals, for species T <sup>2</sup> , T <sup>3</sup> , Q <sup>3</sup> , and Q <sup>4</sup> in the MAPTMS/TMOS hybrid with various content of TEP-----	<b>180</b>
<b>Fig.7.5.</b> Solid state <sup>13</sup> C-NMR spectra of MAPTMS / TMOS containing (A) 0 (B) 0.5 wt % HAp (C) 0.5 wt % HAp (D) 0.3 ml TEP (E) 0.9 ml TEP-----	<b>181</b>
<b>Fig.7.6</b> SEM/EDX images for the prepared MAPTMS/TMOS/TEP-Ti6Al4V systems containing: (A) 0 ml of TEP; (B) 0.3 ml of TEP (C) 0.6 TEP (D) 0.9 ml of TEP	<b>183</b>
<b>Fig.7.7</b> SEM/EDX images for the prepared MAPTMS/TMOS/TEP-Ti6Al4V system containing (A) 5 ml of TEP; (B) 10 ml of TEP; (C) 5 ml of TEP, and (D) 10 ml TEP-----	<b>184</b>
<b>Fig.7.8</b> Change of MAPTMS/TMOS sol viscosity as a function of TEP content-----	<b>185</b>
<b>Fig.7.9</b> Change of thickness of the MAPTMS/TMOS/TEP coatings deposited on Ti6Al4V surfaces as a function of TEP content-----	<b>186</b>
<b>Fig. 7.10</b> Change of contact angle of the MAPTMS/TMOS/TEP coatings deposited on Ti6Al4V surfaces as a function of TEP content-----	<b>187</b>
<b>Fig. 7.11</b> confocal microscope three-dimensional images of the prepared coatings - Ti6Al4V-----	<b>189</b>
<b>Fig.7.12</b> 595 nm Bradford method standard calibration curve-----	<b>190</b>
<b>Fig.7.13.</b> Amount of fibrinogen adsorbed on the prepared hybrid films-----	<b>191</b>
<b>Fig.7.14</b> Absorbance read at 595 nm of aliquot solution after removing the surfaces	<b>192</b>
<b>Fig.7.15</b> Neutral red viability/cytotoxicity assay for NHOst cultured on Ti6Al4V, MAPTMS/TMOS-Ti6Al4V and TEP containing hybrids (0.3-0.9 ml TEP) over a seven day period-----	<b>193</b>
<b>Fig.7.16</b> Fluorescence graphs of OB-cells growing on: un-coated Ti6Al4V and coated surfaces; vinculin (green), actin (red) and nuclei (blue) -----	<b>195</b>
<b>Fig.7.17</b> SEM micrographs and EDX analysis of MAPTMS/TMOS/0.9 TEP -Ti6Al4V system. -----	<b>196</b>
<b>Fig.7.18.</b> Evolution of the impedance plots of the MAPTMS/TMOS/TEP-Ti6Al4V system (0.9 ml/20 ml of TEP/silane ratio) as a function of the immersion time in SBF-----	<b>197</b>
<b>Fig.7.19</b> Experimental impedance plots and fit results obtained for two MAPTMS/TMOS/TEP-Ti6Al4V samples. TEP/silane ratio = 0.9 ml/20 ml. Immersion time in SBF: 1day-----	<b>199</b>
<b>Fig.7.20</b> Evolution of the equivalent circuit parameters during the immersion tests in Kokubo solution for the MAPTMS/TMOS/TEP-Ti6Al4V system. Formula:	

## LIST OF FIGURES

0.9 ml of TEP for 20 ml of silanes mixture-----	203
<b>Fig.7.21.</b> General electrical equivalent circuit of metal/sol-gel coating system in contact with an aqueous electrolyte, taking in account the short circuit terminus $W_s$ , associated to diffusion phenomena in finite length layers	204
<b>Fig.7.22.</b> Graphics produced in the complex plane by the equation $Z=R \cdot \tanh(j \cdot T \cdot \omega)^P / (j \cdot T \cdot \omega)^P$ for: $W_s-R = 1000$ ; $W_s-T = 0.1$ ; $W_s-P = 0.5$ . The frequency of the $Z''$ maximum is at $\omega_{max} = 2.53/W_s-T = 25.3$ rad/sec = 4.03 Hz-----	205
<b>Fig.7.23</b> Bode plots recorded for uncoated and coated Ti6Al4V alloy with hybrid sol-gel films with different contents in TEP: 0 ml (blank sample), 0.3 ml, 0.6 ml and 0.9 ml respectively. Electrolyte: SBF. Immersion Time: 1day-----	206
<b>Fig.7.24.</b> Representation in two different scales of the Nyquist plots of samples of Ti6Al4V hybrid films coated with sol-gel with different contents in TEP: 0 ml (blank sample), 0.3 ml, 0.6 ml and 0.9 ml respectively. Electrolyte: SBF. Immersion Time: 1day-----	207
<b>Fig.8.1</b> TG traces of the prepared MAPTMS/TMOS hybrids contain variable amounts of DMTSP-----	212
<b>Fig.8.2</b> ATR-IR spectra of the MAPTMS/TMOS/ DMTSP -Ti6Al4V system for coatings containing different content of DMTSP-----	213
<b>Fig.8.3.</b> Solid state $^{29}\text{Si}$ -NMR spectra of MAPTMS / TMOS containing (A) 0 (B) 0.3 DMTSP (C) 0.9 DMTSP-----	215
<b>Fig.8.4</b> SEM/EDX images for the MAPTMS/TMOS/ DMTSP-Ti6Al4V coatings contain different content of DMTSP-----	216
<b>Fig.8.5.</b> Neutral red viability/cytotoxicity assay for NHOst cultured on un-coated Ti6Al4V, MAPTMS/TMOS-Ti6Al4V system (control) and hybrids containing DMTSP (0.3 and 0.9 ml) respectively over a 7 day period-----	218
<b>Fig.8.6</b> Fluorescence graphs of OB-cells growing on un-coated Ti6Al4V and coated surfaces for vinculin (green), actin (red) and nuclei (blue) -----	220
<b>Fig.8.7</b> Experimental impedance plots and fit results obtained for three identical samples of MAPTMS/TMOS/DMTSP-Ti6Al4V. DMTSP/silanes ratio = 0.6 ml/20 ml. Immersion time in SBF: 1day-----	222
<b>Fig.8.8</b> Nyquist plots, represented in two different scales[(A) and (B)] and, Bode plots (C) obtained for an uncoated Ti6Al4V sample and Ti6Al4V samples coated with DMTSP sol-gel thin films with different DMTSP contents: 0 ml (blank sample), 0.3 ml, 0.6 ml and 0.9 ml respectively. Electrolyte: SBF. Immersion Time: 1day-----	224
<b>Fig.8.9</b> Evolution of the Nyquist plots with the immersion time in Kokubo solution for a MAPTMS/TMOS/DMTSP-Ti6Al4V system. DMTSP/silanes ratio = 0.9 ml/20 ml. -----	226
<b>Fig.8.10</b> Evolution of the Bode plots with the immersion time in Kokubo solution for	

## LIST OF FIGURES

---

a MAPTMS/TMOS/DMTSP-Ti6Al4V system. DMTSP /silanes ratio = 0.6 ml/20 ml-----	227
<b>Fig.8.11</b> Evolution of the equivalent circuit parameters with the immersion time in Kokubo solution of the MAPTMS/TMOS/DMTSP-Ti6Al4V system. Formula: 0.9 ml of DMTSP per 20 ml of silanes mixture-----	229
<b>Fig.8.12</b> Impedance plots obtained for an uncoated Ti6Al4V sample and for two MAPTMS/TMOS/DMTSP-Ti6Al4V systems based on 1 and 2 coats respectively. DMTSP/silanes ratio = 0.9 ml/20 ml. Immersion time in SBF: 1day-----	231
<b>Fig.9.1.</b> Amount of fibrinogen adsorbed on the prepared hybrid films-----	234
<b>Fig.9.2.</b> Neutral red viability/cytotoxicity assay for NHOst cultured on un-coated Ti6Al4V, MAPTMS/TMOS-Ti6Al4V system (control) and hybrids containing HAp (0.5-1.5 wt%) , TEP and DMTSP (0.3 and 0.9 ml) respectively over a 7 day period-----	236
<b>Fig.9.3</b> Fluorescence graphs of OB-cells growing on un-coated Ti6Al4V and coated surfaces for vinculin (green), actin (red) and nuclei (blue) -----	238
<b>Fig.9.4</b> Evolution of the equivalent circuit parameters associated to the HFA during the immersion tests in Kokubo solution for the MAPTMS/TMOS/HAp-Ti6Al4V system with 1 wt % HAp and MAPTMS/TMOS/TEP-Ti6Al4V system and MAPTMS/TMOS/DMTSP-Ti6Al4V system Formula: 0.9 ml of TEP and DMTSP for 20 ml of silanes mixture-----	240



## *List of Tables*



## LIST OF TABLES

---

### List of Tables

<b>Table 1.1.</b> Effect of the composition variation of 45S5 bioglass -----	<b>6</b>
<b>Table 1.2.</b> Types of tissue–implant attachment -----	<b>10</b>
<b>Table 1.3.</b> Nominal ions concentration of SBF in comparison with those in human blood plasma-----	<b>36</b>
<b>Table 3.1.</b> Thermal treatment temperatures of the as received powder samples-----	<b>53</b>
<b>Table 3.2.</b> Silane and phosphorus precursors used for preparation of different coatings-----	<b>58</b>
<b>Table 3.3.</b> Sample name and compositions of the hybrid coatings-----	<b>64</b>
<b>Table 4.1.</b> Thermal treatment temperatures of the as received sample-----	<b>78</b>
<b>Table 4.2.</b> The degree of crystallinity of the powders thermally treated at different temperatures-----	<b>84</b>
<b>Table 4.3.</b> Comparison between PDF Card No.(9-432) and thermally treated samples-----	<b>86</b>
<b>Table 4.4.</b> Crystallographic (or lattice) parameters of thermally treated samples-----	<b>88</b>
<b>Table 4.5</b> Values obtained for the elements of the proposed equivalent circuits in Figure 4.15, applying CNLS fits of the ZView software on experimental impedance plots of the HAp-coatings/Ti6Al4V system. Sample S6 (600°C/2h). Immersion time in SBF: 5 days-----	<b>105</b>
<b>Table 4.6.</b> CPEDl-P values and % of relative error obtained with the equivalent circuits A and B applying CNLS fits from the ZView software on experimental impedance plots of samples S6 (600°C/2h) and S8 (800°C/2h), for variable immersion time in SBF-----	<b>112</b>
<b>Table 5.1</b> Assignment of the FTIR peaks shown in Figures 5.4 and 5.6-----	<b>117</b>
<b>Table 5.2</b> Relative proportions of T and Q species in the organic–inorganic hybrid	

## LIST OF TABLES

---

materials from the <sup>29</sup> Si spectra in Figure 5.8-----	122
<b>Table 5.3</b> Peak assignments of <sup>13</sup> C liquid state of both MAPTMS and TMOS according to peaks detected in (Figure 5.10) -----	125
<b>Table 6.1.</b> Thermogravimetric results obtained for MAPTMS-TMOS with HAp-----	133
<b>Table 6.2.</b> Assignment of the ATR-IR bands in MAPTMS/TMOS/HAp-Ti6Al4V systems	135
<b>Table 6.3.</b> Chemical shift $\delta$ (ppm) and peak area (%) of T and Q units from deconvoluting the <sup>29</sup> Si-NMR spectra-----	138
<b>Table 6.4</b> Viscosity of sol, contact angle and thickness of MAPTMS/TMOS-Ti6Al4V system in variation with the amount of HAp-----	145
<b>Table 6.5</b> Surface roughness parameters for uncoated and hybrid coated/Ti6Al4V alloy-----	148
<b>Table 6.6 .</b> Values calculated with the Zview software for each one of the elements of the equivalent circuit to analyze the MAPTMS/TMOS/HAp-Ti6Al4V system. 1 wt % HAp/ silane content. Immersion Time SBF: 1day-----	163
<b>Table 6.7</b> Resistance values and CPE parameters associated to the high frequency arc (HFA) obtained for an uncoated Ti6Al4V sample and for MAPTMS/TMOS/HAp-Ti6Al4V systems with different HAp content. Electrolyte: SBF. Immersion time: 1day-----	170
<b>Table 7.1</b> Thermogravimetric results obtained for MAPTMS-TMOS with TEP-----	175
<b>Table. 7.2</b> Assignment of the ATR-IR bands in MAPTMS/TMOS coatings on Ti6Al4V substrates reported by other authors-----	178
<b>Table. 7.3.</b> Chemical shift $\delta$ (ppm) and peak area (%) of T and Q units from deconvoluting the <sup>29</sup> Si-NMR spectra-----	180
<b>Table 7.4</b> Viscosity of sol, contact angle and thckness of MAPTMS/TMOS coatings on Ti6Al4V substrates as a function of TEP content -----	187
<b>Table 7.5</b> Surface roughness parameters for uncoated and hybrid coated/Ti6Al4V	

## LIST OF TABLES

---

alloy-----	188
<b>Table 7.6.</b> Values calculated with the Zview software for each of the equivalent circuit elements for the MAPTMS/TMOS/TEP-Ti6Al4V system. TEP/silane ratio = 0.9 ml/20 ml. Immersion Time SBF: 1day-----	200
<b>Table 7.7</b> CPE and resistance values associated to the high frequency arc (HFA) for MAPTMS/TMOS/TEP-Ti6Al4V systems with different content in TEP. Electrolyte: SBF. Immersion time: 1day-----	208
<b>Table 8.1</b> Thermogravimetric results obtained for MAPTMS-TMOS with DMTSP-----	212
<b>Table 8.2</b> Values obtained for the electrical elements of the equivalent circuit shown in Figure 8.7 Samples: MAPTMS/TMOS/DMTSP-Ti6Al4V. DMTSP /silanes = 0.6 ml/20 ml; Immersion time in SBF: 1day.-----	223
<b>Table 8.3</b> Resistance values and CPE parameters associated to the high frequency arc (HFA) obtained for an uncoated Ti6Al4V sample and for MAPTMS/TMOS/DMTSP-Ti6Al4V systems with different DMTSP content. Electrolyte: SBF. Immersion time: 1day-----.	225
<b>Table 8.4</b> Calculated values for each element of the equivalent circuit of an uncoated Ti6Al4V sample and of two MAPTMS/TMOS/DMTSP-Ti6Al4V systems based on 1 and 2 coats respectively. Immersion time in SBF: 1 day. (DMTSP/silane ratio = 0.9 ml/20 ml).-----	232



## *Bibliographic Research*



### BIBLIOGRAPHIC RESEARCH

- [1]. Ramakrishna S., Mayer J., Wintermantel E., Leong K. W., "Biomedical Applications of Polymer- Composites Materials: A Review", *Composite Science and Technology* . 61, 1189-1224, **(2001)**.
- [2]. Williams D.F., "Definitions in Biomaterials in Proceedings of a consensus conference of the European Society for Biomaterials", Chester, England, 3-5, 1986: Elsevier, New York,**(1987)**.
- [3]. Ratner B.D., Hoffman A.S., Schoen F.J., Lemons J.E., Editors. "Biomaterials science: an introduction to materials in medicine", San Diego, CA: Academic Press; **(1996)**.
- [4]. Sittig C., Wieland M., Xiao S.,J. Textor M., "Characterization and Properties of Titanium Implant Surface", "*Biomedical Technique*".41, pp. 446, **(1996)**.
- [5]. Coombes AG., Meikle MC.,Resorbable synthetic polymers as replacements for bone graft. *Clin Mater* 17(1): 35–67,**(1994)**.
- [6]. Urist MR, Silverman BF, Buring K, Dubuc FL, Rosenberg JM.; The bone induction principle. *ClinOrthop* 53: 243–283, **(1967)**.
- [7]. G. C. Clark, D. F. Williams, *J. Biomed. Mater. Res.* 16, 125,**(1982)**.
- [8]. D. Upadhyay, M. A. Panchal, R. S. Dubey, V. K. Srivastava, *Mater. Sci. Eng. A*, 432, 1, **(2006)**.
- [9]. P. A. Dearnley, *Surf. Coating Technol.* 198, 483,**(2005)**.
- [10].S.J. Lia,b, M. Niinomia,, T. Akahoria, T. Kasugac, R. Yangb, Y.L. Hao" Fatigue characteristics of bioactive glass-ceramic-coated Ti–29Nb–13Ta–4.6Zr for biomedical application" *Biomaterials* 25 3369–3378, **(2004)**.
- [11].L L. Hench"Bioceramics: From Concept to Clinic"*J.Am.Ceram.Soc.*74 1487-1510, **(1991)**.
- [12].Hench, L. L., splinter, R. J., allen, W. C. &greenlee, T. K. Jr, Bonding mechanisms at the interface of ceramic prosthetic materials. *J. Biomed. Muter. Res.*, 2 117-141, **(1972)**.
- [13].Hench LL, Splinter, RJ, Allen WC, Greenlee TK. Bonding mechanisms at the interface of ceramic prosthetic materials. *J. Biomed. Mater. Res. Symp.*; (Part I): pp.117–141, **(1971)**.
- [14].Hench L.L. In *Bioceramics: Materials characteristics versus in-vivo behavior*. *Annals of New York Acad. Sci.* New York; Vol,54 PP,523,**(1998)**.
- [15].Wilson J, Nolletti D. In *Handbook of Bioactive Ceramics*. Yamamuro T, Hench LL, Wilson J Editors. CRC Press, Boca Raton, FL.: pp,283,**(1990)**.
- [16].Martin RI and Brown PW.. Mechanical properties of Hydroxyapatite formed at Physiological Temperature. *J Mater Sci: Mater Med* 6: 138-143, **(1995)**.
- [17].Kawachi EY, Betran CA, dos Reis RR and Alves OL.. *Biocerâmicas: Tendências e Perspectivas de uma Área Interdisciplinar*. *Quim Nova* 23: 518-522 ,**(2000)**.
- [18].T. V. Thamaraiselvi and S. Rajeswari"Biological Evaluation of BioceramicMaterials"*TrendsBiomater. Artif. Organs*, 18 (1), pp 9-17 ,**(2004)**.

## BIBLIOGRAPHIC RESEARCH

---

- [19]. MariaVallet-Regi, Jose MariaGonza'lez-Calbet"" Calcium phosphates as substitution of bone tissues " Progress in Solid State Chemistry 32, 1–31, **(2004)**.
- [20]. Hench, L.L.; Wilson, J. An introduction to bioceramics. Singapore: World Scientific Publishing Co., p. 1-24, **(1993)**.
- [21]. P. Ducheyne, S. Radin and K. Ishikawa "Bone bonding biomaterials" 31-46 in Bone-Bonding Biomaterials, ed. by P. Ducheyne, T. Kokubo and C.A. van Blitterswijk, Reed Healthcare Communications, Leiderdorp, PP. 213-218, **(1992)**.
- [22]. Jarcho, M., Bolen, C.H., Thomas, B.J., Hydroxylapatite synthesis and characterization in dense polycrystalline form. J Mater Sci 11 :2027, **(1976)**.
- [23]. Osborn, J.F., Newesiy, H., The matenal science of calcium phosphate ceramics. Biomaterials 1. 108, **(1980)**.
- [24]. Metsger, D.S., Diskcii, T.D., Paulsrud, T.R. Tricalcium phosphate ceramic- a resorbable bone implant: review current status. J. Am. Dent. Assoc. 105: 1035- 1038, **(1982)**.
- [25]. G. Kh. Gruntovskii and S. V. Malyshkina, "Hydroxyapatite ceramics: Features of reactions with bone tissue," Tr. Krymskogo Meduniversiteta, 135, 127-128, **(1999)**.
- [26]. S. V. Malyshkina, N. V. Dedukh, G. Kh. Gruntovskii, et al., "Morphological features of bone tissue reconstruction in the plastic treatment of defects with hydroxyapatite ceramics," Ortopediya, Travmatologiya I Protezirovanie, No. 3, 110-114, **(1998)**.
- [27]. L.L. Hench, J. Wilson, Science 226 , 630, **(1984)**.
- [28]. Verné E., Brovarone V.C., Moiescu C., Ghisolfi E., Marmo E., "Coatings on Al<sub>2</sub>O<sub>3</sub> by bioactive glass-ceramic", " Acta Materiala", .48, pp. 4667-4671, **(2000)**.
- [29]. V. A. Dubok " Bioceramic-yesterday, today , tomorrow" Powder Metallurgy and Metal Ceramics. 39, Nos. 7-8, **(2000)**.
- [30]. Charnley, J. Anchorage of the femoral head prosthesis to the shaft of the femur. J. Bone Joint Surg. 42B, 28–30, **(1960)**.
- [31]. Hench, L. L. Biomaterials. Science 208, 826–831, **(1980)**.
- [32]. M. Navarro, A. Michiardi, O. Castan~o and J. A. Planell, J. R. Soc. Interface 5, 1137–1158, **(2008)**.
- [33]. Hench, L. & Polak, J. Third generation biomedical materials. Science 295, 1014–1017, **(2002)**.
- [34]. D. GREEN, D. WALSH, S. MANN, R. O. C. OREFFO, Bone Vol. 30, No. 6 :810 – 815, **(2002)**.
- [35]. Netter, Frank H. , Musculoskeletal system: anatomy, physiology, and metabolic disorders. Summit, New Jersey: Ciba-Geigy Corporation ISBN 0-914168-88-66, **(1987)**.
- [36]. Miller, Scott C.; Jee, Webster S. S. . "The bone lining cell: A distinct phenotype?". Calcified Tissue International 41 (1): 1–5, **(1987)**.
- [37]. Martin JY, Schwartz Z, Hummert TW, Schraub DM, Simpson J, Lankford J, Dean DD, Cochran DL, Boyan BD , Effect of titanium surface roughness on proliferation, differentiation, and protein synthesis of human osteoblast-like cells (MG63). J Biomed Mater Res 29:389-401, **(1995)**.

## BIBLIOGRAPHIC RESEARCH

---

- [38]. B.D. Boyan<sup>1,2</sup>, S. Lossdorfer<sup>3</sup>, L. Wang<sup>1</sup>, G. Zhao<sup>1</sup>, C.H. Lohmann<sup>4</sup>, D.L. Cochran<sup>2</sup>, & Z. Schwartz<sup>1,2,5</sup>. *European Cells and Materials* Vol. 5. Suppl. 2, pages 11-12, **(2003)**.
- [39]. K. Anselme, *Biomaterials* 21, 667-681, **(2000)**.
- [40]. Rea SM, Brooks RA, Schneider A, Best SM, Bofield W. Osteoblast-like cell response to bioactive composites surface-topography and composition effects. *J Biomed Mater Res B*;70: 250–261, **(2004)**.
- [41]. Sterinberg D, Klinger A, Kohavi D, Sela MN. Adsorption of human salivary proteins to titanium powder. I. Adsorption of human salivary albumin. *Biomaterials*;16:1339–43, **(1995)**.
- [42]. Bernadi G, Kawasali T. Chromatography of polypeptides and proteins on hydroxyapatite columns. *Biochim Biophys Acta*;160:301–10, **(1968)**.
- [43]. Sterinberg D, Klinger A, Kohavi D, Sela MN. Adsorption of human salivary proteins to titanium powder. I. Adsorption of human salivary albumin. *Biomaterials*;16:1339–43, **(1995)**.
- [44]. Bernadi G, Kawasali T. Chromatography of polypeptides and proteins on hydroxyapatite columns. *Biochim Biophys Acta*;160:301–10, **(1968)**.
- [45]. VROMAN and A. L. ADAMS, *J. Biomed. Mater. Res.* 3, 43, **(1969)**.
- [46]. Wei GB, Ma PX. Structure and properties of nano-hydroxyapatite/polymer composite scaffolds for bone tissue engineering. *Biomaterials*;25:4749–57, **(2004)**.
- [47]. Woo KM, Seo J, Zhang R, Ma PX. Suppression of apoptosis by enhanced protein on polymer/hydroxyapatite composite scaffolds. *Biomaterials* 28:2622–30, **(2007)**.
- [48]. Robert A. Latour, Jr. *Encyclopedia of Biomaterials and Biomedical Engineering* DOI: 10.1081/E-EBBE-120041856, **(2005)**.
- [49]. Landolt, D. *Corrosion and surface chemistry of metals*, EPFL Press, ISBN 978-2-940222-11-7, Lausanne, Switzerland, **(2007)**.
- [50]. C. Garcí'a, S. Cere´, A. Dura´n, *Journal of Non-Crystalline Solids* 352, 3488–3495. **(2006)**.
- [51]. C. Sitting, M. Textor, N.D. Spencer, M. Wieland, P.H. Vallotton, *J. Mater. Sci. Mater. Med.* 10 35, **(1999)**.
- [52]. P.A. Lilley, P.S. Walker, G.W. Blunn, in: *Transaction of the 4th World Biomaterials Congress*, Berlin, , p. 227, **(1992)**.
- [53]. R.T. Foley, *Localized corrosion of aluminium alloys. A review. National Association of Corrosion Engineers* 42 No. 5, 277. 22, **(1986)**.
- [54]. H. Cerjak, editor. *Mathematical modeling of weld phenomena 4*. London. The institute of Materials, . 23, **(1988)**.
- [55]. J M Vitek, S A David, J A Johnson, H B Smartt and T Debroy, editors. *Trends in welding research: Proceedings of the 5th. international conference*. ASM International, Materials, **(1999)**.

- [56].Cristiano C. Gomes; Leonardo M. Moreira; Vanessa J.S.. Santos; Alfeu S. Ramos; Juliana P. Lyon; Cristina P. Soares; Fabio V. Santos. *Genet. Mol. Biol.* 34 , **(2011)**.
- [57].Gomez-Vega, J. M., Saiz, E. and Tomsia, A. P. J. *Biomed. Mater. Res.*, 46, 549–559,**(1999)**.
- [58]..L. Luo, N. Cui, Effects of microencapsulation on the electrode behavior of Mg<sub>2</sub>Ni-based hydrogen storage alloy in alkaline solution, *J. Alloy Compd.* 264 , 299–305,**(1998)**.
- [59].J.E. Gray, B. Luan, Protective coatings on magnesium and its alloys – a critical review, *J. Alloy Compd.* 336 , 88–113, **(2002)**.
- [60].Ralf Supplit, Thomas Koch, Ulrich Schubert, Evaluation of the anti-corrosive effect of acid pickling and sol–gel coating on magnesium AZ31 alloy, *Corros. Sci.* 49 , 3015–3023. **(2007)**.
- [61].A.L.K. Tan, A.M. Soutar, I.F. Annergren, Y.N. Liu, Multilayer sol–gel coatings for corrosion protection of magnesium, *Surf. Coat. Technol.* 198 , 478–482, **(2005)**.
- [62].XiankangZhong, Qing Li , Junying Hu, Yihui Lu, *Corrosion Science* 50 ,2304–2309, **(2008)**.
- [63].A. Schueler, *Sol. Energy Mater. Sol. Cells* 84 , 241,**(2004)**.
- [64].Lee, J.W., Won, C.W., Chun, B.S. & Sohn , Dip-coating of alumina films by the sol-gel method. *Journal of Materials Research* 8: 3151-3157,**(1993)**.
- [65].Carcano, G.; Ceriani, M.; and Soglio, F. "Spin Coating with High Viscosity Photoresist on Square Substrates," *Hybrid Circuits*, Vol. 32, Sept. p. 12, **(1993)**.
- [66].O. De Sanctis, L. Gomez, N. Pellegrini, C. Parodi, A. Marajovsky, and A. Duran, *J. Non-Cryst. Solids* 121, 338 , **(1990)**.
- [67].. P. Innocenzi, M. Guglielmi, M. Gobbin, and P. Colombo, *J. Europ. Ceram. Soc.* 10, 431 ,**(1992)**.
- [68]. K. Izumi, H. Tanaka, Y. Uchida, N. Tohge, and T. Minami, *J. Non-Cryst. Solids* 147&148, 483 ,**(1992)**.
- [69].F. Lange, in *International Symposium on Molecular Level Designing of Ceramics*, Nagoya, edited by Team of the NEDO International Joint Research Program, p. 14,**(1991)**.
- [70].C.J. Brinker and G.W. Scherer, *Sol-Gel Science: The Physics and Chemistry of Sol-Gel Processing* (Academic Press, Boston,**(1990)**.
- [71].H. Schmidt, in *Mat. Res. Soc. Symp. Proc.*, Vol. 32: Organically modified silicates by the sol-gel process, p. 327.**(1984)**.
- [72].A A El hadad, V Barranco, A Jiménez-Morales, E Peon and J C Galván, *J. Phys.: Conf. Ser.* 252 012007 ,**(2010)**.
- [73].J. Masalski, J. Gluszek, J. Zabrzski, K. Nitsch, P. Gluszek, *Thin Solid Films* 349 , 186,**(1999)**.
- [74].Chin MyungWhang, Chang Sun Yeo, Yoo Hang Kim, *Bull. Korean Chem. Soc.* 22 , 1366,**(2001)**.

- [75]. Hoy Yul Park , Dong Pil Kang , Moon Kyong Na, HeeWoong Lee , HyeonHwa Lee , Dong Soo Shin, *J Electroceram* , 22:309–314,(**2009**).
- [76]. R. Zandi-zand, A. Ershad-langroudi, A. Rahimi, *J. Non-Cryst. Solids* 351 , 1307–1311,(**2005**).
- [77]. S.M. Hosseinalipoura, A. Ershad-langroudi, Amir NematiHayatia, A.M. Nabizade-Haghighia *Progress in Organic Coatings* , V. 67, 4, 371-374,(**2010**).
- [78]. E.P. Plueddemann, *Silane Coupling Agents*, second ed., Plenum Press, New York,(**1991**).
- [79]. Danqing Zhu, WimJ. van Ooij . *Corrosion Science* 45 , 2177–2197,(**2003**).
- [80]. Y. Djaoued, SimonaBadilescu, P.V. Ashrit, D. Bersani, P.P. Lottici and R. Brüning, *J.Sol-Gel Sci. Technol.* 24, (3) ,247-254 ,(2002).
- [81]. T.N.M. BERNARDS AND M.J. VAN BOMMEL. *J.Sol-Gel Sci. Technol.* 13, 71–74 ,(1998).
- [82]. Gang Yu, Luyi Zhu, Xinqiang Wang, Jiurong Liu, Dong Xu, *Microporous and Mesoporous Materials*, V. 130, 1-3, 189-196, (**2010**).
- [83]. Amir A. El hadad , Diogenes Carbonell , Violeta Barranco , Antonia Jiménez-Morales , Blanca Casal , Juan Carlos Galván, *ColloidPolymSci* ,289:1875–1883, (**2011**).
- [84]. Dean-Mo Liu, T. Troczynski, Wenjea J. Tseng. *Biomaterials* 22 , 1721-1730, (**2001**).
- [85]. C. S. chai, B. ben-nissan. *journal of materials science: materials in medicine* 10 465-469, (**1999**).
- [86]. J. Gallardo, I. Garcia, L. Celis, M.A. Arenas, A. Conde, A. Duran, *J.Sol-Gel Sci. Technol.* 27 , 175, (**2003**).
- [87]. B. MAVIS and A. C. TAS, *J. Amer. Ceram. Soc.* 83 , 989,(**2000**).
- [88]. W. WENG and J. L. BAPTISTA, *ibid.* 82 , 27, (**1999**).
- [89]. S . W. RUSSELL, K. A. LUPTAK, C. T. A. SUCHICITAL, T. L. ALFORD and V. B. PIZZICONI, *ibid.* 79 , 837,(**1996**).
- [90]. W. SUCHANEK and M. YOSHIMURA, *J. Mater. Res.* 13 , 94,(**1998**).
- [91]. W. L. SUCHANEK and M. YOSHIMURA, *J. Amer. Ceram. Soc.* 81 , 765,(**1998**).
- [92]. Duhua Wang, Gordon. P. Bierwagen, *Progress in Organic Coatings Volume 64, Issue 4, , Pages 327–338*,(**2009**).
- [93]. Shin-HeeJuna, Eun-Jung Leea, Se-Won Yooka, Hyoun-EeKima, Hae-Won Kimb, Young-Hag Kohc , *ActaBiomaterialia*V 6, 1, 302, (**2010**).
- [94]. P. Galliano, J.J.D. Damborenea, M.J. Pascual, A. Duran, *J. Sol–Gel Sci. Technol.* 13 , 723,(**1998**).
- [95]. D.C.L. Vasconcelos, J.A.N. Carvalho, M. Mantel, W.L. Vasconcelos, *J. Non-Cryst. Solids* 273 , 135,(**2000**).
- [96]. Lenka Jonášová, Frank A. Müller, Heino Sieber, Peter Greil, *Key Engineering Materials (Volumes 254 - 256) PP 1013-1016*, (**2004**).
- [97]. A. Valle´ s Lluch ,, G. Gallego Ferrer, M. Monleo´ nPradas, *Polymer* 50 , 2874–2884 , (**2009**).

## BIBLIOGRAPHIC RESEARCH

---

- [98]. Masaki Uchida, Hyun-Min Kim, Tadashi Kokubo, Shunsuke Fujibayashi, Takashi Nakamura, *J. Biomedical Materials Research Part AV*. 64 , 1 , **(2002)**.
- [99]. B. E. Amitha Rani and Bharathi Bai J. Basu , *International Journal of Corrosion* Volume 2012 , Article ID 380217, 15 pages , **(2012)**.
- [100]. Damián A. López , Nataly C. Rosero-Navarro , Josefina Ballarre , Alicia Durán Mario Aparicio, Silvia Ceré, *Surface & Coatings Technology* 202 , 2194–2201, **(2008)**.
- [101]. D. A. Skoog et al., *Principles of instrumental analysis*, fifth edition, Harcourt Publishers, **(2001)**.
- [102]. GreGa klančnik , jožef Medved, PriMož Mrvar. *RMZ – Materials and Geoenvironment*,. 57, 127–142, **(2010)**.
- [103]. Hatakeyama, T., Quinn, F. X.: *Thermal Analysis: fundamentals and applications to polymer science*. 2nd ed. John Wiley & Sons Ltd., 180 p., ISBN 0-471-98362-4, **(1999)**.
- [104]. Hiltner, PA; IM Krieger. "Diffraction of Light by Ordered Suspensions". *Journal of Physical Chemistry* 73: 2306, **(1969)**.
- [105]. T. I. Shaw , *Spectroscopy*, 8, no. 8 , 45, **(1993)**.
- [106]. Nisiyama N, Horie K , *J Appl Polym Sci* 34:1619, **(1987)**.
- [107]. D.Y. Kwok, A.W. Neumann, *Advances in Colloid and Interface Science* 81 , 167–249, **(1999)**.
- [108]. Aparicio C, Maazouz Y, Yang D.. *Methods Mol Biol.* ;811:163-77, **(2012)**.
- [109]. A Piegari, E Masetti. *Thin Solid Films* ,124, 3–4, 22 , Pages 249-257, **(1985)**.
- [110]. William R., Guy Nadeau. *Applications of Scanning Electron Microscopy and Energy Dispersive Spectroscopy (SEM/EDS) To Practical Tribology Problems*. Senior Technical Associate Herguth Laboratories, Inc
- [111]. S. Padilla, J. Roman, A. Carenas, M. Vallet-Reg ! I, *Biomaterials* 26 ,475–483, **(2005)**.
- [112]. Kokubo T, Ito S, Huang ZT, et al. 1990a; Ca,P-rich layer formed on high-strength bioactive glass–ceramic A-W. *J Biomed Mater Res* 24: 331–343, **(1990)**.
- [113]. K. Ohta, H. Monma, J. Tanaka and H. Eda , *J. MATERIALS SCIENCE: MATERIALS IN MEDICINE* 13, 7, 633-637, **(2002)**.
- [114]. Bradford MM. A rapid and sensitive method for the quantitation of microgram quantities of protein utilizing the principle of protein-dye binding. *Anal Biochem*;72:248, **(1976)**.
- [115]. Babich, H. & Borenfreund, E. Applications of the neutral red cytotoxicity assay to in vitro toxicology. *Altern. Lab. Anim.* 18, 129–144 , **(1990)**.
- [116]. C. Hammond, *The Basics of Crystallography and Diffraction*, Oxford University Press, New York, **(2002)**.
- [117]. L. Beaunier, I. Epelboin, J.C. Lestrade, H. Takenouti, *Surface Technol.* 4 ,237, **(1976)**.
- [118]. M. Kendig, F. Mansfeld, S. Tsai, *Corrosion Sci.* 23 (4) ,317, **(1983)**.
- [119]. S.A. Linqvist, *Corrosion* 41 , 69, **(1985)**.
- [120]. S.Feliu, J.C. Galván, M. Morcillo, *Prog. Org. Coatings* 17 ,143. **(1989)**.

## BIBLIOGRAPHIC RESEARCH

---

- [121]. D.H. van der Weijde, E.P.M. van Westing, J.H.W. de Wit. *Electrochim. Acta* 41 , 1103, **(1996)**.
- [122]. P.L. Bonora, F. Florian, L. Fredizzi, *Electrochim. Acta* 41 ,1073, **(1996)**.
- [123]. V. Barranco, S. Feliu Jr, S. Feliu, *Corrosion Sci.* 46 ,2221, **(2004)**.
- [124]. V. Barranco, N. Carmona, J.C. Galván, M. Grobelny, L. Kwiatkowski , M.A. Villegas, *Prog. Org. Coatings* 68 , 347, **(2010)**.
- [125]. V. Barranco, J. Carpentier, G. Grundmeier, *Electrochim. Acta* 49,1999, **(2004)**.
- [126]. V. Barranco, N. Carmona, M.A. Villegas, J.C. Galván, *ECS Transactions* 24 , 277, **(2010)**.
- [127]. Evaluation of Organic Coatings with Electrochemical Impedance Spectroscopy. Part 1: Fundamentals of Electrochemical Impedance Spectroscopy. David Loveday, Pete Peterson, and Bob Rodgers, *JCT CoatingsTech*, 46-52, **(2004)**.
- [128]. K. H. Wu, C. M. Chao, T. F. Yeh, T. C. Chang, *Surf. Coat. Technol.*, 201 ,5782, **(2007)**.
- [129]. Guillermo Repetto, Ana del Peso & Jorge L Zurita. Neutral red uptake assay for the estimation of cell viability/cytotoxicity *NATURE PROTOCOLS . VOL.3 NO.7* , **(2008)**.
- [130]. L.L. Hench, *J. Am. Ceram. Soc.*, 81, 1705 ,**(1998)**.
- [131]. A. Slosarczyk, E. Stobierska, Z. Paszkiewicz, M. Gawlick, *J. Am. Ceram. Soc.*, 79, 2539 ,**(1996)**.
- [132]. M. Yoshimura, H. Suda, K. Okamoto, K. Ioku, *J. Mater. Sci.*, 29, 3399 ,**(1994)**.
- [133]. M.F. Hsieh, L.H. Perng, T.S. Chin, H.G Perng, *Biomaterials*, 22, 2601,**(2001)**.
- [134]. K. de Groot, C.P.A.T. Klein, J.G.C. Wolke, J.M.A. de Blicck-Hogervorst, in "CRC Handbook of Bioactive Calcium Phosphates", Vol. 2, T. Yamamuro, L.L. Hench and J. Wilson Editors, CRC Press, Boca Raton, FL, 3-16 ,**(1990)**.
- [135]. P.F. Doorn, P.A. Campbell, J. Worrall, P.D. Benya, H.C. Amstutz, *J. Biomed. Mater. Res.*, 42, 103, **(1998)**.
- [136]. D.G. Wang, C.Z. Chen, H. Ting, T. Lei, *J. Mater. Sci. Mater. Med.*, 19, 2281,**(2008)**.
- [137]. S. Kim, P. N. Kumta, *Mater. Sci. Eng. B.*, 111, 232, **(2004)**.
- [138]. D.G.Wang, C.Z. Chen, J. Ma, G. Zhang, *Colloid Surf. B-Biointerfaces*, 66, 155 ,**(2008)**.
- [139]. K. Cheng, S. Zhang, W.J. Weng, *J. Sol-Gel Sci. Technol.*, 38, 13 ,**(2006)**.
- [140]. C.Y. Ooi, M. Hamdi, S. Ramesh, *Ceramics International*, 33, 7,1171 ,**(2007)**.
- [141]. A.H. Rajabi-Zamani , A. Behnamghader, A. Kazemzadeh S, Synthesis of nanocrystalline carbonated hydroxyapatite powder via nonalkoxide sol-gel method " *Materials Science and Engineering C* 28 ,1326–1329, **(2008)**.
- [142]. D.M. Liu, Q. Yang, T. Troczynski, *Biomaterials* 23, 691. **(2002)**.
- [143]. A. Bigi, E. Boanini, K. Rubini, *J. Solid State Chem.* 177 ,3092, **(2004)**.
- [144]. S.R. Ramanan, R. Venkatesh, *Mater. Lett.* 58 ,3320,**(2004)**.
- [145]. Lu Gan, Robert Pilliar, *Biomaterials* 25 , 5303,**(2004)**.
- [146]. E. Landi, G. Celotti, G. Logroscino, A. Tampieri, *J. Eur. Ceram. Soc.* 23 2931, **(2003)**.

- [147]. Xianghui Hou, Kwang-Leong Choy, Sian Ellen Leach" Processing and in vitro behavior of hydroxyapatite coatings prepared by electrostatic spray assisted vapor deposition method" *J Biomed Mater Res* 83A: 683–691, **(2007)**.
- [148]. Viorel Marin Rusu, Chuen-How Ng, Max Wilke, Size-controlled hydroxyapatite nanoparticles as self-organized organic–inorganic composite materials " *Biomaterials* 26 , 5414–5426, **(2005)**.
- [149]. M. Epple" Solid-state chemical methods to investigate the nature of calcified deposits " *Z Kardiol* 90: Suppl 3,/64 -67 , **(2001)**.
- [150]. E. Landi, A. Tampieri, G. Celotti, S. Sprio, *J. Eur. Ceram. Soc.* 20 , 2377. **(2000)**.
- [151]. Klung HP, Alexander E. X-ray diffraction procedures for polycrystalline and amorphous materials. New York: John Wiley,, **(1974)**.
- [152]. Liling Yan, Yang Leng, Lu-Tao Weng, *Biomaterials* 24 ,2585, **(2003)**.
- [153]. S.M. Best , A.E. Porter , E.S. Thian , J. Huang "Bioceramics: Past, present and for the future " *Journal of the European Ceramic Society* 28 , 1319–1327, **(2008)**.
- [154]. C. Hammond, *The Basics of Crystallography and Diffraction*, Oxford University Press, New York, **(2002)**.
- [155]. Zafer Evis "Reactions in hydroxylapatite–zirconia composites " *Ceramics International* 33,987–991, **(2007)**.
- [156]. Zafer Evis , Metin Usta , Isil Kutbay"Improvement in sinterability and phase stability of hydroxyapatite and partially stabilized zirconia composites " *J. European Ceramic Society* 29 , 621–628,**(2009)**.
- [157]. R. Z. legeros, M. A. miravite, G. B. quirolgico & M. E. J. curzon"The Effect of some Trace Elements on the Lattice Parameters of Human and Synthetic Apatites" *J. Calcified Tissue International*, Volume 22, 362-367 , **(1976)**.
- [158]. LeGeros RZ, LeGeros JP. Dense hydroxyapatite. In: Hench LL, Wilson J, editors. *An introduction to bioceramics*. London: World Scientific Publishing Co, p. 144}5, **(1993)**.
- [159]. K.A. Gross, C.S. Chai, K. Kannangara, B. Ben-Nissan, and L. Hanley, *J. Mater. Sci. Mater. Med.* 9, 839 , **(1998)**.
- [160]. Elliot, J.C. *Structure and Chemistry of the Apatites and other Calcium Orthophosphates*. *Studies in Inorganic Chemistry* 18: 48-87, **(1994)**.
- [161]. M. kamitakahara, M. kawashita, T. kokubo and T. nakamura, *ibid.* 22 , 3191,**(2001)**.
- [162]. H.-M. Kim, T. Himeno, M. Kawashita, T. Kokubo, T. Nakamura, *J. R. Soc. Interface* 1, 17 , **(2004)**.
- [163]. Bigerelle M, Anselme K, Noe"l B, Ruderman I, Hardouin P, Iost A. Improvement in the morphology of Ti-based surfaces: A new process to increase in vitro human osteoblast response. *Biomaterials* 23(7):1563–1577, **(2002)**.
- [164]. Bagno A, Bello DD. Surface treatment and roughness properties of Tibased biomaterials. *J Mater Sci Mater Med* 15(9):935–949, **(2004)**.
- [165]. Yang Kong et al. *Chinese Science Bulletin* , vol. 52 , no. 2 , 267-271, **(2007)**.

## BIBLIOGRAPHIC RESEARCH

---

- [166]. M.Weil, A.J.Ruys, B.K. Milthorpe, C.C. Sorrell, J.H. Evans, J. Sol-Gel Sci. Technol 21, 39, **(2001)**.
- [167]. J. R. Macdonald, Ann. Biomed. Eng., 20, 289 **,(1992)**.
- [168]. J. R. Macdonald, Ann. Biomed. Eng., 20, 289, **(1992)**.
- [169]. "Corrosion and Degradation of Implant Materials", B. C. Syrett, Amitav Acharya editors, American Society for Testing and Materials, ASTM-STP 684, **(1979)**.
- [170]. M. Pourbaix, Biomaterials 5, 122 **,(1984)**.
- [171]. "Electrochemical Techniques in Corrosion Science and Engineering", R.G. Kelly, J.R. Scully, D. W. Shoesmith, R.G. Buchheit Editors, Marcel Dekker, Inc., New York, Basel **,(2002)**.
- [172]. V. Barranco, M.L. Escudero, M.C. Garcia-Alonso, Electrochimica Acta, 52, 4374 **,(2007)**.
- [173]. M.C. Garcia-Alonso, L. Saldana, C. Alonso, V.Barranco, M. A. Muñoz, M. L Escudero, Acta Biomaterialia, 5, 1374 **,(2009)**.
- [174]. "Uhlig's Corrosion Handbook" (The ECS Series of Texts and Monographs), 3rd Edition edition R. Winston Revie Editor, John Wiley and Sons Inc., Hoboken, NJ, USA , **(2011)**.
- [175]. "Impedance Spectroscopy: Theory, Experiment, and Applications", 2nd Edition, E. Barsoukov and J.R. Macdonald Editors. John Wiley & Sons, Inc., Hoboken, NJ, USA **(2005)**.
- [176]. G.W. Walter, Corr. Sci., 26, 681,**(1986)**.
- [177]. S. Feliu, J.C. Galván, M. Morcillo, Prog. Org. Coat. 17, 143, **(1989)**.
- [178]. J.C. Galván, S. Feliu, M. Morcillo, Prog. Org. Coat. 17, 135 **,(1989)**.
- [179]. S. Feliu, J.C. Galván, M. Morcillo, Corr. Sci., 30, 989 **,(1990)**.
- [180]. B. Chico, J.C. Galván, D. de la Fuente, M. Morcillo, Prog. Org. Coat., 60, 45 **,(2007)**.
- [181]. D.C. Silverman, Corrosion, 47, 87, **(1991)**.
- [182]. C.H. Hsu, F. Mansfeld, Corrosion, 57, 747 **,(2001)**.
- [183]. Brinker CJ, Scherer CW (eds) Academic Press, Boston, **(1990)**.
- [184]. Novak BM ,Adv Mater 5:422, **(1993)**.
- [185]. Sanchez C, Ribot F ,New J Chem 18:1007,**(1994)**.
- [186]. Wen JY, Wilkes GL ,Chem Mater 8:1667,**(1996)**.
- [187]. Stein A, Melde BJ, Schroden RC ,Adv Mater 12:1403,**(2000)**.
- [188]. Gomez-Romero P ,Adv Mater 13:163,**(2001)**.
- [189]. Sanchez C, Soler-Illia GJDA, Ribot F, Lalot T, Mayer CR, Cabuil V ,Chem Mater 13:3061 **,(2001)**.
- [190]. Schottner G .Chem Mater 13:3422, **(2001)**.
- [191]. Sanchez C, Julian B, Belleville P, Popall M . J Mater Chem 15:3559, **(2005)**.
- [192]. Casal B, Ruiz-Hitzky E, Crespín M, Tinet D, Galván JC. J Chem Soc Faraday Trans 1(85):4167, **(1998)**.
- [193]. Ruiz-Hitzky E, Aranda P, Casal B, Galván JC . Adv Mater 7:180, **(1995)**.
- [194]. Wang J, Merino J, Aranda P, Galván JC, Ruiz-Hitzky E. J Mater Chem 9:161, **(1999)**.

## BIBLIOGRAPHIC RESEARCH

---

- [195]. Ruiz-Hitzky E, Aranda P, Casal B, Galván JC . Rev Inorg Chem 21:125, **(2001)**.
- [196]. Rojas-Cervantes ML, Casal B, Aranda P, Savirón M, Galván JC, Ruiz-Hitzky E . Colloid Polym Sci 279:990, **(2001)**.
- [197]. Amarilla JM, Casal B, Galván JC, Ruiz-Hitzky E . Chem Mater 4:62, **(1992)**.
- [198]. Galván JC, Aranda P, Amarilla JM, Casal B, Ruiz-Hitzky E. J Mater Chem 3:687, **(1993)**.
- [199]. Aranda P, Jiménez-Morales A, Galván JC, Casal B, Ruiz-Hitzky E . J Mater Chem 5:817, **(1995)**.
- [200]. Lev O, Tsionsky M, Rabinovich L, Glezer V, Sampath S, Pankratov I, Gun J . Anal Chem 67(1):22A, **(1995)**.
- [201]. Lev O, Wu Z, Bharathi S, Glezer V, Modestov A, Gun J, Rabinovich L, Sampath S .Chem Mater 9:2354, **(1997)**.
- [202]. Wang BQ, Li B, Deng Q, Dong SJ . Anal Chem 70:3170 22. Walcarius A (2001) Chem Mater 13:3351, **(1998)**.
- [203]. Zheludkevich ML, Salvado IM, Ferreira MGS .J Mater Chem 15:5099, **(2005)**.
- [204]. Griffith LG, Naughton G . Science 295(5557):1009, **(2002)**.
- [205]. Kokubo T, Kim HM, Kawashita M . Biomaterials 24:2161, **(2003)**.
- [206]. Langer R, Tirrell DA . Nature 428(6982):487, **(2004)**.
- [207]. Philipp G, Schmidt H , J Non Cryst Solids 63:283, **(1984)**.
- [208]. Schmidt H , Mater Res Soc Symp Proc 32:327, **(1984)**.
- [209]. Park O-H, Eo Y-J, Choi Y-K, Bae B-S , J Sol-Gel Sci Technol 16:235, **(1999)**.
- [210]. Rodriguez MA, Liso MJ, Rubio F, Rubio J, Oteo JL . J Mater Sci 34:3867, **(1999)**.
- [211]. Matinlinna JP, Ozcan M, Lassila LVJ, Vallittu PK . Dent Mater 20:804, **(2004)**.
- [212]. Abdelmouleha M, Boufia S, Belgacemb MN, Dufresne A ,Compos Sci Technol 67:1627, **(2007)**.
- [213]. Franquet A, Terryn H, Vereecken J , Appl Surf Sci 211:259, **(2003)**.
- [214]. Innocenzi P, Brusatin G , J Non Cryst Solids 333:137, **(2004)**.
- [215]. Danqing Z, van Ooij WJ ,J Adhes Sci Tech 16:1235, **(2002)**.
- [216]. Gunji T, Makabe Y, Takamura N, Abe Y , Appl Organomet Chem 15:683, **(2001)**.
- [217]. Jana S, Lim MA, Baek IC, Kim CH, Seok SI , Mater Chem Phys 112:1008, **(2008)**.
- [218]. Nisiyama N, Horie K , J Appl Polym Sci 34:1619, **(1987)**.
- [219]. Salon MCB, Bayle PA, Abdelmouleh M, Boufic S, Belgacem MN ,Colloids Surface Physicochem Eng Aspect 312:83,**(2008)**.
- [220]. Glaser RH, Wilkes GL ,Polym Bull 19:51,**(1988)**.
- [221]. Chiang CL, Ma CCM , Polym Degrad Stab 83:207, **(2004)**.
- [222]. Han YH, Taylor A, Mantle MD, Knowles KM , J Non Cryst Solids 353:313–320, **(2007)**.
- [223]. Miyatake K, Ohama O, Kawahara Y, Urano A, Kimura A Sei Tech Rev 65:21–24, **(2007)**.
- [224]. Osterholtz, F.D.; Pohl, E.R., Journal of Adhesion Science and Technology, Volume 6, Number 1, pp. 127-149(23),**(1992)**.

## BIBLIOGRAPHIC RESEARCH

---

- [225]. Salon MCB, Abdelmouleh M, Boufi S, Belgacem MN, Gandini A, *J Colloid Interface Sci* 289:249–261, **(2005)**.
- [226]. Seok SI, Kim JH, Choi KH, Hwang YY. *Surf Coat Technol* 200(11):3468-3472, **(2006)**.
- [227]. Lev O, Wu Z, Bharathi S, Glezer V, Modestov A, Gun J, Rabinovich L, Sampath S. *Chem Mater* 9(11):2354-2375, **(1997)**.
- [228]. Judeinstein P, Sanchez C. *J Mater Chem* 6(4):511-525, **(1996)**.
- [229]. Letailleur AA, Ribot F, Boissiere C, Teisseire J, Barthel E, Desmazieres B, Chemin N, Sanchez C. *Chem Mat* 23(22):5082-5089, **(2011)**.
- [230]. Sanchez C, Belleville P, Popall M, Nicole L. *Chem Soc Rev* 40(2):696-753, **(2011)**.
- [231]. Jiménez-Morales A, Galván JC, Aranda P, Ruiz-Hitzky E. *Mater Res Soc Symp Proc* 519:211-216, **(1998)**.
- [232]. Jiménez-Morales A, Aranda P, Galván JC. *J Mater Process Technol* 143-144:5-10, **(2003)**.
- [233]. García-Heras M, Jiménez-Morales A, Casal B, Galván JC, Radzki S, Villegas MA. *J Alloy Compd* 380(1-2): 219-224, **(2004)**.
- [234]. Liu Y, Sun DZ, You H, Chung JS. *Appl Surf Sci* 246 (1-3):82-89, **(2005)**.
- [235]. Phanasaonkar A, Raja V.S. *Surf Coat Tech* 203(16):2260-2271, **(2009)**.
- [236]. van Ooij WJ, Zhu D, Stacy M, Seth A, Mugada T, Gandhi J, Puomi P. *Tsinghua Sci Technol* 10(6):639-664. doi:10.1016/S1007-0214(05)70134-6, **(2005)**.
- [237]. Quinet M, Neveu B, Moutarlier V, Audebert P, Ricq L. *Prog Org Coat* 58(1):46-53, **(2007)**.
- [238]. Park HY, Kang DP, Na MK, Lee HW, Lee HH, Shin, D S. *J Electroceram* 22(1-3):309-314, **(2009)**.
- [239]. Yu S, Wong TKS, Hu X, Pita K. *J Electrochem Soc* 150(5):F116-F121, **(2003)**.
- [240]. Jing CB, Hou JX. *J Appl Polym Sci* 105(2):697-705, **(2007)**.
- [241]. D. MURESAN, M. DRAGAN BULARDA, C. POPA, L. BAIA, S. SIMON. *Rom. Journ. Phys.*, Vol. 51, Nos. 1–2, P. 231–237, Bucharest, **(2006)**.
- [242]. Jiménez-Morales A, Galván JC, Aranda P. *Electrochim Acta*, 47(13-14):2281-2287, **(2002)**.
- [243]. Gunawidjaja PN, Lo AYH, Izquierdo-Barba I, García A, Arcos D, Svensson B, Grins J, M. Vallet-Regí M, Eden M. *J Phys Chem C* 114(45):19345-19356, **(2010)**.
- [244]. Li LH, Kommareddy KP, Pilz C, Zhou CR, Fratzl P, Manjubala I. *Acta Biomater* 6(7):2525-2531, **(2010)**.
- [245]. Yuanjing Cui, Guodong Qian, Lujian Chen, Junkuo Gao, Minquan Wang, *Optics Communications* 270 414-418, **(2007)**.
- [246]. Makoto Takemori. *Ceramics International* 35 ,1747-1755, **(2009)**.
- [247]. Wang D, Bierwagen GP. *Prog Org Coat* 64(4):327-338, **(2009)**.
- [248]. Lalit M. Pandey, Sudip K. Pattanayek, *Applied Surface Science* 257 , 4731–4737, **(2011)**.
- [249]. Ishizawa H, Ogino M. *J Biomed Mater Res* 29(1):65-72, **(1995)**.

## BIBLIOGRAPHIC RESEARCH

---

- [250]. Cortada M, Giner LL, Costa S, Gil FJ, Rodriguez D, Planell JA . J Mater Sci Mater Med 11(5):287-293, **(2000)**.
- [251]. Aparicio C, Gil FJ, Fonseca C, Barbosa M, Planell JA. Biomaterials 24(2):263-273, **(2003)**.
- [252]. Hodgson AWE, Mueller Y, Forster D, Virtanen S . Electrochim Acta 47(12):1913-1923, **(2002)**.
- [253]. N. Hijo'n, M. V. Caban~ as, I. Izquierdo-Barba, and M. Vallet-Regi' Chem. Mater. 2004, 16, 1451-1455,**(2004)**.
- [254]. Cavanaugh, P.F. et al. A semi-automated neutral red based chemosensitivity assay for drug screening. Invest. New Drugs 8, 347–354 ,**(1990)**.
- [255]. Filman, D.J., Brawn, R.J. & Dankler, W.B. Intracellular supravital stain delocalization as an assay for antibody-dependent complement-mediated cell damage. J. Immunol Methods 6, 189–207, **(1975)**.
- [256]. Albrektsson T, Hansson HA. An ultrastructural characterization of the interface between bone and sputtered titanium or stainless steel surfaces. Biomaterials 1986;7:201–5, **(1996)**.
- [257]. Healy KE, Ducheyne P. Hydration and preferential molecular adsorption on titanium in vitro. Biomaterials;13:553–61, **(1992)**.
- [258]. G.B. Sigal, M. Mrksich, G.M. Whitesides, Effect of surface wettability on the adsorption of proteins and detergents, J. Am. Chem. Soc. 120 ,3464–3473, **(1998)**.
- [259]. Paul Roach. David Eglin. Kirsty Rohde. Carole C. Perry J Mater Sci: Mater Med 18:1263–1277, **(2007)**.
- [260]. H. Niknejad , H. Peirovi , M. Jorjani , A. Ahmadiani, J. Ghanavi, A. M. Seifalian. European Cells and Materials Vol. 15 ( 88-99), **(2008)** .
- [261]. Borenfreund, E. & Puerner, J.A. A simple quantitative procedure using monolayer cultures for cytotoxicity assays (HTD/NR90). J. Tissue Cult. Methods 9, 7–9 ,**(1984)**.
- [262]. Babich, H. & Borenfreund, E. Applications of the neutral red cytotoxicity assay to in vitro toxicology. Altern. Lab. Anim. 18, 129–144 ,**(1990)**.
- [263]. Cavanaugh, P.F. et al. A semi-automated neutral red based chemosensitivity assay for drug screening. Invest. New Drugs 8, 347–354 ,**(1990)**.
- [264]. Filman, D.J., Brawn, R.J. & Dankler, W.B. Intracellular supravital stain delocalization as an assay for antibody-dependent complement-mediated cell damage. J. Immunol Methods 6, 189–207 ,**(1975)**.
- [265]. Albrektsson T, Hansson HA. An ultrastructural characterization of the interface between bone and sputtered titanium or stainless steel surfaces. Biomaterials;7:201–5, **(1986)**.
- [266]. Healy KE, Ducheyne P. Hydration and preferential molecular adsorption on titanium in vitro. Biomaterials;13:553–61, **(1992)**.
- [267]. French HG, Cook SD, Haddad RJ. Correlation of tissue reaction to corrosion in osteosynthetic devices. J Biomed Mater Res;18:817–28, **(1984)**.

## BIBLIOGRAPHIC RESEARCH

---

- [268]. Finnegan M. Tissue response to internal fixation devices. *Crit Rev Biocompat*;5:1–11, **(1989)**.
- [269]. Albrektsson T, Branemark PI, Hansson HA, Kasemo B, Larsson K, Lundstrom I, McQueen DH, Salak R. The interface zone of inorganic implants in vivo: titanium implants in bone. *Ann Biomed Eng*;11:1–27, **(1983)**.
- [270]. Greenwood, J.A., J.E. Murphy-Ullrich, Signaling of de-adhesion in cellular regulation and motility. *Microsc Res Tech* 4 3: 420–432, **(1998)**.
- [271]. Burridge, K., M. Chrzanowska-Wodnicka, Focal adhesions, contractility, and signaling. *Annu Rev Cell Biol* 12: 463–518, **(1996)**.
- [272]. Sahil Jalota, Sarit B. Bhaduri, A. Cuneyt Tas, *Materials Science and Engineering C* 27, 432–440, **(2007)**.
- [273]. Y Oshida, *Bioscience and Bioengineering of Titanium Materials*, 1st Edition Elsevier Science, **(2006)**.
- [274]. Niida, H.; Takahashi, M.; Uchino, T.; Yoko, T., "Preparation and structure of organic-inorganic hybrid precursors for new type low-melting glasses," *Journal of Non-Crystalline Solids* 306(292-299, **(2002)**.
- [275]. J. FIKE, B. COZAD, C.R. FERNANDEZ, R. SPEARS, C.J. NELSON, and L.A. OPPERMAN, Texas A&M Health Science Center, Baylor College of Dentistry, Dallas, TX, 2Lynntech Inc, College Station, TX, Phosphate treatment increases osteoblast proliferation on SLA-titanium (IADR/AADR/CADR 87th General Session and Exhibition, **(2009)**.
- [276]. Zanchetta P, Guezennec J. Surface thermodynamics of osteoblasts: relation between hydrophobicity and bone active biomaterials. *Colloid Surf B*;22:301–307, **(2001)**.
- [277]. Giavaresi G, et al, A novel multiphasic anodic spark deposition coating for the improvement of orthopedic implant osseointegration: An experimental study in the cortical bone of sheep. *J Biomed Mater Res Part A*; 1022-1031, **(2007)**.
- [278]. Y.Y. Yu, C.Y. Chen, W.C. Chen, *Polymer* 44, 593, **(2003)**.
- [279]. Z.H. Huang, K.Y. Qiu, *Polymer* 38, 521, **(1997)**.
- [280]. Qi Chen, Noboru Miyata, Tadashi Kokubo, Takashi Nakamura" *J. Biomedical Materials Research*, 51, 4, 605–611, **(2000)**.
- [281]. Helmut Schweikl, Rainer Müller, Carsten Englert, Karl-Anton Hiller, Richard Kujat, Michael Nerlich, Gottfried Schmalz. *J Mater Sci: Mater Med*, 18:1895–1905, **(2007)**.
- [282]. K. ANSELME, *Biomaterials* 21, 667, **(2000)**.
- [283]. K. ANSELME and M. BIGERELLE, *Biomaterials* 27, 1187, **(2006)**.
- [284]. Anselme K.. Osteoblast adhesion on biomaterials. *Biomaterials*. 21, 667–681, **(2000)**.
- [285]. Y. TAMADA and Y. IKADA, *J. Biomed. Mater. Res.* 28, 783, **(1996)**.
- [286]. G. ALTANKOV, F. GRINNELL and T. GROTH, *J. Biomed. Mater. Res.* 30, 385, **(1996)**.
- [287]. H. DU, P. CHANDAROY and S. W. HUI, *Biochim. Biophys. Acta.* 1326, 236, **(1997)**.
- [288]. T. GROTH, B. SEIFERT, G. MALSCH, W. ALBRECHT, D. PAUL, A. KOSTADINOVA, N. KRASTEVA and G. ALTANKOV, *J. Biomed. Mater. Res.* 61, 290, **(2002)**.

## BIBLIOGRAPHIC RESEARCH

---

- [289]. N. FAUCHEUX, R. SCHWEISS, K. LUTZOW, C. WERNER and T. GROTH, *Biomaterials* 25 , 2721, **(2004)**.
- [290]. M. A. LAN, C. A. GERSBACH, K. E. MICHAEL, B. G. KESELOWSKY and A. J. GARCIA, *Biomaterials* 26 , 4523, **(2005)**.

## *Published Articles*



## Multifunctional sol-gel derived thin film based on nanocrystalline hydroxyapatite powders

This article has been downloaded from IOPscience. Please scroll down to see the full text article.

2010 J. Phys.: Conf. Ser. 252 012007

(<http://iopscience.iop.org/1742-6596/252/1/012007>)

View [the table of contents for this issue](#), or go to the [journal homepage](#) for more

Download details:

IP Address: 161.111.91.195

The article was downloaded on 29/08/2012 at 08:48

Please note that [terms and conditions apply](#).

# Multifunctional sol-gel derived thin film based on nanocrystalline hydroxyapatite powders

A.A. El hadad<sup>1</sup>, V. Barranco<sup>2</sup>, A. Jiménez-Morales<sup>3</sup>, E. Peon<sup>4</sup>, J.C. Galván<sup>1</sup>

<sup>1</sup>Centro Nacional de Investigaciones Metalúrgicas (CSIC), Madrid, Spain. <sup>2</sup>Instituto de Ciencia de Materiales de Madrid (CSIC), Madrid, Spain. <sup>3</sup>Universidad Carlos III de Madrid.

Departamento de Ciencia e Ingeniería de Materiales e Ingeniería Química. (Madrid), Spain.

<sup>4</sup>Centro de Biomateriales, Universidad de La Habana, Havana, Cuba

E-mails: amirelhada@cenim.csic.es, jcgalkan@cenim.csic.es

**Abstract.** The aim of this work was to prepare bioactive hydroxyapatite coatings by sol-gel method and to study the effect of thermal treatment temperature upon the bioactivity and corrosion protection of these coatings on Ti6Al4V alloy. The application of (DTA/TGA) and (XRD) has provided valuable information about the phase transformation, mass loss, identification of the phases developed, crystallite size and degree of crystallinity. (SEM/EDX) has been applied to study the surface morphology of coated samples before and after immersion in simulated body fluid (SBF) to detect the biomimetic precipitation of the bone-like apatite. The obtained results show that all the prepared samples are ceramic nanocrystalline with crystal structure and composition like hydroxyapatite, with little deviations from that present in the human bone. The bioactivity of the studied samples is found to be closely related to the thermal treatments applied. That is, the bioactivity decreases as the temperature of the thermal treatment increase. Coatings from such prepared hydroxyapatite sol have been accomplished by dip-coating technique on non-toxic Ti6Al4V alloy for biomedical applications. The corrosion behaviour of the resulting hydroxyapatite coatings in a (SBF) has been studied by electrochemical impedance spectroscopy (EIS). The hydroxyapatite coated Ti6Al4V alloy displayed excellent bioactivity when soaked in the (SBF) and acceptable corrosion protection behaviour.

## 1. Introduction

The bone tissue is considered as a natural composite, composed of two constituents organic and inorganic solid, the inorganic solid is carbonated hydroxyapatite (CHA) while the organic one is collagen. The hydroxyapatite (HA) which has the formula  $\text{Ca}_{10}(\text{PO}_4)_6(\text{OH})_2$ , amounts to 65% of the total bone mass, with the remaining mass formed by organic matter "mostly collagen" and water<sup>[1]</sup>. The collagen molecules are bonded together forming fibrils, which bound together to form fibers. Between these fibers there are small interstitial empty spaces, where apatite nanocrystals are deposited. For this reason, the most used calcium phosphate in implant fabrication is HA, a biological active material with different forms, particles, films, coatings, fibers which has extensive biomedical applications<sup>[2]</sup>. Nano-sized HA powders have a high specific surface area and therefore exhibit enhanced activity toward chemical and biological interactions in the human body. HA has been known to form *in vitro* and *in vivo* a bioactive bone-like apatite layer spontaneously on its surfaces. The formed apatite layer act as interface between the implant and tissue, facilitate the formation of chemical and biological bond with the osseous tissue. Therefore, the essential prerequisite for a biomaterial to bond

directly to living bone is the formation of an apatite layer on its surface when implanted in the body. As this layer is formed, the protein absorption onto the surface of such layer will trigger the osteoblasts, "new bone forming cells", to differentiate and reproduce, leading the formation of new bone tissue.

The HA can be synthesized by many methods<sup>[3,4]</sup>. Among all of them, the sol-gel process is the most used technique for production of HA because it offers many advantages over other traditional methods. It allows the production of ultra fine and pure ceramic powders with relatively low cost, low synthesis temperature, ability to coat porous and complex surfaces with high control of composition and microstructure of the obtained film<sup>[5-7]</sup>. The HA synthesized by sol-gel will form strong chemical bonds with bone *in vivo*, all of these mentioned properties place the HA into a class of biomaterials known as bioactive materials. Unfortunately brittleness limits its usage for load bearing applications. For that it can only be used as bone fillers and bone graft substitutes in orthopedics<sup>[8]</sup>. The only exception where HA is applied in dynamically loaded situations is the use of HA as a coating material.

In the present study, HA was synthesized by adopting a sol-gel approach. The resultant HA was characterized using DTA, TGA, XRD and SEM/EDX techniques. Sol-gel-derived HA coatings on Ti6Al4V substrate were evaluated via electrochemical studies involving impedance measurements in Kokubo's simulated body fluid (SBF) solution.

## 2. Experimental

### 2-1. Preparation of Hydroxyapatite Powders.

The prepared HA sol-gel was obtained by hydrolysis and condensation of two precursors. Triethyl phosphite,  $(C_2H_5O)_3P$  (Fluka) and calcium nitrate tetrahydrate,  $Ca(NO_3)_2 \cdot 4H_2O$  (Panreac) were employed as phosphorus and calcium precursors respectively. In brief, 0.03mol of triethyl phosphite was first diluted in ethanol and hydrolyzed for 24 h with a fixed amount of distilled water in a parafilm-sealed glass container under vigorous stirring.

A stoichiometric amount, 0.05 moles, of  $Ca(NO_3)_2 \cdot 4H_2O$  is dissolved first in 25 ml of anhydrous ethanol then added dropwise into the hydrolyzed phosphite sol. The mixed sol solution was then continuously agitated for additional 30 min and kept static (aging) at 45°C. The pH value was adjusted to be 7.5; the sol was aged static at 60°C for 16 h. The solvents were then driven off resulting in a viscous liquid. Further drying at 80°C was done to obtain the prepared material in a powder form. The obtained powder was placed in a steel die, and pressed to 7 GPa to produce 12.9 mm diameter pellets which were sintered at various temperatures (600, 800, and 1200°C).

### 2-2. Preparation of HA Coatings on Ti6Al4V Substrates

Ti6Al4V disks of 2 cm of diameter and 0.4 cm of thickness were polished using different silicon carbide grit up to 1200 grade. The substrates were ultrasonically degreased with acetone for 10 min and washed with distilled water. Finally, the substrates were dried at 200°C for 1 hour in an air oven to form a titanium oxide surface. These substrates were dip coated with the HA sol solution, with a dipping and withdraw speed of 12 cm/min. The sol-coated substrates were then immediately transferred into an air oven and held at 80°C for 30 min. To increase the thickness of the coating, the above process was repeated for three times and finally it was sintered at various temperatures (600, 800°C).

## 2.3 Characterization of HA Powder Samples

### 2.3.1 Thermal Behaviour (DTA/TGA)

The thermal behavior and mass loss of the powder was carried out using ( **SETARAM DTA-TG** Setsys Evolution -1750), with  $\alpha$ -Al<sub>2</sub>O<sub>3</sub> powders as a reference material. HA powder samples with a weight of about 50 mg were analyzed. The samples and the reference material were heated in air from ambient temperature to 1300°C in argon at a heating rate of 20°C/min.

### 2.3.2 X-ray Diffractometer Analysis (XRD)

X-ray diffraction patterns have been recorded using a Siemens diffractometer D5000 equipped with scanning rate 0.1° in the 2 $\theta$  ranging from 10° to 100° step time 1 sec. The prepared HA powder samples (S1 "as-prepared", S6 "treated at 600°C", S8 "treated at 800°C" and S12 "treated at 1200°C") were examined with a high-resolution X-ray powder diffractometer using monochromatic Cu K $\alpha$  radiation ( $\lambda$ = 0.15406 nm). The results have been used to notice the change of developing phases, crystal structure of HA and degree of crystallinity, with the variation of heat treatment temperatures.

## 2.4. Evaluation of Bioactivity and Corrosion Protection

### 2.4.1 Immersion Tests of HA-Coatings/Ti6Al4V System in SBF

The *in vitro* bioactivity of the prepared HA-coatings/Ti6Al4V samples was tested by soaking in Kokubo's simulated body fluid (SBF). The pH of the SBF solution was buffered at 7.4. The specimens were immersed in separate plastic containers then incubated for 15 days at 37.5°C. After 15 days the specimens were removed from the solution, rinsed with distilled water and left to dry at room temperature.

### 2.4.2 Corrosion Behaviour

The corrosion behaviour of the HA-coatings/Ti6Al4V system was evaluated by applying electrochemical impedance spectroscopy measurements (EIS). For this purpose a potentiostat/galvanostat AutoLab EcoChemie PGSTAT30 (Eco Chemie, Utrecht, The Netherlands) equipped with a FRA2 frequency response analyzer module was used. A three electrode setup was applied. The working electrode was the investigated sample with an area of 2.14 cm<sup>2</sup>. The reference and the counter-electrode were a saturated calomel electrode (SCE) and a large size graphite sheet, respectively. The electrochemical cell was filled with Kokubo's solution. The EIS measurements were made at the open circuit potential (OCP). Logarithmic frequency scans were carried out by applying sinusoidal wave perturbations of  $\pm 10$ mV in amplitude, in the range of 10<sup>5</sup>-10<sup>-3</sup>Hz. Five impedance sampling points were registered per frequency decade. The impedance data were analysed by using the 'EQUIVCRT' program developed by Boukamp (AC-Immittance Data Analysis System, Version 4.51, University of Twente, The Netherlands, 1993). The electrical resistance values were obtained by applying the fitting routines of the ZView® software version 3.1c (Scribner Associates Inc, Southern Pines, NC, USA).

### 2.4.3 Scanning Electron Microscopy (SEM/EDX)

The surface morphology of selected specimens, before and after immersion in SBF, was carried out by scanning electron microscopy (SEM) with a field emission gun (FEG) coupled with an energy dispersive X-ray (EDX) system (Oxford Inca microanalysis system and a windowless detector) for chemical analysis. The samples were examined in a JEOL-6500F microscope at 15 kV acceleration voltages. The samples were coated with ultra thin carbon conductive layer to avoid the charging due to the non conductive nature of the studied samples.

## 3. Results and discussion

Differential Thermal Analysis (DTA) and thermogravimetry (TG) diagrams of the obtained powders are given in Figure 1. The DTA was employed to determine the temperature at which the as-prepared powder, amorphous calcium phosphate (ACP), transforms to crystalline HA.

In the DTA curve of dry gel (powder), the first endothermic peak appeared at 38.8°C which was due to the evaporation of the absorbed water (residual moisture evaporation)<sup>[9]</sup>. The two endothermic peaks which appeared at 123.3°C and 443.2°C were attributed to elimination of crystalline water in unreacted calcium nitrate tetra hydrate  $\text{Ca}(\text{NO}_3)_2 \cdot 4\text{H}_2\text{O}$  and removal of  $\text{NO}_3^-$  groups, as well as, to the condensation "dehydration" of hydrogen phosphate ions ( $\text{HPO}_4^{2-}$ ) to form amorphous pyrophosphates ( $\text{P}_2\text{O}_7^{4-}$ ) which is a component of amorphous calcium phosphates that forms during processing of HA synthesis<sup>[10-12]</sup>. The endothermic peak at 532.5°C is representative of the endothermic reaction indicating the crystallization of HA. The last endothermic peak observed at 1197.6°C may be attributed to the decomposition of the HA.

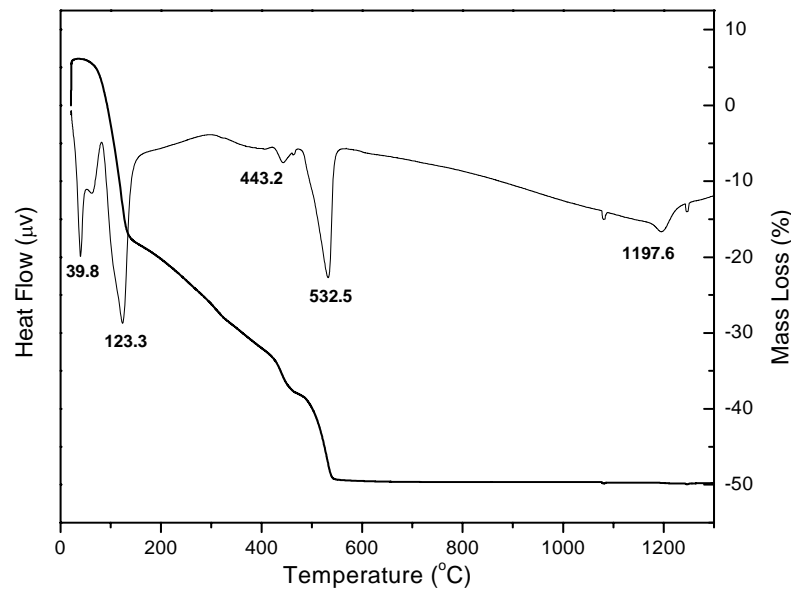


**Figure 1.** DTA/TG of the as prepared powder

In the TG, the weight loss was complete at about 570°C and three discrete weight-loss regions occurred as seen in the TG diagram. The first region at 44-172°C with 25% weight loss corresponds to the elimination of adsorbed water. This process was indicated as endothermic peak at 38.8°C and shoulder at 60°C in the DTA diagram. The second weight loss region appeared at 172-479°C in the TGA with 18% weight loss which corresponded to elimination of lattice water and was indicated as endothermic peak in the DTA diagram at 443°C. The third weight loss observed in the TG diagram at 479-570°C with a weight loss of 11 % corresponds to the decomposition of the nitrate salts which is also indicated as an endothermic peak at 532°C in the DTA curve.

X-ray diffractometry (XRD) identifying the developed phases, showed following features: a highly crystalline sample gives rise to narrow peaks and a poorly crystalline sample gives rise to broad peaks. "Crystallinity" refers to the degree of structural order in a solid. In a crystal, the atoms or molecules are arranged in a regular, periodic manner. In this respect means the degree of order within the crystal lattice<sup>[13]</sup>. According to Landi et al., the fraction of crystalline phase ( $X_c$ ) can be calculated through the equation below<sup>[14]</sup>:

$$X_c = 1 - \frac{V_{112/300}}{I_{300}}$$

$I_{300}$ : Intensity of peak diffracted from the (300) crystallographic planes of HA.

$V_{112/300}$ : Intensity of the valley between the peaks of the planes (112) and (300) of HA.

The average crystallite size was calculated from the broadening in the XRD pattern. According to the Scherrer's equation<sup>[15]</sup>:

$$L_c = \frac{K\lambda}{\beta \cos \theta}$$

$L_c$ : Average crystallite size (nm).

$K$ : Shape coefficient (value between 0.9 and 1.0).

$\lambda$ : Wavelength of X-ray beam - Cu  $K\alpha$  radiation ( $\lambda = 0.15406$  nm).

$\beta$ : Full width at half maximum (FWHM) of HA(211).

$\theta$ : Diffraction angle

The diffraction peak corresponding to the (002) was chosen for calculation of the crystalline size, as it is relatively sharper than the other peaks.

Figure 2 illustrates the XRD patterns of S1 aged gel, dried at 80°C for 48 hours and of the "S6, S8, S12" samples thermally treated at 600, 800, 1200°C for 2 h, respectively. It can be interpreted by the discussion that sharp reflection peak appears in the range of 31.8–40° 2 $\theta$  for the thermally treated samples "S6, S8, S12", representing the characteristic peak of HA apatite phase (JCPDS09-0432).

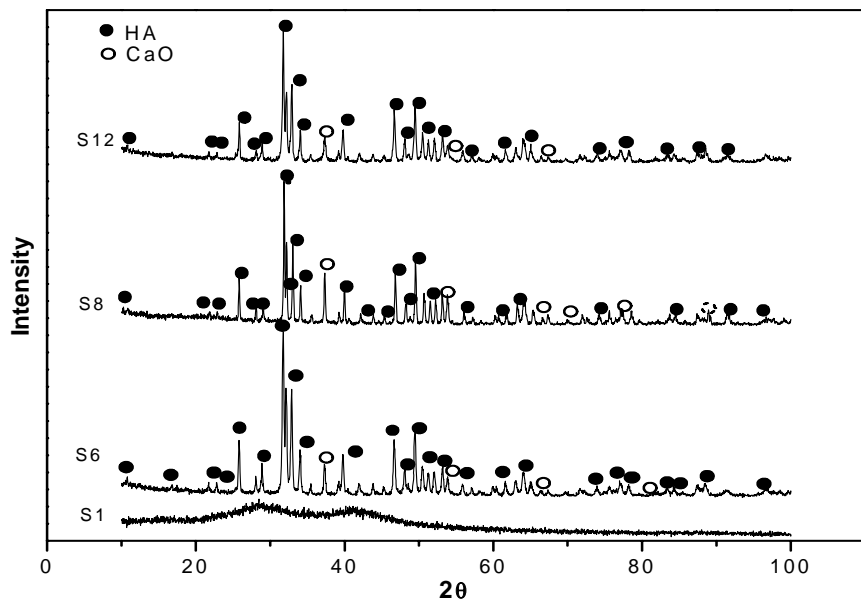


**Figure 2.** XRD patterns and developed phases of the dried gel (S1) and the powders thermally treated at different temperatures; 600°C (S6), 800°C (S8) and 1200°C (S12).

The XRD pattern of the as-prepared sample S1 is mainly amorphous, and there is no obvious diffraction peak observed. This fact is reported by many authors [16]. As the temperature increases, several peaks appear, which ascribed to the diffraction peaks of the HA phase. The XRD pattern of the S6, S8 and S12 sample thermally treated at 600, 800 and 1200°C respectively, indicates the existence of calcium oxide as traces, together with HA as main phase. The presence of CaO is due to the remaining  $\text{Ca}(\text{NO}_3)_2$  in the precursor system, that can be directly transferred to CaO at high temperature [6]. The degree of crystallinity and calculated crystal size for the thermally treated samples can be seen in Table 1. The degree of crystallinity of HA is increased when increasing the temperature from 600 to 800°C (Table 1), but decrease as the temperature increase to 1200°C. The decrease in crystallinity of the 1200°C thermally treated sample (S12) is attributed to the decomposition of HA at corresponding temperature 1200°C, in agreement with the results obtained from the DTA results (Figure 1), while the increase of the crystal size, when compared to 600°C and 800°C thermally treated samples is attributed to an increase of ion migrations when increasing the temperature (Table 1).

**Table 1.** Crystal size, degree of crystallinity, and electrochemical parameters of the powders thermally treated at different temperatures

Samples	Powders			Coatings		
	Thermal Treatment T(°C)	Degree of Crystallinity (%)	Crystallite Size (nm)	R <sub>i</sub> /ohms·cm <sup>2</sup> (after 5 minutes in SBF)	R <sub>f</sub> /ohms·cm <sup>2</sup> (after 15 days in SBF)	ΔR/R <sub>i</sub>
S6	600	85	40	78610	134550	0.71
S8	800	89	51	5923	1208	-0.8
S12	1200	82	54	-	-	-

Electrochemical impedance spectroscopy (EIS) was used for evaluating the corrosion protection properties of the HA-coatings/Ti6Al4V system. Figure 3 shows the evolution of the electrochemical impedance spectra (Nyquist plots) with the immersion time in SBF for HA-coatings/Ti6Al4V system thermally treated at (A) 600°C/2h, (B) 800°C/2h, respectively. Initially, both samples exhibit very similar EIS behaviour. For short immersion time (5 min) the Nyquist plots draw very open arcs with high impedance values. Between 5 min and 1 day of immersion a fast decrease of the impedance values is observed which may be due to the penetration of the SBF through the pores present within the coating as a result of the evaporation of water and ethanol during thermal treatment. However, over time, the evolution of the impedance plots shows a different trend, which depends on the thermal treatment applied for preparing the HA coatings.

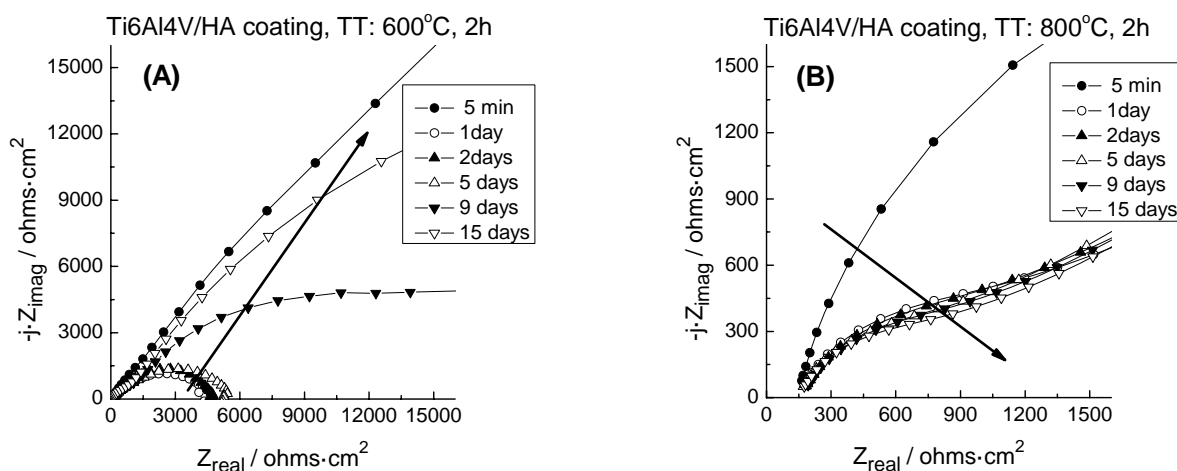


**Figure 3 (a, b).** Evolution of the electrochemical impedance spectra with the immersion time in SBF for HA-coatings/Ti6Al4V system thermally treated at (A) 600°C/2h, (B) 800°C/2h.

The sample thermally treated at 600°C/2hours exhibits a slow increase of the impedance between 1 day and 5 days. After that, the curvature of the Nyquist arcs are opening quickly and the total impedance reaches comparable values than those observed at the beginning of the immersion tests in the SBF. This behaviour can be due to the blocking of the pores by the formation of precipitates from the solution which prevent further penetrations. For the HA-coatings obtained at 800°C, the total impedance of the coating decrease continuously upon exposure to the SBF (Figure 3B) and the recovering of the impedance values observed in the samples coated at 600°C is not here evidenced, i.e. 15 days of immersion in the SBF are not enough to block all the pores present in the surface of the HA-coatings obtained at 800°C.

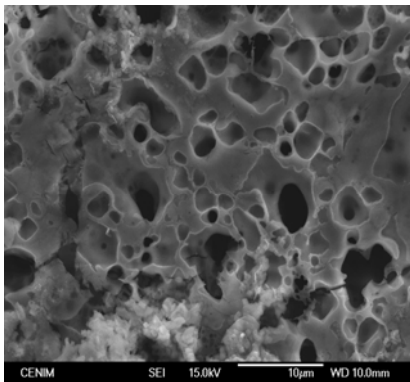
The evolution of the total resistance of the HA-coatings/Ti6Al4V thermally treated samples during the immersion time in Kokubo's simulated body fluid (SBF) was calculated from the impedance spectra by using the ZView software.

For the determination of the relative variation of total resistance of the metal/coating system,  $(\Delta R/R_i)$ , the following equation was used:

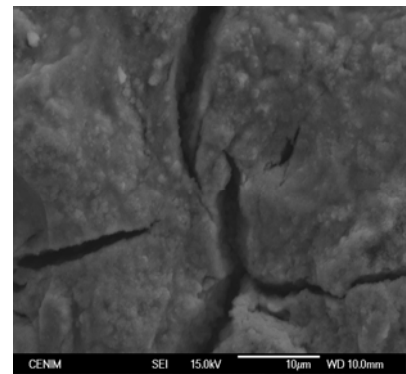
$$(\Delta R/R_i) = \frac{R_f - R_i}{R_i}$$

where  $R_i$  is the initial resistance of the metal/coating system,  $R_f$  is the final resistance and,  $\Delta R = R_f - R_i$ .

Table 1 shows the values of the  $(\Delta R/R_i)$  coefficient obtained for thermally treated samples at 600 and 800°C, respectively. Samples treated at 600°C showed  $(\Delta R/R_i)$  coefficients with positive values (+0.71). This behaviour can be due to the blocking effect of the biomimetic precipitation of HA coming from the SBF which limits the liquid pathways to the metal surface. In contrast, the samples thermally treated at 800°C show a coefficient with negative values (-0.80) which can be due to the existence of surface cracks which are not able to be blocked by soaking these samples in the SBF.



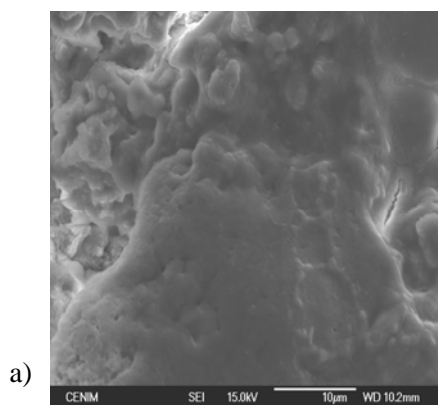
a)



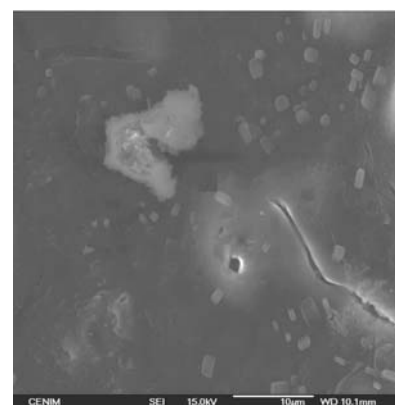
b)

**Figure 4 (a, b).** SEM micrographs obtained for the HA-coatings/Ti6Al4V system thermally treated at (a) 600°C/2h, (b) 800°C/2h before immersion in SBF.

The SEM micrographs obtained for the surface of the HA coatings before immersion in SBF are shown in Figure 4 (A, B). The surface of the sample thermally treated at 600°C (Figure 4A) shows the presence of pores due to the evaporation of both, water and ethanol during thermal treatment. While the surface of the sample thermally treated at 800°C (Figure 4B) show the presence of extensive cracks probably due to a thermal expansion coefficient mismatch between the coating and the substrates during cooling<sup>[17]</sup>.



a)



b)

**Figure 5.** SEM micrographs obtained for the HA-coatings/Ti6Al4V system thermally treated at (a) 600°C/2h, (b) 800°C/2h after immersion in a SBF solution.

After 15 days of immersion in SBF the surface of both samples is covered with a bone-like apatite layer which proved that both samples are bioactive. The surface of the sample thermally treated at 600°C is completely covered with these precipitations from SBF (Figure 5A), while the surface of the sample thermally treated at 800°C is not completely covered (Figure 5B), as still some cracks are observed by SEM at the surface. These results are in agreement with those obtained by EIS.

## 5. Conclusions

- The crystallite size and degree of crystallinity of the HA sol-gel powders, which are precursors of the hydroxyapatite nano-crystalline coatings, strongly depends on the thermal treatment applied.
- Based on this knowledge, hydroxyapatite nano-crystalline coatings on Ti6Al4V alloy can be obtained by sol-gel route.
- Among all the coatings prepared, the HA coating/Ti6Al4V system obtained by thermal treatment at 600°C for 2 hours shows the best barrier properties against the *in vitro* corrosion of the metal substrate.
- All the prepared samples exhibit good bioactivity upon immersion in SBF at 37.5°C for 15 days. Among all of them, the 600°C thermally treated sample shows the best behaviour in terms of *in vitro* bioactivity.

## Acknowledgements

This work has been supported by the National Program for Materials, Spanish Ministry of Science and Innovation (Project MAT2006-04486). A.A. El hadad acknowledges a pre-doctoral contract JAE financed by CSIC; V. Barranco acknowledges a Ramon y Cajal researcher contract financed by CSIC-MICINN.

## References

- [1] M. Vallet-Regi, J.M. Gonzalez-Calbet, *Prog. Solid State Chem.*, **32**, 1(2004).
- [2] L.L. Hench, *J. Am. Ceram. Soc.*, **81**, 1705 (1998).
- [3] A. Slosarczyk, E. Stobierska, Z. Paszkiewicz, M. Gawlick, *J. Am. Ceram. Soc.*, **79**, 2539 (1996).
- [4] M. Yoshimura, H. Suda, K. Okamoto, K. Ioku, *J. Mater. Sci.*, **29**, 3399 (1994).
- [5] D.M. Liu, T. Troczynski, W.J.J Tseng, *Biomaterials*, **22**, 1721(2001).
- [6] M.F. Hsieh, L.H. Perng, T.S. Chin, H.G Perng, *Biomaterials*, **22**, 2601(2001).
- [7] E. Peon, A. Jimenez-Morales, E. Fernandez-Escalante, M.C. Garcia-Alonso, M.L. Escudero, J.C. Galván, *Rev. Metal. Madrid, Sp. Iss.* 479 (2005).
- [8] K. DeGroot, C.P.A.T. Klein, J.G.C. Wolke, J.M.A. De Blicck-Hogervorst, in “*CRC Handbook of Bioactive Calcium Phosphates*”, edited by T. Yamamuro, L.L. Hench and J. Wilson, p. 3 (CRC Press, Boca Raton, FL, 1990).
- [9] Diangang Wang, Chuanzhong Chen, Ting He, Tingquan Lei, *J. Mater. Sci.: Mater. Med.*, **19**, 2281(2008)
- [10] Seok Kim, Prashant N. Kumta, *Mater. Sci. Eng. B.*, **111**, 232 (2004).
- [11] D.G.Wang, C.Z. Chen, J. Ma, G. Zhang, *Colloid Surf. B-Biointerfaces*, **66**, 155 (2008).
- [12] Kui Cheng, SAM Zhang, W.J. Weng, *J. Sol-Gel Sci. Technol.*, **38**, 13 (2006).
- [13] M. Epple, *Z Kardiol.* 2001;90 Suppl 3:64-7.
- [14] E. Landi, A. Tampieri, G. Celotti, S. Sprio, *J. Eur. Ceram. Soc.*, **20**, 2377 (2000).
- [15] H.P. Klung, E. Alexander, “*X-Ray Diffraction Procedures: For Polycrystalline and Amorphous Materials*”, 2nd Edition New York: John Wiley; (1974).
- [16] Yanbao Li, Dongxu Li, *J. Appl. Ceram. Technol.*, **5**, 442 (2008).
- [17] M.Weil, A.J.Ruys, B.K. Milthorpe, C.C. Sorrell, J.H. Evans. *J. Sol-Gel Sci. Technol* **21**, 39–48, (2001).

# Preparation of sol–gel hybrid materials from $\gamma$ -methacryloxypropyltrimethoxysilane and tetramethyl orthosilicate: study of the hydrolysis and condensation reactions

Amir A. El hadad · Diogenes Carbonell ·  
Violeta Barranco · Antonia Jiménez-Morales ·  
Blanca Casal · Juan Carlos Galván

Received: 10 August 2011 / Revised: 27 August 2011 / Accepted: 29 August 2011 / Published online: 25 September 2011  
© Springer-Verlag 2011

**Abstract** Organic–inorganic hybrid materials suitable for the development of sol–gel coatings for metallic surfaces were prepared by hydrolysis and condensation of  $\gamma$ -methacryloxypropyltrimethoxysilane (MAPTMS) and tetramethyl orthosilicate (TMOS). The hydrolysis of MAPTMS/TMOS was carried out in an ethanol/water solution. The prehydrolysis stage of MAPTMS/TMOS system was monitored by Fourier transform infrared spectroscopy (FTIR) and liquid-state  $^{29}\text{Si}$  and  $^{13}\text{C}$  nuclear magnetic resonance ( $^{29}\text{Si}$  and  $^{13}\text{C}$  NMR). FTIR analysis indicated that the hydrolysis of MAPTMS/TMOS was accomplished as far as the (SiOMe) band corresponding to unhydrolyzed silane disappeared. The concentration of the alkoxy groups and the extent of self-condensation of mono-, di-, and trisubstituted siloxanes (T species) in the sol were estimated by using liquid-state  $^{29}\text{Si}$  NMR spectroscopy. The hydrolysis of the prepared sol was also evaluated by liquid-state  $^{13}\text{C}$  NMR spectroscopy. The results indicated that under the

adopted synthesis strategy conditions, the hydrolysis process requires 4 h to be completed.

**Keywords** Sol–gel · Silica · Organic–inorganic materials · Organopolysiloxane precursors · Si-29 and C-13 NMR · FTIR · Structural characterization

## Introduction

The interest in developing novel organic–inorganic hybrid coatings in recent years is due to the unique properties derived from combining inorganic and organic components into a single system [1–7]. Inorganic and organic–inorganic sol–gel materials have many applications in diverse fields as optics, electronics, ionics, mechanics, energy, environment and biology [8, 9], separation, catalysis and sensing [10–15], electrochemistry [16–24], functional smart materials and corrosion protection coatings [8, 9, 25, 26], or biomaterials and biomedical applications [9, 27–30]. The sol–gel route, originally directed towards the synthesis of purely inorganic materials, is increasingly being extended to the preparation of organic–inorganic hybrid materials. The organic–inorganic hybrids combine the desirable properties of organic polymers (toughness, elasticity) with those of inorganic solids (hardness, chemical resistance). The sol–gel method as a materials processing technique has attracted intense and growing interest of the researchers because of its advantages over the other traditional preparation methods. This route enables the obtaining of high reactivity, better purity, avoidance of corrosive by products, improved control of the product structure and

---

A. A. El hadad · B. Casal · J. C. Galván (✉)  
Centro Nacional de Investigaciones Metalúrgicas (CSIC),  
Madrid, Spain  
e-mail: jcg galvan@cenim.csic.es

A. A. El hadad  
e-mail: amirelhadad@cenim.csic.es

D. Carbonell · A. Jiménez-Morales  
Departamento de Ciencia e Ingeniería de Materiales e Ingeniería  
Química, Universidad Carlos III de Madrid,  
Madrid, Spain

V. Barranco  
Instituto de Ciencia de Materiales de Madrid (CSIC),  
Madrid, Spain

provides an easy, cost-effective, and excellent way to incorporate inorganic compounds into an organic one [1, 31, 32]. The organic–inorganic hybrid materials can be easily prepared at room temperature by hydrolysis and condensation of metal alkoxides of the type  $M(OR)_n$ , where M is Si, Ti, Al, Sn, Zr, etc. This method comprises a chemical synthesis of materials having an oxide backbone and an additional organic component as a network modifier. Starting from hydrolyzable molecular compounds, such as alkoxy compounds of silicon, for instance tetramethyl orthosilicate (TMOS), the hydrolysis and condensation is induced by addition of water and a catalyst giving to the formation of an inorganic silica network. The organic silane precursor, for instance  $\gamma$ -methacryloxypropyltrimethoxysilane (MAPTMS), contains organic groups which act as network modifiers. Due to the presence of these modifiers, the final silicon network gains different properties (e.g., hydrophobicity, flexibility) depending on the nature of the organic group used [33]. The hydrolyzed Si–OH silanol groups are able to react with hydroxyl groups present on inorganic or metal surfaces, to form hydrogen bonds [34, 35], followed by condensation to form oxane bonds [36, 37]. Figure 1 shows a simplified view of the cascade reactions of hydrolytic deposition of silanes on inorganic or metal surfaces.

The excess Si–OH groups adsorbed on the surface can also condense among themselves to form Si–O–Si siloxane films [38]. Sol–gel coatings based on siloxane bonded units can be prepared starting from an organic–inorganic hybrid system. Thus the cohydrolysis and polycondensation of the MAPTMS and TMOS mixture produces a polymeric structure (Fig. 2), exhibiting properties of chemical compatibility and flexibility able to accommodate other species, as selected ionophores or corrosion inhibitors, without showing phase segregation nor cracking formation. We have used these precursors for multifunctional purposes to develop electrode membranes [39, 40], ion selective sensors [41, 42], and self-repairing coatings for delaying the corrosion advance in metals [43]. The aim of the current paper has been to study the structural changes which take place during the hydrolysis and condensation processes of an MAPTMS/TMOS solution after the addition of water and ethanol. FTIR and liquid-state  $^{29}\text{Si}$  and  $^{13}\text{C}$  nuclear magnetic resonance (NMR) have been applied for this purpose.

## Materials and methods

### Sol preparation

As described in detail elsewhere [41–43], sols were prepared starting from a mixture of 4 mol of  $\gamma$ -methacryloxypropyltrimethoxysilane (Aldrich) and 1 mol of tetramethoxysilane (Fluka). Ethanol ( $\text{C}_2\text{H}_5\text{OH}$ , 99.8%)

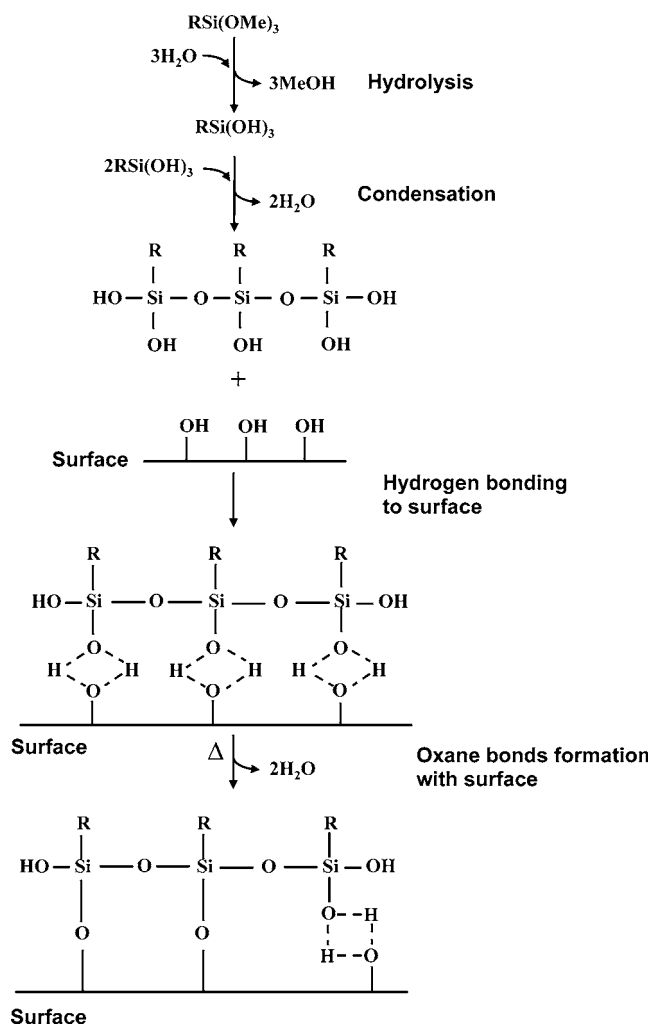


**Fig. 1** Reaction and bonding mechanism of alkoxy silanes

and water were added with the molar ratio silane/water/ethanol of 1/3/3. The resulting sol solution was completely transparent and without phase separation.

### POLYMERIZATION:

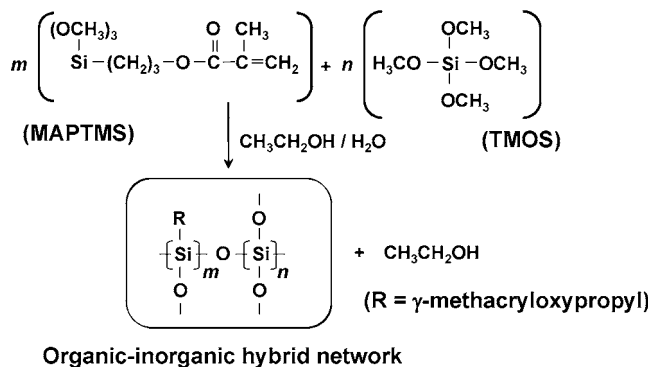


**Fig. 2** Schematic representation of the polymerization reaction of the MAPTMS and TMOS mixture producing a 3D organic–inorganic hybrid network

## Fourier transform infrared spectrometer

The prepared sol samples were analyzed by Fourier transform infrared spectrometer (FTIR) spectral analysis. Each sample was prepared by mixing about 0.5 ml of sol with 200 mg of CsI, which was subsequently pressed into pellet in an evacuated die. All the spectra were measured by using a Nicolet Magna 550 infrared spectrometer at room temperature, which covers the wave number range of 4,000–400  $\text{cm}^{-1}$ .

## Liquid-state nuclear magnetic resonance

$^{29}\text{Si}$  and  $^{13}\text{C}$  NMR spectra of the liquid samples were recorded at 79.49 and 100.62 MHz, respectively, in a Bruker AVANCE-400 spectrometer. The external magnetic field was 9.4 T. The single-pulse NMR spectra were obtained after excitations with a  $\pi/2$  pulse length of 6  $\mu\text{s}$ , for  $^{29}\text{Si}$  and intervals between successive accumulations (recycle delay) of 5 s for each type of signal. NMR spectra were registered for  $^{13}\text{C}$  with a  $\pi/2$  pulse length of 5  $\mu\text{s}$  and a recycle delay of 10 s. The number of scans was 1,600 in the case of  $^{29}\text{Si}$  and 128 for  $^{13}\text{C}$ . The  $^{29}\text{Si}$  and  $^{13}\text{C}$  chemical shift values are given relative to  $\text{Si}(\text{CH}_3)_4$ . The deconvolutions of the NMR spectra were carried out with the WINFIT program so that the different components, and their contributions, could be determined.

## Results and discussion

The reaction between silanes species in liquid media occurs, in general, by sol–gel process in which hydrolysis and condensation of the silane groups take place. In

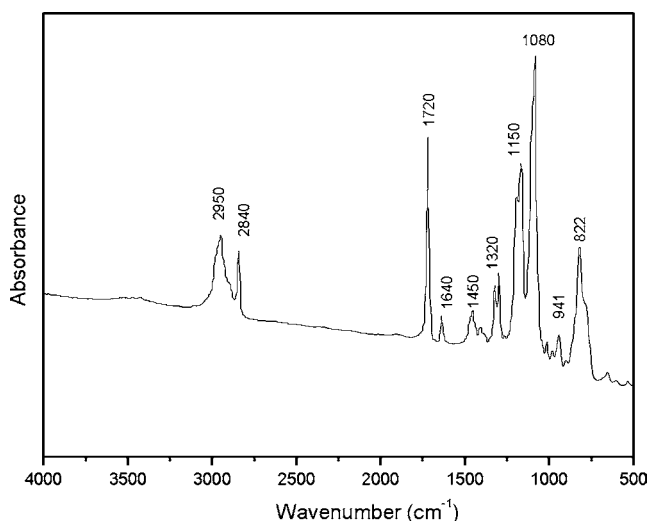


**Fig. 3** FTIR spectrum of the MAPTMS/TMOS mixture in EtOH–H<sub>2</sub>O solvent system upon mixing

**Table 1** Assignment of the FTIR peaks shown in Figs. 3–6

Wave number ( $\text{cm}^{-1}$ )	Assignment	References
2,950	$\nu_{\text{as}} \text{C-H}(\text{CH}_3)$	[45]
2,840	$\nu_{\text{s}} \text{C-H}(\text{O-CH}_3)$	[45]
1,720	$\nu_{\text{s}} \text{C=O}(\text{methacryloxy group})$	[45–47]
1,640	$\nu_{\text{C=C}}(\text{methacryloxy group})$	[45–47]
1,450	$\delta_{\text{CH}_2}(\text{Si-R organic group})$	[48, 49]
1,320	$\nu_{\text{as}} \text{C-O}(\text{C-O-C bonds})$	[48]
1,300	$\nu_{\text{s}} \text{C-O}(\text{C-O-C bonds})$	[48]
1,080	$\nu_{\text{as}} \text{Si-O}(\text{Si-O-CH}_3)$	[50]
1,187	$\nu_{\text{as}}(\text{Si-O-Si})$	[52]
1,085	$\nu_{\text{s}}(\text{Si-O-Si})$	[52]
3,100–3,600	$\nu_{\text{O-H}}(\text{Si-OH})$	[52]

*s* symmetric, *as* asymmetric

particular by mixing the two precursors (MAPTMS/TMOS) with H<sub>2</sub>O/ethanol at ambient temperature, the hydrolysis taking place in the solution must be considered [44].

In this sense, FTIR is a rapid, nondestructive, and sensitive analytical method for identifying functional groups presented. The FTIR spectrum of the MAPTMS/TMOS upon mixing with EtOH/H<sub>2</sub>O solvent system can be seen in Fig. 3. The corresponding band assignments are present in Table 1. The absorption bands around 2,950 and 2,840  $\text{cm}^{-1}$  are attributed to stretching vibrations of C–H bonds in alkyl and methoxy groups, respectively [45]. The band close to 1,720  $\text{cm}^{-1}$  is associated to the stretching vibrations of C=O carbonyl groups of MAPTMS, while that one at 1,640  $\text{cm}^{-1}$  is attributed to C=C groups of the methacrylate groups from the MAPTMS precursor [45–47].

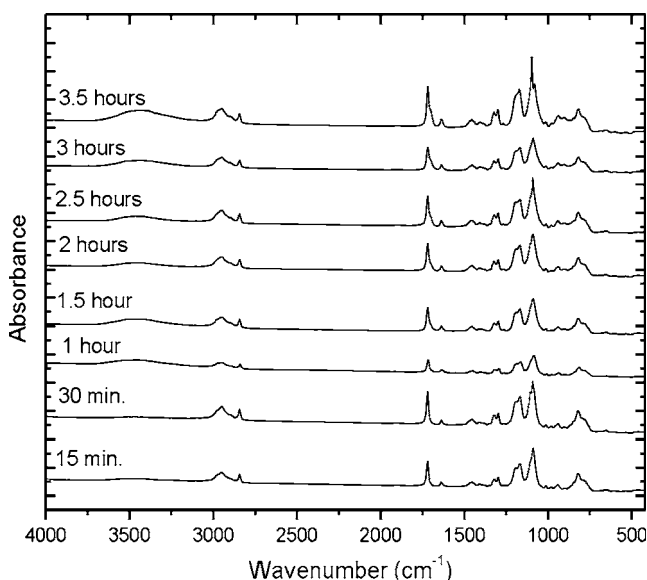


**Fig. 4** FTIR spectra of the MAPTMS/TMOS mixture in EtOH/H<sub>2</sub>O solvent system. Hydrolysis time up to 3.5 h

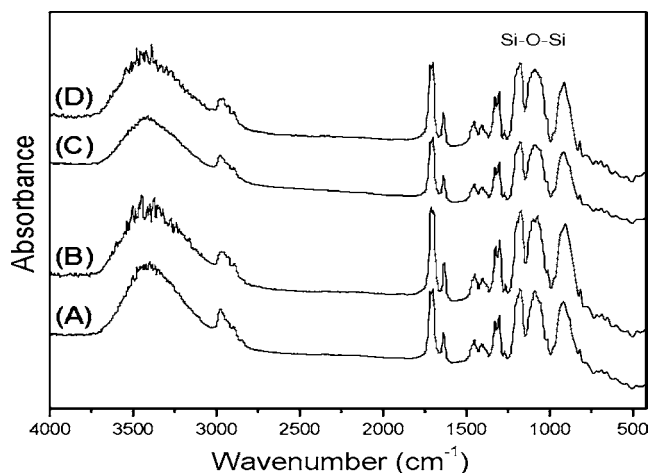


**Fig. 5** FTIR spectra of MAPTMS/TMOS mixture in EtOH/H<sub>2</sub>O solvent system. Hydrolysis time up to 24 h. A 4 h, B 8 h, C 12 h, D 24 h

The bands at 1,450 and 1,150  $\text{cm}^{-1}$  are attributed to deformation vibrations of C–H in CH<sub>2</sub> and CH<sub>3</sub> bonds [48, 49]. The asymmetric and symmetric stretching vibrations of C–O of C–O–C bonds are attributed to bands at 1,320 and 1,300  $\text{cm}^{-1}$ , respectively [48]. Finally, the bands at 941 and 822  $\text{cm}^{-1}$  are assigned to the C=C vibrations of the C=C–C=O group, while that assigned to C–C–O skeleton vibration for pure ethanol appear at 1,090  $\text{cm}^{-1}$  [49]. All those bands (except the one at 2,840  $\text{cm}^{-1}$ ) are related with the nonhydrolyzable part of the MAPTMS–TMOS mixture and should appear in the FTIR spectra carried out after the hydrolysis process.

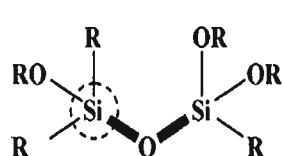
The band at 1,080  $\text{cm}^{-1}$  is attributed to stretching vibrations of Si–O–C bonds. Other authors have also made

the same attribution in different silanes [50, 51]. This band is the one that is expected to be broken during the hydrolysis process. Presence of the very little bands assigned to Si–O–Si bonds at 980  $\text{cm}^{-1}$  indicates that certain condensation of the silane chains has taken place immediately upon mixing [52]. These bands prove the existence of condensation phenomena together with the hydrolysis one.

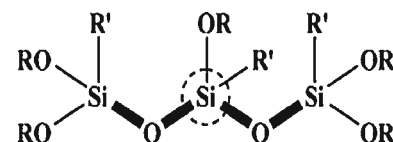
The FTIR spectra of the MAPTMS/TMOS aqueous mixture are shown in Fig. 4, for hydrolysis time varying from 15 min up to 3.5 h. In these spectra it is clearly observed that the FTIR spectrum of 3.5 h is very similar to that after 1 min of mixing (Fig. 3), which would indicate incomplete hydrolysis of the mixture.

As the hydrolysis time increases, 4 h of hydrolysis, the spectra change substantially [Fig. 5 (A)]. The band at 2,840  $\text{cm}^{-1}$ , associated with the methoxy group, which appeared upon mixing (Fig. 3), disappears for hydrolysis times of 4 h [Fig. 5 (A)]. This allows establishing the beginning of optimal hydrolysis conditions at about 4 h. The same happens with the asymmetric stretching vibration of the Si–O–C, which appeared at 1,080  $\text{cm}^{-1}$  (Fig. 3). This bond is the one that must be broken during the hydrolysis, and its absence in Fig. 5 (A) implies the end of the hydrolysis process [52]. This band disappeared and was replaced by two bands corresponding to Si–O–Si; results from the condensation process. Disappearance of the band of Si–O–CH<sub>3</sub> groups at 2,840  $\text{cm}^{-1}$  was also evidenced together with the increase of a broad band at 3,420  $\text{cm}^{-1}$ , assigned to OH groups from SiOH formed through hydrolysis [52]. Figure 5 shows that for the hydrolysis

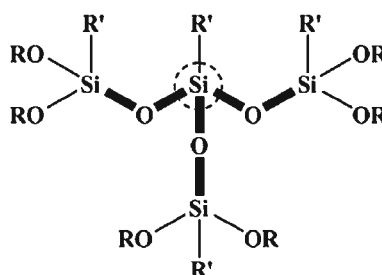
**Fig. 6** Schematic representation of T<sup>n</sup> silane structures; n=1, 2, or 3



**T<sup>1</sup> structure**  
Dimer or chain end

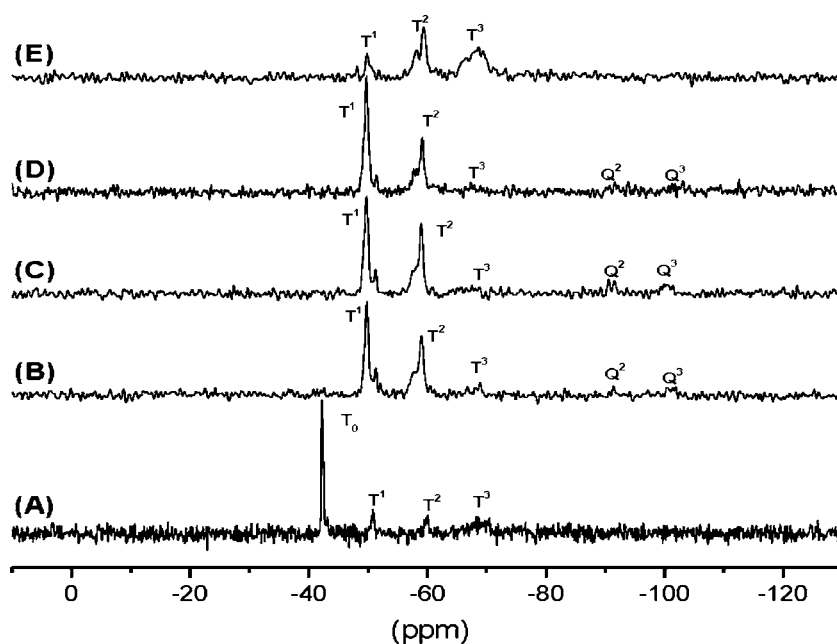


**T<sup>2</sup> structure**  
Linear link



**T<sup>3</sup> structure**  
Three dimensional

**Fig. 7** Liquid-state  $^{29}\text{Si}$  NMR spectra of MAPTMS/MOS mixture in EtOH–H<sub>2</sub>O solvent system. *A* upon mixing of MAPTMS and TMOS, *B* after 1 h, *C* after 2 h, *D* after 3 h, *E* after 4 h



time of 8 up to 24 h, the slight broadening of Si–O–Si bands results from a highly cross-linked network mainly consisting of linear polysiloxanes with a mixture of small and long chains.

NMR is a useful tool to study the silane hydrolysis; the NMR relaxation time measurements are sensitive to short-range interactions and can be used to estimate the scale of miscibility of an organic–inorganic hybrid [53]. This is due to the good resolution and quantitative assignment of the NMR peaks of silane molecules in comparison with the FTIR analysis [54].

Liquid-state  $^{29}\text{Si}$  and  $^{13}\text{C}$  NMR have been applied to study the hydrolysis mechanism of the MAPTMS/TMOS mixture in EtOH–H<sub>2</sub>O solution. In the  $^{29}\text{Si}$  NMR spectroscopy, the chemical shift of silicon is determined by the chemical nature of their neighbors, namely T, and Q structures [55].

A Q species is one in which the Si atom is capable of producing four siloxane bonds, which results from TMOS precursor, whereas a T can only achieve three siloxane bonds and results from MAPTMS [1]. According to the nomenclature, four T signals of different nature can be present ( $T^n$ , where  $n=0, 1, 2, \text{ or } 3$ , respectively) [31]. Figure 6 shows a schematic representation of  $T^n$  silane structures.  $T^0$  appears in a spectral range from  $-37$  to  $-39$  ppm which is assigned to  $\text{RSi}(\text{OCH}_3)_3$  unhydrolyzed species from MAPTMS.  $T^1$  occurs in the range defined between  $-46$  and  $-48$  ppm, assigned to condensed silicon units bearing only one bridging oxygen atom (Si–O–Si),  $T^2$  is defined in the spectral range defined between  $-53$  and  $-57$  ppm which is assigned to doubly condensed silicon centers (two bridging oxygen atoms), and  $T^3$  is defined into the  $-61$  to  $-66$  ppm range, fully condensed silicon units (three bridging oxygen atom) as sketched in Fig. 6 [55].

**Table 2** Relative proportions of T and Q species in the organic–inorganic hybrid materials from the liquid-state  $^{29}\text{Si}$  NMR spectra in Fig. 7

Time in M	Proportions <sup>a</sup> (%)						Relative <sup>b</sup> proportions (%)				Relative proportions <sup>c</sup> (%)		Ratio <sup>d</sup> (%)	
	T <sup>0</sup>	T <sup>1</sup>	T <sup>2</sup>	T <sup>3</sup>	Q <sup>2</sup>	Q <sup>3</sup>	T <sup>0</sup>	T <sup>1</sup>	T <sup>2</sup>	T <sup>3</sup>	Q <sup>2</sup>	Q <sup>3</sup>	T <sup>n</sup>	Q <sup>n</sup>
1	47.66	10.87	9.64	31.83	0	0	47.66	10.87	9.64	31.83	–	–	1	–
60	–	40.28	38.48	11.08	3.21	6.95	–	44.83	42.83	12.34	31.5	68.5	89.8	10.2
120	–	41.38	36.80	7.83	6.52	7.47	–	48.11	42.78	9.11	46.6	53.4	86	14
180	–	50.41	35.35	4.45	4.2	5.59	–	55.88	39.18	4.93	42.90	57.1	90	10
240	–	9.91	35.56	54.53	–	–	–	9.91	35.56	54.53	–	–	1	–

<sup>a</sup>These were calculated by the deconvolution technique. Error value assumed is  $\pm 1\%$

<sup>b</sup>(Each T species/total T species)  $\times 100\%$

<sup>c</sup>(Each Q species/total Q species)  $\times 100\%$

<sup>d</sup> $T^i = [\text{total T species}/(\text{T species} + \text{Q species})] \times 100\%$ ,  $Q^j = [\text{total Q species}/(\text{T species} + \text{Q species})] \times 100\%$

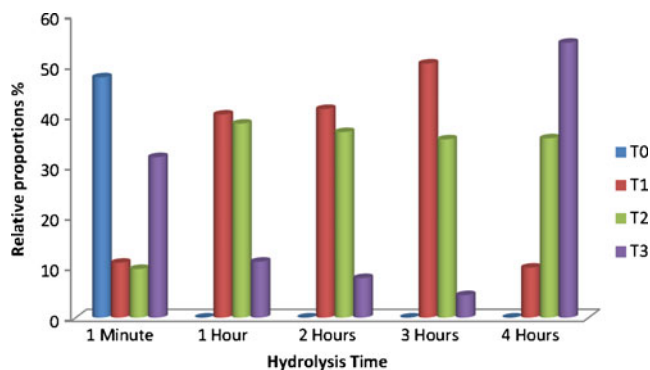
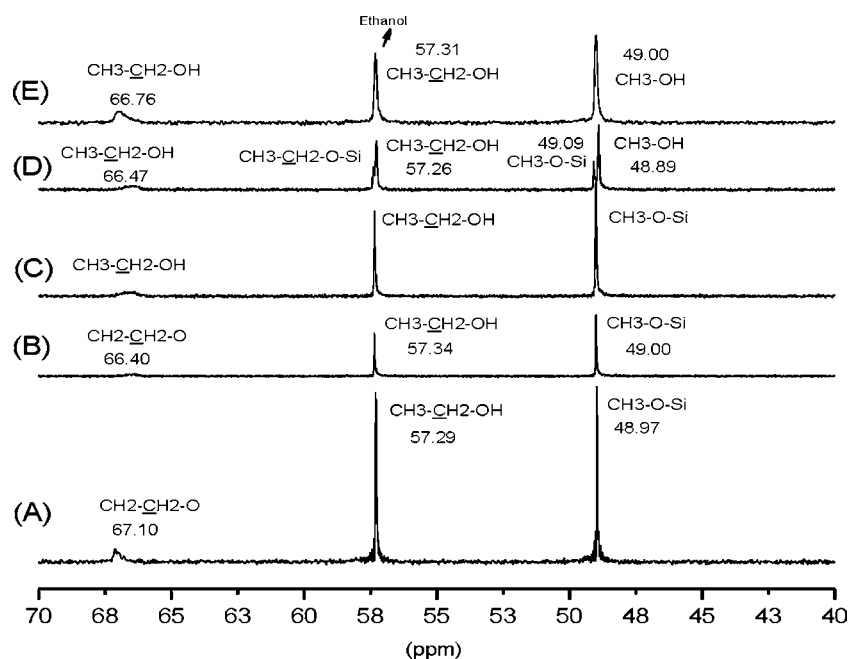


**Fig. 8** Relationship of the signals, for species T<sup>0</sup>, T<sup>1</sup>, T<sup>2</sup>, and T<sup>3</sup> in the MAPTMS/TMOS hybrid

The <sup>29</sup>Si spectra of MAPTMS/TMOS in EtOH–H<sub>2</sub>O solution are shown in Fig. 7. Upon mixing of the two precursors [Fig. 7 (A)], the RSi(OCH<sub>3</sub>)<sub>3</sub> species from nonhydrolyzed MAPTMS (T<sup>0</sup> units) give a well-detectable singlet signal at –42 ppm. The appearance of mono-, di-, and trisubstituted siloxanes T species (T<sup>1</sup> units at –50 ppm, T<sup>2</sup> units at –59 ppm, and T<sup>3</sup> units between –68 and –71 ppm) is a result of the self-condensation. These observations are in agreement with the FTIR results which showed the presence of condensed siloxane species at 980 cm<sup>-1</sup> upon mixing of the two precursors, indicated by the presence of the Si–O–Si band (Fig. 3). The Si(OCH<sub>3</sub>)<sub>4</sub> unhydrolyzed species from TMOS were not detected in the <sup>29</sup>Si spectra upon mixing of the two precursors with H<sub>2</sub>O/ethanol, and this is because TMOS was used in small amount and so has been hydrolyzed upon mixing.

**Fig. 9** Liquid-state <sup>13</sup>C NMR spectra (0–30 ppm range) of prehydrolyzed MAPTMS/TMOS mixture. *A* upon mixing of MAPTMS and TMOS, *B* after 1 h, *C* after 2 h, *D* after 3 h, *E* after 4 h



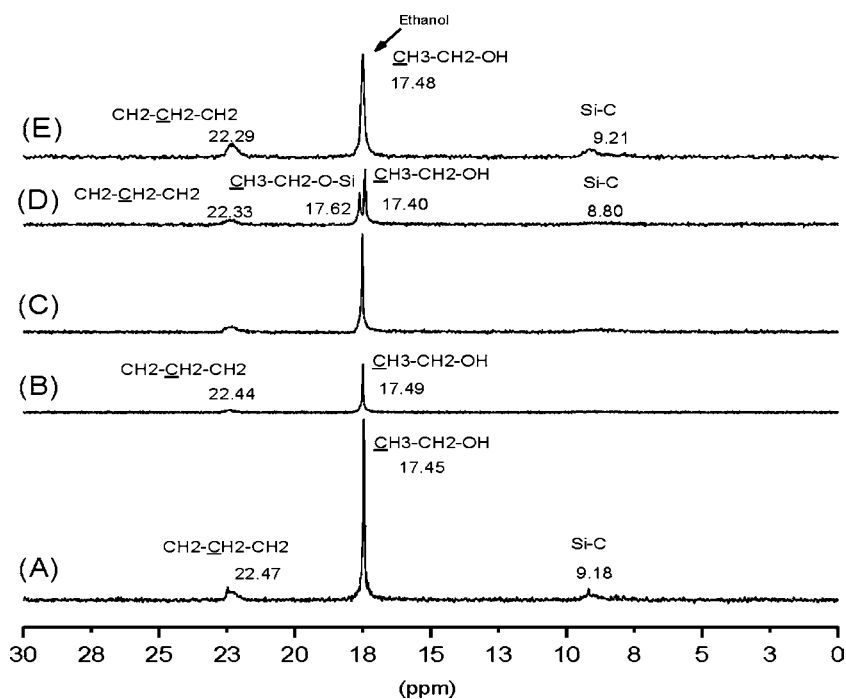
After 1 h of the reactive mixing, both the T<sup>1</sup> at 49.81 ppm and T<sup>2</sup> at 58 became clear and dominate the entire spectrum which indicates the progress of the hydrolysis process [Fig. 7 (B)]. Also the T<sup>3</sup> of hydrolyzed MAPTMS and Q<sup>2</sup> and Q<sup>3</sup> of hydrolyzed TMOS appear as very small signals at 67.55, 91.78, and 101.66 ppm, respectively. After 2 h of hydrolysis and up to 3 h [Fig. 7 (C, D)], there is not a significant change between these spectra and that of after 1 h and the concentrations of condensed T<sup>2</sup> and T<sup>1</sup> species units remain constant [Fig. 7 (B)].

After 4 h of hydrolysis, the T species in the form of T<sup>1</sup>, T<sup>2</sup>, and T<sup>3</sup> at –50, –58, and –68 ppm dominate the entire spectrum [Fig. 7 (E)]. These results shed light upon two important observations which indicate that 4 h was enough for the hydrolysis of the of MAPTMS/TMOS mixture, in a similar way as the FTIR spectra has indicated. It can observe:

- The absence of unhydrolyzed TMOS, Si(OCH<sub>3</sub>)<sub>4</sub>, as it hydrolyzed very rapidly,
- The disappearance of the signal T<sup>0</sup> corresponding to the initial unhydrolyzed MAPTMS [Fig. 7 (A)], and
- The appearance of the signal T<sup>3</sup>, which corresponds fully to condensed silicon units with three siloxane bonds (three bridging oxygen atom) dominated all the spectrum of 4 h.

The <sup>29</sup>Si NMR spectra provide the proportions of T<sup>n</sup> species (*n*=1, 2, or 3), where T represents a Si atom oxygen bridged to another Si atoms. These allowed the quantification of the cross-linking degree within the silicate network. The T<sup>1</sup>, T<sup>2</sup>, and T<sup>3</sup> units arose from the self-condensation reactions only. The T<sup>1</sup> units represented dimers or chain

**Fig. 10** Liquid-state  $^{13}\text{C}$  NMR spectra (40–70 ppm range) of the prehydrolyzed MAPTMS/TMOS mixture. *A* upon mixing of MAPTMS and TMOS, *B* after 1 h, *C* after 2 h, *D* after 3 h, *E* after 4 h



ends.  $\text{T}^2$  were associated with the linear siloxane sequences, and the  $\text{T}^3$  units witnessed about the appearance of three-dimensional siloxane networks. In fact, the nonreacted silane molecules ( $\text{T}^0$  units) from MAPTMS gave a well-detectable singlet signal at  $-42$  ppm [Fig. 7 (A)]. This singlet disappeared from the spectrum after 1 h of reactive mixing, indicating beginning of the hydrolysis reaction.

As it was expected from the FTIR results, the maximum of self-condensed products was observed after 4 h of reaction. The proportions of the T species in each hybrid system quoted in Table 2 were obtained from deconvolution of the  $^{29}\text{Si}$  NMR spectra with the WINFIT software. The spectra were deconvolved into individual Gaussian line shapes, thus allowing a quantitative analysis of the spectra based on the peak areas of each species. From Fig. 8, it can be seen that after 4 h of hydrolysis, the amount of  $\text{T}^3$  silicon content increased while that of  $\text{T}^2$  and  $\text{T}^3$  silicon content decreased in the matrix of the Si–O–Si structure. Thus hydrolysis was accompanied by a condensation reaction among the silanol groups to give oligomeric structures.

The  $^{13}\text{C}$  NMR spectra of MAPTMS/TMOS in EtOH– $\text{H}_2\text{O}$  are shown in Figs. 9 and 10. This mixture was hydrolyzed for 4 h in EtOH– $\text{H}_2\text{O}$  solution. In comparison with the  $^{29}\text{Si}$  NMR spectra, the patterns of the  $^{13}\text{C}$  NMR peak positions are significantly exhibiting multiple peaks. This suggests that there are several chemical compounds within the hybrid systems containing carbon-bonding structures. Peaks assignments for carbon-bonding types which can be attributed to the MAPTMS and TMOS precursors are given in Table 3. The peaks from TMOS and MAPTMS in the  $^{13}\text{C}$  NMR spectra are in good agreement with earlier reports [56]. The hydrolysis of the MAPTMS/TMOS system was followed by the evolution of the peaks corresponding to the methyl groups attached to the silane and those liberated during the hydrolysis ( $\text{CH}_3\text{–OH}$  and  $\text{CH}_3\text{–CH}_2\text{–OH}$ ).

Upon mixing of the two silane precursors with EtOH– $\text{H}_2\text{O}$  solution, the peaks at 17.45 and 57.29 ppm are from ethoxy groups of ethanol and to  $\text{CH}_3\text{–C}$  of MAPTMS [57] [Figs. 9 (A) and 10 (A)]. The peaks at 48.97 are ascribed to unhydrolyzed  $\text{CH}_3\text{–O–Si}$  units of MAPTMS and TMOS.

**Table 3** Peaks assignments of liquid-state  $^{13}\text{C}$  NMR spectra of both MAPTMS and TMOS according to peaks detected in Figs. 9 and 10

MAPTMS (Aldrich)		TMOS (Aldrich)		Ethanol	
Nature of carbons	Ass. (ppm)	Nature of carbons	Ass. (ppm)	Nature of carbons	Ass. (ppm)
$\text{CH}_2\text{–CH}_2\text{–O}$	67.10	$\text{CH}_3\text{–O–Si}$	48.97	$\text{CH}_3\text{–CH}_2\text{–OH}$	57.29
$\text{CH}_3\text{–O–Si}$	48.97			$\text{CH}_3\text{–CH}_2\text{–OH}$	17.45
$\text{CH}_2\text{–CH}_2\text{–Si}$	22.47				
$\text{CH}_3\text{–C}$	17.45				
$\text{CH}_2\text{–Si}$	9.18				

The peak at 67.10 ppm is attributable to CH<sub>2</sub>–CH<sub>2</sub>–O units of MAPTMS while those that appear at 22.47 ppm are due to CH<sub>2</sub>–CH<sub>2</sub>–Si units of the same precursor. Finally, the peak at 9.18 ppm is attributed to Si–C of MAPTMS.

Up to 2 h of reaction, no changes can be detected [Figs. 9 (B, C) and 10 (B, C)]. The spectrum exhibits the same peaks corresponding to the carbon within the hybrid systems containing carbon-bonding structures. After 3 h of hydrolysis, the spectrum exhibits significant changes [Figs. 9 (D) and 10 (D)]. The peak that appears at 49 ppm corresponds to the release of methanol as a result of the beginning of the condensation process. The emergence of this peak indicates the hydrolysis of the methoxy group in (H<sub>3</sub>C–O–Si) of both precursors. The hydrolysis of methoxy groups caused by water in ethanol contributed to the yielding of methanol as a reaction product that is seen in the liquid-state <sup>13</sup>C NMR spectra [58]:



At the same time, during the hydrolysis of TMOS in ethanol, methoxy groups of TMOS are exchanged for alkoxy groups. This reaction is an equilibrium reaction. Almost all of methoxy groups are exchanged for ethoxy groups. This gives well-developed bands at 17.62 and 57.26 ppm in the spectrum of 3 h hydrolysis [Figs. 9 (D) and 10 (D)], corresponding to Si–O–CH<sub>2</sub>–CH<sub>3</sub> units, and methanol is released into the solution following the previous reaction.

After 4 h of hydrolysis, it takes place the disappearance of the methoxy groups of the initial silanes at 48.97 ppm and the concomitant formation of free methanol, as indicated by the peak growing at 49 ppm of the hydrolyzed mixture [59] [Fig. 10 (E)]. Thus the disappearance of the resonances assigned to the CH<sub>3</sub>–O–Si group is accompanied by the increase of the CH<sub>3</sub>–OH signal. All these facts can confirm that 4 h is enough for the hydrolysis reactions to be completed. These results indicated that the hydrolyzable Si–O–CH<sub>3</sub> groups of both precursors were hydrolyzed and formed silanol groups that could be derived in Si–O–Si bonds due to subsequent condensation. This agrees well with the results obtained in <sup>29</sup>Si NMR spectra that showed that the hydrolysis was accompanied by a condensation reaction among the silanol groups to give oligomeric structures. The evidence of the presence of such structures was provided by the broadening of the different peaks in the <sup>13</sup>C NMR spectra.

## Conclusions

The sol–gel reaction of the MAPTMS/TMOS system in EtOH/H<sub>2</sub>O solution was studied by FTIR and NMR. The

aim of the study was to optimize the prehydrolysis times of both silanes and consequently their use as precursors for hybrid materials. The early step of the condensation process was studied by collecting <sup>29</sup>Si NMR spectra. The quantitative analysis of the condensed species was calculated in terms of T<sup>1</sup>, T<sup>2</sup>, and T<sup>3</sup> silicon units. It could be concluded that the hydrolysis of the two silane precursors under the adopted synthesis strategy conditions is completed after approximately 4 h at room temperature. The quantitative analysis of NMR indicates the presence of self-condensation species after mixing the two precursors. The hydrolysis was accompanied by a condensation reaction between the silanol groups to give oligomeric structures.

**Acknowledgments** This work has been supported by the Ministry of Science and Innovation of Spain (Projects MAT2006-04486 and MAT2009-13530) and the Regional Community of Madrid (Project 2009/MAT-1585). AA El hadad acknowledges a predoctoral contract JAE financed by CSIC, and VB acknowledges a Ramon y Cajal researcher contract financed by CSIC-MICINN.

## References

1. Brinker CJ, Scherer CW (eds) (1990) Sol–gel science: the physics and chemistry of sol–gel processing. Academic Press, Boston
2. Novak BM (1993) *Adv Mater* 5:422
3. Sanchez C, Ribot F (1994) *New J Chem* 18:1007
4. Wen JY, Wilkes GL (1996) *Chem Mater* 8:1667
5. Stein A, Melde BJ, Schroden RC (2000) *Adv Mater* 12:1403
6. Gomez-Romero P (2001) *Adv Mater* 13:163
7. Sanchez C, Soler-Illia GJDA, Ribot F, Lalot T, Mayer CR, Cabuil V (2001) *Chem Mater* 13:3061
8. Schottner G (2001) *Chem Mater* 13:3422
9. Sanchez C, Julian B, Belleville P, Popall M (2005) *J Mater Chem* 15:3559
10. Casal B, Ruiz-Hitzky E, Crespín M, Tinet D, Galván JC (1989) *J Chem Soc Faraday Trans 1* (85):4167
11. Ruiz-Hitzky E, Aranda P, Casal B, Galván JC (1995) *Adv Mater* 7:180
12. Wang J, Merino J, Aranda P, Galván JC, Ruiz-Hitzky E (1999) *J Mater Chem* 9:161
13. Ruiz-Hitzky E, Aranda P, Casal B, Galván JC (2001) *Rev Inorg Chem* 21:125
14. Rojas-Cervantes ML, Casal B, Aranda P, Savirón M, Galván JC, Ruiz-Hitzky E (2001) *Colloid Polym Sci* 279:990
15. Nicole L, Boissiere C, Grosso D, Quach A, Sanchez C (2005) *J Mater Chem* 15(35):3598
16. Amarilla JM, Casal B, Galván JC, Ruiz-Hitzky E (1992) *Chem Mater* 4:62
17. Galván JC, Aranda P, Amarilla JM, Casal B, Ruiz-Hitzky E (1993) *J Mater Chem* 3:687
18. Aranda P, Jiménez-Morales A, Galván JC, Casal B, Ruiz-Hitzky E (1995) *J Mater Chem* 5:817
19. Lev O, Tsionsky M, Rabinovich L, Glezer V, Sampath S, Pankratov I, Gun J (1995) *Anal Chem* 67(1):22A
20. Lev O, Wu Z, Bharathi S, Glezer V, Modestov A, Gun J, Rabinovich L, Sampath S (1997) *Chem Mater* 9:2354
21. Wang BQ, Li B, Deng Q, Dong SJ (1998) *Anal Chem* 70:3170
22. Walcarius A (2001) *Chem Mater* 13:3351

23. Walcarius A, Mandler D, Cox JA, Collinson M, Lev O (2005) *J Mater Chem* 15:3663
24. Popall M, Andrei M, Olsowski B (1998) *Electrochim Acta* 43:1155
25. Zheludkevich ML, Salvado IM, Ferreira MGS (2005) *J Mater Chem* 15:5099
26. Barranco V, Carmona N, Galván JC, Grobelny M, Kwiatkowski L, Villegas MA (2010) *Prog Org Coat* 68:347
27. Hench LL (1991) *J Am Ceram Soc* 74:1487
28. Griffith LG, Naughton G (2002) *Science* 295(5557):1009
29. Kokubo T, Kim HM, Kawashita M (2003) *Biomaterials* 24:2161
30. Langer R, Tirrell DA (2004) *Nature* 428(6982):487
31. Philipp G, Schmidt H (1984) *J Non Cryst Solids* 63:283
32. Schmidt H (1984) *Mater Res Soc Symp Proc* 32:327
33. Park O-H, Eo Y-J, Choi Y-K, Bae B-S (1999) *J Sol-Gel Sci Technol* 16:235
34. Osterholz FD, Pohl ER (1992) *J Adhes Sci Tech* 6:127
35. Blum FD, Meesiri W, Kang HJ, Gambogi JE (1991) *J Adhes Sci Tech* 5:479
36. Arkles B, Steinmetz JR, Zazyczny J, Mehta P (1992) *J Adhes Sci Tech* 6:193
37. Walker P (2003) In: Pizzi A, Mittal KL (eds) *Handbook of adhesive technology*, 2nd revised edn. Marcel Dekker, New York, pp 205–221. Taylor and Francis Inc, New York (USA)
38. Chu CW, Kirby DP, Murphy PD (1993) *J Adhes Sci Tech* 7:417
39. Jiménez-Morales A, Galván JC, Aranda P, Ruiz-Hitzky E (1998) *Mater Res Soc Symp Proc* 519:211
40. Ruiz-Hitzky E, Galván JC, Aranda P, Jiménez-Morales A (1999) Spanish Patent, P. 9900956
41. Jimenez-Morales A, Galvan JC, Aranda P (2002) *Electrochim Acta* 47(13–14):2281
42. Jiménez-Morales A, Aranda P, Galván JC (2003) *J Mater Process Tech* 143–144:5
43. Garcia-Heras M, Jimenez-Morales A, Casal B, Galvan JC, Radzki S, Villegas MA (2004) *J Alloy Comp* 380(1–2):219
44. Wang D, Bierwagen GP (2009) *Prog Org Coat* 64:327
45. Rodriguez MA, Liso MJ, Rubio F, Rubio J, Oteo JL (1999) *J Mater Sci* 34:3867
46. Matinlinna JP, Ozcan M, Lassila LVJ, Vallittu PK (2004) *Dent Mater* 20:804
47. Abdelmouleha M, Boufia S, Belgacemb MN, Dufresne A (2007) *Compos Sci Technol* 67:1627
48. Innocenzi P, Brusatin G (2004) *J Non Cryst Solids* 333:137
49. Franquet A, Terryn H, Vereecken J (2003) *Appl Surf Sci* 211:259
50. Danqing Z, van Ooij WJ (2002) *J Adhes Sci Tech* 16:1235
51. Gunji T, Makabe Y, Takamura N, Abe Y (2001) *Appl Organomet Chem* 15:683
52. Jana S, Lim MA, Baek IC, Kim CH, Seok SI (2008) *Mater Chem Phys* 112:1008
53. Nisiyama N, Horie K (1987) *J Appl Polym Sci* 34:1619
54. Salon MCB, Bayle PA, Abdelmouleh M, Boufic S, Belgacem MN (2008) *Colloids Surface Physicochem Eng Aspect* 312:83
55. Glaser RH, Wilkes GL (1988) *Polym Bull* 19:51
56. Chiang CL, Ma CCM (2004) *Polym Degrad Stab* 83:207
57. Han YH, Taylor A, Mantle MD, Knowles KM (2007) *J Non Cryst Solids* 353:313–320
58. Miyatake K, Ohama O, Kawahara Y, Urano A, Kimura A (2007) *Sei Tech Rev* 65:21–24
59. Salon MCB, Abdelmouleh M, Boufi S, Belgacem MN, Gandini A (2005) *J Colloid Interface Sci* 289:249–261

## *Participations in Conferences*



### Conference communications

**Conference :** BIO-COAT 2010, Zaragoza, Spain

**Title :** Multifunctional Sol-gel Derived Thin Film Based on Nanocrystalline Hydroxyapatite Powders

**Authors :** A A El hadad, V Barranco, A Jimenez-Morales, E Peon, JC Galvñ

**Participation:** Oral

**Abstract :** The aim of this work was to prepare bioactive hydroxyapatite coatings by sol-gel method and to study the effect of thermal treatment temperature upon the bioactivity and corrosion protection of these coatings upon Titanium alloy Ti6Al4V. The application of (DTA/TGA) and (XRD) has provided valuable information about the phase transformation, mass loss, identification of the phases developed, crystallite size and degree of crystallinity. (SEM/EDX) has been applied to study the surface morphology of coated samples before and after immersion in simulated body fluid (SBF) to detect the biomimetic precipitation of the bone-like apatite. The obtained results show that all the prepared samples are ceramic nanocrystalline with crystal structure and composition like hydroxyapatite, with little deviations from that present in the human bone. The bioactivity of the studied samples is found to be closely related to the thermal treatments applied. That is, the bioactivity decreases as the temperature of the thermal treatment increase. Coatings from such prepared hydroxyapatite sol have been accomplished by dip-coating technique on non-toxic Ti6Al4V alloy for biomedical applications. The corrosion behaviour of the resulting hydroxyapatite coatings in a (SBF) has been studied by electrochemical impedance spectroscopy (EIS). The hydroxyapatite coated Ti6Al4V alloy displayed excellent bioactivity when soaked in the (SBF) and acceptable corrosion protection behaviour.

-----

**Conference :** National Conference of Materials XII IBEROMAT 2012, Alicante, Spain

**Title :** Preparación, caracterización y estudio del comportamiento anticorrosivo de recubrimientos órgano-inorgánicos bioactivos aplicados sobre superficies de Ti6Al4V

**Authors :** A.A. El hadad, D. Carbonell, A. Jiménez-Morales, V. Barranco, B. Casal, J.C. Galvñ

**Participation:** Oral

## Conference communications

---

**Abstract** : Se han preparado recubrimientos órgano-inorgánicos multifuncionales a partir de mezclas  $\gamma$ -metacriloxipropiltrimetoxisilano (MAPTMS), tetrametoxisilano (TMOS) y trietilfosfito (TEP) por la ruta sol-gel. Dichos recubrimientos se han aplicado sobre superficies de Ti6Al4V mediante técnicas de inmersión. Los grupos funcionales existentes en los recubrimientos se han estudiado mediante (FTIR-ATR). El comportamiento hidrofóbico y el espesor de los recubrimientos se han evaluado mediante la aplicación de medidas del ángulo de contacto y métodos perfilométricos, respectivamente. La morfología de la superficie y la composición de los recubrimientos se han estudiado por (SEM/EDX). Por último, se han estudiado la bioactividad y la resistencia frente a la corrosión de los recubrimientos en la solución fisiológica simulada propuesta por Kokubo. Los estudios de corrosión se han llevado a cabo con la espectroscopía de impedancia electroquímica. Los resultados obtenidos han mostrado que los recubrimientos son películas protectoras uniformes, y libres de grietas. La optimización del contenido de TEP de los recubrimientos ha permitido desarrollar recubrimientos bioactivos que muestran, al mismo tiempo, buenas propiedades protectoras.

-----

**Conference** : 1<sup>st</sup> International Symposium on Colloids and Materials, 2011.Holland

**Title** : Sol gel derived hybrid materials based on  $\gamma$ -methacryloxypropyltrimethoxysilane and tetramethyl orthosilicate: Kinetic studies

**Authors** : A.A. El hadad\*, D. Carbonell, A. Jiménez-Morales, V. Barranco, B. Casal, J.C. Galván.

**Participation:** **Poster**

**Abstract** : Organic-inorganic hybrid materials suitable for coating upon metallic surfaces were prepared by hydrolysis and condensation of  $\gamma$ -methacryloxypropyltrimethoxysilane (MAPTMS) and tetramethoxysilane (TMOS). The hydrolysis of MAPTMS/TMOS was carried out in an ethanol/water solution. The prehydrolysis stage of this MAPTMS/TMOS system was monitored by FTIR, <sup>13</sup>C and <sup>29</sup>Si NMR liquid state spectroscopies. FTIR analysis indicated that the hydrolysis of the two precursors accomplished as far as the Si-OMe band, corresponding to unhydrolyzed silane, disappear. Kinetic studies about the MAPTMS and TMOS reaction were also carried out by using <sup>29</sup>Si liquid state NMR spectroscopy. The concentration of the alkoxy groups and the extent of self condensation of mono-, di-, and tri-substituted siloxanes (T species) in the sol were estimated applying this last technique. The hydrolysis of Si-OMe groups in the prepared sol was also evaluated by <sup>13</sup>C liquid state NMR spectroscopy. The

results indicated that under the adopted synthesis strategy conditions, the hydrolysis process require four hours to be accomplished. Finally SEM/EDX analyses were applied to study the morphology of the hybrid coating indicating that the prepared coating was homogenous, colourless, transparent and cracks-free.

**Conference** : 1<sup>st</sup> International Symposium on Colloids and Materials, 2011.Holland

**Title** : Development of bioactive and corrosion resistant organic- inorganic hybrid sol-gel coatings on Ti-6Al-4V surfaces

**Authors** : A.A. El hadad\*, A. Jiménez-Morales, V. Barranco, E. Peón, J.C. Galván

**Participation:** **Poster**

**Abstract** :Organic-Inorganic hybrid materials were prepared by hydrolysis and condensation of  $\gamma$ -methacryloxypropyltrimethoxysilane (MAPTMS) and tetramethoxysilane (TMOS). TMOS in hybrid coatings tend to impart durability, scratch resistance, and improved adhesion to the metal substrates. MAPTMS contribute to increase flexibility, density and to achieve tailored properties, such as hydrophobic properties. The resulting organic–inorganic sol–gel coatings were modified with the adding of hydroxyapatite (HA) particles during the first steps of the sol-gel process with the aim of generating bioactivity. The effects of curing temperature on the gel films with and without HA particles were examined using DTA/TGA. The surface of the coatings was analyzed by XPS. The application of XRD has provided information about the crystalline and/or amorphous features of the prepared coatings. FTIR-ATR has been utilized for studying the functional groups within the prepared coatings before and after immersion in simulated body fluid (SBF). The hydrophobic behaviour and thickness of the prepared coatings were evaluated by application of both contact angle measurements and profilometer. Inductively Coupled Plasma (ICP) has been used to detect the concentration of calcium and phosphorus ions released and re-precipitated on the surface of the prepared samples upon immersion in SBF. SEM/EDX has been applied to study the surface morphology of coated samples before and after immersion in SBF to detect the biomimetic precipitation of the bone-like apatite. The corrosion behaviour of metal/coating system in a SBF has been studied by electrochemical impedance spectroscopy (EIS). The Ti6Al4V alloy/HA-Hybrid coatings systems displayed excellent bioactivity when soaked in the SBF and acceptable corrosion protection behaviour.

## Conference communications

---

**Conference** : School of Science and Technology Research Conference **2011. UK**

**Title** : Preparation, Characterization and Corrosion Behaviour of Bioactive Organic-Inorganic Coatings on Ti6Al4V Surfaces

**Authors** : A.A. El hadad, D. Carbonell, A. Jiménez-Morales, V. Barranco, C.C Perry .J.C. Galván.

**Participation:** **Poster**

**Abstract:** Organic-Inorganic hybrid coatings were prepared by co-hydrolysis and polycondensation of  $\gamma$ -methacryloxypropyltrimethoxysilane (MAPTMS) and tetramethoxysilane (TMOS) and triethyl phosphite (TEP) through the sol-gel route. Mixtures of these three precursors with different molar ratios have been tested. The coatings were applied on Ti6Al4V alloys by immersion in freshly prepared MAPTMS-TMOS-TEP sols. The effects of TEP doping on the thermal stability of the prepared hybrids were investigated by using thermal analysis (TG/DTG). The application of X-ray Diffraction (XRD) has provided information about the crystalline and/or amorphous features of the prepared coatings. Attenuated total reflectance Fourier Transformer Infrared Spectroscopy (FTIR-ATR) has been utilized for studying the functional groups within the prepared coatings. The hydrophobic behaviour and thickness of the prepared coatings were evaluated by application of both Contact Angle and Profilemeter measurements. Scanning Electron Microscopy (SEM) coupled with an Energy Dispersive X-ray (EDX) system has been applied to study the surface morphology and composition of coated samples. Corrosion resistance of the prepared coatings immersed in simulated body fluid (SBF) was studied by Electrochemical Impedance Spectroscopy (EIS). The results showed the formation of uniform, homogeneous and crack free protective coatings on the Ti6Al4V surfaces. These Hybrid coatings displayed excellent bioactivity when soaked in the SBF and acceptable corrosion protection behaviour.

